THE UNIVERSITY OF SYDNEY

Characterisation of Additive Manufactured Metallic Materials

A thesis submitted in fulfillment of the requirements for the degree of

Doctor of Philosophy

Hoda Eskandari

Faculty of Engineering & IT/ Department of Mechanical Engineering

The University of Sydney

2021

Dedicated to my dearest;

Mom, Dad and Hossein

Statement of originality

This is to certify that to the best of my knowledge, the content of this thesis is my own work. This thesis has not been submitted for any degree or other purposes. I certify that the intellectual content of this thesis is the product of my own work and that all the assistance received in preparing this thesis and sources have been acknowledged.

Signed _____

Hoda Eskandari

March 2021

Acknowledgments

To Hossein, the most patient mate, who was the main reason for me doing this degree! I am more grateful to him than he'll ever know. He has my deepest thanks for giving me full free availability to focus on my work by managing all other aspects of our life all alone. His love made me strong in this journey.

I would like to express my sincere appreciation to my mother and father, who have inspired me every day from thousands of miles away. I am genuinely grateful to them for everything they did for me. Thanks for every single moment that they encouraged me with their unlimited love. Mehdy, and Tamara, thanks for supporting me emotionally and mentally during these years. Thank God for gifting me them as my main motivation.

I would like to extend my sincere gratitude for Professor Lin Ye's unique supervision. His unlimited support, continuous encouragement, and guidance are truly appreciated. Thanks for trusting and empowering me. Self equity was the most precious prosperity I achieved during this journey from his wisdom. I am privileged to work with such a prestigious academic. I also appreciate the guidance of my co-supervisor, Dr Li Chang.

I gratefully acknowledge Dr Mehdi Eizadjou, who was a lifesaver for me in this journey. His insightful knowledge, incredible patience, and excellence coaching style enhanced my motivation for this study at every turn. My deep gratitude goes to him for his unlimited availability to support me during this research. His attitude is unforgettable, and I will strive to follow his example in supporting others during my future career.

I gratefully acknowledge Dr Andy (Hongjian) Wang for his kind support, valuable suggestions and discussions. I remember him in both personal and professional aspects of life to help people making life easier. I was delighted to have him as a mentor in the office and advanced materials lab in J07. Thanks for being available Andy.

Thanks to the Australian government for the Australian Postgraduate Award (APA) that supported me financially while I conducted this research. I would like to acknowledge Professor Stefan Williams, Dr Gareth Vio for their consideration and support during these

years. I also greatly appreciated the support of the University's Higher Degree Research Administration office.

I thank Ms Bronwyn Sexton, a most intelligent and supportive administrative officer, dear Natasha Klansek, Ms Shirley Ali, and Peter Nguyen for IT and computer technical support.

I am grateful to Trevor Shearing, Dr Shao Cong Dai, Duncan Stenger, Greg Elder for his exceptional supportive attitude, Greg Riviere, Stanley Karkada, Robert O'Shannessy, and Daniel Lancaster for his all support at J07 during my research.

Sincere gratitude to my considerate friend, Warwick Holmes, who motivated me weekly, to Dr Matthew Dunn for being a supportive friend, and to Dr Andrei Lozzi.

I thank Melville McNair for his attention to detail when producing sample prints, from equipment set up, to delivery of print data, it was a pleasure to work with him and Advanced Manufacturing Services. To Dr Tony Dong (sales manager at MSC software) for his unlimited support for simulation part in this research.

Thank you to my dear officemates Qinghai He, Allen Jialun Cheng, Haoruo Zhou and Dr Xianghai AN for being supportive and friendly.

Special gratitude goes to Dr Hamidreza Lashgari for our fruitful discussion and for reviewing my research work.

To Dr Dara Tafazoli and Jo Tusek, who kindly reviewed this dissertation and provided feedback for its improvement.

To lovely Keren Reynolds, how wonderful it was to have your input during this journey, giving me the industrial perspective on my work. Neda and Omid, my dearest friends in Newcastle, I am grateful for your unlimited support in all aspects of my life during these years. I thank Samira and Farzaneh, my dearest friends for their continuous encouragement, Jessica, my dear friend; with whom I spent two years of university life, and Awais, my caring coffee friend from the combustion group.

Dr Rasoul Moharami (my former supervisor in Iran) and Dr Ho-Sung Kim (my former supervisor in Newcastle) thanks to both of you for helping me to achieve my goals.

I sincerely acknowledge the Australian Centre of Microscopy and Microanalysis (ACMM) for providing their facilities.

I acknowledge Dr Campbell Aitken, who provided professional editing services in accordance with the Institute of Professional Editors' *Guidelines for editing research theses*.

Abstract

Selective laser melting (SLM) is an additive manufacturing (AM) process with great promise for the production of customised, complex geometry end-use components for metallic materials. The main concern in the industrial application of SLM is ensuring that the resulting microstructural features and mechanical properties of the materials are comparable to or superior to those of conventionally manufactured ones. Hence, the process-structure-property relationship must be fully characterised in great depth to improve SLM products' quality. Most SLM products go through extensive post-processing, including heat treatment, to tailor their microstructure and performance. Adjusting microstructural constituents via post-strengthening treatments can produce parts with desired and optimum properties.

17-4 precipitation-hardened stainless steel (PHSS) is used in applications requiring high strength and moderate levels of corrosion resistance; it is commonly used in AM, and was the main material studied in this research. The titanium-aluminium-vanadium alloy Ti6Al4Va, which has sophisticated characteristics and diverse applications, was also studied.

The effect of the SLM process and subsequent post-heat treatments on the mechanical properties of 17-4 PHSS were studied as follows. Firstly, the microstructural and mechanical properties of SLMed 17-4 PHSS were characterised thoroughly to find the relationship between the SLM process and the intended mechanical properties of the resulting parts. The SLM process consisted of sophisticated induced thermal histories and reheating cycles, which can be assumed as complex applied heat treatment inherently. Secondly, the deformation mechanism and microstructural evolution of the SLM parts were investigated during in situ tensile loading. Thirdly, the SLM parts' properties were compared with those of conventionally manufactured ones. To enhance the SLM parts' mechanical properties and make them comparable to conventional ones, post-heat treatments were applied. The effect of a variety of industry-standard and non-standard heat treatment procedures on the microstructure and mechanical properties of SLM 17-4 PHSS were investigated comprehensively.

The evolution of microstructure and properties were studied using various techniques. Hardness, tensile and wear tests were applied to evaluate mechanical properties. The

microstructures were investigated by optical microscopy, scanning electron microscopy, and predominantly the electron backscatter diffraction technique.

The SLM 17-4 PHSS's tensile strength was inferior to that of the wrought parts. The total elongation to failure of the SLM part was slightly lower than that of the wrought one, although a higher retained austenite fraction ($\%\gamma$) was detected, related to induced flaws during SLM fabrication. Due to the lower %C and higher retained %γ, a transformation-induced-plasticity effect and consequently high strain hardening capacity was observed for the SLM part under tensile loading. The in situ tensile test showed that low-angle grain boundaries density and their corresponding misorientation increased as loading progressed and evolved into high-angle grain boundaries, leading to grain subdivision and consequent strengthening.

A solutionised-aged procedure enhanced the SLM 17-4 PHSS's elastic and yielding properties, due to the precipitation hardening mechanism, compared to the direct-aged process without solutionising. The elimination of the metastable γ during solutionising led to a lessening of strain hardening, and elongation to failure. When solutionising was not applied in direct-aged conditions, the precipitation hardening mechanism did not occur, attributed to the high solubility of Cu element in γ.

Despite the SLM parts' low hardness compared to the wrought equivalents, SLM wear loss was minor. The wear loss of the solutionised aged parts was lower than that of the direct-aged parts, and was correlated to their higher hardness.

In a separate sub-study, the mechanical behaviour and the microstructural evolution of SLM Ti6Al4Va parts were compared to those of the wrought parts. The built orientation effect (i.e. vertical and horizontal built parts) of the SLM process was also studied. Necessity in enhancing ductility at the expense of strength, was concluded since SLM Ti6Al4Va showed superior strength with inferior ductility compared to wrought parts.

The research demonstrates that, by implementing the proper post-heat treatment procedures, SLM 17-4 PH SS and SLM Ti6Al4Va parts can be given useful properties that enable them to have much wider application. As the central part of this study, the heat treatment effect highlights the post-treatments' efficiency and applicability for practical cases.

Table of contents

List of Figures

List of Tables

List of Abbreviations

AM	Additive Manufacturing
ANNs	Artificial Neural Networks
ASTM	American Society for Testing and Materials
BC	Band Contrast
BCC	Body Centred Cubic
CRSS	Critical Resolved Shear Stress
EBSD	Electron Backscatter Diffraction
FCC	Face Centred Cubic
FCG	Fatigue Crack Growth
HAGB	High-Angle Grain Boundary
HCP	Hexagonal Close-Packed
HV	Hardness Value
IPF	Inverse Pole Figure
IQ	Image Quality
KAM	Kernel Average Misorientation
KS OR	Kurdjumov–Sachs (KS) orientation relationship (OR)

LAGB	Low-Angle Grain Boundary
LoF	Lack of Fusion
L-PBF	Laser-Powder Bed Fusion
PBF	Powder Bed Fusion
PHSS	Precipitation-Hardening Stainless Steel
PIII	Plasma Immersion Ion Implantation
SEM	Scanning Electron Microscopy
SiC	Silicon Carbide
SLM	Selective Laser Melting
TB	Twin Boundary
TRIP	Transformation-Induced Plasticity
UNS	Unified Numbering System
US	United States
XRD	X-Ray Diffraction
3D	Three Dimensions/Three-Dimensional
2D	Two Dimensions/Two-Dimensional

Chapter 1 Introduction

1.1 Additive manufacturing

The American Society for Testing and Materials (ASTM) defines additive manufacturing (AM) as the "process of joining materials to make parts from 3D model data, usually layer upon layer, as opposed to subtractive and formative manufacturing methodologies"[1]. AM commonly known as 3D printing has existed since the 1980s, but it has only come into the mainstream spotlight in the last decade, and its use has grown almost exponentially ever since [2-4]. In the early days of AM technology, the most popular applications were production of prototypes for design verification, form and fit checking. After decades of intensive research and development in AM resources, processes AND software, applications such as tools, dies and moulds were developed, and AM began to be used to manufacture small or medium-sized end-use products. The direct fabrication of functional end-use products has now become the main application of AM technology [4]. AM technology developments led to improvements in fabrication speed, quality and accuracy, and in the products' properties. In addition, modern AM allows the production of sophisticated geometries with functionally graded material features [5]. Figure 1-1 shows the different rates of additive manufacturing embracement, according to Barnatt [6].

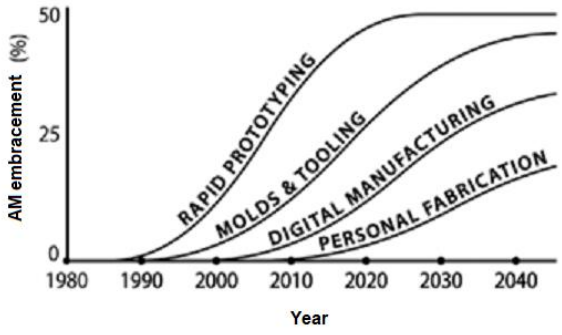

Figure 1-1 Additive manufacturing embracement curves [6]

Additive manufacturing can produce complex geometrical shapes, and enables cost-effective, low-volume production of customised and personalised parts with minimal waste using many types of materials [7]. The use of AM technology in health and medical systems means more and better surgical instruments and individualised implants and protheses, and AM's ability to manufacture parts rapidly will reduce patient waiting and recovery times [8-17]. Moreover, AM offers the ability to manufacture and repair defective metallic parts at sea, or even in space, using remote control. This technology's remarkable features have established a new production paradigm for the aerospace, medical, energy and automotive industries [2, 18-24], and has a vast range of other applications.

There are many ways to classify AM technology. Because the focus of this research is on metallic materials, the type of raw material (i.e. powder, wire) and type of applied heat/energy source (i.e. electron beam, laser, arc) are considered the key elements for the purposes of categorization (Figure 1-2 (a)). Figure 1-2 (b) represents the most common metallic AM classification scheme based on the combination of raw materials and energy sources [24].

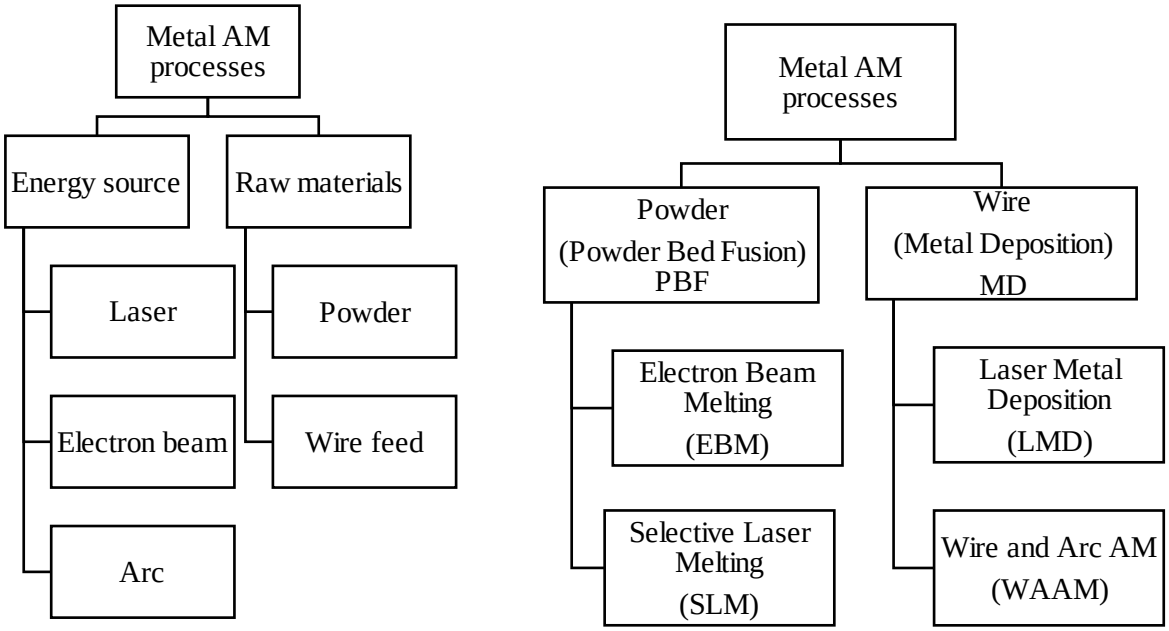

Figure 1-2 (a) Energy sources and feed stock materials in AM classification, and (b) common metallic AM processes.

1.2 Research gaps and Challenges

The main concern with AM technology, in comparison to conventionally manufactured products, is reliability. It is a big challenge for industries to trust AM technology for commercial applications, particularly sensitive ones.

The mechanical properties of AM parts are different from those of parts made using conventional methods. Although AM can fabricate end-use components, the mechanical response of AM parts under various loading conditions is not fully conceptualised. Due to variables such as loading types and environmental parameters, performance prediction is not entirely possible to date [21]. Moreover, processing, design and post-processing parameters increase the complexity of AM performance prediction.

Different microstructures, and consequently, different properties are formed due to the imposed thermal histories during AM processing and post-processing. This means that the performance of laboratory specimens does not represent that of parts in practical (industrial) applications due to design parameter effects. The mechanical testing methods for AM products and coupon design for AM requires further research. Post-processing treatment protocols used for conventionally manufactured materials cannot be applied to AM materials due to AM's distinct effects on the microstructure. Accordingly, the development of post-processing treatment protocols specifically for AM parts is vital.

1.3 Aims

This study examined state-of-the-art of AM metallic materials, emphasising the relationship between AM process/post-process, microstructure, and properties. Its general aim was to characterise the relationship between processing/post-processing, material microstructure and material properties of AM parts to overcome the uncertainty in worthiness. Characterisation of AM parts gives the ability to manufacture reliable components. It helps us enhance AM products' qualities by allowing the modification of processing parameters to eliminate induced AM defects, particularly residual stresses and microstructural heterogeneity. It also guides us to apply proper post-processing treatments to achieve desired mechanical properties for intended applications.

Researchers predict mechanical performance based on microstructures. Prediction is possible by understanding the interrelationship between processing parameters, thermal history, solidification, resulting microstructure and mechanical behaviour. This study aimed to identify the microstructural and mechanical properties of AM components for simulation and verification of predictive models.

A specific aim of this work was to investigate the mechanical properties and microstructural features of 17-4 precipitation-hardened stainless steel (PHSS) parts produced using selective laser melting (SLM) and compare them to those of conventionally manufactured parts to determine their reliability. The location dependency of microstructural features induced by SLM processing was explored to tackle AM products' geometry effect issues in order to understand the relationship between lab specimen dimensions and components. This may also help to improve the standard for test coupons design. Another specific aim was to investigate the effects of heat treatment procedures on the tensile and wear properties of SLM 17-4 PHSS to improve post-processing protocols. A third aim was to comprehensively characterise Ti6Al4Va alloy manufactured additively (using SLM) and conventionally one to explore SLM's impact on Ti6Al4Va's mechanical properties and investigate built direction dependency purpose.

This work was designed to improve our understanding of the key characteristics of SLM 17-4 PHSS and Ti6Al4Va to improve SLM properties for intended applications. It was intended that this study would produce a new understanding of SLM technology's current state and demonstrate how it can be applied for end-use industrial products.

1.4 Outline of the thesis

This thesis is organised as follows.

- Review of the literature is provided in Chapter 2.
- Chapter 3 described an investigation of the mechanical properties and microstructural features of wrought 17-4 PHSS. As-built SLM 17-4 PHSS properties were studied comprehensively to determine the manufacturing technique effect compared to conventional manufacturing method. The microstructural

features of as-built SLM 17-4 PHSS were investigated in multiple locations of 3D-printed parts to explore location dependency properties.

- The deformation behaviour of the as-built SLM part supported by the transformation-induced plasticity (TRIP) effect was studied during in-situ loading; this work is described in Chapter 4.
- Heat treatment is a way to achieve intended properties after fabrication. Chapter 5 outlines how the age-hardening heat treatment procedure (the standard heat treatment approach for traditionally manufactured PHSS) influence the properties. Heat-treating procedures were conducted using two methods; the first one labelled as prior solutionised parts as standard procedure and the second one without using solutionising so-called a direct aged method. (to evaluate if the SLM process has a similar influence on the direct aged parts as solution process for strengthening mechanism.) The resultant microstructure of each heat-treated condition is studied correlated to tensile properties to find the intended applications' optimum treatment procedure. Concisely, providing an authentic article of conventional heat treatment procedures' effect on the as-built SLM manufactured parts' performance is targeted. It is used to designate the proper heat-treatment(s) for the industrial applications. Also, predicting the non-standard heat treatment procedures' effect on developing the properties as the optimal procedures is another objective in this sub-study.
- Chapter 6 describes an investigation of wear performance as another mechanical property of SLM 17-4 PHSS parts. The wear performance of SLM and wrought parts was investigated under different testing conditions. Parameters such as speed, load, and environment were considered to assess their effect on tribology performance. The effects of heat treatment procedures (see Chapter 5) on wear performance and mechanism were studied.
- Chapter 7 presents a comparison of the mechanical behaviour of Ti6Al4Va alloy manufactured additively (using SLM) and conventionally. The SLM process effect on microstructural and mechanical properties – notably, the built orientation effect (horizontally and vertically built) – of products was investigated.
- Chapter 8 summarises and synthesises the research findings about the interrelationship between the applied SLM process/heat treatment and the materials' microstructure and properties. Ideas for future work are proposed.

Chapter 2 Mechanical Metallurgy of SLM 17-4 PHSS and Ti6Al4Va

This chapter contains a review of the essential literature. Firstly, a brief overview of the AM technique applied in this study, SLM, is given, focusing on effective processing parameters. Then, this study's materials – 17-4 PHSS and Ti6Al4Va alloy – are discussed from a metallurgical perspective. Their chemical compositions and their role, microstructural features (when conventionally manufactured), their real-world applications, and common post-processes for strengthening purposes are explained. Then, research on γ to α' phase transformation and vice versa, and the TRIP phenomenon, is reviewed. Strengthening mechanisms are explained briefly, and microstructural evolutions in SLM products are reviewed comprehensively. Induced SLM defects, particularly residual stresses, solidification, grains, and textures, are discussed as the keys in characterization. Finally, a short assessment of recent literature on the characterisation of SLM 17-4 PHSS and Ti6Al4Va is provided.

2.1 Selective laser melting

As explained earlier, additive manufacturing involves the formation of objects from raw materials by converting a 3D model into a series of thin layers and then integrating the layers using an energy source. In this manufacturing method, objects are created by accumulating raw materials, rather than subtracting them, until the desired object is formed.

Understanding the capabilities and complexities of different AM techniques is required to select the appropriate one for a particular material. Type of heat/energy sources (e.g. laser, electron beam, plasma arc, metal arc), type of raw feedstock materials (e.g. powder, wire, sheet), stacking mechanisms (e.g. fusion, deposition), production quality, leading time, size, and cost are the criteria considered in AM classification and technique selection for the intended applications [21].

Powder bed fusion (PBF) is one of the most common powder-based AM techniques for metal manufacturing. SLM is a PBF process that uses a laser as an energy source, and is highly

suitable for the manufacture of metallic parts additively. In SLM, a thin layer of metal powder is selectively melted/sintered by a laser, and components are built up layer by layer in a bed of powder. The laser tip imparts a high thermal shock to powder particles, forming micro-sized melt pools. Laser tip movement in a defined pattern (a so-called scan strategy) solidifies melt pools rapidly, and an individual track is formed. The integration of individual laser tracks within a plane forms a layer, and this process is repeated until the final part is generated (refer to Figure 2-1). Then, products are detached from the substrate by machining, and often require additional surface operations to achieve the required surface quality. Parts with hanging features may need a support structure during AM fabrication to prevent distortion caused by heat or the object's weight [25-27].

Selective laser melting products have lower residual stresses and fewer internal defects than other AM metal products, making them suitable for critical components (such as aerospace or automotive parts). High precision and dimensional accuracy (ability to produce small pieces), powder efficiency, and high-quality surface finishes are other characteristics of SLM parts; however, they are costly and time-consuming to produce [7],[28].

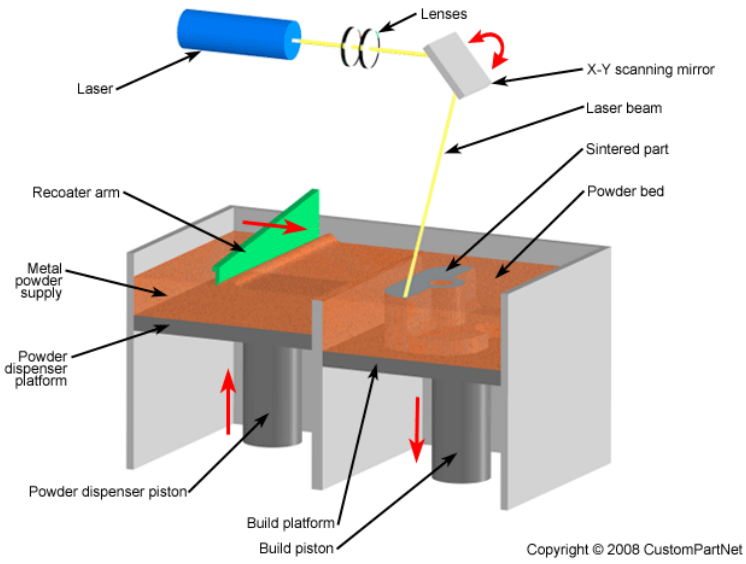

Figure 2-1 Schematic of the SLM process [29]

Further study of effective processing/post-processing parameters in SLM products is essential. SLM products experience different thermal histories during fabrication and post-fabrication; consequently, different microstructure and properties are achieved. Processing parameters such as laser power, laser speed, layer thickness, hatching pitch, scanning strategy (pattern) and

chamber atmosphere during fabrication are the most influential parameters in SLM product properties. Post-processing (e.g. heat treatment, surface treatment, hot isostatic pressing) [30-39] and design parameters (e.g. built orientation, size, and geometry of products) add more complexity to characterisation [35, 40-44].

In AM, raw materials' energy absorption affects temperature profiles, molten pool geometry, solidification microstructure, and properties. Energy absorption depends on the heat source characteristics. For lasers, the heat energy source in the SLM technique, radius, and power density distribution are important properties [45].

Powder particles are used as a feedstock for powder-based AM techniques. Fabricating high-quality powder particles is challenging due to their high sensitivity to oxidation and absorption of moisture and other contaminants. Hence, it is crucial to evaluate powder particle production methods and their performance during the AM process. Powder particle characteristics include shape, size distribution, surface morphology, powder chemical composition, and flowability. Particle size in the SLM method typically is in the range of 10–60 μm [46].

In the SLM process, all the energy from the source is transferred to the powder bed as heat. When a laser beam penetrates a particle, part of the energy is absorbed by the powder particles, and the rest is reflected until the beam emerges from the powder bed. The heat absorbed by the particles in the powder bed depends on the particle size, the density of the powder bed, and the material's properties.

Figure 2-2 shows the heat transfer during SLM fabrication. The mechanical properties and product quality depend directly upon the materials' physical behaviours, controlled by the processing parameters. The heat transmits from the laser action zone to its surrounding area by conduction, convection and radiation, and the heat ultimately dissipates via metal evaporation mechanisms.

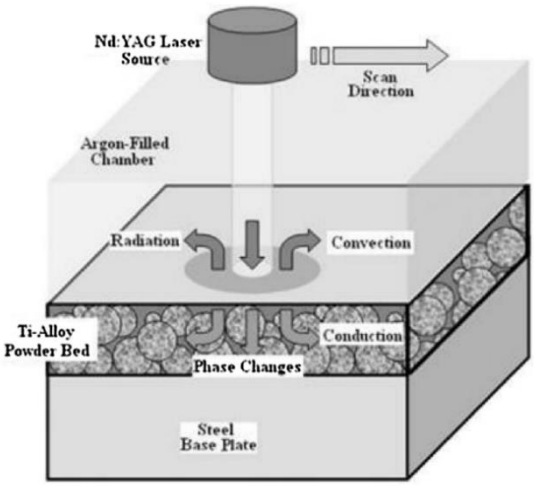

Figure 2-2 Interaction of laser beam and powder particles in the SLM process [47]

2.2 **Materials**

Various metal alloys can be processed using the SLM technique. As noted already, this project focused on 17-4 PHSS and Ti6Al4Va alloy. Table 2-1 indicates industrial sectors that typically employ these two groups of alloys.

Table 2-1 Stainless steels and titanium alloys – common applications [4]

Applications	Stainless Steels	Ti alloys
Aerospace	✓	✓
Medical	✓	✓
Energy (oil & gas)	✓	
Automobile	✓	✓
Naval	✓	✓
Welding & machinery	✓	✓
Corrosion resistance	✓	✓
Elevated temperature	✓	✓
Tools & dies and moulds	✓	
Consumer	✓	

2.3 17-4 Precipitation-hardening stainless steel

The selection of stainless steel as a material for study in this project was based on its corrosion resistance, fabrication characteristics, availability, mechanical properties in specific temperature ranges, and the cost of products.

Stainless steels are iron-based alloys containing at least 10.5% Cr [48]. Most stainless steels' mechanical properties, particularly ductility and toughness, are higher than those in carbon steels. Stainless steels are generally categorised into five groups: martensitic, ferritic, austenitic, duplex (ferritic-austenitic), and PHSSs. PHSSs are Cr-Ni alloys containing precipitation-hardening elements such as Cu, Al, or Ti. In most cases, PHSSs attain high strength from precipitation hardening in the martensitic matrix structure. PHSSs are categorised by their dominant microstructures as austenitic, semi-austenitic, and martensitic. Martensitic PHSSs, so-called maraging stainless steels, are strengthened from precipitation hardening by nanometer precipitates; further strengthening comes from their martensitic matrix. They are generally heat-treated for end-use products [49].

17-4 PHSS (american iron and steel institute (AISI) Type 630 or unified numbering system (UNS) S17400) is low-carbon precipitation-hardened martensitic stainless steel containing chromium and nickel. It is used extensively due to its combination of high strength, toughness, resistance to corrosion, wear, and weldability at typical service temperature below 300°C [50, 51]. 17-4 PHSS's weldability makes it suitable for AM/SLM technology.

17-4 PHSS is the most commonly used PHSS. It is used in many applications requiring high strength and moderate corrosion resistance levels, such as in the chemical, aerospace, marine and nuclear industries. Heat exchangers, superheater tubes, turbine blades, valves, shafts, fasteners, gears, springs, fittings, machinery tools and surgical instruments are some of its many applications [52-57].

2.3.1 Chemical composition

Table 2-2 shows 17-4 PHSS's chemical composition, which conforms to UNS classification 17-4 equivalent to the ASTM A564/A564M. Each element's known effect on PHSS microstructure and mechanical properties, enabling prediction of designed microstructures in SLM process fabrication, is discussed in this section [58, 59].

Table 2-2 Chemical elements wt.% requirements for S17400 UNS designation [48]

Alloying elements wt-%	Fe	C	Mn	Si	S	P	Ni	Cr	Mo	Cu	Nb
ASTM A564/A564M Limits	Bal	max. 0.07	max. 1	max. 1	0.03	0.04	3–5	15–17.5	max. 0.5	3 - 5	0.15–0.45

The chemical elements shown in Table 2-2 are characterised below.

- Carbon (C) is essential for hardening and controlling hardness, strength, and weldability.
- Manganese (Mn) is the austenite (γ) phase stabiliser. Mn combines with sulphur (S) and forms globular MnS sulphides beneficial for machinability by reducing brittleness from S. MnS sulphides prevent the further destructive formation of FeS. Iron sulphide (FeS) formation causes cracks in welding structures and SLM parts.
- Silicon (Si) stabilises the ferrite (α) phase and reduces strength. It works as a deoxidiser in steel production by eliminate welding contamination. To overcome α stability, Si is balanced with chromium (Cr) and nickel (Ni) elements due to their γ stabiliser feature.
- Chromium (Cr), a crucial element in corrosion resistance alloys, increases yield strength. Cr forms a surface layer to protect against oxidation. The presence of C, along with a large amount of Cr, results in the development of chromium carbide $Cr_{23}C_6$ along grain boundaries.
- Nickel (Ni) is another key element in stainless steels; it is beneficial for corrosion resistance, and improves toughness, especially fracture toughness. It has no detrimental effect on weldability. Ni is often used in combination with Cr and molybdenum (Mo).
- Copper (Cu) is another corrosion-resistant element. Cu is the main element in the formation of precipitates to increase strengths and hardening. A low fraction of Cu indicates this element's complete solubility in the γ phase; therefore, a minimum fraction of Cu is crucial for precipitation strengthening.

- Niobium (Nb) refines grain sizes and consequently, is a strength enhancer. Nb combines with C to form very hard, fine carbides (NbC). However, Nb is used to reduce the formation of $Cr_{23}C_6$ carbides.
- Molybdenum (Mo) is added as an anti-corrosion agent in stainless steel. Mo is a strong carbide former.
- Nitrogen (N) stabilises the γ phase, and prevents the formation of $Cr_{23}C_6$ precipitates, generating smaller Cr_2N precipitates instead.

Slight variations in element concentrations causes a remarkable modification in PHSS products' resultant phase fractions, as Vunnam et al. proved in SLM 17-4 PHSS products [60].

2.3.2 Overview of equilibrium and non-equilibrium 17-4 PHSS

In the Fe-Cr-C equilibrium phase diagram in Figure 2-3 (a), the dashed line shows the position of 0.05% C. By cooling 17-4 PHSS, the cubic body centred cubic (BCC) δ ferrite phase is transformed to the cubic face centred cubic (FCC) γ phase. With a further temperature reduction, γ becomes the BCC α ferrite phase complement $Cr_{23}C_6$.

During rapid cooling in casting, welding and SLM processes, non-equilibrium phase transformation occurs. The chromium-nickel composition of 17-4 PHSS after quenching is plotted in Figure 2-3 (b). The diagram shows that it lies in the composition region where rapid cooling produces a α' structure. In this steel, the final strengthening precipitation occurs when the alloy has a α' matrix structure. (A detailed ternary phase diagram of 17-4 PHSS at temperatures corresponding to standard heat treatment procedures is provided in 5.3.1.)

Microstructural evolution during standard heat treatments occurs as the following. In the solutioning step, 17-4 PHSS is heated to temperatures above AC_3 to create a solid solution. After heating, the PHSS is quenched to produce a solid supersaturated state. During quenching, α' laths structures, free from internal twins with high dislocation density, are mostly formed. The transformation from the γ to the α' is nearly complete in the as-quenched condition, which may contain both α ferrite and γ. Simultaneously, second phase precipitates, as well as carbides, are nucleated during cooling. Note that a higher number of nuclei with smaller sizes is formed by applying a higher cooling rate. Clustering may also occur by the segregation of solute atoms during cooling. Thus, the final structure of the 17-4 PHSS, after quenching, remains in the form of an α' background with a small amount of α and γ.

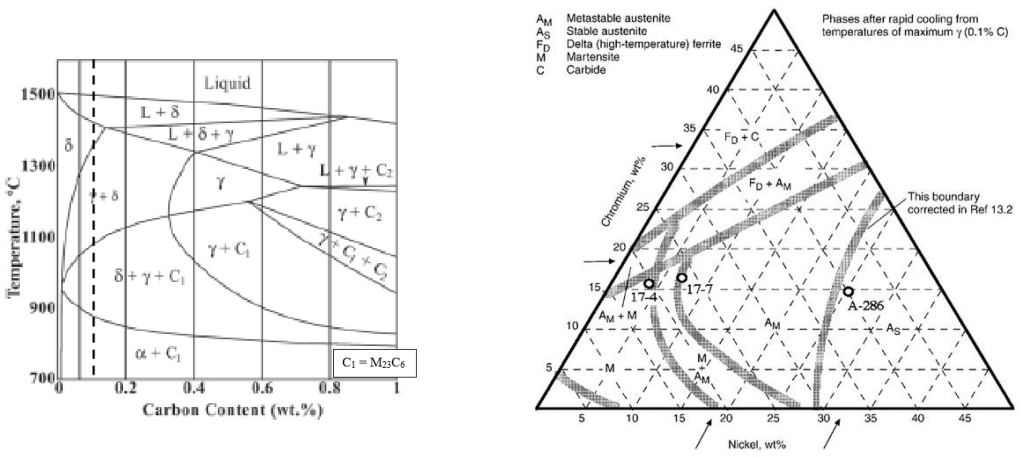

Figure 2-3 (a) Fe-Cr-C equilibrium phase diagram for %17 Cr in the composition [61], (b) non-equilibrium phase diagram plotted on the metastable phase diagram [62]

After solutionising and quenching, the 17-4 PHSS's primary martensitic microstructure is supersaturated with Cu-rich nanometer precipitates. Next, for the purpose of age-hardening, the material is held at temperatures below AC_3 (the typical temperature range of 480–620℃) for precipitation formation, followed by quenching [48]. Briefly, the hardening process is dominated by the Cu precipitate in the α' matrix after formation of a high-temperature solid solution and subsequent ageing heat treatment.

The chemical composition of the age-hardening precipitates is associated with the chemical composition of the alloy. The precipitate's formation and evolution from BCC Cu → 9R→ 3R→ FCC ε-Cu is achieved by increasing temperature and soaking time in ageing procedures. Formation of FCC ε-Cu precipitates at an ageing temperature above 470℃ has been reported [61, 63].

Standard ageing heat treatment procedures are provided in detail in 5.2.1, but are summarised here. At an ageing temperature of 480℃ for 1 hr (the H900 condition), the precipitation begins with Cu-rich precipitates. Maintaining a coherent relationship with the matrix leads to an increase in tensile strength and toughness. These precipitates transform into non-coherent Cu-rich particles from the matrix structure after extended ageing at 550–620℃. By increasing ageing temperature and soaking time, the precipitates grow. Simultaneously, their number decreases, and their coherence with the matrix is demolished. These alterations lead to a reduction in strength and enhancement of ductility and impact toughness [62].

As mentioned, carbides ($Cr_{23}C_6$, NC) are formed during the age-hardening procedure. $Cr_{23}C_6$ are shaped along the grain boundaries, and their growth strengthens the alloy.

Mirzadeh and Najafizadeh [64] studied the influence of ageing condition and the precipitation kinetics of 17-4 PHSS. The effect of ageing temperature and soaking time on this steel's strengthening behaviour was modelled and analysed using artificial neural networks (ANNs). The hardening, over-ageing and softening outcomes of ageing reactions (precipitation and coarsening of Cu, recovery, and reversion of α' to γ) were determined from this ANN model [64].

2.3.3 Phase components; austenite & martensite

There are two forms of austenite (γ) phases in 17-4 PHSS microstructure [30, 65, 66]. The first type, retained γ, which refers to the γ not being converted to α' during rapid cooling, is often observed in prior γ grain boundaries and along the grain boundaries of α' laths. The fraction of retained γ in the final microstructure depends on the α' transformation finish temperature (M_f) and cooling rate. This means that by cooling to a temperature higher than M_f, retained γ is residue, because the α' transformation has not been completed. Due to the similarity of the SLM process and welding, microsegregation leads to regions around boundaries enriched in γ stabiliser elements, increasing γ stability. Retained γ often reduces yield and ultimate strengths, but increases ductility and impact toughness.

The second γ type, reverted γ, is formed during age treatment. As the applied heat temperature lies in the γ reversion line (γ starting temperature), α' is converted to γ after heating up. Reverted γ is randomly distributed in the microstructure and typically has a block morphology, while retained γ forms along α' lath boundaries in a lath-shaped morphology. Reverted γ is also located close to the precipitates region, where it is enriched by γ stabiliser elements. Reverted γ, affects strength and ductility like retained γ, but has a lower impact. Reverted γ is enriched in Ni and Mn, so they stabilise the γ and consequently postpone α' transformation under mechanical loading compared to retained γ. Chemical composition, α' parent grain after solutionising, ageing temperature and holding time, and heating rate are influential factors in reverted γ formation and fraction.

Martensite (α') is a very hard phase which forms from rapid cooling (quenching) of steels to room temperature from γ temperature. Due to rapid cooling, diffusionless transformation

occurs. (Because the cooling time is concise, C atoms cannot diffuse and remain in a new phase.) α' transformation results from γ deformation, and ultimately results in volume expansion via a shear mechanism.

The structure of α' is a set of packets, blocks and laths (Figure 2-4). Prior γ grains form the packets, which contain the blocks. Laths are formed in the blocks, and they are divided by low-angle grain boundaries (LAGBs) while high-angle grain boundaries (HAGBs) divide the blocks. Applying heat treatment modifies the boundaries and consequently tailors the properties.

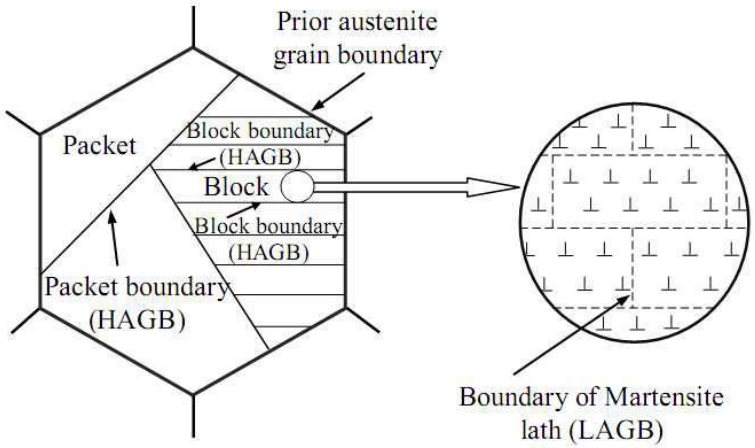

Figure 2-4 Hierarchy in the structure of the α' structure [67]

Due to the C fraction, different morphology of α' forms. For %C<0.5, α' is lath-shaped or plate-shaped in a fully dislocated form.

α' fraction depends on the cooling temperature in quenching and the difference between it and the α' finish temperature. The extent of α' formation is calculated using the Koistinen-Marburger equation [68]:

$$f_{\alpha'} = 1 - \exp\left[-\beta - \left(M_s - T_Q\right)\right] \qquad \text{Equation 2-1}$$

Where $f_{\alpha'}$ is the extent of the α' phase, β is constant and equals -0.011, and T_Q is the quenching temperature. The starting α' temperature depends on the chemical composition and γ parent grain size. (As will be described, chemical composition and parent γ grain size are the most influential parameters in γ stability.)

The Barbier equation describes the chemical composition's effect on the starting α' transformation temperature M_s [69]:

$$M_s(°C) = 545 - 601.2(1 - \exp(-0.868[C])) - 344[Mn] - 1.4[Al] - 1.7[Si] - 15.4[Mo] - 9.2[Cr] - 17.3[Ni] + 10.8[V] + 4.7[Co] - 16.3[Cu] - 361[Nb] - 2.44[Ti] - 3448[B] \quad \text{Equation 2-2}$$

Where [X] is the chemical composition of element X in wt.%.

This study involved fresh and tempered α'. Brittle fresh α' after quenching converts to tempered α' after the ageing processes, which give higher toughness and lower brittleness. Tempered α' can be distinguished from fresh α' by the presence of carbides and precipitates.

2.3.4 Austenite stability

α' transformation progression, which occurs through heat treatment and mechanical loading (stresses), gives rise to γ stability. Modifying M_s and M_f alters the stability of γ and the extent of retained γ after rapid cooling. γ stability can lower M_s to below room temperature. Note that retention of γ has a linear relationship with lowered M_s. Effective factors in γ stability are listed below [66]:

- Chemical composition has a key role in γ stability and phase(s) fraction. C, Mn, Ni and Cu are γ stabilisers, and they increase γ stability towards α' transformation.
- Prior γ grain size has a prominent role in γ stability. By reducing γ grain size, the required energy to progress α' transformation increases. Refined γ grains lower the starting α' transformation temperature, and stabilise the γ. It is worth mentioning that, after reaching a certain size, α' transformation does not progress.
- Morphology of prior γ grains is another parameter that affects the γ stability. Lath-shaped γ grains have higher mechanical stability than block-shaped ones. Lath-shaped morphology results from higher cooling rates. Lath-shaped γ grains have a higher interaction area so can allocate more γ stabiliser elements.
- Mechanical γ stability is mainly defined by dislocation density. Generally, the level of dislocation density in γ grains determines the stability and governs the α' transformation progression.

- Stress and the strain domain are the other factors that influence the γ stability, which controls the α' transformation progression. Due to high regional stress in prior γ grain boundaries and triple junctions, α' transformation of γ grains located in those regions is increased. The probability of α' transformation in retained γ located in prior grain boundaries and triple junctions is higher than in reverted γ, which is dispersed in random places inside grains.

To sum up, γ stability results from multiple sources. They consist of the chemical composition of the material, supersaturated γ fraction, dislocation density, residual stress, prior γ grain size and morphology, the chemical composition of the retained γ and the size and morphology of retained γ grains.

2.3.5 Transformation-induced plasticity

In this section, the γ stability effect on non-equilibrium α' transformation in the TRIP effect and deformation mechanism is discussed [66]. Chemical composition and prior γ grain size are the main influences on the TRIP effect, but there are other important parameters. Figure 2-5 shows a schematic of γ/α' evolution at different strains when stress is applied. Metastable γ progresses α' transformation.

For lower %C, α' transformation starts (yields) in lower strain; in other words, occurs faster under loading. Accordingly, strain hardening rate and formability increases. It is worth mentioning that, in TRIP-assisted steels, the deformation mechanism relies on γ fraction and its stability. The certain fraction of γ is essential for having a TRIP effect in steels.

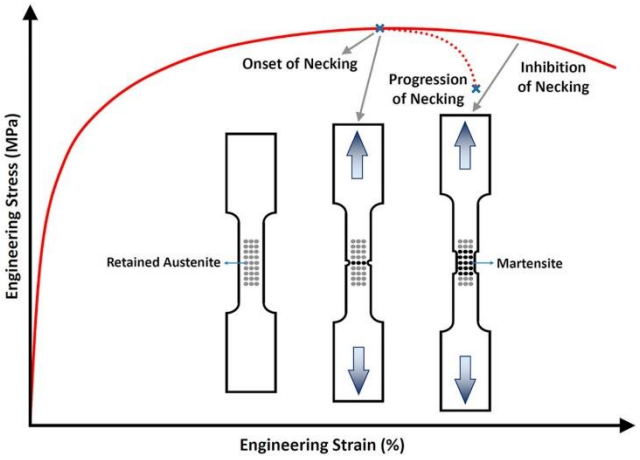

Figure 2-5 Schematic of the TRIP effect displaying that retained γ transforms to α' when the stress is applied [70]

Increasing applied tensile load and strain increases the fine γ grain fraction by reducing average austenite grain sizes. Along with γ grain refinement, mechanical stability (dislocation density pile-up) increases and α' transformation progression becomes harder. In other words, the required shear stress to start α' transformation, which is begun by plastic deformation, becomes greater, defined by the Hall–Petch relationship, as below:

$$\Delta\sigma_{GS} = \sigma_0 + K * d^{-1/2} \qquad \text{Equation 2-3}$$

Where $\Delta\sigma_{GS}$ is requisite shear stress, σ_0 is the friction stress (or Peierls–Nabarro stress), K is the Hall–Petch parameter, and d denotes the grain size.

The slope of a plot of $\Delta\sigma_{GS}$ versus d is K, which denotes the extent of dislocations pile-up at grain boundaries. The intercept σ_0 shows the stress required to drive a dislocation against the resistance of precipitates, impurities, LAGBs and the Peierls–Nabarro force.

It is worth mentioning that α' transformation during loading starts with coarser prior γ grains, which have lower stability and mean transformation develops more easily. The morphology of γ is another influential factor in γ stability. Lath-shaped γ grains are more stabilising than globular-shaped ones, since chemical elements such as C and Mn can be absorbed more easily in those regions due to longer paths. Indeed, elongated lath-shaped γ grains cause α' transformation at higher strain. The dislocation density in γ stability is the other factor in α' progression. Dislocation density inside the γ grains increases with loading progress; hence,

higher stability and lower transformation results. (Dislocation density pile-up occurs in loading, which makes the progression harder due to higher interaction of newly formed dislocation (from Frank-Reed sources) during loading [71].)

2.3.6 Strengthening mechanisms

Plastic deformability of metal materials is associated with the ease of dislocation motion; the formation of any barriers against them is called strengthening. In this section, strengthening mechanisms are discussed briefly, focusing on precipitation hardening. The plastic deformation behaviour of polycrystalline metal materials is affected considerably by grain and sub-grain boundaries, solid solution characteristics, and dispersion of secondary phases [71]. Figure 2-6 presents a schematic of the types of strengthening mechanisms.

- *Grain boundaries*

Since the lattice structure of neighbouring grains varies in orientation, it requires more energy for a dislocation to change direction and travel into the adjacent grain. As a result, increasing grain boundaries – particularly HAGBs acting as barrier points against dislocation motion – impede dislocation propagation, and consequently higher load/stress is vital to progress plastic deformation.

Grain size has a quantifiable effect on hardness, yield and tensile strength, fatigue strength, and impact at room temperature. (Refer to Equation 2-3 for the Hall–Petch relation.) The effect of grain size is significant for properties correlated to the early stages of tensile properties, mainly elastic region ones. Grain size is not a controlling variable in the later stages of deformation after yielding, and the strength is mostly controlled by complicated dislocation interactions within the grains. As a result, grain size has a greater influence on yield stress than tensile strength. [71].

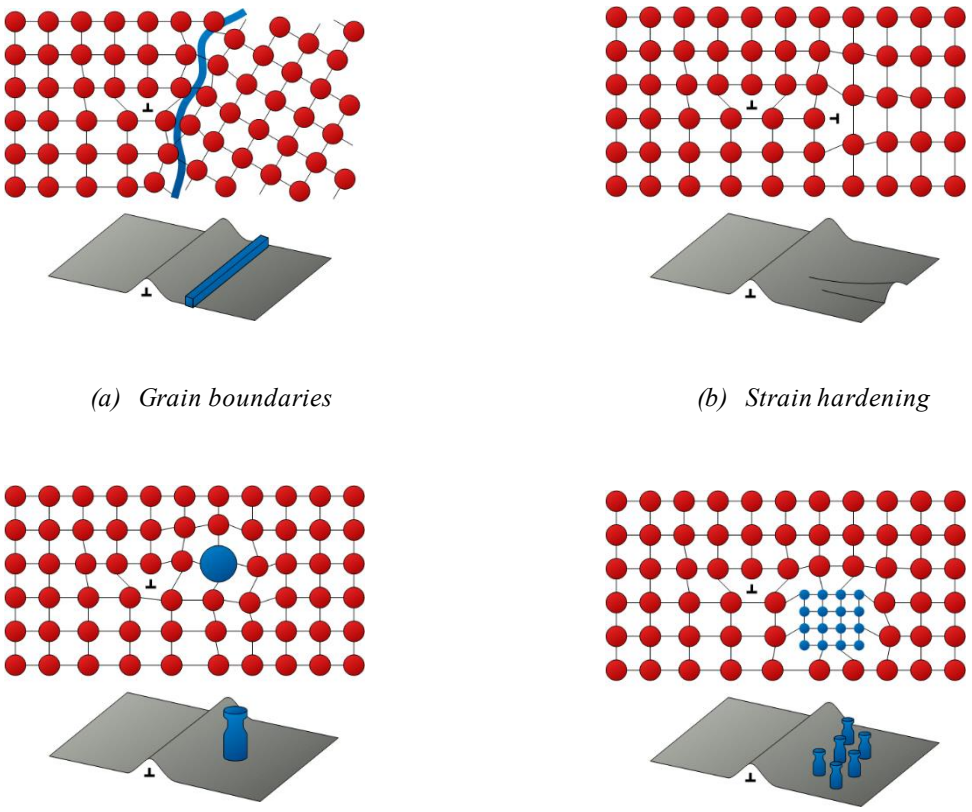

(a) Grain boundaries *(b) Strain hardening*

(c) Solid solution *(d) Age hardening*

Figure 2-6 Strengthening mechanisms as (a) grain boundary, (b) strain hardening, (c) solid solution, and (d) age-hardening mechanisms [6]

- *Strain hardening*

Strain hardening, also known as work hardening, is the increase in the required stress to create slip as a result of progressed plastic deformation. The first theories for strain hardening are explained by piling up new introduced dislocations on slip planes at boundaries. Piling up of new dislocation blocks each other's movement and consequently hardening occurs in the material [71].

- *Solid solution*

Solvent atoms in solutions change the ease of dislocation density motion based on the atom's size compared to solution atom sizes. With solid solution hardening, foreign atoms block the dislocation movement. Worth to mention that solute atoms preferentially aggregate near dislocations, stacking faults, LAGBs, and grain boundaries [71, 72].

- *Age hardening*

In precipitation/ age hardening strengthening mechanism, solubility of the second phase at the elevated temperature is vital and solubility should be decreased by lowering temperature. Formation of a coherent structure in a precipitation mechanism happens in two steps; solutionzing, and aging. In solutionizing step, the alloy is heated up to the single-phase temperature to be in solid solution condition. Later, by rapid cooling to room temperature, super saturated solution is formed. In aging step, during cooling, second phase particles are generated depending on the rate of cooling, increasing rate creates higher number of particles with smaller sizes. By fast cooling, sometimes in solutionized step, and mainly in aging step, aggregation of the second phase atoms, so-called clustering, occurs. Clustering causes localized strain and therefore increases the hardness (GP1). Hardness enhancement continues by ordering in clusters (GP2). With increasing temperature and aging time in a specific condition, precipitation formation is started and coherent structure forms (GP3). Afterwards, there is a specific condition in terms of temperature and aging time which creates the highest strength in the material. With increasing temperature and aging time, coherency is decreased and lowered the hardness consequently. Figure 2-7 shows the variation of strength during aging progression and precipitation particles growth. It is quite common for a coherent precipitate to form and then lose coherency when the particle grows to a critical size.

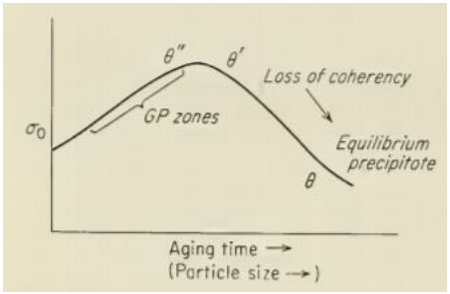

Figure 2-7 Variation of yield stress with aging time [71]

Dislocation movement is prevented by the coherent and semi-coherent precipitates and finally the dislocations shear through the particles. In the presence of non-coherent precipitations, dislocations bend to pass the precipitates.

The Freidel equation shows the relationship between shear stress and spherical particle size as:

$$\tau_p = A\Delta^{\frac{2}{3}}(\frac{rf}{2S})^{\frac{1}{2}}$$ Equation 2-4

Where τ_p is critical resolved shear stress (CRSS), A is constant, Δ is the interaction term between particle and matrix, S is dislocation line tension, r is particle radius size, and f is volume fraction. The equation shows that with increasing the particle size, the CRSS also increase which is an indicative of hardness measurement.

Equation 2-4 shows that as the particle's size increases, so the stress required for a particle to shear increases as well. It is understood that the strength increases due to precipitation depends on the stress it takes for dislocation lines to shear a particle. Suppose the alloy is held at a high enough temperature; in that case, the precipitates will continue to grow because larger precipitates are more thermodynamically favourable, increasing the shear stress and subsequently the strength. Eventually, the particles' growth reaches a point where the particles become incoherent, and the lattice planes of the precipitate no longer line up with the matrix. At this point, the dislocations will climb around the particles rather than shearing through them, which decreases the material strength. When the dislocations begin to climb around rather than shear through the particles, Equation 2-4 is no longer applicable because larger particles will be growing at the expense of smaller particles. The radius (r) increases, but the volume fraction (f) will remain constant. This theory can be used to interpret the ageing response [71].

2.3.7 Wear performance of 17-4 PHSS

The american society for metals (ASM) defines wear as "mechanically induced surface damage that results in the progressive removal of material" [73]. Wear is one of the most destructive processes in industries. Wear characteristics are crucial material properties that should be considered in the practical usage of SLM parts.

The most critical criterion in selecting steel for components subjected to wear is hardness. Corrosion resistance is another crucial factor due to the acidity, humidity and high temperatures in many applications. PHSS can fulfil the combination of high hardness, toughness and good corrosion resistance. As a result of PHSS's importance in industrial applications, degradation mechanisms – wear, corrosion, and tribocorrosion – in martensitic stainless steels were recently reviewed comprehensively by Dalmau et al. [74].

Wear performance is governed by how a solid body's surface can dissipate energy applied to it from external sources. The shaded bar in Figure 2-8 represents the division of the existing energy into a surface. Though, not all frictional energy chances into heat; part of it forms new surfaces by deforming and rupturing the material. A good wear-resistant material should scatter heat well and minimise the energy going into fracturing, plastic deformation or microchip cutting.

The most typical wear mechanisms identified in heat-treated and non-heat-treated martensitic PHSS are ploughing (abrasive) and adhesive wear. Due to the significant influence of precipitates and particles in the wear mechanism and wear performance transition of 17-4 PHSS, the addition of NiB to increase the wear resistance of injection-moulded 17-4 PHSS was explored [75]. The authors reported decreased weight loss and rate in sliding wear tests. Plastic deformation and delamination in surface were also reduced by NiB addition.

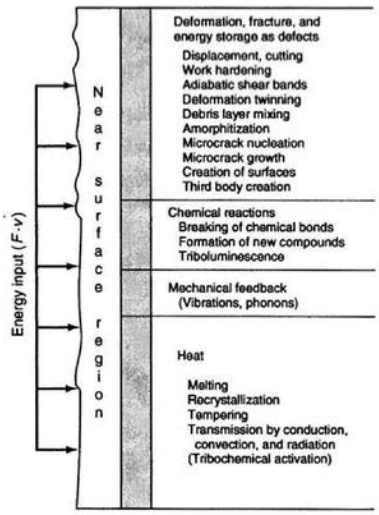

Figure 2-8 Distribution of energy from the surface contact [73]

Martensitic PHSSs display high surface hardness; the presence of carbides/precipitates stimulates formation of hard wear debris and three-body abrasive wear. Figure 2-9 (1) shows a schematic illustration of the main wear mechanism while wearing in a dry contact.

Microstructure plays a vital role in the wear behaviour of martensitic PHSSs. The amount of retained/reverted γ and the number of carbides and precipitates in heat-treated conditions alter the wear behaviour. The schematic representation of abrasive groove formation in tool steel with retained γ (Figure 2-9 (2a,2b)) shows stress-induced α' transformation [74]. It was concluded that the stress-induced transformation of the retained γ in the studied material (up to

15% γ) into α' resulted in high work hardening capacity; it decreased the wear coefficient while increasing the applied load. Accordingly, once the material with high strain hardening capacity is worn, there is probably high uniform plastic toughness, which hinders failure if the strength and hardness are high enough.

Figure 2-9 (2c,2d) presents a microstructure containing precipitates and carbide particles dispersed in a martensitic matrix conducting wear loading [76]. Once carbides/precipitates are present in the microstructure the extraction of these carbide particles (depends on the size and coherency of them) governs wear mechanism.

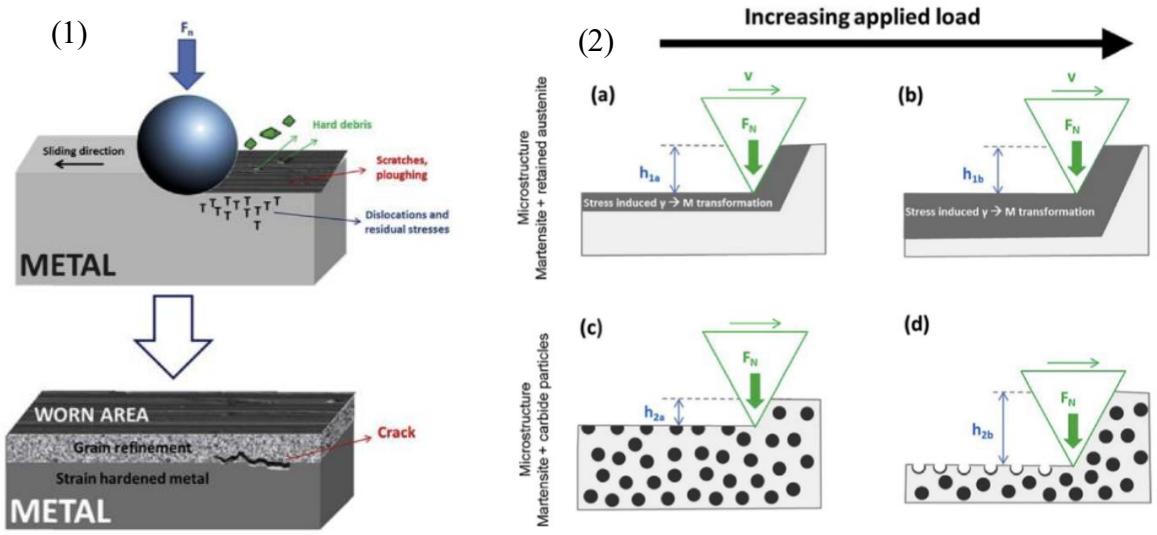

Figure 2-9 (1) Illustration of the main wear mechanism of martensitic PHSSs in a dry contact [74], (2) wear mechanism combined with α' transformation and also in the presence of carbides/precipitates [76]

Much research effort has been directed towards minimising the wear rate in martensitic SSs. Most studies have focused on surface treatments and coatings applied to martensitic SSs to expand bulk materials' wear resistance. Esfandiari and Dong investigated the effect of a plasma nitriding process on corrosion and corrosion–wear behaviour of 17-4 PHSS [77]. They found that the applied plasma nitriding treatments significantly improved the surfaces' hardness and enhanced wear resistance. Manova [78] investigated the wear behaviour of PHSS after plasma immersion ion implantation (PIII) surface treatment to screen surface treatment effect. He concluded that PIII nitriding of martensitic steel is a promising method of enhancing wear behaviour.

2.4 **Ti6Al4Va**

The element titanium (Ti) was recognised for 200 years, but only in the last 40, it came to the mainstream only in 40 years. Ti6Al4Va was developed in the early 1950s, and counts as main supplier titanium alloy for the market in the United States (US). Titanium and its alloys show the highest strength-to-weight ratios of all metals at temperatures up to 550°C. High reactivity with oxygen causes an advantageous property of titanium, namely its corrosion resistance. The titanium industry's rapid growth is testimony to titanium's useful combination of low density, high strength and corrosion resistance [79].

Titanium exists in two crystallographic forms. At room temperature, unalloyed (commercially pure) titanium has a hexagonal close-packed (HCP) crystal structure referred to as alpha (α) phase. At 883°C, this transforms into a BCC structure known as the beta (β) phase. The manipulation of these crystallographic variations through alloying additions and thermomechanical processing is the basis for developing a wide range of alloys and properties. These phases also provide a convenient way to categorise titanium alloys. Based on the phases present at room temperature, titanium alloys can be classified as (α) alloys, (β) alloys or (α+β) alloys.

α+β alloys have compositions that support a mixture of α and β phases and may contain 10–50% beta phase at room temperature. α+β alloys possess one or more α stabilisers plus one or more β stabilisers. Heat treatment and thermomechanical processing are used to strengthen these alloys. Generally, when strengthening is desired, the properties of these alloys can be controlled through heat treatment. The alloys are rapidly cooled from a temperature high in the α–β range or even above the β transus temperature. Solution treatment, followed by ageing at 480–650°C, results in a fine microstructure of α and β in a matrix of retained or transformed β phase. The most widely used α+β alloy is Ti6Al4Va. Although this particular alloy is relatively difficult to form even in the annealed condition, α+β alloys generally have good formability, weldability and fabrication characteristics (Figure 2-10 (a)).

In titanium alloys, alloying elements' principal effect is their effect on the α to β transformation temperature. Some elements stabilise the α crystal structure by raising the α to β transformation temperature, while other elements stabilise the β structure by lowering this temperature. Al, O, Ni and gallium (Ga) are alphazen, and on the other hand, Mo, Va, tungsten (W) and tantalum (Ta) stabilise β. By increasing Va's fraction to 4%, with Al as the α stabiliser, Ti6Al4Va is

produced. Its high specific strength, biocompatibility and corrosion resistance characteristics make it ideal for biomedical implants and aerospace components [79, 80] (Figure 2-10 (b)).

(a) (b)

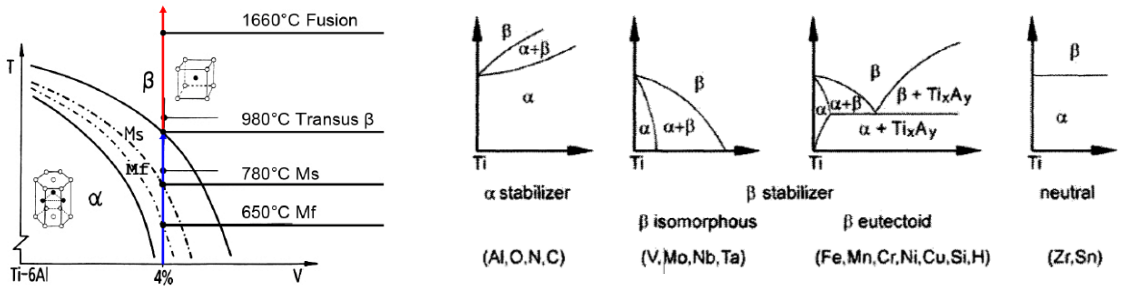

Figure 2-10 (a) Ti6Al4Va phase diagram, (b) effect of chemical elements on phase stability in Ti alloys [81]

2.5 Characterisation

Characterisation of AM products is the key to AM field development [80, 82, 83]. Figure 2-11 shows the processing and post-processing parameters and the design parameters that affect the induced thermal history. This thermal history includes cooling rate, thermal gradient, and reheating cycles. During fabrication, the imposed thermal history influences solidification and all the microstructural features (grain size, morphology, orientation and texture). It also affects residual stress and the size, morphology and density of defects. The resultant microstructure dictates mechanical properties. Therefore, it is crucial to identify the relationships between all the aforementioned parameters to achieve the desired characteristics. It is possible to design particular microstructures for intended applications by applying specific processing and post-processing parameters.

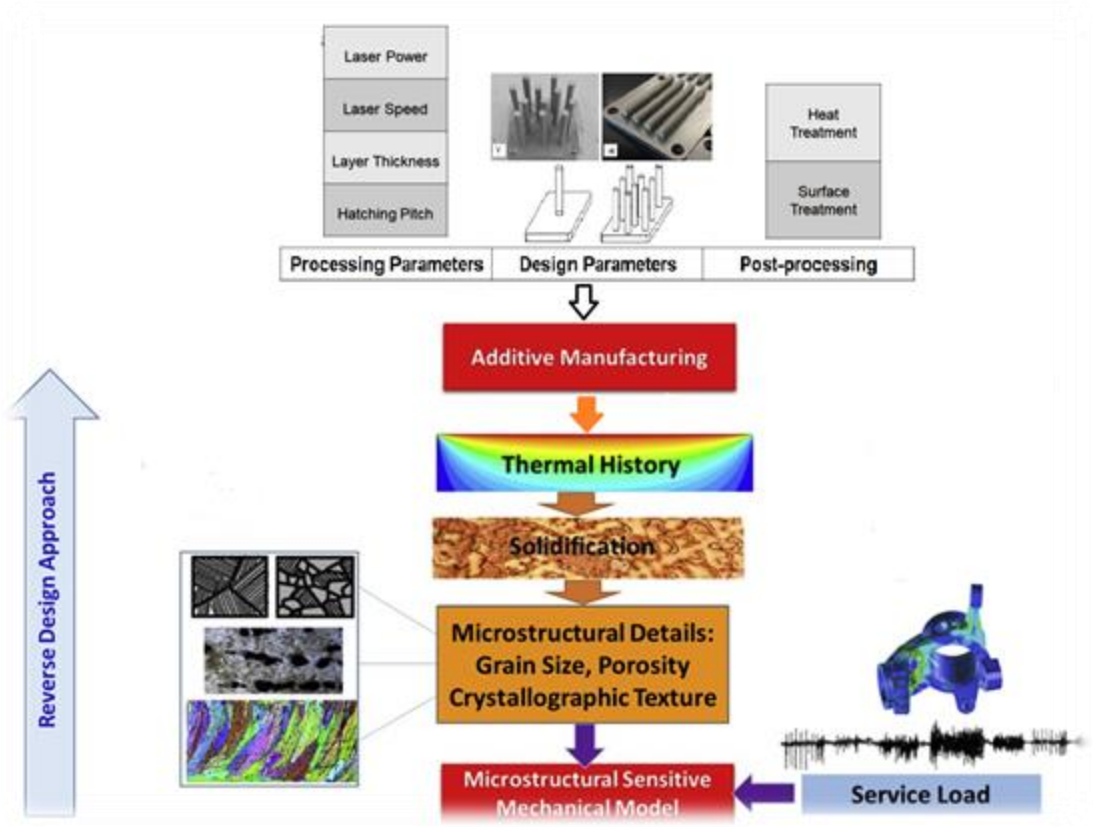

Figure 2-11 Relationship between applied processing and post-processing parameters, induced thermal history, solidification, microstructure and mechanical properties in AM products [82]

2.6 **Induced SLM defects**

Eight physical and thermal zones are distinguished around the region affected by the laser on the SLM fabricated object during SLM fabrication. (Figure 2-12). To form a microstructure free from induced SLM defects, all zones should transfer from one to the other zone smoothly. [84].

As the melt pool is responsible to create integrated material during SLM fabrication free from porosity/ induced SLM defects, cooling rates and melt pool stability are the effective factors, which both are controlled by the sufficient combination of the SLM design and processing parameters.

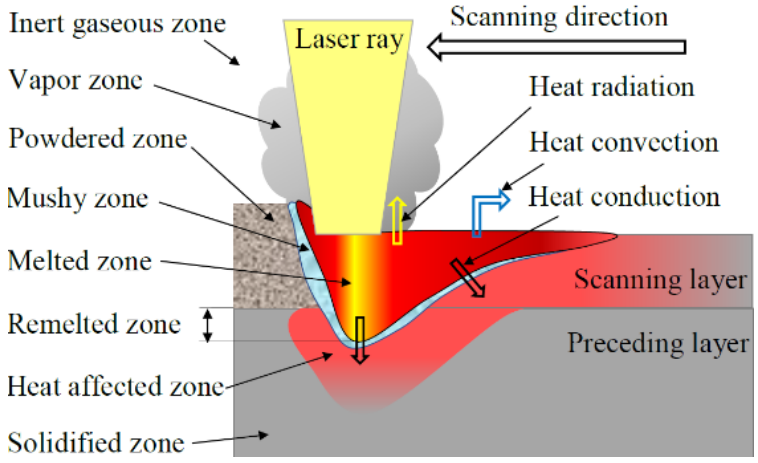

Figure 2-12 A schematic model of the thermal and physical zones in SLM technology [85]

There are so many sources of error which induces defects in SLMed products. Obviously, the induced defects decrease density and forms higher porosities in the products. All sources of errors should be controlled by the design, processing parameters, and thermal physical properties of the materials. The destructive phenomenon that happens in the SLMed products can be listed as partially and un-melted powder particles, plashing of material, the keyhole effect, the balling effect, vaporisation, the Marangoni effect, the capillary effect, vortices, gas entrapment, chemical elements vapour entrapment, explosion and instability of the pool, excess heating, bending and shrinking [85].

2.6.1 Residual stress formation mechanism in the SLM process

Residual stresses are generally caused by the incompatibility of the surrounding environment, leading to a heterogeneous microstructure [86]. The residual stresses are the intensive accumulation of dislocations in one region (i.e. surface crystals, bulk crystals, and around grain boundaries or second phase particles). Due to the difference in the temperature gradient between the molten surface and the solid surface, thermal strain and consequent residual stresses are produced. The imposed residual stresses lead to distortion, probably delamination of deposited layers, and reduce the final material quality [87].

Thermal load, mechanical loads, and phase transformation are the possible sources of residual stresses. To reduce residual stress, one must follow an appropriate heat treatment at a specific temperature.

Depending on the type of residual stress generated in the material during SLM processing and post-processing, tensile or compressive types can affect the plastic deformation performance, accelerating or postponing plastic deformation. However, their effect on degradation under static loading is not very strong; they have more significant effects under fatigue loading [88]. Residual stresses act either constructively or destructively. Shaped tensile stresses due to centre shrinkage, depending on the material properties, can cause distortion and even cracking in SLM products (Figure 2-13).

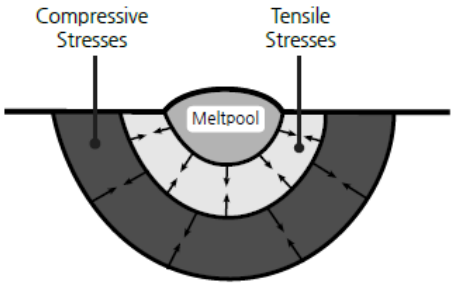

Figure 2-13 Residual stresses generated in the molten pool and heat-affected zone

Applying compressive stresses to surface using post-process shot peening helps to postpone crack nucleation and propagation. This effect is more pronounced under fatigue loading [31].

To reduce, control, and optimise residual stress, it is necessary to understand thermal stresses during AM processes. Any parameters that influence thermal history change the imposed

residual stresses. In SLM, molten pool temperature rises to approximately 2000℃ under heating. The molten powder layer expands thermally, producing pressure in the surroundings. Subsequently, the compressive stress results in elastic and plastic strain behaviour. By lowering the temperature (by removing the laser) of the molten region to about 100°C, the plastic strain causes tensile strain in the sample, and a compressive strain in the surrounding environment. A schematic of how residual stress is generated in the SLM process is presented in Figure 2-14 in a simplified form (it is very complicated in reality).

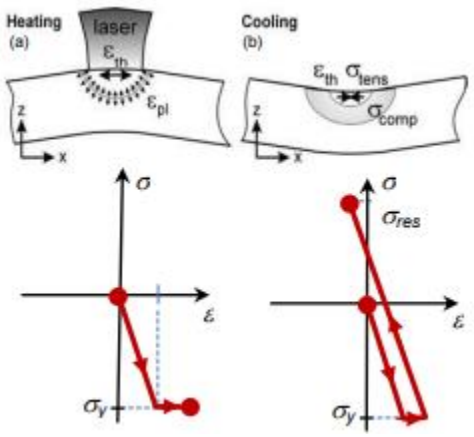

Figure 2-14 Residual stress formation in (a) heating and (b) cooling in an interacted area between laser and powder [89]

In this process, laser power, laser speed and laser scanning length are influential factors; higher power results in a higher temperature gradient. In addition, increasing the scanning length increases the thermal gradient, and scan strategy has a significant effect on stress levels and deformations.

Due to the nature of SLM 17-4 PHSS, experiencing α' transformation during fabrication leads to useful compressive stress in the interior regions of SLM components. α' transformation causes a volume expansion, brings roughly high distortion. This distortion may be large enough to prevent the float from moving in the printer compartment.

Figure 2-15 shows the distortion of SLM Ti6Al4Va specimens in this study, leading to the process's termination.

Figure 2-15 Distorted Ti6Al4Va specimens in this study

2.6.2 Elimination of induced SLM residual stresses

One way to reduce residual stresses during fabrication is preheating the powder bed and powder feedstock. Substrate plate preheating reduces thermal strain and thus reduces stress. Methods such as changing manufacturing parameters are also possible, and mechanical approaches such as laser peening and rolling in situ can be considered. While reduced power and input energy and increased scanning speed generally reduce residual stresses, they are not considered feasible due to their impact on the molten pool's dimensions. The scanning strategy has a powerful influence on the amount of stress; by reducing the length of the scan strips and scanning in smaller islands, residual stress can be reduced. It is also possible to prevent distortion by applying appropriate support. Optimal use and design of supports is one way to reduce the residual stress. The supports are often preheated in the production process due to reducing the thermal gradient between the molten and substrate layers [89].

Post-SLM process, including thermal and mechanical consisting stress relief, and shot peening are other ways to eliminate destructive residual stress after fabrication. Stress relief treatments take place at a specific temperature over a particular soaking time for each material. In addition to improving the final quality of the surface finish, surface operations reduce destructive residual stresses [30, 31].

2.6.3 Other defects

Porosity and lack of fusion are the most common defects in AM parts. Elimination of these defects is necessary due to their highly detrimental effect on the AM material's mechanical properties under loading [90].

Three main factors are responsible for porosities (typically spherical morphology flaws) in SLM parts (Type I in Figure 2-16). The trench and ripple forms of pores act as stress concentrators and thus initiate cracks. Porosities are formed due to non-ideal powder particle preparation, in which gas is trapped in the powder during atomisation. It is also common for purging inert/semi-inert gas to become trapped inside the SLM chamber. Semi-inert shielding gases, such as nitrogen (N), have been shown to diminish porosity in stainless steel welds by dissolving into the liquid melt pool before it solidifies [91].

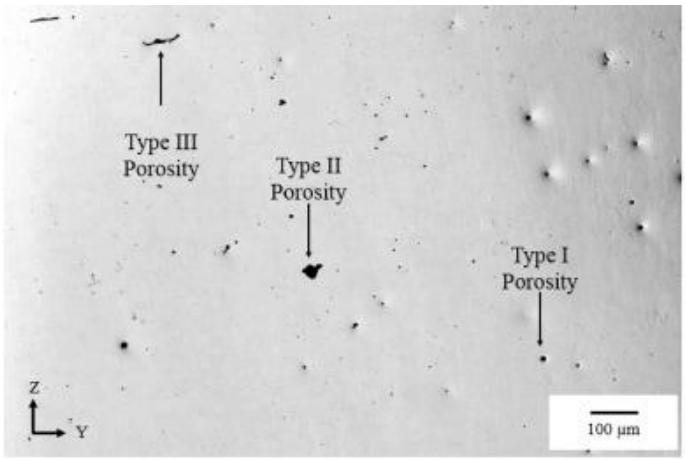

Figure 2-16 Optical micrograph of 90-BF-F AM within the grip section indicating representative defects observed in all samples in the present study. The load direction is normal to the page, and the build direction is parallel to the z-direction. [92]

The other porosity formation source is the evaporation of chemical elements during SLM manufacturing and their entrapment during fabrication. Dilip et al. measured Al percentages in SLM Ti6Al4Va before and after fabrication to track fraction changes. They found that at higher power levels, a keyhole effect was observed associated to the vaporization [84].

Lack of fusion (LoF) defects are mostly formed as a result of insufficient penetration of the upper layer's molten pool into the previously deposited layer. Partially melted regions are found to be irregularly shaped, and mostly slit-shaped (Type III in Figure 2-16). The stress

concentrations related to slit-shaped voids can be more severe than those related to spherical pores resulting from entrapped gases. Such voids impact the mechanical properties, particularly elongation to failure and fatigue failure. Porosity can affect the as-built parts' tensile properties, because the corner edge of the LoF initiates microcracks. Internal voids (rather than external and surface voids) can be reshaped using a hot isostatic pressing, but this process is time-consuming and costly. For this reason, it is desirable to reduce and eliminate voids by changing and controlling the power, speed and thickness.

Control over the combination of laser power (P) and laser speed (V) is beneficial for the resultant microstructure of SLM materials. It helps to control the cooling rate and temperature gradient during fabrication. Dilip et al. [84] used a single laser pass method to optimise input parameters such as energy and heat source speed. By applying different values of these two variables, the powder's structure after melting helps select the looked-for P and V (Figure 2-17).

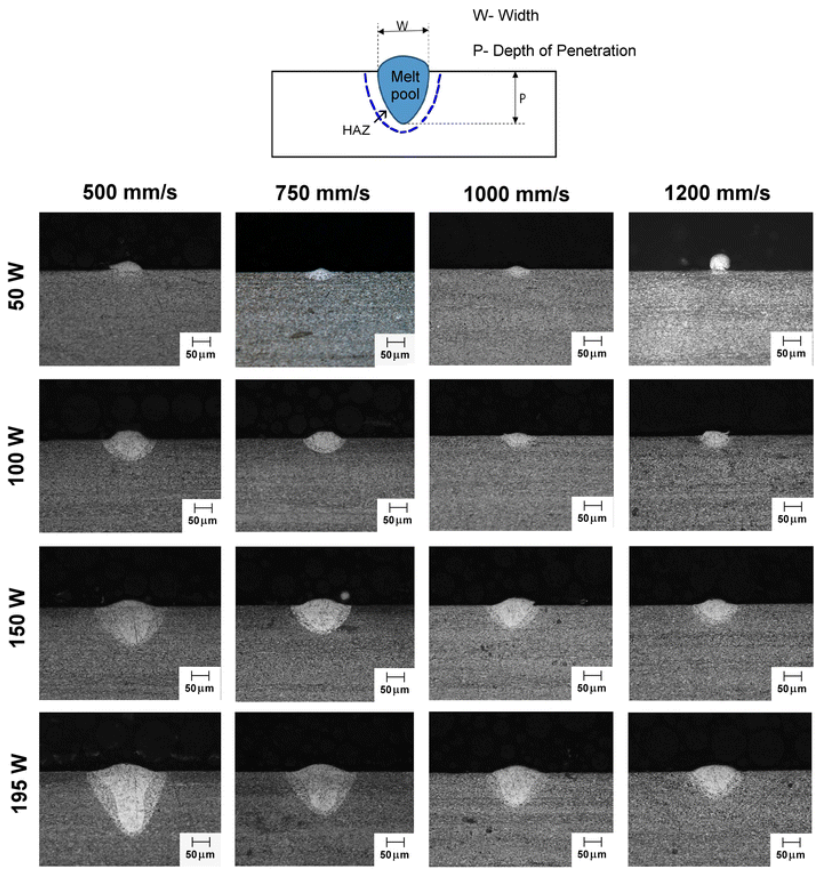

Figure 2-17 Optical images of the cross-sectional SLM Ti6Al4Va specimens at differing values of power and speed [84]

As shown in Figure 2-17, the laser beam's penetration depth increases to the previous layer under high-power and low-speed conditions. Due to the high input energy, some evaporated material and defects appear in the form of keyholes. Conversely, under low-power and high-velocity conditions, the depth of penetration is insufficient, so the particles do not completely melt and remain spherical.

Certain combinations of laser power and laser speed provide optimal structure and lowest porosity. This interval in terms of composition (P and V) is calculated from Equation 2-5:

$$E_\rho = \frac{P}{vst} \left(\frac{J}{mm^3}\right) \qquad \text{Equation 2-5}$$

E_ρ is the energy density, v is the velocity of the laser vector, s is the distance between the laser vector lines, and t is the layer thickness. At a specific power, the speed of the vector is changed and the density is recorded; with the help of curve fitting, the optimal point can be obtained.

Research has examined the effect of laser power and laser velocity on 17-4 PHSS [93] (Figure 2-18). According that, although increasing energy density improves final density, high input energy causes a high thermal gradient, resulting in increased residual stresses and subsequent product distortion. In summary, increasing the laser beam's penetration depth due to the heat source's high power makes the molten pool larger, creating a stronger bond between the particles and causing the least amount of non-fusion neighbouring.

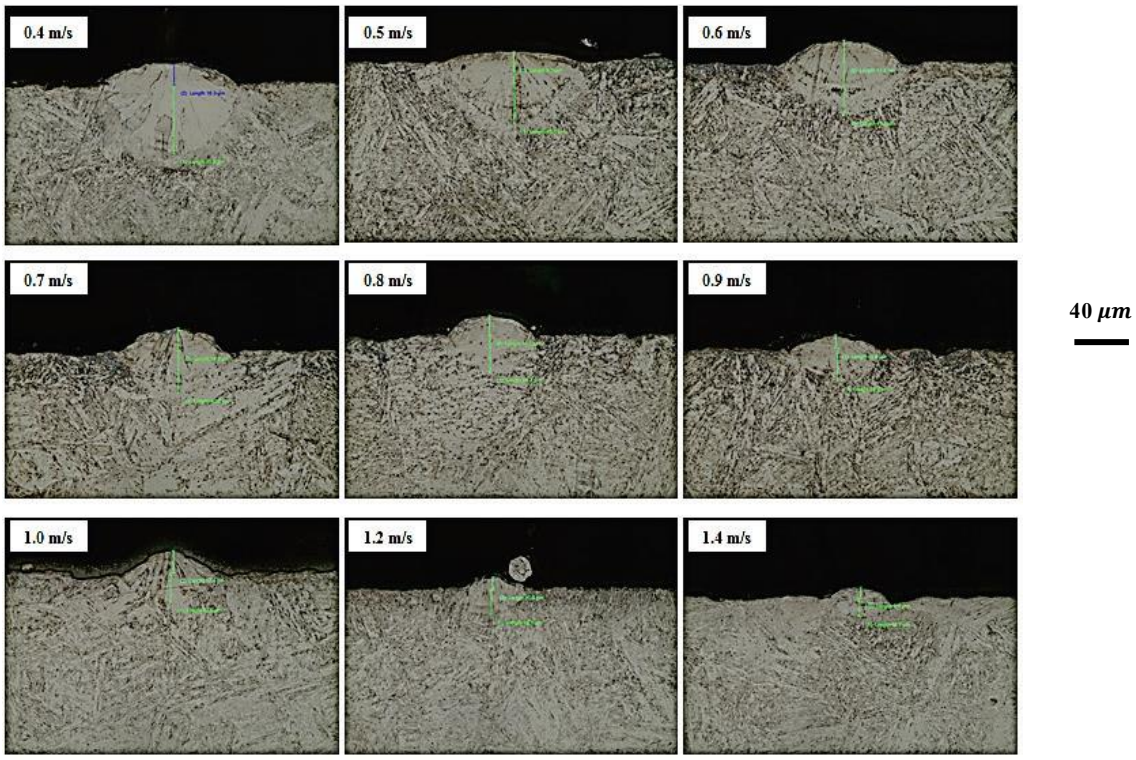

Figure 2-18 Effect of speed alteration on the specified amount of input power for stainless steel alloy 17-4 PH for single-pass [93]

2.7 Structure

Due to the particular imposed thermal histories and the heat cycles (i.e. reheating and recooling), unique microstructures are achieved in as-built SLM products.

2.7.1 Solidification

The structure of the grain and the texture depends on the melting and cooling of the molten pools. The shape of the molten pools varies according to the processing parameters. It can be elliptical or teardrop-shaped at the top view. Pools appear semicircular or keyhole-shaped along with the built orientation, based on the applied energy and the scanning speed. The geometric features of the molten pools are important because they affect subsequent grains in the microstructure.

Laser power (P) and velocity (V) affect the molten pool's geometry (as discussed in 2.6.3). The conduction mode is often desired for AM products. As shown in Figure 2-19, the combination

of P and V should be considered for designation of AM processing parameters. The unstable keyhole mode, balling up and LoF (as discussed in 2.6) are undesirable conditions that should be avoidable if using appropriate P and V selection.

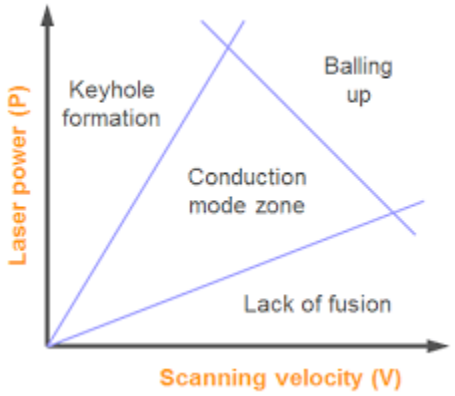

Figure 2-19 Relationship between the laser power and speed and the state of the formed molten pool

First, nucleation and growth in solidification during AM is studied by focusing on the temperature gradient (G), cooling rate (R), and undercooling (ΔT). G, R, and ΔT are all affected by the combination of laser power and laser velocity.

In the cooling process, the dominant structure near the melt pool boundary is the base metal structure. In contrast, at a distance from the molten pool boundary, the competitive microstructure dominates. It is easy to grow in <100> for FCC and BCC polycrystalline materials along the maximum heat flow direction [90]. In a similar study, Yadollahi acknowledged the competitive growth of 17-4 PHSS [41].

2.7.2 Factors affecting the solidification structure

Correlating the processing parameters with solidification rules enables achievement of desired properties. The solidification microstructure depends on G, R and ΔT. A solidification map is achieved from combination of G and R. The G/R ratio, defined as the cooling state, indicates the solidification morphology, and G*R shows the total microstructure's dimensions. As shown in Figure 2-20 (a), the cooling structure appears planar, cellular, columnar and equiaxed. Solidified dimensions are reduced with increasing G*R, which is provided separately for each alloy. Columnar and equiaxed solidification structures are the most common solidification microstructure in AM parts reported in [90].

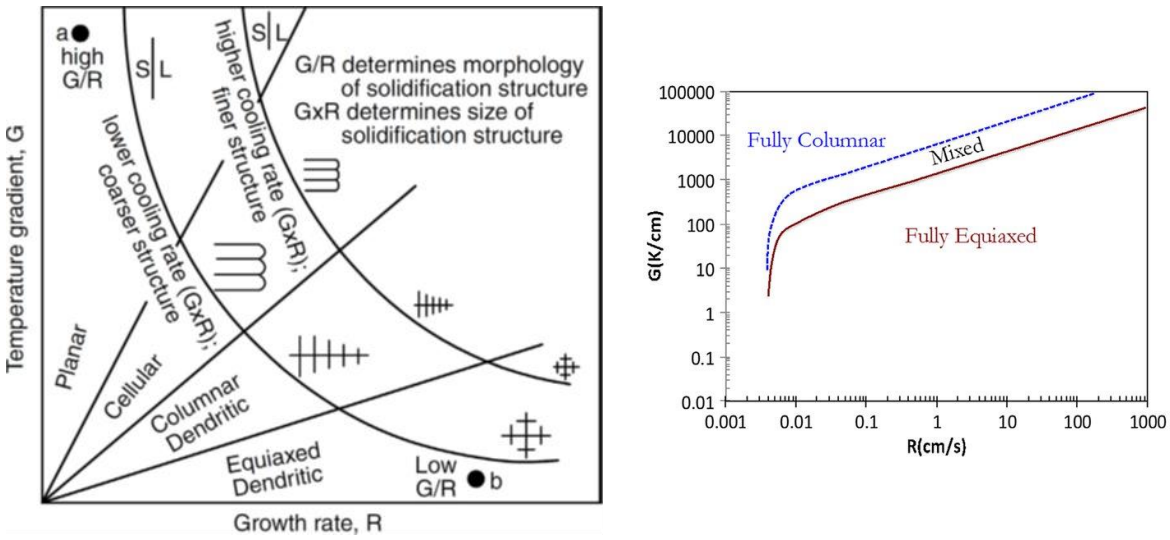

Figure 2-20 (a) The effect of temperature gradient and growth rate on morphology and microstructural dimensions of solidification structure [94], and (b) Ti6Al4Va solidification map [95]

Figure 2-20 (b) shows the Ti6Al4Va solidification map [96]. By manipulating G and R, the desired microstructure can be achieved.

2.8 Mechanical properties of SLM alloys

2.8.1 Research on SLM 17-4 PHSS

A schematic overview of basic tensile properties after AM processing for different types of steels is presented in Figure 2-21. For comparison, the values for equivalent, conventionally produced steels are given.

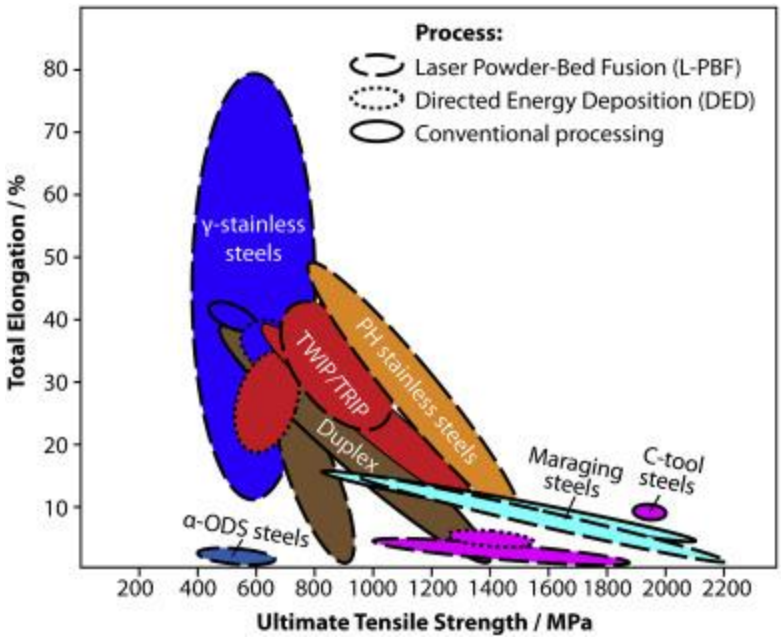

Figure 2-21 A general comparison of properties obtained by conventional processing and by the AM processes DED and L-PBF. The kind of steel is denoted by field colour, while the field border indicates the method of production. ODS: Oxide Dispersion-Strengthened, C-tool steels: Carbon-bearing tool steels, TWIP/TRIP: Twinning/Transformation-induced Plasticity, PH: precipitation hardening [97]

This section provides a brief review of recent research on the mechanical properties and microstructural features of SLM 17-4 PHSS.

As discussed, microstructural and mechanical properties are formed as a result of sequential manufacturing processes. Figure 2-22 illustrates schematics of fabrication steps. The process starts with the preparation and manufacturing of feedstock powders. Then, a sophisticated SLM process and post-processing treatments are applied to tailor the material's properties and eliminate the additive product's induced defects.

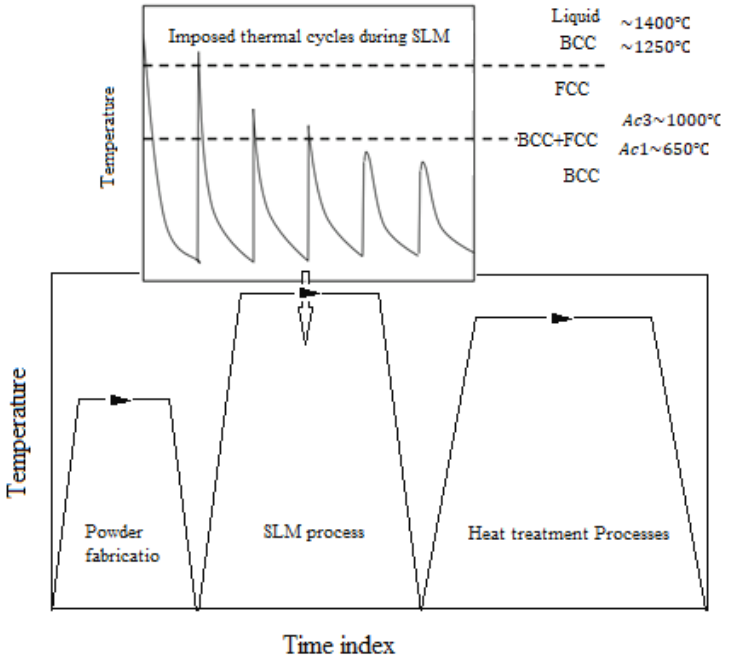

Figure 2-22 Schematic representation of an imposed thermal cycle from powder fabrication, SLM process with details of the thermal cycles in a melt pool during SLM along with phase stability division of 17-4 PHSS [98] and post-heat treatment

Murr et al. studied the effect of powder feedstock preparation and the protective inert atmosphere during the SLM process on the microstructural features and mechanical properties of 17-4 PHSS [99]. Murr et al. reported that due to argon's (Ar's) low thermal conductivity compared to N gas, AM parts showed martensitic microstructure with either an austenitic or martensitic pre-alloyed 17-4 PHSS powder in an Ar environment. Rafi [36] also studied the protective inert atmosphere effect, and reported a higher fraction of retained γ in SLM samples made in an N environment than in samples fabricated in Ar gas. The effect of powder chemical composition on the microstructural and mechanical evolution of SLM 17-4 PHSS in the as-built condition was recently investigated by Vunnam et al. [100]. They concluded that relatively minor differences in the powder chemical composition, particularly concentrations of ferrite and austenite stabiliser elements, significantly affect the phase composition of as-built samples.

Due to the sophisticated thermal histories and reheating cycles generated during the SLM process, unique microstructures are achieved in as-built SLM products. Hu et al. studied SLM processing parameters' effects on tensile properties, focusing on induced defects and resultant density [101]. They found that modifying manufacturing processing parameters (laser speed,

hatch spacing, and layer thickness at a constant laser power) made a remarkable difference in resulting density and consequently influenced the molten pool's characteristics. Rashid et al. investigated the effect of scan strategy on density and metallurgical properties, as well as the effect of remelting (double scan strategy) [102]. They claimed a hardness value (HV) of ~458 was achieved for samples printed with a remelting strategy, higher than in other published literature. In 2020, Lashgari et al. [103] published work on the effect of remelting on microstructural features and mechanical properties; the double scan strategy led to a decrease in retained γ. Although some research has been carried out on the effect of the SLM process on mechanical properties, there have been few investigations of the deformation mechanism of SLM 17-4 PHSS. The deformation mechanism of SLM 17-4 PHSS – particularly in situ – is a topic that requires further investigation.

Post-processing options, consisting of heat treatment procedures to tailor microstructure and surface treatment techniques to improve surface quality, have been studied widely. In 2012, Murr et al. explored the effect of the SLM process on 17-4 PHSS [104], and found that heat treatment's impact on tensile, hardness, fatigue, and fracture properties enhanced tensile properties during post-processing [36]. Bhambroo et al. [65] studied heat treatment of 17-4 PHSS wrought material. Peak strength was measured in 0.2 hr at 580℃; he concluded that mechanical properties were mainly controlled by Cu-rich precipitates rather than reverted γ during ageing. In comprehensive research published in 2015 by LeBrun et al., standard and non-standard heat treatment procedures were applied to investigate heat treatment effects on 17-4 PHSS's mechanical properties [30]. The results suggested pre-ageing solution annealing is required to improve mechanical properties for SLM products.

In other work, Yadollahi et al. studied the effects of heat treatment (solution annealing and ageing) and building orientation (horizontal and vertical orientation) on the mechanical properties of SLM 17-4 PHSS. It was concluded that yield and ultimate tensile strengths of SLM parts were lower than those of wrought materials in the H900 condition. The building orientation effect exposed noticeable effects on tensile properties during fabrication [41]. Refinement due to the higher cooling rates in horizontal specimens led to higher strength than in vertical ones. Yadollahi et al. claimed that elongation to failure of vertical specimens was lower than for horizontal ones, due to the direction of sharp-edged defects (which act as stress concentration points) perpendicular to the loading direction (Figure 2-23). Sun et al. [37] studied the effect of heat treatments on both SLM and wrought microstructural evolution. They

commented that comparable microstructures and hardness could be achieved with heat treatment of as-built and wrought components.

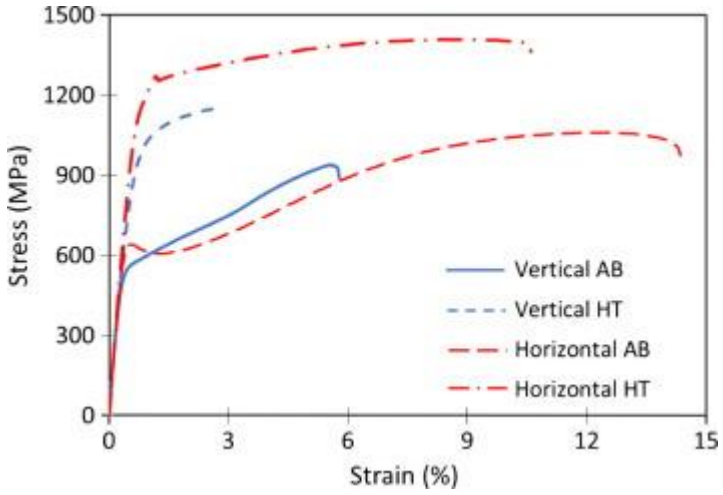

Figure 2-23 Engineering stress-strain curves of SLM 17-4 PH SS in different condition [41]

Mahmoudi et al. explored the influences on mechanical properties of built orientation, heat treatment, processing parameters and the number of samples during fabrication [40]. They concluded that the tensile properties of vertical specimens were lower than those of horizontal ones due to the induced defects between layers, which provide a more convenient path to failure. The fraction of the retained γ in the single sample was greater than in the multiple samples owing to lower cooling rates.

The effect of shot peening on the surface roughness and mechanical properties of SLM 17-4 PHSS parts was investigated by AlMangour and Yang; they found surface roughness, microhardness, compressive yield strength and wear resistance were improved [31]. More recently, AlMangour and Yang investigated the effect of applied heat treatment after surface severe plastic deformation processing [32]. They concluded that high fraction of martensite phase, precipitation particles, and work hardening improved material performance of shot-peened and aged 17-4 PH SS in comparison to the only shop-peened one.

Nezhadfar et al. performed an excellent investigation of the effect of heat treatment on tensile and uniaxial fatigue behaviour [34], as well as applied heat treatment's effect on fatigue crack growth (FCG) [35]. FCG in two different built orientations, in CA-H900 and H1025 heat treatment procedures (based on [34]), was compared to wrought in the CA-H900 condition.

Figure 2-24 (a, b) indicates monotonic tensile behaviour of L-PBF 17-4 PHSS for non-heat-treated and various heat treatment procedures.

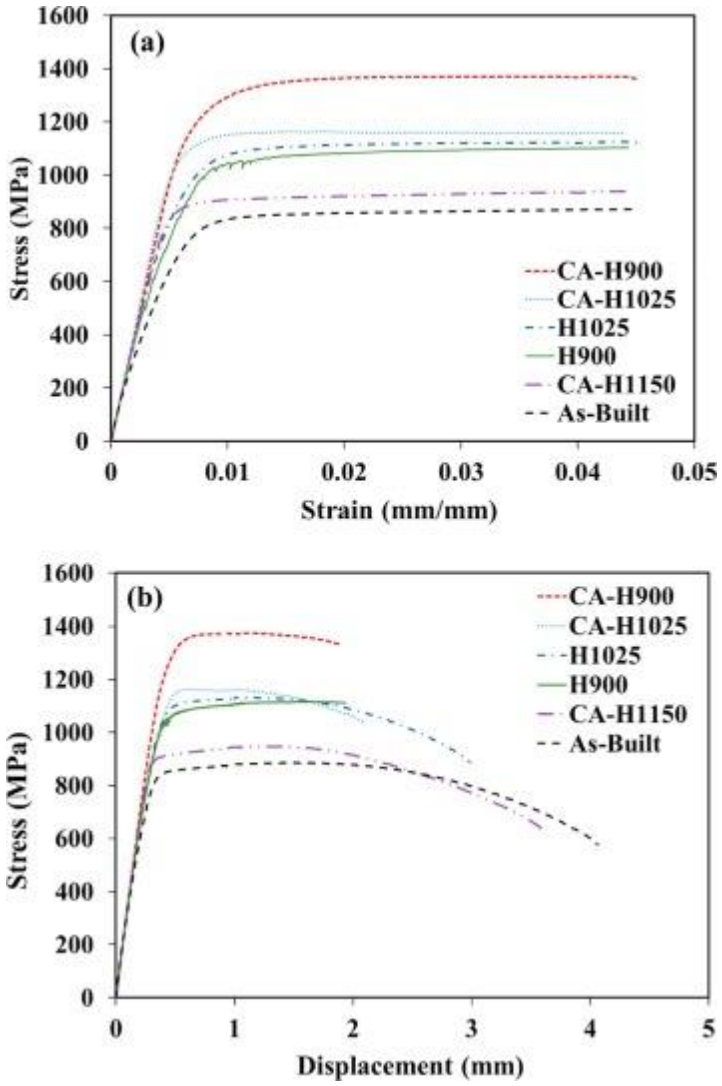

Figure 2-24 Monotonic tensile behaviour of L-PBF 17-4 PHSS for non-heat-treated and heat treatment procedures utilised in [34], represented by (a) engineering stress-engineering strain curve up to the extensometer removal point, and (b) engineering stress-displacement curve all the way to fracture

Due to PHSS's importance in a vast range of applications, [97, 105], much uncertainty still exists about the relationship between standard precipitation hardening heat treatment and resultant properties in SLM products. There is a need to develop effective heat treatment procedures suitable for SLM-manufactured 17-4 PHSS.

From a tribology perspective, investigation of wear and friction behaviour of SLM materials started in the early 2000s [106]. Zhu [107] investigated the material characterisation and

lubricating behaviours of porous stainless steel fabricated by SLM. However, most researchers have focused on eliminating pores to improve mechanical properties, which is the primary concern for many SLM parts. On the other hand, the presence of pores improves lubricating behaviours by reducing wear; therefore, there is a tradeoff between part integrity and lubrication. Indeed, in hydraulic valves, failure due to wear greatly limits – and is the dominant factor in – the life of the part. In this case, surface pores can improve lubrication. Of course, part strength must be tested before the technology is applied.

Recently, Sanjeev et al. [108] investigated the tribological behaviour, of 17–4 PHSS manufactured conventionally and additively. They concluded that AM PHSS with a slightly higher hardness value is likely to have less wear resistance than conventional specimens. The wear mechanism in dry conditions was considered to be abrasive wear. Lashgari et al. performed a comprehensive study on the wear performance of AM 17-4 PHSS [103, 109], they concluded that surprisingly, as-printed specimen showed great wear resistance compared to the designed heat treated AM parts.

Wear resistance of wrought 17-4 PHSS under various heat treatment conditions was studied by [110] for a chain conveyor application. The main wear mechanism present in these chains is relative wear due to metal–metal sliding. While the heat treatment effect on the wear performance of SLM 17-4 PH SS was not investigated in the literature review, it is highly recommended that such a review be undertaken and the topic studied further.

2.8.2 Research on SLM Ti6Al4Va

The impact of AM techniques on the mechanical properties of Ti6Al4Va were studied by [111] and [39]. Both identified substantial differences in the resultant properties. Figure 2-25 indicates Ti6Al4Va's basic tensile properties for several processing and post-processing methods.

Microstructural and mechanical properties of SLM Ti6Al4Va have been studied thoroughly. Thijs et al. and Yadroitsev et al. [112, 113] studied the influence of process parameters and scanning strategy on the microstructural evolution of Ti6Al4Va during the SLM process. The resulting microstructure was reported as acicular α' as a consequence of very high cooling rates during the SLM process. Lu et al. investigated the deformation behaviour of laser direct metal deposition Ti6Al4Va using an in situ tensile test. They concluded that the location and direction

of specimens extracted from the AM build strongly affect the microstructure and tensile properties of laser-processed Ti6Al4V [114]. In other work, post-processing heat treatment was applied to investigate its influence on microstructure/small-scale properties of Ti6Al4Va [38]; Aged specimens exhibited the highest microhardness of all the heat-treated samples. In addition, Leuders et al. applied post-processing heat treatment to Ti6Al4Va to eliminate the induced residual stresses; no residual stress was detected after treating at 800℃ for two hours [115].

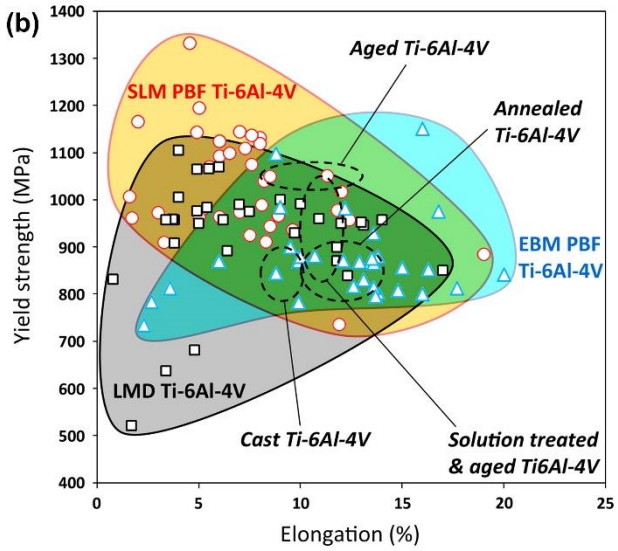

Figure 2-25 Yield strength vs elongation of additively manufactured Ti6al4v alloys [80] and conventionally manufactured alloys (dashed lines) [116]

Due to the machine-to-machine and process variability during processing and post-processing, further experimental data is needed to support modelling and empirical models based on the variation in effective parameters. Research to date has been designed to improve the mechanical properties of AM metals by optimising the processing and design parameters and post-processing. Therefore, this study sought to make a major contribution to SLM technology by exploring the effect of SLM processes on printed products' performance, and consequently, of the designated heat treatment procedures' development on SLM products' microstructure and properties.

Chapter 3 Microstructure and Mechanical Performance of SLM 17-4 PHSS

This chapter describes an investigation of SLM parts' mechanical properties and a comparison of their properties with those of parts fabricated conventionally. The effects of the SLM process in different locations of the parts are also studied to determine location dependency impact.

3.1 Experimental procedures

Various techniques and items of equipment were employed to evaluate the mechanical properties and microstructural characterisation of SLM and wrought 17-4 PHSS products. This section explains the SLM and wrought manufacturing processes, mechanical testing set-ups, microscopy set-up, and sample preparation methods for microstructural observations.

3.1.1 Feedstock powder, SLM and shot-peen processes

Gas-atomised (Ar) 17-4 PHSS powder was used as a feedstock in this study. The typical morphology of the powder was obtained by scanning electron microscopy (JEOL JCM-6000PLUS NeoScope Benchtop SEM), and is presented in Figure 3-1. The 17-4 PHSS powder has a roughly spherical morphology. A Malvern Mastersizer Hydro EV was used for particle size analysis. The particle size distribution result was $D_v(50) \leq 39.8$ μm in this work, where $D_v(50)$ indicates the size of 50% of the particles. The particle size range was 23–73 μm, with an average diameter of 40 μm. Precise chemical element weights of the initial powder were measured by Spectrometer Service Pty Ltd. Table 3-1 presents the chemical composition of Ar gas-atomised 17-4 PH SS powder, which conforms to US classification 17-4 equevalent to ASTM A564/A564M.

An EOSINT M270 Direct Metal Laser Sintering (SLM) system equipped with a maximum 200W solid-state Yb-fibre laser was used to fabricate specimens. The laser was operated in a continuous wave mode. Laser beam diameter and laser spot size were 200 μm and 80 μm respectively (Figure 3-2 (a)). The powder layer thickness for each melting cycle was 40 μm.

Applied laser parameters are reported in Figure 3-2. The build plate was made of low carbon steel pre-heated to 80℃ and kept at this temperature to remove any residual moisture in the powder. The powder was not heated during fabrication. All the specimens were created under a protective inert atmosphere (continuous flushed nitrogen) to minimise oxidation at elevated temperature. The scanning strategy was an EOS system standard, often referred to as "stripes", in which the direction of scanning is rotated by 67° between following build layers (Figure 3-2 (b)). All processing parameters were kept constant in this study using the manufacturer-recommended process parameters to achieve full-density parts. An electric discharge machine was used for detaching the samples from the substrate and support structure. Shot peening was applied to SLM parts using glass beads with 100 µm diameter at 200 KPa pressure in PEENMATIC 750 S Microblasting equipment.

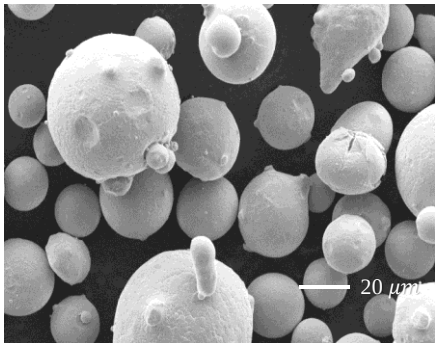

Figure 3-1 Typical morphology of 17-4 PHSS powder; note the spherical morphology with a rough surface of particles attributed to the gas atomisation fabrication process.

3.1.2 Wrought 17-4 PHSS conventional manufacturing process

For comparison with SLM 17-4 PHSS, forged, cold drawn, turned and centreless ground bars were provided by Interalloy Pty Ltd. Wrought samples were prepared in H1150 (H620) condition, obtained by solution annealing, followed by a single high-temperature age-hardening treatment. Applied heat treatment consisted of solution annealing at 1040℃ for 30 minutes of oil quenching below 30℃, followed by ageing at 620℃ for 4 hours of air cooling.

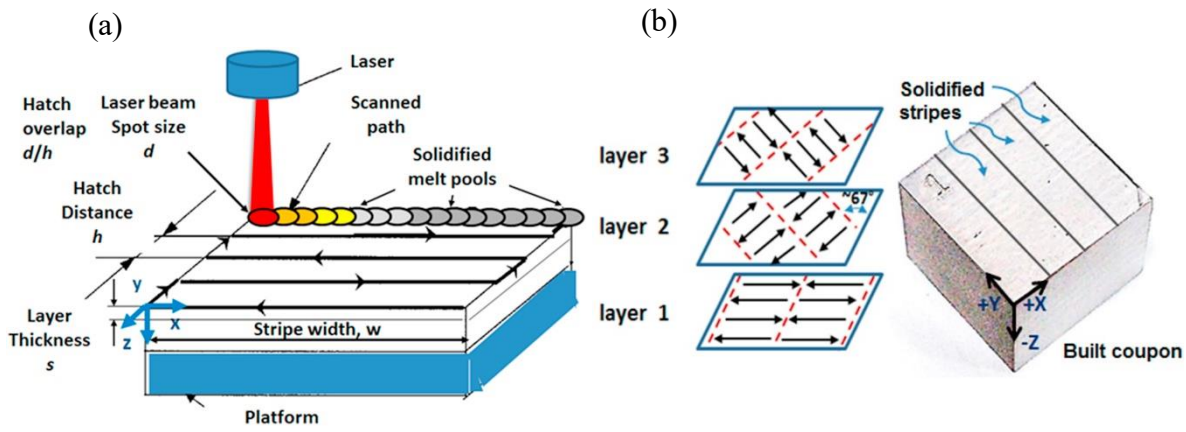

Figure 3-2 (a) SLM process schematic, (b) schematic of a stripe scan pattern with 67° rotation between consecutively built layers [117]

Table 3-1 Chemical composition of starting 17-4 PH SS powder, and chemical requirements for S17400 UNS designation [48]

Alloying elements **wt-%**	**Fe**	**C**	**Mn**	**Si**	**S**	**P**	**Ni**	**Cr**	**Mo**	**Cu**	**V**	**Nb**	**Ti**	**Al**
Provided powder	Bal	0.05	0.57	0.61	0.01	0.02	4.55	15.6	0.11	4.51	0.02	0.21	<0.01	0.01
ASTM A564/A564M Limits	Bal	max. 0.07	max. 1	max. 1			3–5	15–17.5	max. 0.5	3–5		0.15–0.45		

Table 3-2 SLM parameters used in fabricating the 17-4 PHSS specimens

Laser Power (W)	**Scan Speed (mm/s)**	**Thickness of layer (µm)**	**Atmosphere**
175	1050	40	Nitrogen

3.1.3 Hardness test

All hardness assessments for wrought, as-built SLM and heat-treated SLM parts (for heat treatment effect study, refer to Chapter 5) were performed on the cross-section of the horizontally round tensile specimen. For hardness measurements, grip sections of round specimens were cut in 5 mm thickness. Each specimen was mounted in epoxy and ground and polished using 320, 400, 600, 1200 and 4000-grit silicon carbide (SiC) grit sandpapers to create a mirror-finish surface. To avoid martensitic transformation during mechanical polishing (and thereby maintain the experimental control condition), grinding was carried out very carefully. Hardness measurements were taken using a Vickers microhardness tester (Shimadzu Seisakusho Ltd) with a diamond indenter using a load of 500 g and a dwell time of 15 seconds [118]. To achieve repeatable and reliable hardness values, 26 measurements were taken in the built direction labelled BD (bottom to the top of a round specimen's cross-section in the grip section) (Figure 3-3). The mean value was reported as a hardness value for the specimens.

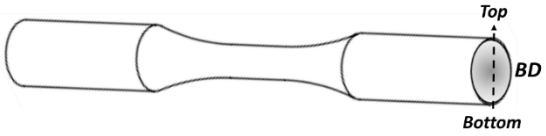

Figure 3-3 Hardness measurement from bottom to top in the built direction, labelled BD

3.1.4 Tensile test

Round specimens were designed and fabricated according to ASTM E466-15, as displayed in Figure 3-4 (a, b) [119]. The gauge length and gauge width of the tensile specimens were 25 mm and 6.25 mm, respectively. All SLM specimens were fabricated horizontally. All as-built SLM specimens were assumed as shot-peened SLM ones in this study. No grinding or polishing was applied to the as-built SLM parts to involve the roughness effect on tensile properties. The effect of surface roughness on tensile properties was also studied by turning specimens to eliminate defects from the surface. Due to the limited printed specimens, a sample was turned 0.5 mm in gauge length. Polishing was applied after machining to reduce machining marks.

Tensile tests were performed at room temperature using an Instron 8501 machine with a 100 kN maximum loading cell capacity with a 1 mm/min crosshead speed corresponding to a 0.04

strain rate sec^{-1} (Figure 3-5). The tensile test was conducted to fail specimens. In order to achieve repeatable tensile properties, tensile testing was carried out at least three times for each condition. The tests were performed for each condition with random order of runs to reduce the possibility of bias due to unknown external influences. A 10 mm contact extensometer was applied to monitor the precise strain of tensile specimens. The tensile axis was perpendicular to the built orientation of the SLM specimens' fabrication.

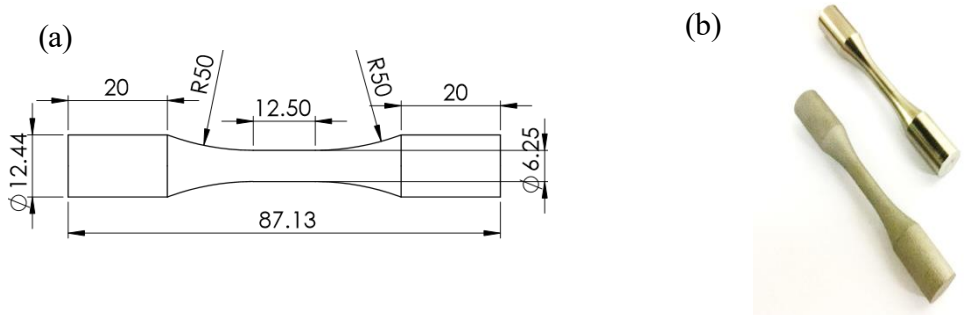

Figure 3-4 (a) Dimensions of specimens according to ASTM E466 and (b) horizontal SLM and wrought 17-4 PHSS

Figure 3-5 Instron 8501 mechanical testing machine

3.2 Microscopy

Specimens in the transverse plane from multiple locations of tensile coupons were cut and mounted in epoxy, ground, polished and etched (specific preparation if required), and prepared for microstructural characterisation (Figure 3-6). Microstructural characterisation of each group (SLM and wrought) was studied using optical microscopy (Leica DMi8M microscope) and a field emission SEM equipped with an electron backscatter diffraction (EBSD) detector (Zeiss Ultra Plus Field Emission Scanning Electron Microscope). The specimens for microstructure evaluations were cut from multiple locations of SLM and wrought coupons, using a Struers Accutom-50 armed Al2O3-blade water-cooled diamond saw.

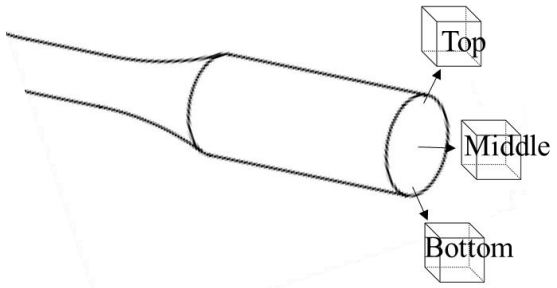

Figure 3-6 Designated areas for location dependency investigation

3.2.1 EBSD microscopy

Electron backscattered diffraction microscopy was the main tool for evaluating the microstructure in this study. Sample preparation for the sub-studies was one of the most challenging parts of this research, and many techniques were trialled in attempts to achieve sufficient quality maps.

Electron backscattered diffraction microscopy has been a valuable technique for materials characterisation since its development in 1973 [120]. In this technique, Kikuchi patterns are formed by the interaction of the reflected electron beams from the surface of the material. Constructed Kikuchi patterns are decoded by the software and is used to detect the present phases in the material. Crystalline structure and the orientation can also be extracted for the further study in sub-structural features.

To investigate the microstructure's location dependency in the as-built SLM part, samples were cut and prepared in the transverse plane (refer to Chapter 3). In order to compare heat treatment effects on microstructural features, samples were prepared at the centre of the specimens in the tensile coupons' cross-section (refer to Chapter 5). Microstructure variations related to built orientation effect (horizontal and vertical) of as-built SLM Ti6Al4Va were investigated by sample preparation in multiple planes and orientations (refer to Chapter 7).

A Schottky field emission gun enable to provide high resolution and beam current was used in this study attached to the Zeiss Ultra Plus SEM (Figure 3-7). Oxford Instruments AZtec integrated EDS and EBSD system detector was applied to detect and collect abundance of the elements as well as EBSD patterns. Symmetry CMOS EBSD detector, allowing 0.3ms per point acquisition, was the one applied in this package. AZtecHKL Channel-5 software was run to analysis and post process EBSD maps. Tango modulus of the Channel5 was mainly applied to process and analysis the EBSD maps.

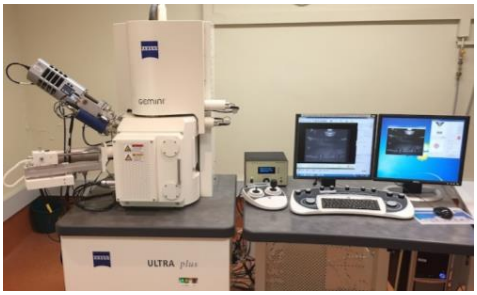

Figure 3-7 Zeiss ULTRA Plus SEM equipped with a field emission gun

20 kV energy beam in high current mode were applied in all sub studies. Tilt correction and dynamic focus were applied in order to attain high quality maps. All specimens were tilted at 70 ° . EBSD detector was positioned in approximately 180 mm from the specimens. 14-15 mm working distance was selected for the SEM aperture position. The aperture size was set to 120 μm. Different settings were applied to achieve the best indexing and highest resolution. Set reflectors for the BCC, FCC and HCP were chosen as 43, 42 and 38 respectively. 200 nm and 300 nm were set as step sizes for the EBSD pattern acquisition. Worth to mention that indexing in different sub studies were associated to the substructure of materials in different conditions. Indexing rate of the all acquired kikuchi pattern were higher than %80 and rate was reached to higher than %85 indexing in all the scanning by noise reduction and further filtering in Aztec

software. For reliability, scanning of the designed regions was carried out at least twice for all specimens.

Specimens were mechanically polished using 320, 400, 600, 1200 and 4000-grit silicon carbide sandpapers. To prevent the phase transformation of γ to α' during the mechanical polishing of the specimens, this step was performed very carefully. Then, specimens were electropolished to a mirror-like finish using a Struers Lectropol-5 electropolisher. The final electrolytic polishing was conducted at room temperature with 6% perchloric acid ($HClO_4$) in acetic acid (CH_3COOH) using a voltage of 9 V, a flow rate of 10, and polishing time of 35 s for most of the specimens. (Due to different resultant microstructures in sub-studies, the applied set-up sometimes changed to reach an acceptable indexing level which undoubtedly can claim achieving the correct settings was the most challenging part of this research work) The electropolished specimens were instantly rinsed by ethanol to save the surface from oxidation during preparation. Depending on the acquired indexing level, ion milling was applied using 3 Kve, 4°, for 1 to 8 hours by a Gatan PIPS II ion mill instrument.

3.2.2 X-ray diffraction

An X-ray diffractometer (XRD Shimadzu S6000) was applied instead of EBSD analysis in some studies to determine the phases present. X-ray diffraction (XRD) spectral analysis was performed on the powder particles and as-built SLM and wrought specimens. Specimens were cut from the round tensile specimens' grip section and applied setting reported as (X-ray tube, target Cu, voltage 40 V, and current 30 mA).

3.3 Results and discussion

3.3.1 Surface roughness

The surface condition has a significant impact on mechanical properties. Surface roughness is dictated by scan speed, powder particle size, and layer thickness. Higher scanning speed leads to the balling phenomenon (giving greater roughness) due to improper melting of powder particles. It can also originate from elongated molten pools that break into tiny islands. Coarse powder particles are another source of roughness, and the stair-step effect results in higher layer thickness and, consequently, inferior surface quality. In contrast, higher applied power improves surface quality. Depending on the application, the rough surface could be beneficial for example for implants due to better osseointegration or detrimental if the fatigue performance is the main concern.

In this study, average surface roughness in one dimension (D) of the as-built SLM PHSS was 11.2 ± 1.2 µm, while the average among wrought specimens was 1.8 ± 0.3 µm. The difference shows that the as-built specimens have higher roughness, which is detrimental to mechanical properties, because rough surfaces can act as crack nucleation sites under loading, mainly fatigue one (Figure 3-8).

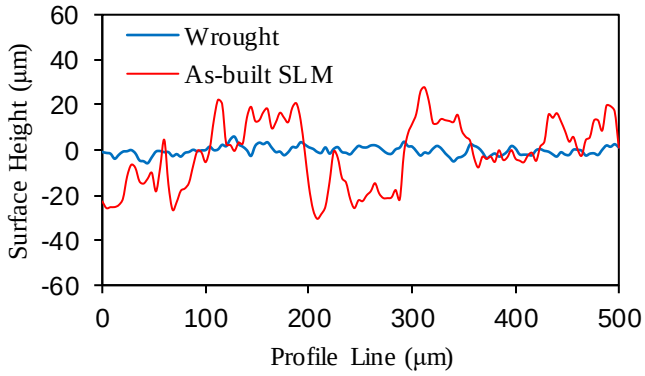

Sample ID	Average roughness, Ra (µm)
As-built SLM	11.2 ± 1.2
Wrought	1.8 ± 0.3

Figure 3-8 Surface roughness of the as-built SLM and wrought 17-4 PHSS

The surface finishes of 1 mm*1 mm areas of both sets were measured in two dimensions (2D) and 3D using a Bruker Contour Elite-K 3D microscope. The average surface roughness of the as-built PHSS was 9.129 µm, while the average wrought value was 1.052 µm. These results

illustrate that no considerable balling effect was observed on the surface of the as-printed samples which could be due to the applied shot peening process and elimination of this defect from the surface. The surface of the wrought PHSS displays the turning of a mechanical cutting tool and a considerably smoother surface (Figure 3-9).

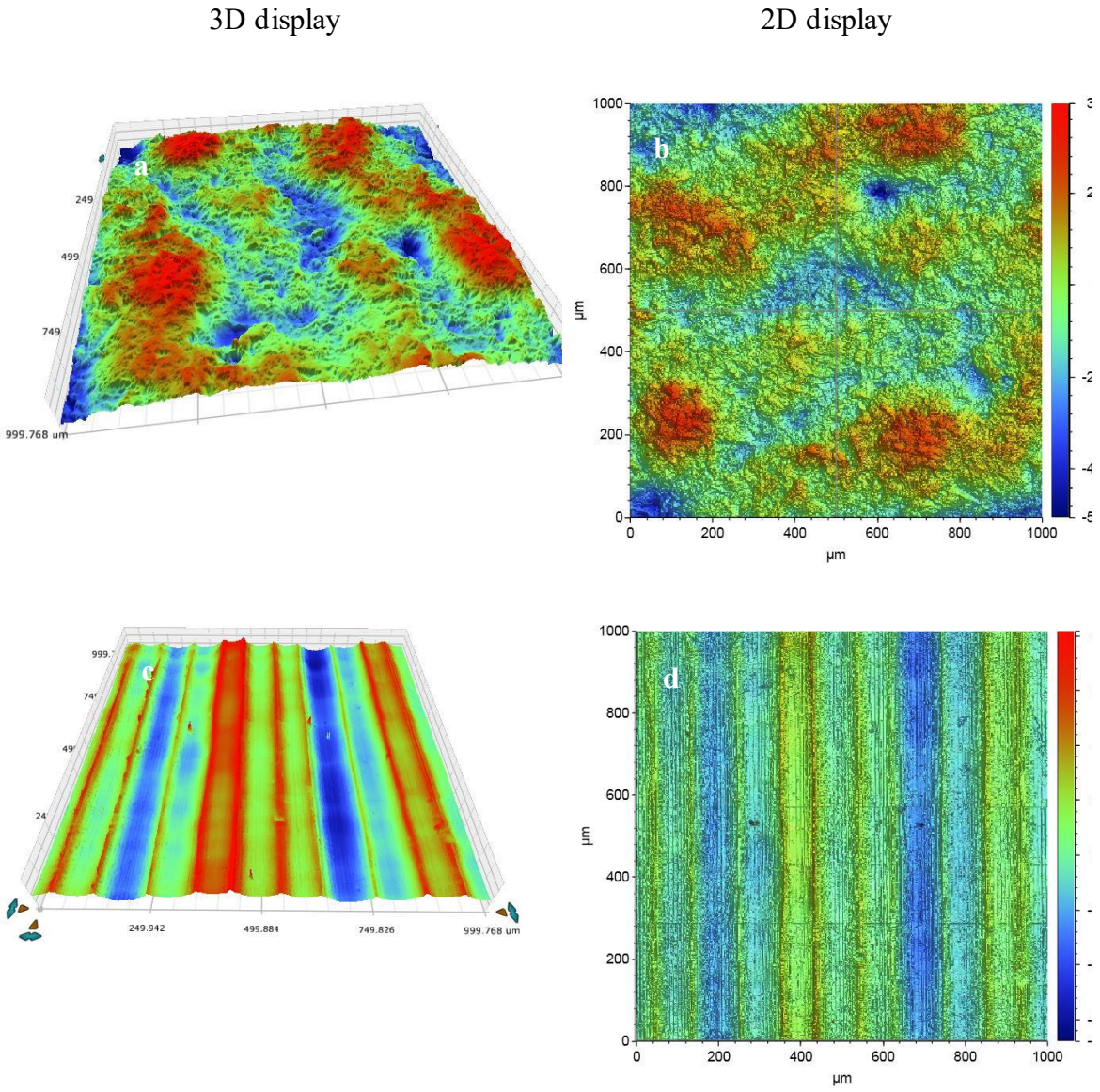

Figure 3-9 Surface finishes of (a, b) the as-built SLM, and (c, d) wrought 17-4 PHSS

Average roughness of less than 1 µm is a prerequisite for AM components to be licensed for commercial applications. So, the surface would have to be treated to allow the as-built SLM products in this study to be used in industrial applications. Surface finishing such as machining and/or shot-peeing can smoothen the surface, but it can also bring the sub-surface defects close to the surface affecting the fatigue resistance. The fatigue study is not the subject of the present

study, but the effect of surface finish on the monotonic tensile properties is investigated and discussed in this chapter. AlMangour and Yang investigated the effect of shot peening on the surface quality and mechanical performance of SLM 17-4 PHSS [31]. They claimed that the mechanical properties of the PHSS improved due to the smoothed surface.

3.3.2 X-ray diffraction

The XRD patterns of the feedstock powder, the as-built SLM PHSS, and wrought PHSS are presented in Figure 3-10.

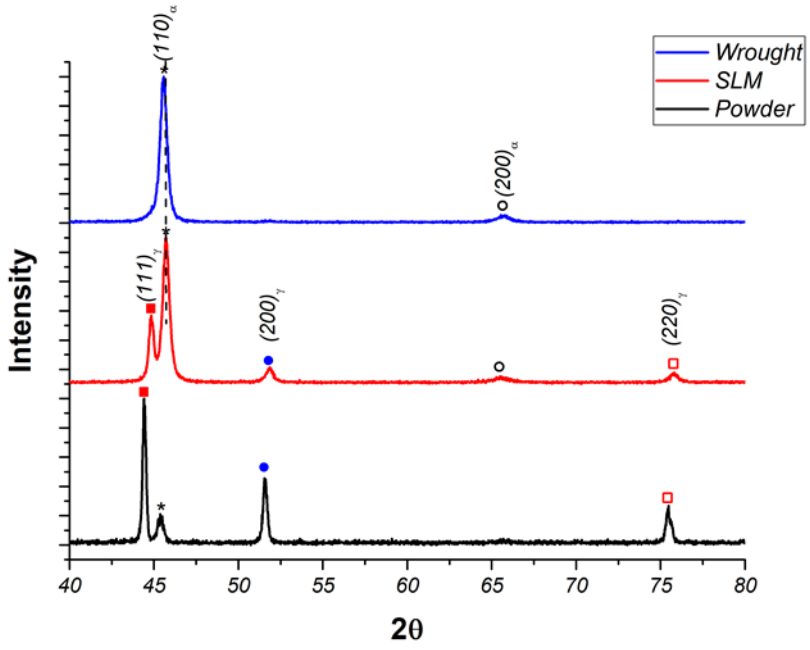

Figure 3-10 XRD profiles of pre-alloyed powder, the as-built SLM, and wrought 17-4 PHSS

The feedstock powder pattern displays peaks of the γ phase with a strong (111) γ reflection. The extremely rapid melting and solidification of the SLM process cause a mixture of both γ and α' phases, with higher intensity α' peaks than γ peaks, proving that the as-built SLM PHSS is mostly martensitic, but the wrought PHSS is completely martensitic with a strong intensity of (110) reflection. Due to the applied ageing treatment for the wrought (H1150 condition) PHSS, this analysis is not entirely accurate; retained γ should be detected as well as α'. The absence of the retained austenite in the XRD pattern of the wrought alloy can be attributed to: (I) extremely low volume fraction of austenite in the matrix, which is below the XRD detection limit, and (II) transformation of retained austenite to martensite during mechanical grinding

and polishing. Murr's study [104] on as-built PHSS showed that Ar-atomized powder produced by SLM in a N environment resulted in a fully martensitic microstructure. However, a combination of α' and γ was formed in the present study using Ar-atomized powder in the N environment. This could be due to the slight difference in chemical composition, manufacturing process parameters, and sample geometry leading to different thermal histories during manufacturing. For example, larger contact area of the horizontally printed tensile samples with the build-plate in the present study versus small cylindrical shape samples in Murr's work would increase the cooling rate leading to larger strains and residual stresses during manufacturing [121]. The slight shift of $(110)_\alpha$ peak towards higher 2θ angles (see dotted line in Figure 3-10) is ascribed to the generation of microstrains and grain refinement during heating and rapid solidification.

Other researchers have studied processing parameters, built orientation, and heat treatment effects on γ phase fraction formation. Mahmoudi et al. concluded that XRD patterns of SLM PHSS in various conditions have a higher intensity of α' peaks than γ ones, showing that they are mainly martensitic, while the fraction of retained γ varies for different conditions due to the different γ stability sources [40]. Similar observations confirm the presence of both phases in SLM 17-4 PHSS samples [36].

3.3.3 Microstructure features

A typical porosity of ~0.3% is reported for the as-built SLM PHSS. (Refer to 2.6.3 for a description of the defects induced during the SLM process.) As Figure 3-11 (a_1, a_2, a_3, c) shows, the as-built SLM specimen contains notable flaws.

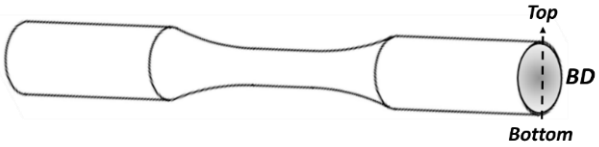

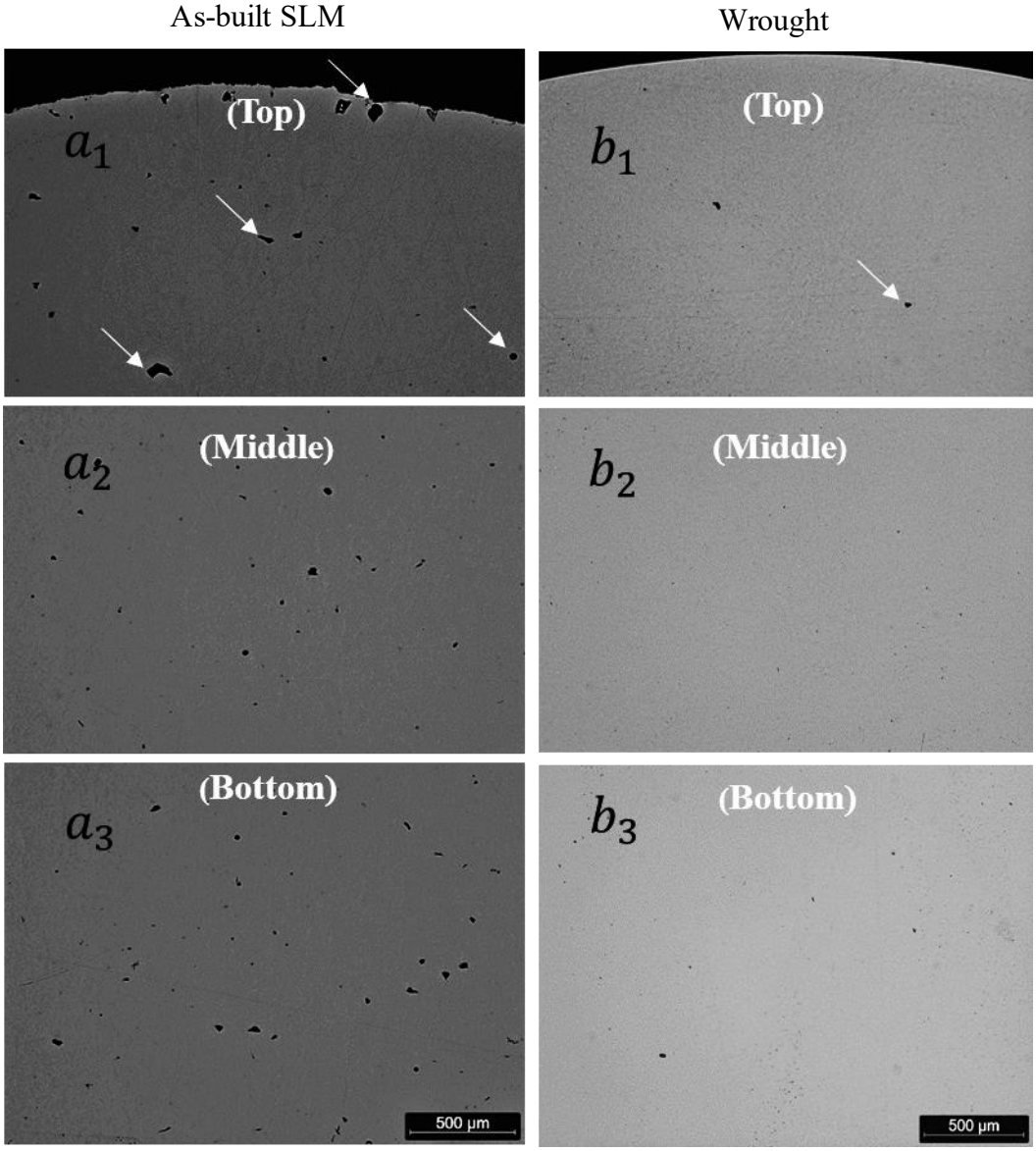

Longitudinal plane of the as-built SLM part

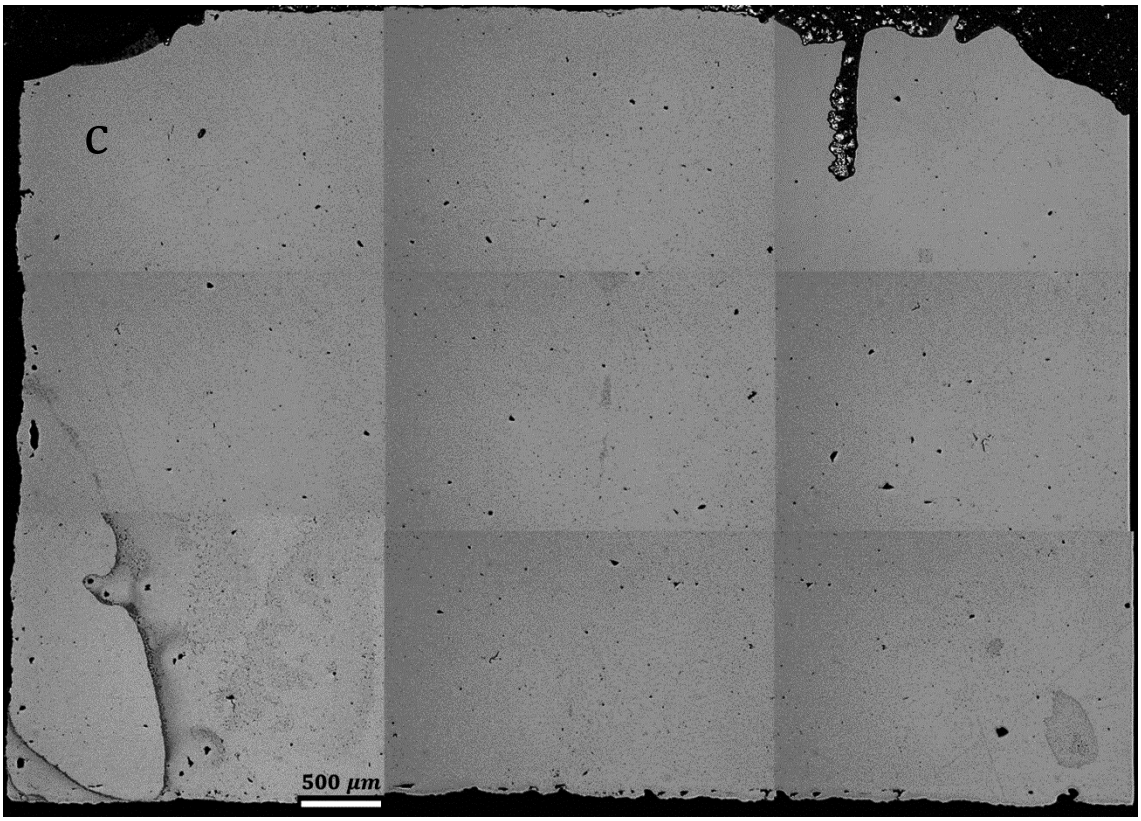

Figure 3-11 Optical images of the as-built SLM 17-4 PHSS in cross-section (a_1, a_2, a_3) and wrought PHSS in cross-section (b_1, b_2, b_3) as shown in the schematic and (c) the as-built SLM 17-4 PHSS in the longitudinal plane as shown in the schematic

Specimens were prepared in the transverse and longitudinal planes. The bottom and top regions of the transverse plane of the as-built PHSS (Figure 3-11 (a_1, a_2, a_3)), contain slightly more defects than the middle region due to the higher thermal transfer, explained by the cooling rates and the extent of fusion. There was conduction between the as-built SLM PHSS and substrate in the bottom region and convection and radiation in the top region (Refer to 2.6). Consequently, variation in defect statistics and morphologies is due to the different thermal histories in different locations. Pores with spherical morphology in various sizes, partially melted and unmelted particles, lack of fusion regions with slit-shaped and irregular morphology

were detected in the specimens and surfaces. In contrast, the defects induced during fabrication of the wrought PHSS consist of a few tiny pores (Figure 3-11 (b_1, b_2, b_3)).

Yadollahi and Shamsaei [82] showed that the interlayers temperature could influence the degree of remelting of the previous layers. In other words, the higher the temperature of the previous layers, the deeper the laser penetration depth would be. As a result, the accumulation of heat during repetitive heating/cooling cycles could lead to better bonding and interlayer fusion in the middle region.

Figure 3-12 shows the selected regions as the bottom, middle and top areas of the transverse plane of the as-built SLM 17-4 PHSS. To achieve reliable microscopy data, a 600*800 μm^2 area was selected for scanning.

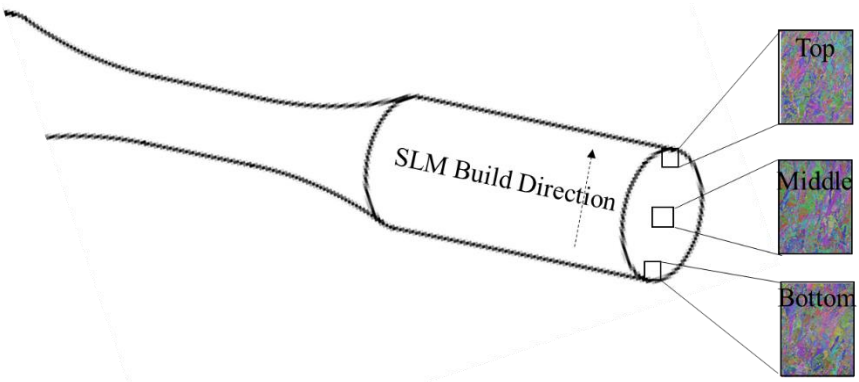

Figure 3-12 Designated areas for location dependency investigation

EBSD maps were used to identify and quantify the phases, microstructure (e.g. grain size distribution, and the average grain size, morphology, and orientation), grain boundaries form and distribution, phase boundary orientation relationship, strain distribution in phases, and the crystallographic texture of specimens.

Electron backscatter diffraction maps of the wrought specimen are presented in Figure 3-13. The phase map shows α' microstructure and small amount of retained γ. The α' laths are mostly too fine to be revealed clearly (particularly in Figure 3-13 maps magnification); the dominant features are blocks of parallel α' laths within prior γ grains. It reveals that the microstructure of γ prior grain size is roughly equiaxed. γ is available as both retained and reverted. Retained γ are formed in prior grain boundaries, boundaries of packets (HAGB locations), block

boundaries, α' lath boundaries due to the larger strains and/or microsegregation of γ-stabilizing elements at grain boundaries [37, 109]. Their morphology are columnar and blocky. However, the nucleation and growth of the reversed γ depend on the diffusion and segregation of γ-stabilizing elements (such as Ni, C, N etc.) during thermal aging. Song et al. [122] showed that the nucleation of the reverted γin low carbon martensitic stainless steel (≈0.05wt.% C) took place near the $M_{23}C_6$ carbides (M=Cr, Mo, etc.) and Ni-partitioning near the carbide particles played a major role in stability of the reverted γ. In addition to the formation of reverted γ, the recrystallization of ferrite can also occur during thermal aging. However, it is difficult to discern between low carbon α' (BCT) and ferrite (BCC) in XRD and EBSD analysis. The low concentration of carbon (≈ 0.05wt.%) in the studied alloy decreases the tetragonality and the amount of expansion along the C-axis [123]. It was shown that when the concentration of carbon is less than 0.07wt.%, the lattice parameter of BCT α' and BCC ferrite would be very identical [37, 124]. Reverted γ is formed randomly inside grains with blocky morphology [65].

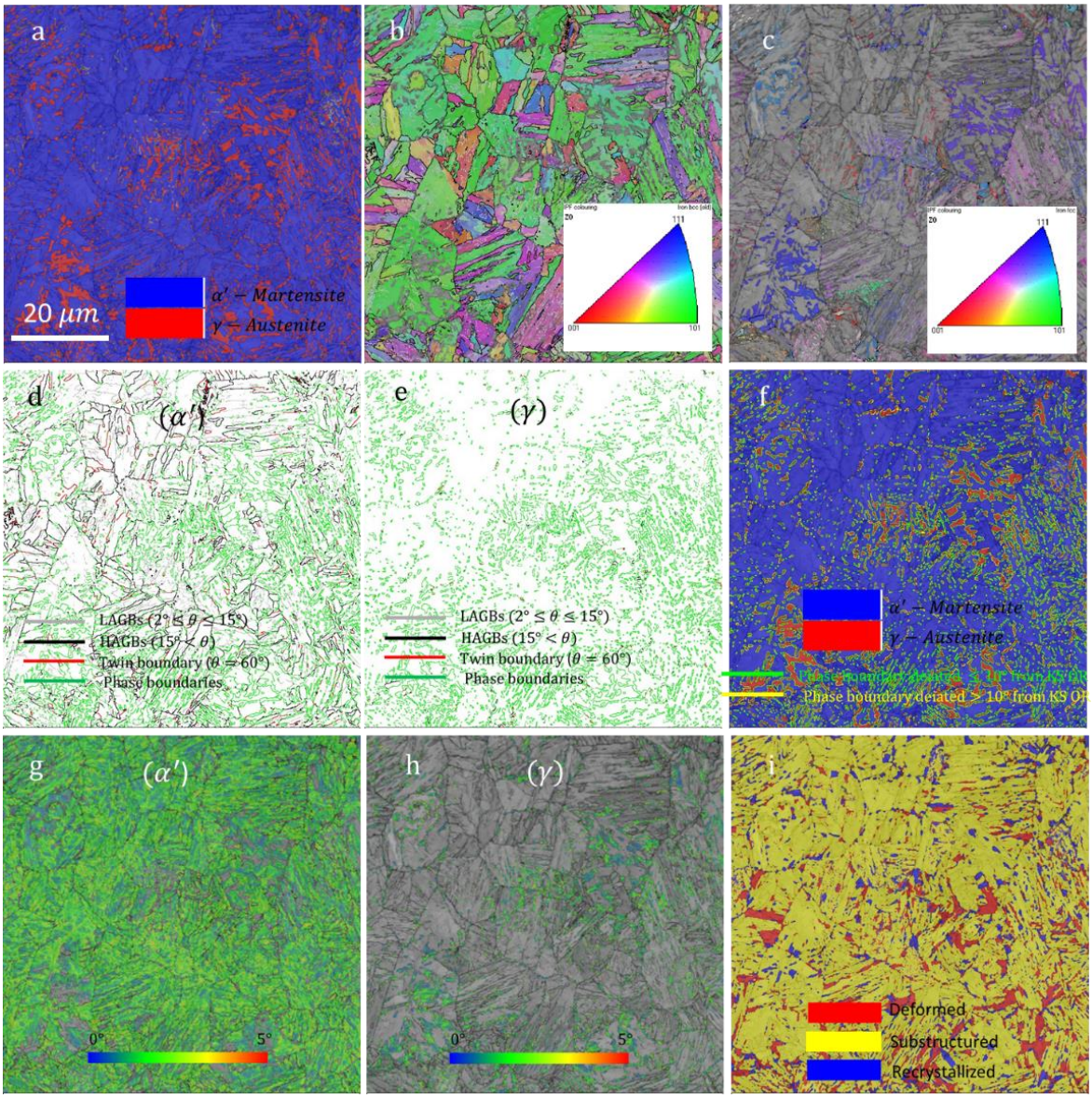

Figure 3-13 EBSD maps of the wrought PHSS along with normal direction (ND) direction (a) Band Contrast (BC)+phase map (γ in red, and α'in blue), (b) BC+inverse pole figure (IPF)-Z with LAGBs and HAGBs, for α', (c) BC+IPF-Z with LAGBs and HAGBs, for γ, (d) grain boundaries including (LAGBs in Silver, HAGBs in black, Interface boundaries in green, and Twin boundaries in red) for α', (e) grain boundaries for γ (f) BC+Phase boundary orientation relationship as BC+phase map+phase boundaries (based on Kurdjumov–Sachs relationship), (g) BC+Local misorientation maps of α', (h) BC+Local misorientation maps of γ, and (i) recrystallised, substructure, and deformed maps

Phase fraction

Due to higher cooling rates in SLM than wrought fabrication, as [97] mentioned, the γ stability range remains a short time around 6 ms and α' transformation mainly happens during SLM fabrication. Starting and finishing α' transformation of 17-4 PHSS manufactured conventionally was measured at 132℃ and 32℃, respectively [125]. In this study, based on the reported chemical composition percentages measured by spectroscopy, -50.72℃ was calculated as the starting temperature of α' transformation, using Equation 2-2. The cooling rate of the applied SLM process for fabrication in this study was high enough to achieve full α' transformation [98]; however, some effective γ stability (discussed in 2.3.4) changes the α'transformation progression.

The distribution of phases in the wrought and as-built SLM PHSS are presented in Figure 3-13 and Figure 3-14 (a_2) respectively. The phase fractions for the wrought and as-built SLM PHSS in different locations are represented in Table 3-3.

Table 3-3 γ and α′ fraction of the wrought and as-built SLM PHSS in different locations

Specimen ID	Zero solution, %	(γ),%	(α′),%
Wrought	3.7	15.0	81.3
As-built-Transverse-Top	0.6	43.8	55.6
As-built-Transverse-Middle	1	28.2	70.8
As-built-Transverse-Bottom	2	44.3	53.7

Investigation of the as-built SLM PHSS (with the middle region as the target area) indicates approximately 30% retained γ and 70% of fresh/tempered α', while wrought specimen (supplied in CA-H1150 condition) shows 15% γ, both retained and reverted, and 81.3% tempered α' (Table 3-3).

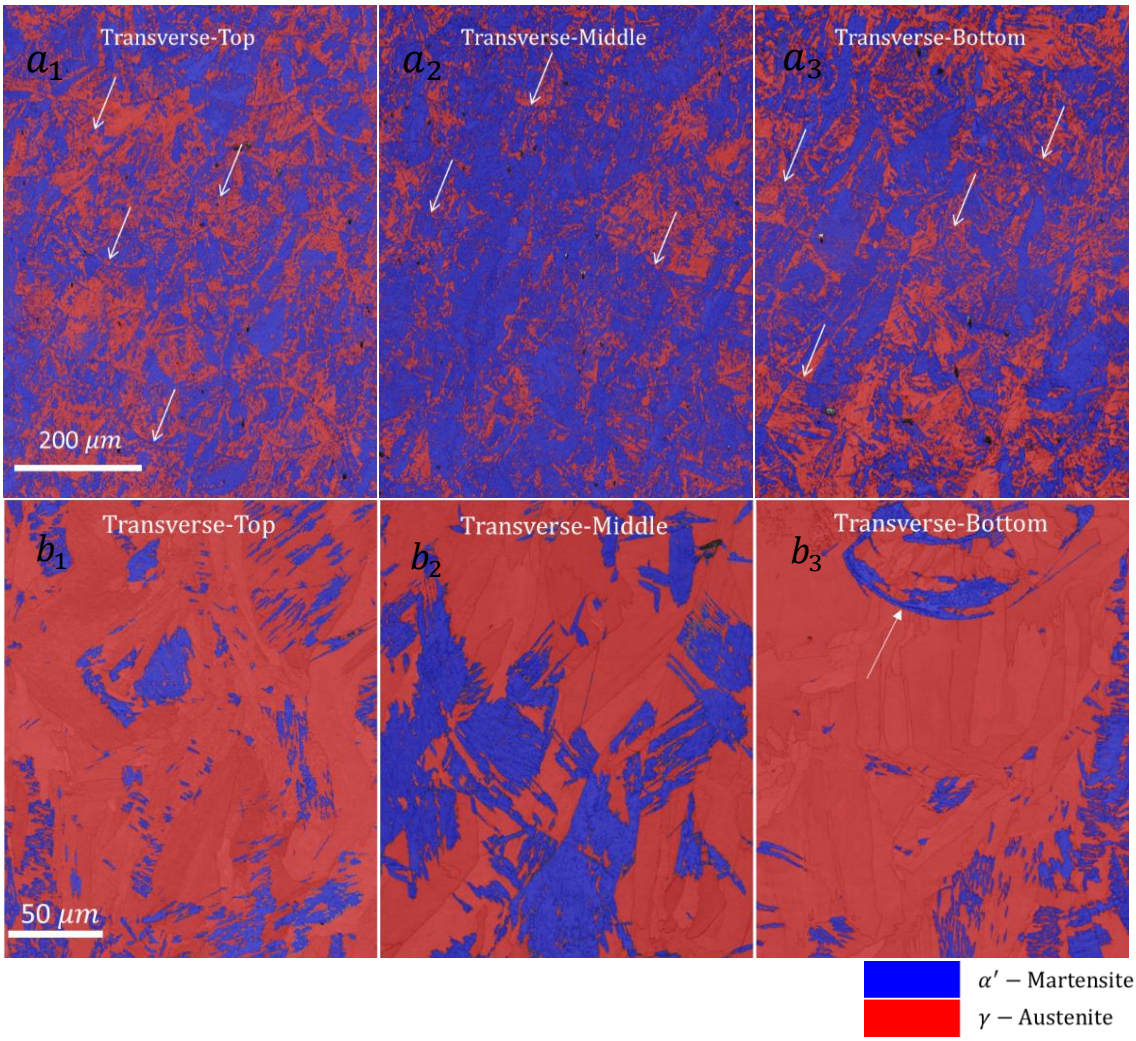

Figure 3-14 BC+Phase maps (γ in red, and α' in blue), (a_1, a_2, a_3) in top, middle, and bottom regions of the transverse plane in low magnification, and (b_1, b_2, b_3) in high magnification

As shown in Figure 3-14, the SLM microstructure is a mixture of fine equiaxed and coarse columnar grains, which provides isotropic behaviour, while a fine equiaxed microstructure was discovered in the wrought parts (Figure 3-13). Columnar and equiaxed solidification structures are the most common solidification microstructures reported in AM parts [90].

To study the effect of the SLM process on resultant microstructures, three regions were considered in the transverse plane of the horizontal built specimens (refer to Figure 3-12), labelled top, middle and bottom. As given, quite well indexed acquisition is recorded for the provided maps, ~%2 non-indexed points. Image quality (IQ)-phase maps of the as-built SLM PHSS showing phase fraction and distribution in these three regions are presented in Figure 3-14. The low magnification maps expose the distribution of dominant α' and less prevalent γ (Figure 3-14 (a_1, a_2, a_3)).

Melt pool boundaries are visible for SLM 17-4 PHSS (Figure 3-14), identified by white arrows. Melting and solidifying the melt pools during the SLM process results in particular grain structures and crystallographic textures. Geometry and the melt pools' size during SLM fabrication affect the subsequent grains' shape and orientation.

Melt pool boundaries in the middle region are not as visible as in the bottom and top regions, probably due to lower cooling rates and higher diffusion in the middle region than in the bottom and top. The middle region of the as-built SLM samples has clearly less retained γ than the bottom and top regions. This can be explained by lower cooling rate and higher temperature of the middle zone which decreases the concentration of γ-stabilizing elements (Ni in particular) in γ grains leading to instability of γ and transformation of $\gamma \rightarrow \alpha'$ upon cooling. For more visual detail, Figure 3-14 (b_1, b_2, b_3) also presents high magnification images.

Grain Orientation and Misorientation Profiles

The IPF maps of SLM products, which denotes grain orientation, demonstrate the complexity of the 17-4 PHSS microstructure fabricated by SLM as Debroy claimed [90]. Yadollahi et al. reported a competitive growth phenomenon observed in SLM 17-4 PH SS [41]. In the SLM technique with a fast scanning speed, grain growth direction is mainly <001> [90]. The 17-4 PHSS's grain growth direction is parallel to the heat flow direction, normal to the melt pool's solidifying surface. The various colours correspond to the orientation of grains for crystal lattice, and each colour corresponds to the unique combination of Euler angles. So, grains with the same crystallographic orientation have similar colours.

The IPF maps in the Z direction of the as-built SLM PHSS in different locations for α' and γ are shown in magnifications in Figure 3-15 and Figure 3-16 respectively. As already noted, Figure 3-13 shows the IPF-Z of the wrought specimen. As the figure shows, [111] is more dominant in the α' (Figure 3-15 (a_2)), but [001] is more visible in the γ phase (Figure 3-16 (a_2)). Overall, random textures were detected for both phases in the microstructure.

Measured average grain sizes of $\alpha'$and γ are tabulated in Table 3-4. The average grain sizes of α' and γ correspond to those of the as-built SLM PHSS at the transverse plane, are higher than those in the wrought PHSS (refer to Figure 3-12). The α' grain size of the as-built SLM PHSS is more than twice that of the wrought PHSS. Similar to α', the grain size of the γ of the as-built SLM PHSS is 2.5 times that of the wrought PHSS.

It can also be seen that average grain size of $\alpha'$is slightly larger in the middle region as compared to top and bottom regions. This is attributed to the heat accumulation in the middle region and lower cooling rate during manufacturing.

The grain size of the bottom zone is the finest due to rapid dissipation of heat through the build-plate (conduction mode). One important factor that affects the M_s temperature is the grain size of the parent γ. The refined grain size due to rapid solidification during SLM process reduces the M_s temperature. This can result in the formation of considerable retained austenite in the matrix, as shown in Figure 3-14. Retained α is formed at the grain boundaries where the atomic rearrangement is irregular, and α' cannot grow further [126].

Table 3-4 Average grain size of γ and α′ in the wrought and as-built SLM PHSS in different locations

Specimen ID	Average grain size γ (μm)	Average grain size α' (μm)
Wrought	0.62	1.47
As-built-Transverse-Top	2.00	2.24
As-built- Transverse-Middle	1.62	2.80
As-built- Transverse-Bottom	1.07	1.07

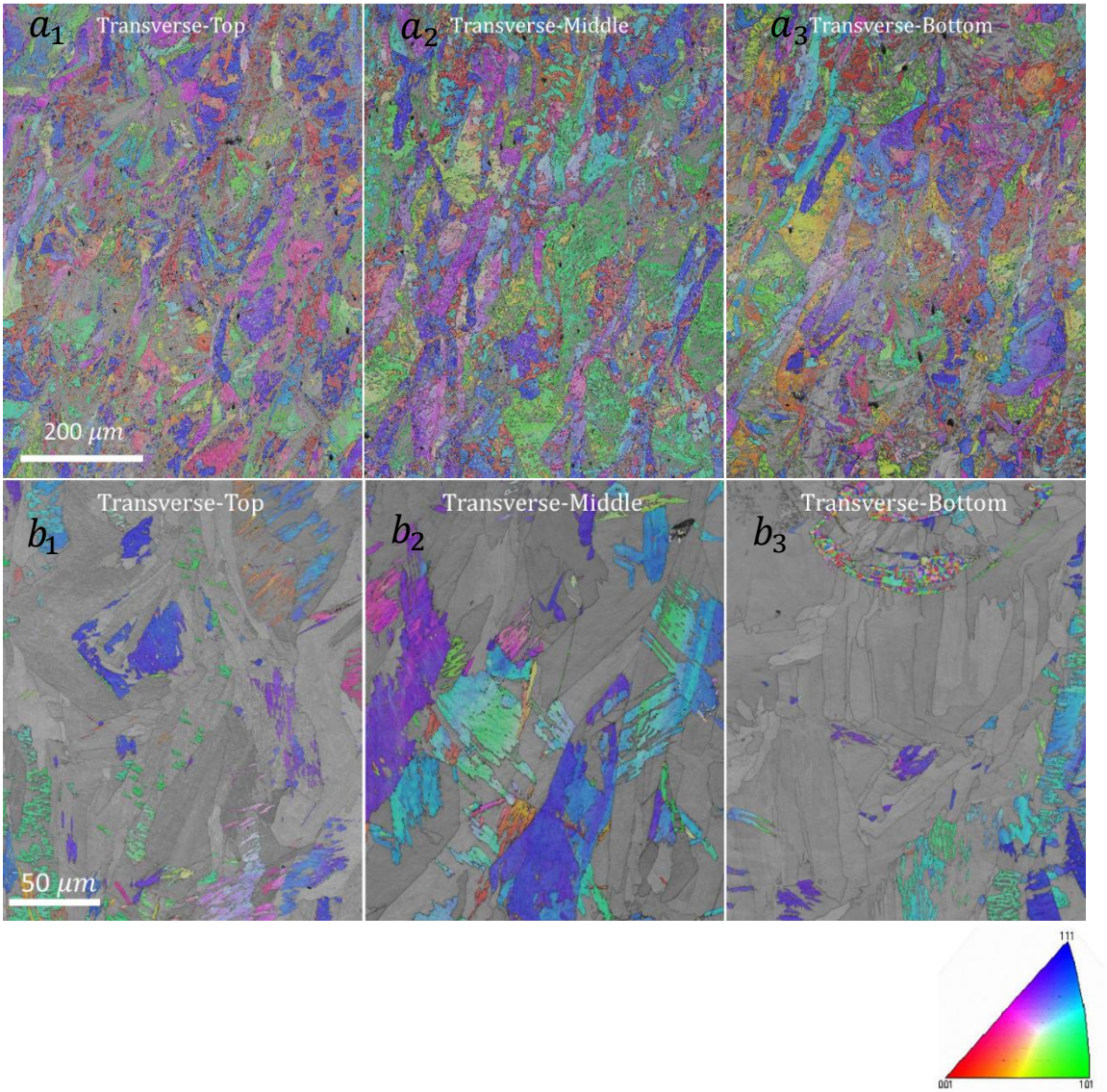

Figure 3-15 BC+IPF-Z with LAGBs and HAGBs for α'(a_1, a_2, a_3) in top, middle and bottom regions of the transverse plane in low magnification, (b_1, b_2, b_3) in high magnification

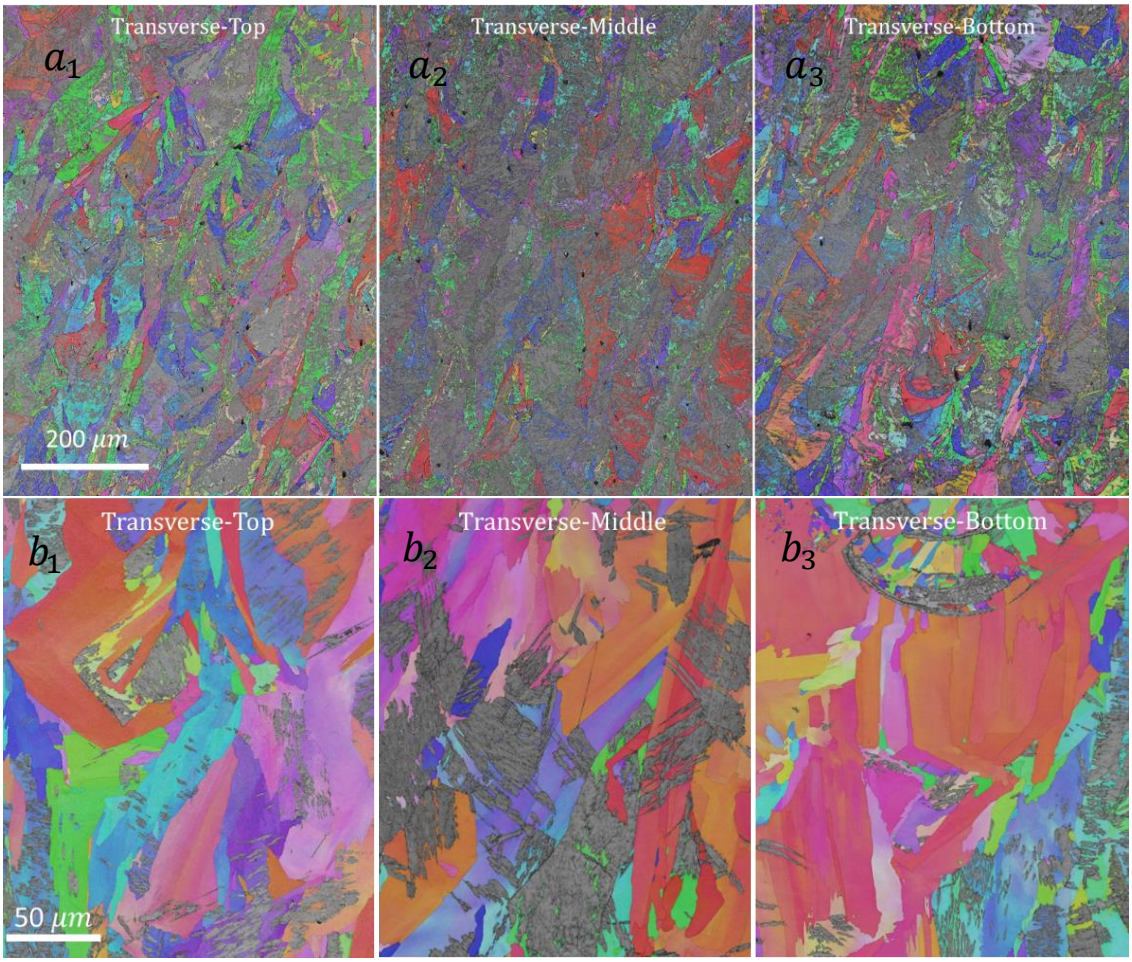

Figure 3-16 BC+IPF-Z with LAGBs and HAGBs for γ (a_1, a_2, a_3) in top, middle, and bottom regions of the transverse plane in low magnification, (b_1, b_2, b_3) in high magnification

The microstructure features (average grain size) near the substrate and the top regions are slightly different from those in the middle region. This follows the pattern of defect distribution and morphology due to different thermal histories. In the bottom region, heat is quickly conducted away by the substrate, and in the top region, radiation and convection heat loss are more prevalent.

The cooling rate is the most critical factor for grain size and scale. Higher cooling rates create finer grain microstructure due to shorter growth times. Grain size turns out to be coarser in the upper layers (of the middle region) due to a lower local cooling rate than in the lower layers. The fine microstructure is produced more like tempering and ageing microstructure in the bottom and top of the as-built SLM PHSS. Similar to the phase fraction, α' grain size in the middle region is larger than in the bottom and top regions, while the average γ phase in the top region is the highest and in the bottom, the lowest.

Grain boundaries evolution (subdivision of a grain)

Two factors explain the effect of grain boundary on strength. First, grain boundaries act as barriers to slip deformation. And second, the requirement for continuity between grains during loading is having complex modes of deformation in grains [71].

Owing to high energy at grain boundaries, they are favoured sites for phase transformations, solid-state activities such diffusion and precipitation activities. A significant point to consider is that the high energy of a grain boundary usually results in a higher concentration of solute atoms at the boundary than in the grain's interior. Usually, they are a site for the precipitation of new phases and initiation of corrosion.

Boundary types can be identified by misorientation between the two grains. LAGBs or subgrain boundaries typically have a misorientation of less than 15°, while HAGBs generally have a misorientation greater than 15°. Special boundaries or twin boundaries (TBs) involve a 60° rotation about the [111] direction. In grain boundary engineering, it is essential to enhance or reduce the relative richness of certain grain boundary types to optimise the final material properties.

The fraction of LAGBs, HAGBs and TBs of γ and α' of the wrought and as-built PHSS in different locations are presented in Table 3-5.

Table 3-5 Fractions of LAGBs, HAGBs, TBs of γ and α' of the wrought PHSS and as-built SLM PHSS in different locations

Specimen ID	LAGBs	HAGBs	Twin Bs	LAGBs	HAGBs	Twin Bs
	(α')%			(γ)%		
Wrought	70.96	25.30	3.74	79.88	14.59	5.53
As-built-Transverse-Top	87.4	11.61	0.99	72.76	26.30	0.94
As-built-Transverse-Middle	87.35	12.00	0.65	80.44	19.25	0.31
As-built-Transverse-Bottom	85.01	14.21	0.79	66.33	32.81	0.86

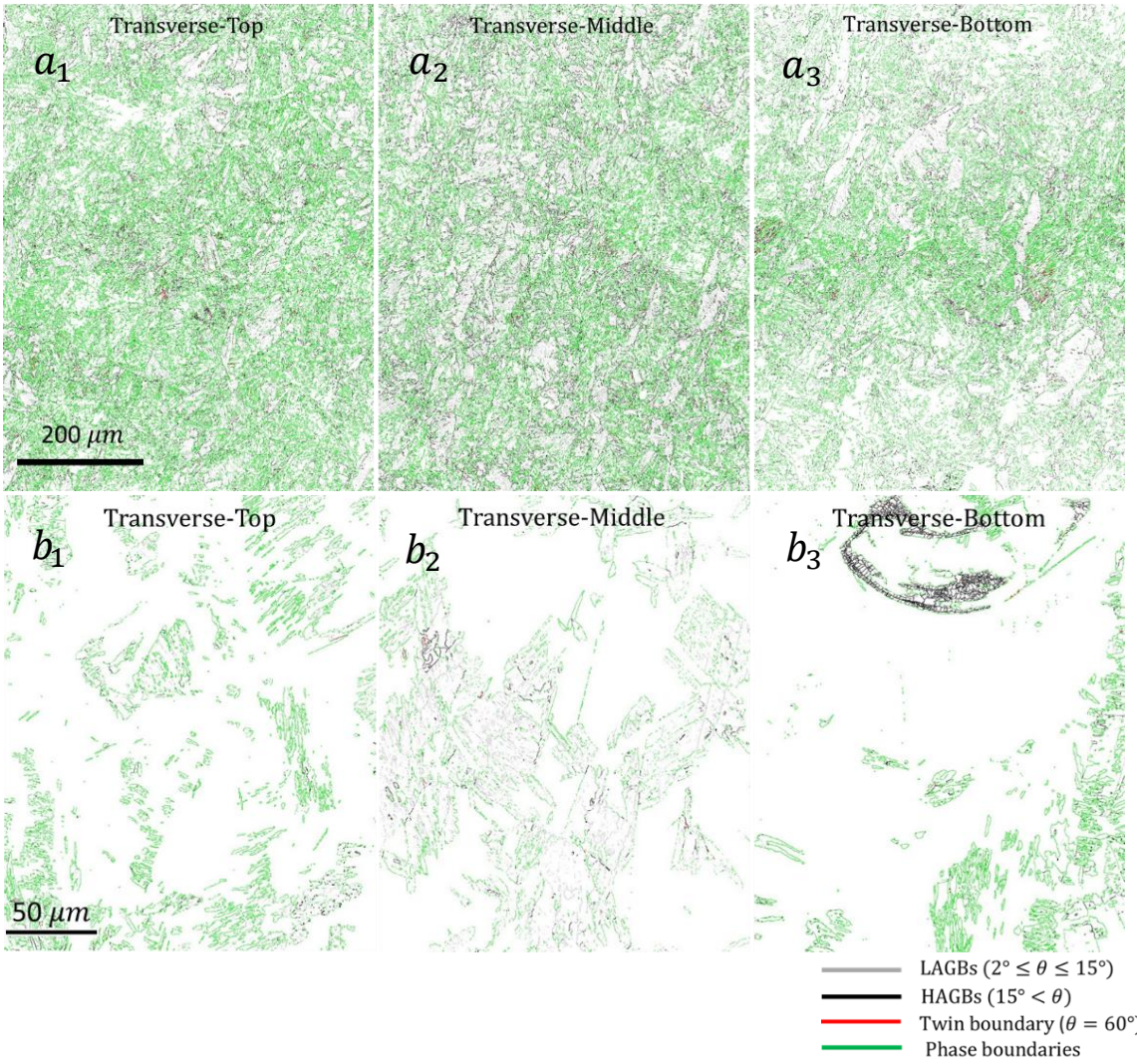

Figure 3-17 Grain boundaries (LAGBs; Silver, HAGBs; black, Interface Bs; green, Twin Bs; red) of α' (a_1, a_2, a_3) in bottom, middle, and top of the transverse plane in low magnification, (b_1, b_2, b_3) in high magnification

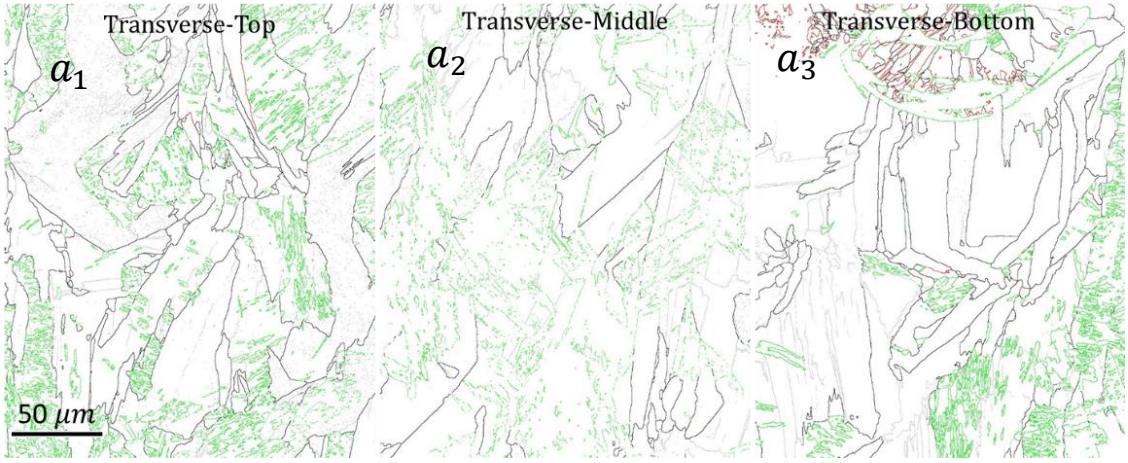

Figure 3-18 Grain boundaries, (LAGBs; Silver, HAGBs; black, Interface Bs; green, Twin Bs; red) of γ in bottom, middle, and top of the transverse plane at high magnification

Figure 3-13 shows grain boundary maps for the wrought PHSS. Figure 3-17 (a) and Figure 3-18 (a) are grain boundary maps for the as-built SLM PHSS for α' and γ respectively.

The fraction of LAGBs in as-built SLM of α' is ≈20% more than wrought alloy. This indicates higher dislocation densities in the α' laths. This is attributed to the thermal stresses introduced during repetitive heating/cooling cycles in SLM process. It has been shown that the dislocations introduced during SLM process are statistically stored dislocations and unlike geometrically necessary dislocations (GNDs) do not generate lattice misorientation and contribute to recrystallization [127]. This could explain the low fraction of twin boundaries and recrystallized grains in the as-built samples. Twin boundaries of the wrought alloys in both α' and γ are considerably more than as-printed samples. This can be ascribed to the H1150 condition of wrought alloy (i.e., solution treatment + aging) and formation of twin grains in the matrix driven by a decrease in the interfacial energy of the grain boundaries. In contrast to α', the fraction of LAGB in γ phase varies along the build direction. This indicate the variation of dislocation densities along the build direction in γ phase which is softer and more densely packed than α'.

KS OR relationship

The orientation relationships are explained according correlated crystallographic planes and directions in two phases or a rotation axis/rotation angle pair ω, revealing the misorientation between the two phases. Kurdjumov-Sach (KS) orientation relationship (OR) is a one which shows that one austenite grain with a neighbouring α' grain on the other side can maintain an approximate $(111_\gamma) \parallel (110_\alpha)$ and $[1\bar{1}0]_\gamma \parallel [1\bar{1}1]_\alpha$ relation or the misorientation between adjacent austenite and ferrite grains with KS OR is close to <0.97 0.18 0.18> 42.85°.

For further assessments, the EBSD maps were used to evaluate the phase boundary orientation between γ and α' phases. A list of the fractions of the phase boundaries close to KS OR is shown in Table 3-6.

Figure 3-13 and Figure 3-19 (a_2) are used to qualitatively shows this relationship between α' and γ in the wrought and the as-built PHSS.

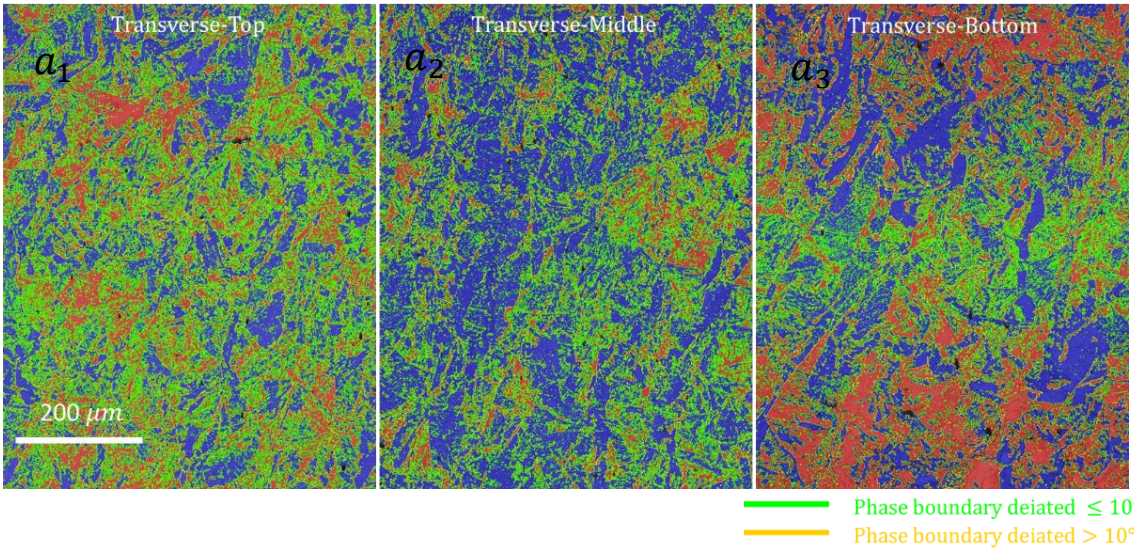

Figure 3-19 Phase boundary orientation relationship; BC+Phase maps+Phase boundaries between γ and α' (green and yellow lines indicate phase boundaries with deviation angles less and more than 10 °from KS OR.

It seems that the KS-OR of α' and γ in wrought alloy is almost similar to as-built samples. In transverse plane of the as-built samples, the deveiation≤10° (close to KS-OR) increases from bottom region (89.31%) to top region (93.11%), denoting higher coherency between α' and γ in the top region.

Table 3-6 Distribution of deviation angles of the phase boundaries from KS-OR of γ and α′

Specimen ID	x<10° KS OR (%)	x>10° KS OR (%)
Wrought	93.30	6.70
As-built-Transverse-Top	93.11	6.88
As-built-Transverse-Middle	92.77	7.23
As-built-Transverse-Bottom	89.31	10.69

Kernel average misorientation

A kernel average misorientation (KAM) map calculates the average misorientation between each pixel and its nearest neighbours. It is employed to analysis the local grain misorientation and helps to point out the dislocation densities, lattice distortion and localized plastic deformation. Higher dislocation densities and lattice distortion in grains lead to larger KAM values. In this study, KAM maps were used for qualitative and quantitative study of the strain distributions of γ and α'.

Figure 3-13, Figure 3-20 (a) and Figure 3-21 (a) show qualitative KAM maps for the wrought as well as the as-built SLM PHSS in γ and α' respectively. KAM values of γ and $\alpha'$are tabulated in Table 3-7.

Table 3-7 KAM values of γ and α'

Specimen ID	KAM (α'),	KAM (γ)
Wrought[1]	0.68	0.58
As-built-Transverse-Top	0.98	0.62
As-built-Transverse-Middle	1.02	0.65
As-built-Transverse-Bottom	0.83	0.50

Kernel average misorientation values are similar for γ and α' for the wrought specimen. KAM values are 0.65 for γ and 1.02 for α' for the as-built specimen in the middle region. KAM values in both phases for the wrought specimen were lower than those for the as-built specimen, which can be attributed to lower residual stresses in the wrought specimen, as expected.

Comparison of KAM values for desired regions as mentioned before showed that α' KAM in the middle region is higher than in other regions, consistent with expectations. The α' KAM values for the top, middle, and bottom regions are 0.98, 1.02 and 0.83, respectively. A similar

[1] Should be mentioned in relation to the KAM maps in Figure 3-13; the calculated value for the wrought specimen is in a different setting and only can be used in the qualitative comparison.

trend for γ was observed: the γ KAM values for the top, middle, and bottom are 0.62, 0.65 and 0.5, respectively. Higher KAM values in the middle regions can be explained by the higher fraction of α' there.

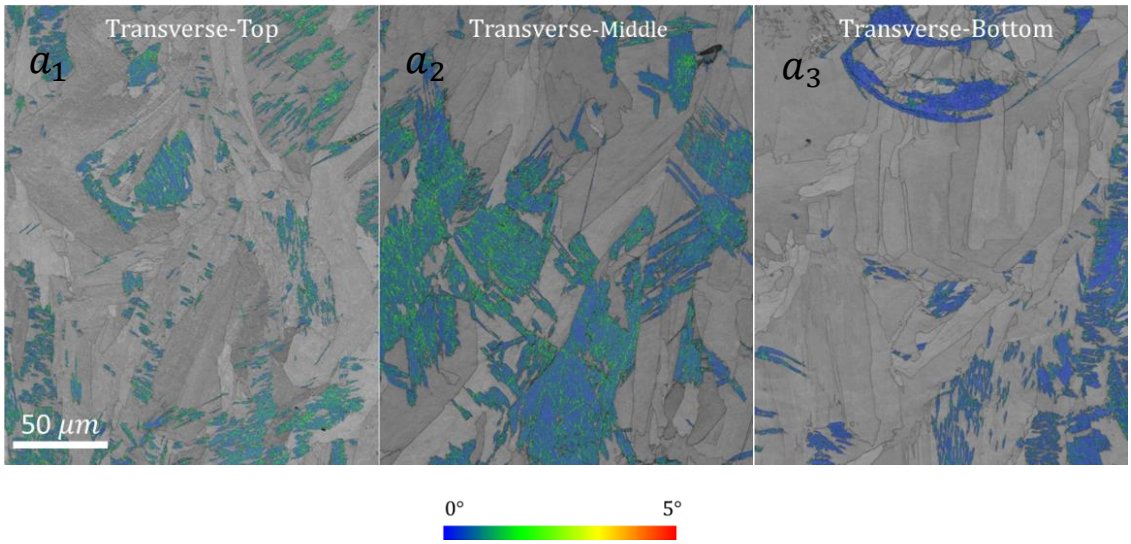

Figure 3-20 Kernel Average Misorientation (KAM) of α' (a, b, c) in bottom, middle, and top of the transverse plane at high magnification

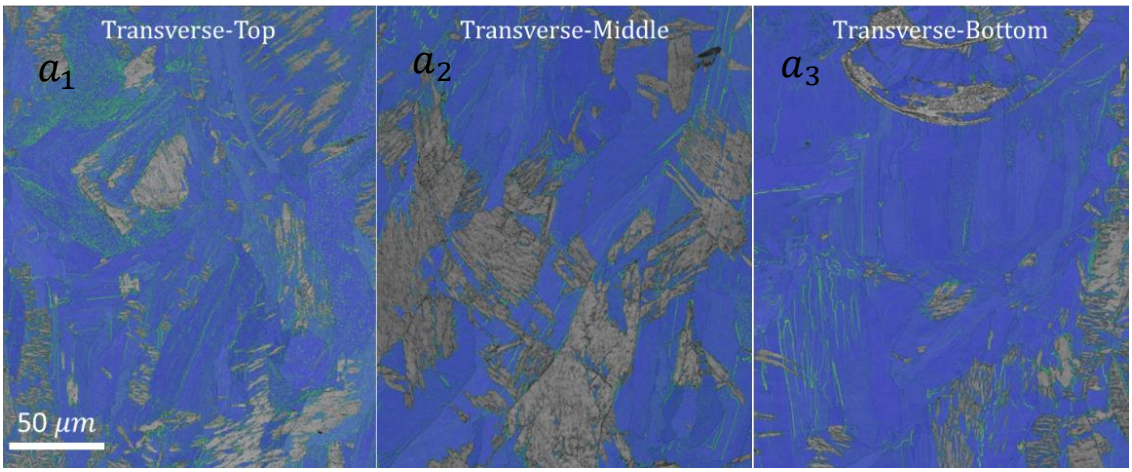

Figure 3-21 KAM of γ (a) in the bottom, middle, and top of the transverse plane at high magnification

3.3.4 Mechanical properties

This section describes the characterisation of mechanical properties by hardness and tensile testing.

Hardness

To study anisotropy and location dependency, the hardness of as-built in built orientation (bottom to the top direction shown with the dashed arrow in Figure 3-22 labelled as BD) was measured. The wrought specimen hardness measurement was conducted in the transverse plane (normal direction ND).

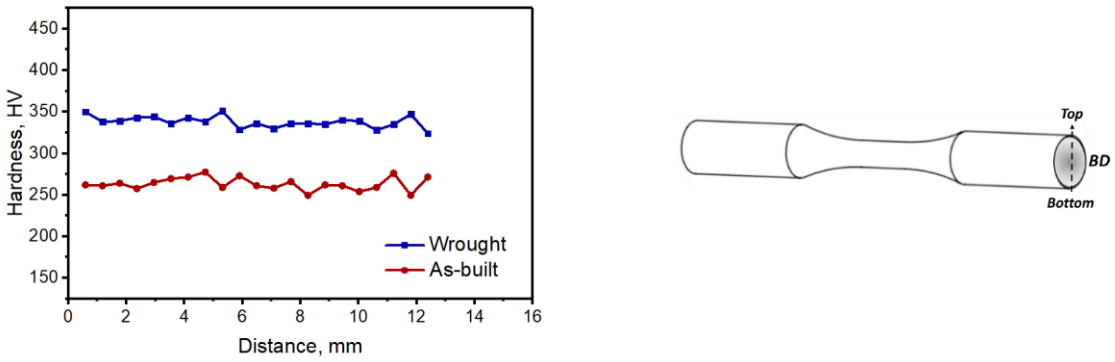

Figure 3-22 Hardness of the as-built SLM and wrought 17-4 PHSS

Figure 3-22 shows the Vickers hardness values plotted against the number of indentations for the as-built SLM and wrought PHSS. Hardness values of 269±34 and 339±79 were measured for the as-built SLM and wrought PHSS respectively (Figure 3-22). The HV of the wrought specimen is considerably higher than that of the as-built specimen. The wrought one is provided in H1150 condition, and has lower hardness than the conventionally manufactured specimens produced in aged conditions [48]. Hardness in the wrought and the as-built specimens shows a similar trend, which indicates there is no significant inhomogeneity in either microstructure.

γ in the as-built SLM PHSS is approximately 28%, compared to 15% in the wrought specimen. Thus, a higher fraction of γ leads to lower hardness. The wrought specimen underwent precipitation hardening post-treatment, strengthened by coarse enriched Cu as the overaged condition. However, no precipitates were detected in the as-built specimen, due to no

solutionising [128] [30]. The grain size of the as-built SLM PHSS is coarser than that of the wrought specimen, further proof of lower hardness in the former (refer to Table 3-4). Presence of microporosities and microvoids can be the other reason. The volume of the microvoids is compressed during indentation leading to lower hardness values.

It was expected that hardness variation would be slightly convex from botto to top due to the slight difference in microstructures across locations (refer to 4.2.2 for $\%\alpha'$ in different locations). Despite this expectation, very consistent trend values were measured for the bottom and top sites in the as-built SLM PHSS.

Tensile properties

To compare the mechanical properties of the as-built and wrought PHSS, a monotonic tensile test was implemented. The effect of surface finish was also examined on the as-built. For the as-built specimen, as all the coupons were fabricated horizontally, the tensile loading axis was perpendicular to the utilised build direction, resulting in a parallel direction with scan lines. Tensile properties of as-built 17-4 PHSS parts are usually lower than those of wrought PHSS parts [82]. However, superior tensile properties for as-built 15-5 PHSS compared to wrought have been reported [44]. Stress–strain curves of the as-built, surface-finished, and wrought PHSS (in H1150 condition) are presented in Figure 3-23.

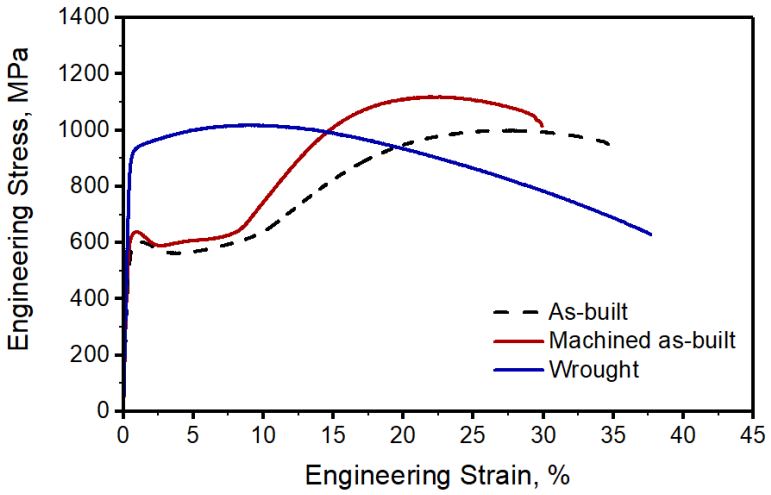

Figure 3-23 Stress-strain curves of the as-built SLM, wrought, and surface-finished SLM 17-4 PH SS

Corresponding values of the stress–strain curves are shown in Table 3-8.

Table 3-8 Hardness and tensile properties of the as-built SLM, wrought, and surface-finished SLM specimen

	E	σ_y(MPa)	σ_UTS(MPa)	Strength ratio ($\frac{\sigma_y}{\sigma_{UTS}}$)	UEL (%)	TEL (%)	UTS*TEL (MPa*%)
As-built	176±1	605±2	1007±11	0.602±0.005	27.32±0.02	35.4±0.55	35651±951
Wrought	209±14	914±7	1017±2	0.898±0.008	9.00±0.56	38.96±0.02	39622±1828
Surface-finished	182	638	1118	0.571	21.82	29.9	33452

Young's modulus (E), as a structure-independent property, mainly depends on the chemical composition, phase fraction and atomic bondings of a material. The E of the as-built SLM PHSS was found to be lower than that of the wrought PHSS. Differences in %wt of chemical composition elements in two sets influence phase fractions and consequently γ stability and E values. Despite chemical composition, N semi-inert gas used to purge the machine during the SLM process induced greater γ stability in the as-built SLM PHSS than the wrought PHSS due to the former's higher γ fraction. Also, the vaporization of elements during SLM process due to laser/powder interaction can cause metal loss and change the composition of raw material. The chemical composition of the wrought PHSS was not measured by spectrometry, so data was taken from the manufacturer's datasheet. Thus, accurate %wt was not available for comparison.

Yield strength (σ_y) was lower for the as-built SLM PHSS than the wrought specimen, which can be explained by various factors, as follows.

Yield strength denotes required shear stress for plastic deformation, so it is equal to the shear stress needed to move several dislocations in a perfect lattice – so-called critical resolved shear stress (τ_{CRSS}). Grain sizes influence this property significantly. As already mentioned with respect to the strengthening mechanism (see 2.3.6), grain refinement is one of those strengthening mechanism. The as-built SLM part has larger grain sizes for γ and α' phases than the wrought part (Refer to 3.3.3). The grain size of γ in the as-built SLM part is 2.6 times higher than that in the wrought part. Overall refinement of the wrought microstructure in standard H1150 condition can be proof of this claim. Moreover, by focusing the phase fraction effect, retained γ fraction is destructive for strengths. As a higher fraction of retained γ exists in the as-built SLM PHSS, it is logical that it should have lower strength. The yield strength result corresponds to the outcomes of the bulk hardness tests.

The as-built SLM PHSS exhibited a discontinuous yield form of stress–strain behaviour (upper and lower yield points), with yield starting from lower stress at lower strain, but strain hardening began rapidly afterwards. It was evident that by 1% strain a gradual relaxation occurred, and strengthening appeared after that. Discontinuous yielding produces heterogeneous and localised deformation as well as softening, which is highly undesirable. This behaviour can be attributed to high density of dislocations and perhaps higher N content of the as -built sample as compared to the wrought alloy. The printing environment used in this study was N and it is possible that N was absorbed during SLM process. It has been shown that N can be picked up during SLM process and cause reverse transformation of $\alpha' \rightarrow \gamma$ during aging in a very short period of time [129]. Ordinarily, the yield point can be associated with small amounts of interstitial or substitutional impurities.

The interstitial elements such as C and N in solid solution can diffuse and anchor the dislocations during plastic deformation (upper yield point). With this regard, N is more effective than C because of higher solubility and diffusion coefficient. When dislocations are pulled free from the solute atoms, slip can take place at lower stress (lower yield point). As a result, the freed dislocations can move at lower stress. This behaviour was not observed in the wrought alloy perhaps due to the lower concentration of interstitial elements and lower density of dislocations because of thermal treatment (solution treatment + aging). Wrought specimen shows flow stress-strain one which is desired for industrial applications. Surface finishing and elimination of surface defects slightly improved the yield stress and UTS of the as-built SLM samples.

Due to lower C% and higher metastable retained γ% (prerequisites for TRIP behaviour), the as-built 17-4 PHSS showed TRIP behaviour under tensile loading. High strain hardening capacity was observed by the strength ratio (yield strength/ultimate strength). As noted in 2.3.5, strengthening occurs from yield strength to ultimate one due to α' transformation progression under the applied load. α' transformation progression leads to new dislocations which cause high dislocation interaction at higher strengths. In the plastic region (after transition from the elastic region), strengthening is mainly controlled by dislocation interactions. It is also worth noting that; TRIP progression accompanies grain refinement. This behaviour of the as-built PHSS will be discussed by focusing on microscopy in Chapter 4.

The ultimate tensile strength of the wrought PHSS is only marginally higher than its yield strength, indicating the work hardening rate beyond the yield point is low. However, the opposite is true for the as-built SLM PHSS, which suggests its ability to undergo strain hardening. Lower interaction between dislocations results in a lower strain hardening rate and lower slope of the stress-strain curve in uniform plastic region. As the applied stress increases, more and more dislocations pile up at grain boundaries.

Uniform elongation of the as-built PHSS was approximately three times higher than in the wrought PHSS due to strain hardening. Retained γ is beneficial for stretching, so a higher fraction of γ explains this difference. Total elongation of the as-built SLM PHSS was lower than in the wrought PHSS, a result strongly associated with the higher fraction of destructive internal defects originating from SLM fabrication. It rapidly departed integrity and quick fracture after necking compared to wrought one with a considerable non-uniform elongation. It can be concluded that if SLM processing can fabricate parts free of imperfections, the ductility of as-built PHSS could be even higher than that of wrought PHSS. Yadollahi et al. concluded that elongation to failure of SLM parts is higher than for wrought parts; however, there are more defects in SLM parts than wrought parts [41, 130].

Total elongation multiply ultimate strength index is similar to toughness shows the required energy for failure. The index is higher for wrought PHSS, which makes it more suitable for industrial applications.

Compared to the data reported in [30], lower yield and ultimate strengths for the as-built SLM part were observed in this study. The effect of the utilised process parameters on thermal histories during fabrication, and consequently, the resultant microstructure (i.e. grain size and phase proportion) may explain such observations.

Fractography

Tensile fracture surfaces were inspected by SEM to determine fracture characteristics. The tensile fracture surface morphology of the as-built SLM PHSS and wrought PHSS are shown in Figure 3-24. Substantial variances were detected for both specimens that are in conformation with the tensile properties.

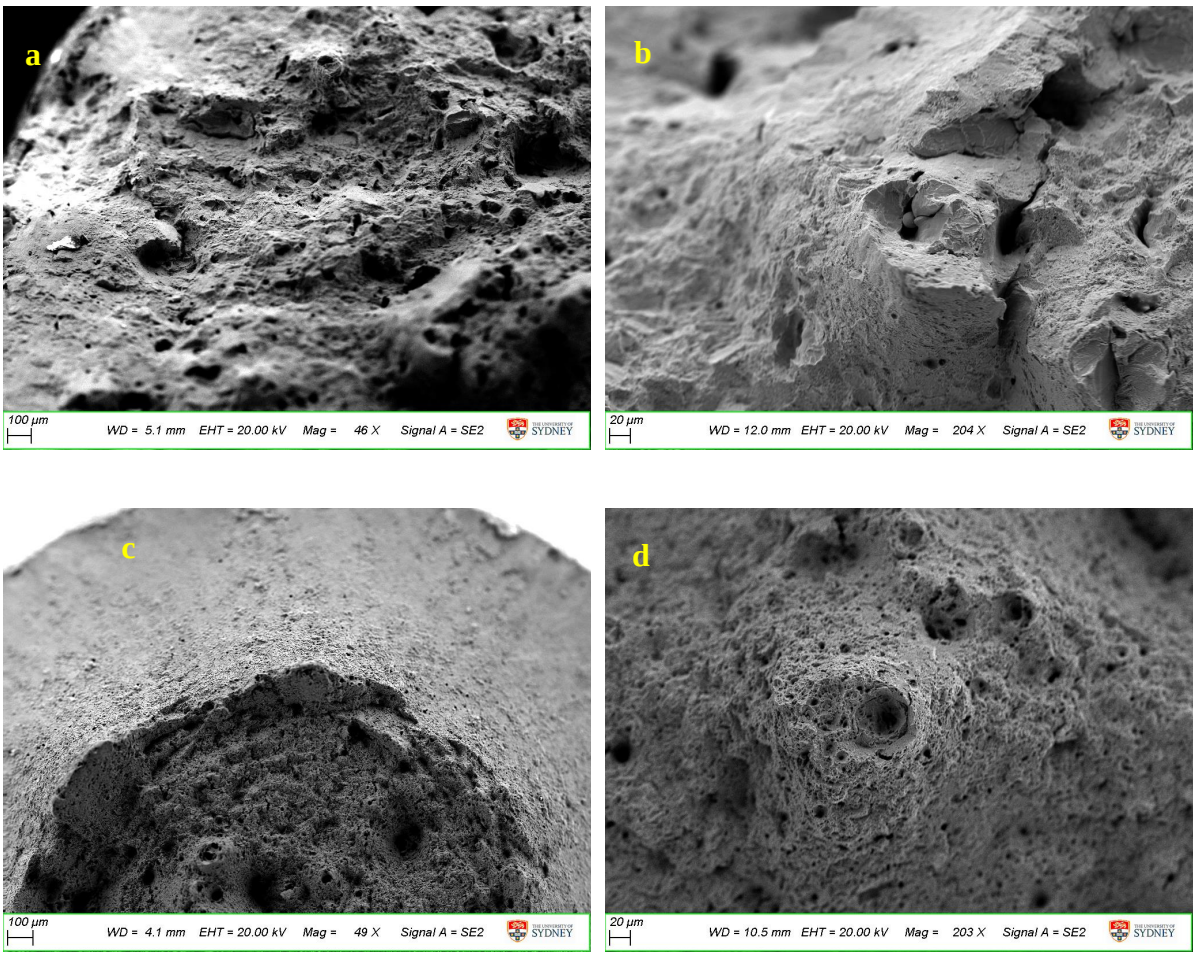

Figure 3-24 SEM images of the tensile fractured surfaces of (a) the as-built SLM PHSS, at (b) higher magnification, and (c) wrought PHSS, (d) with higher magnification

The tensile fractured surface of the as-built SLM PHSS (Figure 3-24 (a,b)) shows that it failed in quasi-cleavage mode (a mixed mode of brittle and ductile fracture). The quasi-cleavage mechanism includes micro-void coalescence and cleavage mode. The as-built fracture is characterised by tiny/shallow dimples, indicating less intense plastic deformation around micro-voids with a less fibrous surface. Intergranular fracture is mostly detected showing dominant brittle behaviour.

As noted earlier (2.6), induced defects in the SLM process create pores and unmelted regions and particles that can be detected on the tensile fractured surface of the as-built SLM. Pores and unmelted regions can act as crack nucleation sites under applied loading. Particle matrix interfaces (including unmelted particles and secondary phase particles) also serve as crack nucleation sites under loading.

Wrought parts fractured by cup and cone profiles are shown in Figure 3-24 (c,d). This type of failure occurs more often in commercial parts due to the formation of porosities and micro-voids. In cup and cone fractures, existing plastic flow causes very tiny voids to form within the part. As the flow continues, these voids grow and coalesce, and shear fracture leads to rupture.

3.4 Summary

SLM process was magnificently employed to manufacture dense 17-4 PHSS. Though the particular application was not targeted in this study, 17-4 PH SS should have met high strength with moderate corrosion resistance requisite. The presence of γ can either be detrimental or beneficial for a combination of strength and corrosion, depending on the intended application. Due to the intended mechanical properties, the fraction of γ can be tailored by the SLM processing parameters or post-processing. Worth mentioning that corrosion resistance and its correlation with γ is out of the scope and suggested to investigate in future work.

High heating and cooling rates imposed during SLM process was considered enough for fully α' transformation; however, the XRD pattern, as well as phase maps of the as-built SLM, showed a dual-phase α' and γ structure. Roughly $\sim$30% of γ and $\sim 70\%$ of α' were reported for the as-built SLM one. The retained γ at room temperature was associated with the γ stabilizers during fabrication. The effect of Mn, Ni, Cu elements, purged N gas during SLM fabrication and the grain refinement ($\sim 2\ \mu m$) during manufacturing could be the reasons for γ stability in the as-built SLM.

SLM processed 17-4 PHSS exhibited a sophisticated, inhomogeneous microstructure. Anisotropic microstructure was created due to the massive thermal incline between the melt pool regions and the previous solidified layers. Elongated coarse grains along the built direction were observed. Porosities, partially/ unmelted particles, lack of fusion regions were also detected within the as-built SLM specimens.

An investigation of the SLM process effect on the microstructure and hardness property was aimed to monitor if the SLM process impact is high enough to be considered in different locations of the component or is negligible. Remarkable differences in the microstructural features have been observed in as-built SLM alongside built direction however hardness evolution in built direction did not show notable variations.

Relatively significant inconsistencies of microstructural features were observed in the multiple locations alongside the built direction. It was found out that the middle region of as-printed SLM had fewer microporosities compared to bottom and top regions which was attributed to the lower cooling rate in the middle-area and greater extent of fusion during manufacturing. The middle region had less retained γ% compared to top and bottom ones. Average grain size was also quite different. α' grain size was coarse in the middle region due to the imposed heating. In transverse plane of the as-built SLM parts, the deviation≤10° (close to KS-OR) increased from bottom region (89.31%) to top one (93.11%), denoting higher coherency between α' and γ in the top region. Residual stresses of both phases were the highest in the middle region. Higher strain values in the middle regions could be explained by the higher fraction of α' there.

The Resultant mechanical properties, hardness evolution, in built direction did not show remarkable variations surprisingly. It showed a negligible effect in properties concerning the locations. Thus, based on the small variation of hardness in built direction, effect of the SLM process is insignificant in this geometry.

Comparison of the SLM technique and conventional manufacturing effect on the microstructural features and mechanical properties of 17-4 PHSS exposed substantial changes in microstructural features and consequently mechanical properties.

The average Vickers hardness of as-built SLM part was ≈ 25% less than the commercial wrought alloy (in H1150 condition) which can be attributed to more retained γ, larger grain size, and more microporosities in the matrix.

The as-built SLM specimen showed generally inferior tensile properties than the conventional one. The inhomogenous coarse microstructure of the as-built SLM led to having lower yield strength than the enhanced tensile strength of the wrought one. The tensile behaviour of the as-built one was characterized by exceptional work-hardening via the TRIP effect of the metastable retained γ. High γ% showed positive characteristics resulting in a substantial elongation before fracture. TRIP behaviour was not observed in the conventionally manufactured 17-4 PH SS one.

To improve the inferior strengths in SLMed parts, γ fraction is required to be reduced, so designed post-treatments are applied to alter γ stability. Designed post heat treating effect on

mechanical properties are investigated comprehensibly by focusing on microstructural features in Chapter 5.

The as-built SLM total elongation was slightly smaller than the wrought, which was expected higher due to the higher retained γ%. Non-uniform elongation beyond necking also remained relatively short in as-built SLM comparably. As a result, effects of SLM induced defects on ductility and elongation were proved. The as-built SLM specimen failed in quasi-cleavage mode with a highly irregular fractured surface; however, wrought one showed the desirable cup and cone failure mode.

Results exposed that the as-built SLM requires microstructural tailoring to be comparable with the conventional ones. They implied that ductility was more affected by the defects; however, phase fractions mostly influenced yield and ultimate strengths. As a suggestion, reducing imposed SLM defects helps to improve the elongation to failure. Reduction and smoothening of the imposed SLM defects are out of the scope and mainly alters with the SLM processing parameters during fabrication.

Chapter 4 Microstructure Evolution in 17-4 PHSS Processed by SLM Using EBSD During In Situ Tensile Deformation

The deformation mechanism of the as-built SLM 17-4 PHSS under in situ tensile loading was investigated in this study, focusing on microstructural evolution.

4.1 Experimental procedures

4.1.1 In situ tensile test

For the in situ tensile tests, a Kammrath & Weiss GmbH tensile stage fitted with a 5 kN load cell was applied via a compatible EBSD version within the SEM chamber [131] (Figure 4-1). MDS 4.0 acquisition software was used to control the stage and display the force-extension curve. The rate of displacement was set as 0.6 mm/min. A mini-extensometer was applied to collect strain measurements. The in situ tensile tests w periodically interrupted for EBSD map collection. Before specimen preparation for the in situ tensile test, the gauge section thickness of polished parts was measured as 1.8±0.2 mm. Due to the limitations of the equipment, the thickness was reduced to 1.1 mm. The gauge length and width of the specimens were 12 mm and 3 mm respectively ex situ (refer to 5.1).

4.1.2 Microscopy

Samples for EBSD analysis during the in situ tensile test were prepared via conventional mechanical polishing. To achieve a mirror-like surface, specimens were mechanically polished with # 320, 400, 600, 1200 and 4000-grit SiC sandpapers and then electropolished. The final electrolytic polishing was conducted at room temperature with 6% perchloric acid ($HClO4$) in acetic acid (CH_3COOH) using a voltage of 28 V, a flow rate of 10, and polishing time of 25 s for gauge length.

Figure 4-2 shows the force–strain curve of the in situ stretched miniature specimen, with blue dots corresponding to paused strain during loading. Table 4-1 presents the corresponding load when the tensile loading was paused to collect data by scanning.

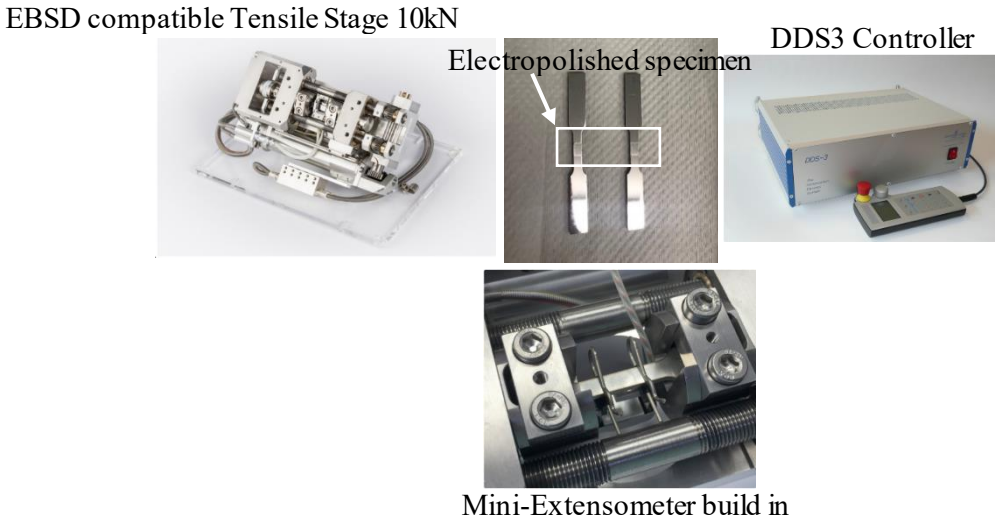

Figure 4-1 Graphical methodology of the in situ tensile testing [131]

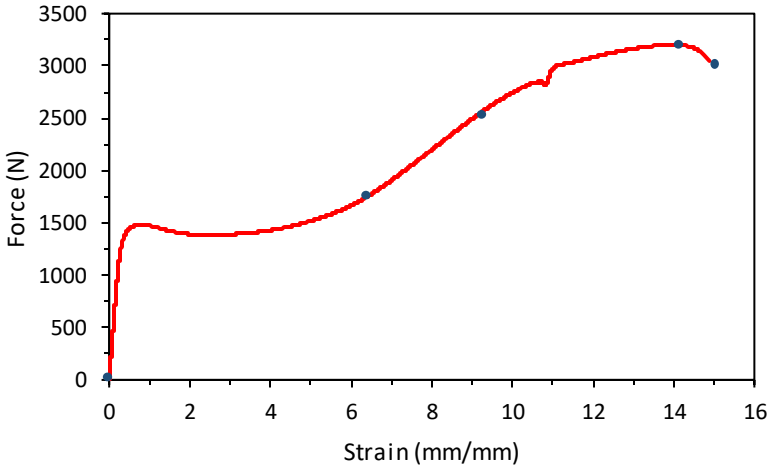

Table 4-1 Applied load at pauses to scan microstructure

	Load (KN)
0-load	
1st load	1.7
2nd load	2.5
3rd load	3.2
Failed	

Figure 4-2 Force–strain curve of the miniature SLM 17-4 PHSS specimen

Figure 4-3 shows the fractured specimen at the failed point at two different magnifications. After passed paused, loss of atomic cohesion resulted in failure. The fractured cross-section shows an approximately 45° fracture, a semi-ductile failure.

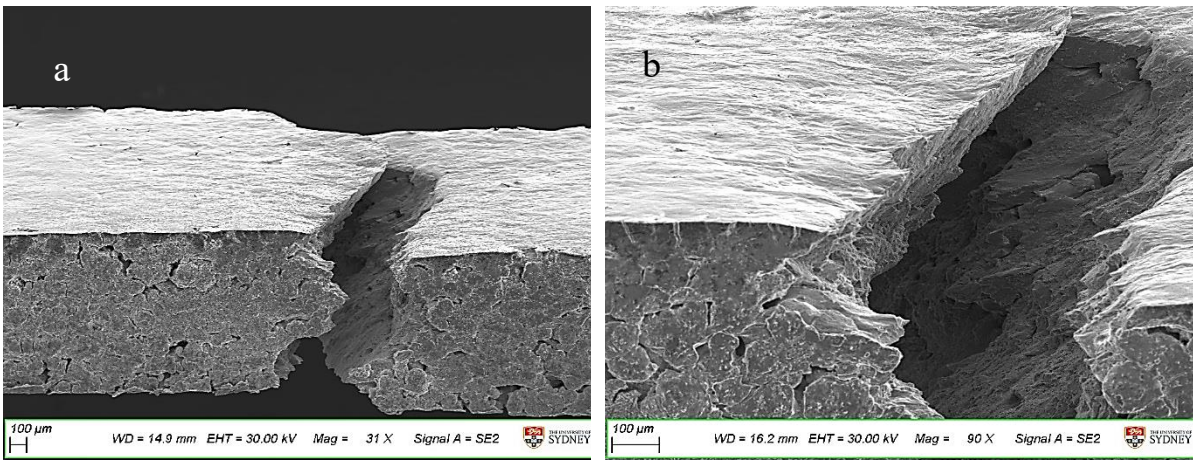

Figure 4-3 SEM images of the fractured in situ miniature SLMed 17-4 PHSS specimen (a) at lower magnification, and (b) at high magnification

The EBSD technique enabled observation of deformation of surface grains of the as-built SLM PHSS specimen during in situ tensile testing. Figure 4-4 shows EBSD maps of the specimen before the test was conducted. Figure 4-5 exhibits the as-built SLM maps stretching from 0 kN to failure point as microstructural features evolution. Below quantitative microstructural features are provided from the acquisition of the maps during loading. Loading progression during the in situ tensile test led to an increase in non-indexing.

4.2 **EBSD measurements**

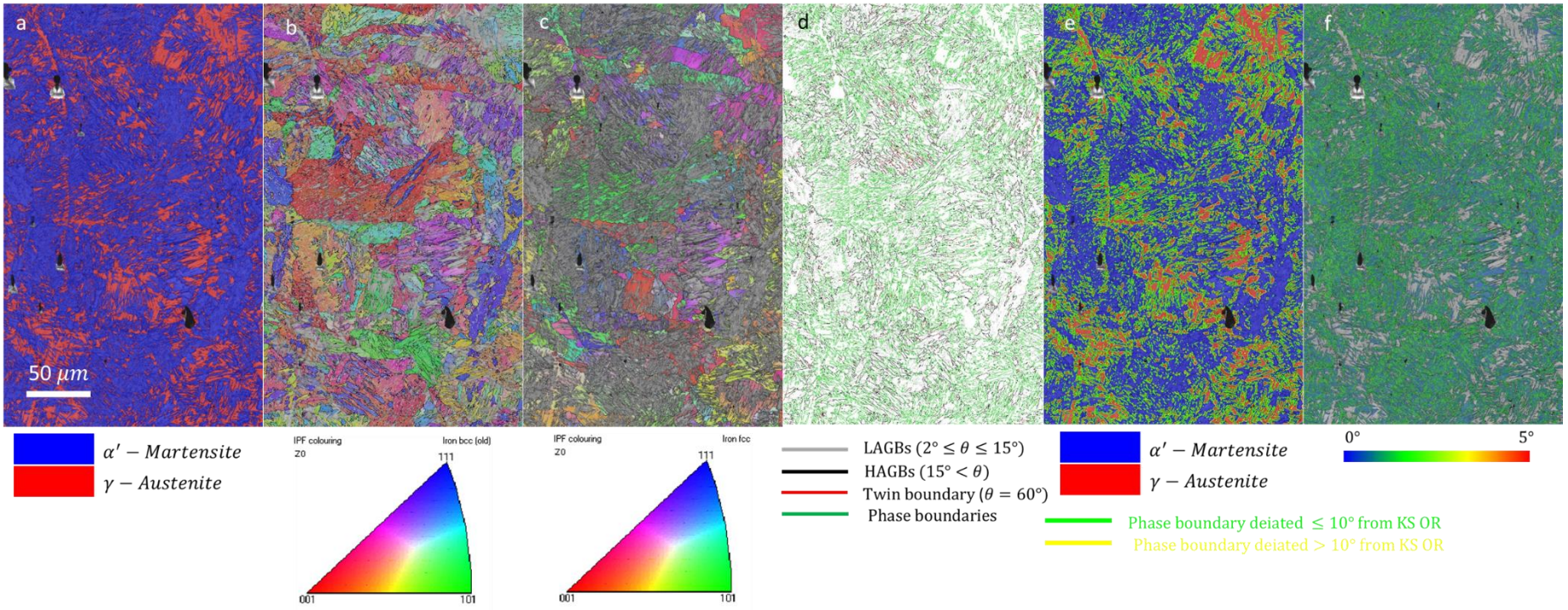

Figure 4-4 (a) BC+Phase maps of α′ and γ, (b) BC+IPF-Z with LAGBs and HAGBs of α′, (c) BC+IPF-Z with LAGBs and HAGB, of γ, (d) grain boundaries of α′ (including LAGBs; Silver, HAGBs; black, Interface Bs; green, and Twin Bs; red), (e) phase boundary orientation relationship map as BC+Phase maps+Phase boundaries between γ and α′ during loading (green and yellow lines indicate phase boundaries with deviation angles less and more than 10 ° from KS OR respectively.), and (f) KAM of α′.

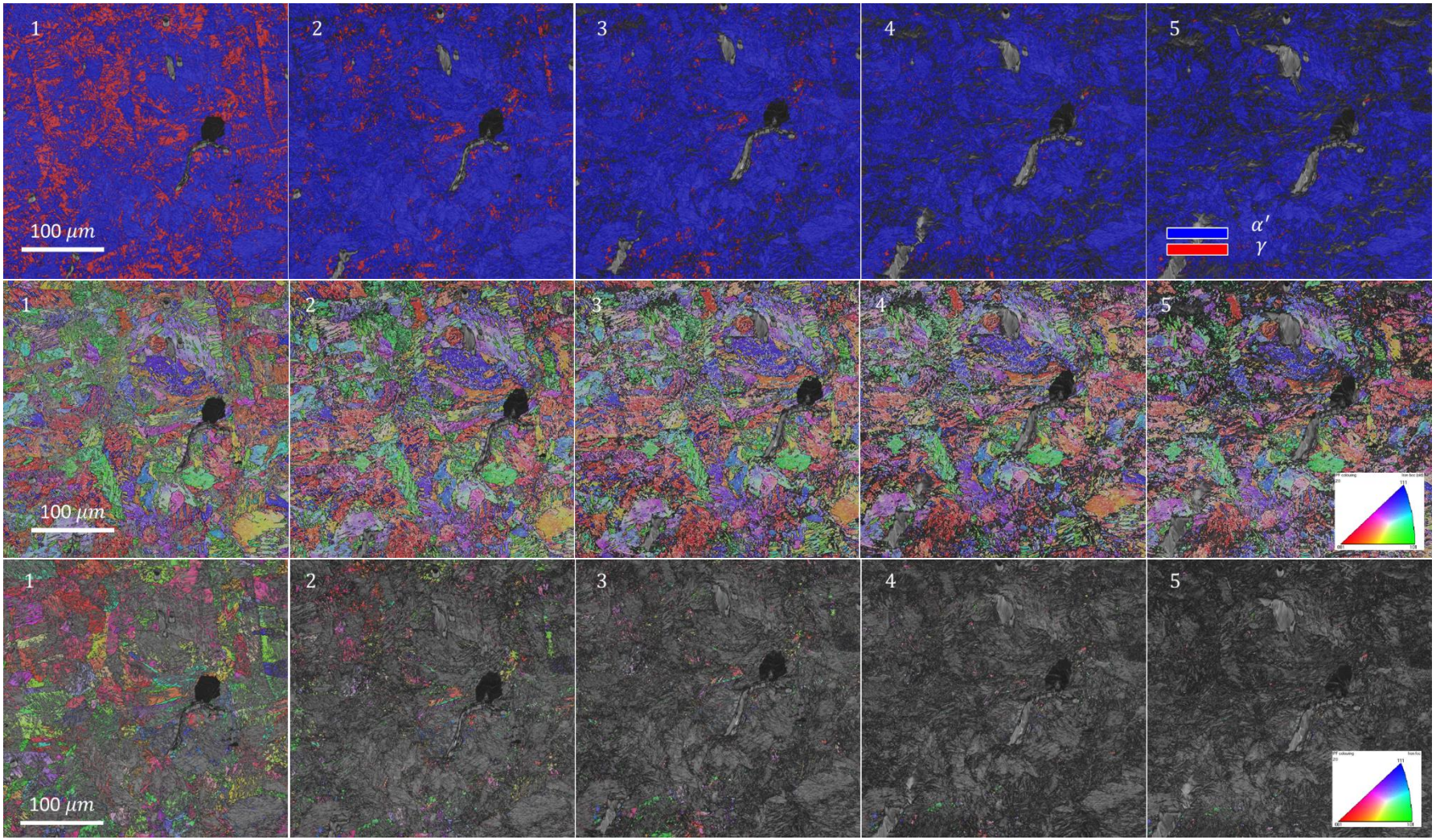
1
2
3
4
5
100 μm
α′
γ
1
2
3
4
5
100 μm
1
2
3
4
5
100 μm

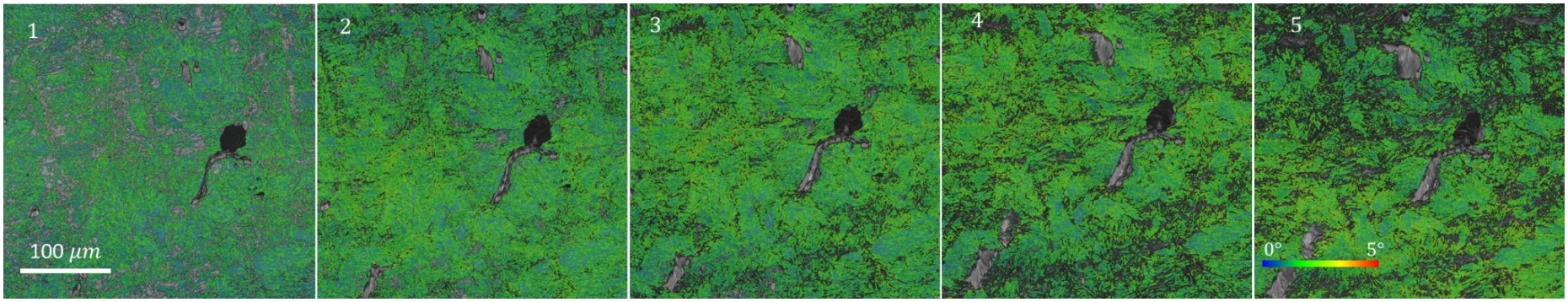

Figure 4-5 (a) BC+Phase maps of α′ and γ, (b) BC+IPF-Z with LAGBs and HAGBs of α′, (c) BC+IPF-Z with LAGBs and HAGBs of γ, (d) KAM of α′

The observed TRIP effect in the current as-built samples explains the localized strain-hardening after lower yield point on the engineering stress-strain curve which delays the onset of local necking leading to better energy absorption and enhanced elongation. This has made the total elongation of as-built samples almost comparable to the wrought alloy despite having more microporosities.

The low concentration of carbon (≈ 0.05wt.%) and presence of elongated columnar grains in as-built microstructure can make the retained γ less stable leading to progressive stress-induced transformation of retained γ to α'. As mentioned earlier, the blocky-shape γ is less stable and transforms easier to α' than acicular and lath-type γ. This has been attributed to the lower hydrostatic pressure (σ_p) in the retained γ when its morphology is blocky-shape or in the form of isolated islands [132]. In general, the yield stress and strain hardening rate of a given phase (martensite and/or ferrite in this study) surrounding retained γ determine the magnitude of σ_p. In addition, lath-type γ has more interface to volume ratio resulting in more path to absorb γ stabilizer elements such as C, N, Ni, Mn, etc. than that of blocky-shape γ. The diffusion path in lath-type γ is shorter leading to better distribution of γ stabilizer elements within the γ grain and higher mechanical stability of the γ when subject to plastic deformation. According to EBSD phase map in Figure 4-5, the stability of γ phase decreases as the amount of plastic deformation increases. The average grain size of γ also decreased. The formation of dislocation cells and increase of dislocation densities during plastic deformation can stabilize the remaining γ and prevent the growth of α' lath.

It should be added that the α' phase surrounding retained γ in as-built microstructure in low carbon 17-4PH stainless steel is not as hard as α' in carbon steels. This perhaps applies less resistance against TRIP effect and triggers the stress-induced transformation of γ to α'. In other words, stronger and harder α' (higher concentration of carbon) results in a smaller mean-stress level in neighbouring γ grains which postpones the stress-induced transformation whereas the presence of softer phase (such as extremely low carbon martensite) transfers higher stress to γ encouraging the TRIP effect.

The following section presents analysis of microstructural features from EBSD maps.

4.2.1 Phase fraction

The identification and distribution of γ and α' evolution under tensile loading are presented in phase maps in Figure 4-5 (a). Regardless of zero solution, as shown in Table 4-2, and based on visualised gradual phases alteration during loading, γ% decreases with increasing load, and consequently α'% is increasing due to the progression of α' transformation – the so-called TRIP effect (as discussed comprehensively in 2.3.5). γ% in the as-built SLM PHSS was 26.2%, and 0.49% in the failed specimen. The presented α' fraction cannot be used as a reference due to the low indexing by loading progression. As shown, the majority of γ phase transformed into α' after applying ≈10% strain.

Table 4-2 γ% and α′% evolution during tensile loading

	Zero solution, %	γ %	α' %
0-strain	4.6	26.2	69.1
1st load	12	6.42	81.5
2nd load	18	2.94	78.5
3rd load	30	1.05	68.5
Failed	40	0.49	59

4.2.2 Grain sizes and orientations

The IPF-Z maps, along with the IPF colour key, denote the grain orientation evolutions for α' and γ during loading in Figure 4-5 (b) and (c) respectively. Random texture for α' is revealed at 0 strain. Figure 4-5 (b) shows grain rotation, while γ transforms to α' by the progression. No substantial changes in α' texture can be detected.

As shown in Table 4-3, the average γ grain size decreases as stretching increases. In terms of grain size evolution, as mentioned already, loading will result in more refined γ grains as well as greater α' (Table 4-3). Hence, both phases' average grain sizes decrease with loading progression.

Refinement of the γ grains leads to higher stability; in other words, higher mechanical stability is achieved in more refined grains. Refinement and sub-grain formation develop yield strength.

Table 4-3 Average grain size of γ and α' during loading

	Average grain size of γ (μm)	**Average grain size of α' (μm)**
0-strain	1.54	2.32
1st load	1.20	2.76
2nd load	1.10	2.71
3rd load	0.99	2.55
Failed	0.93	2.45

4.2.3 Grain boundaries evolution (subdivision of a grain)

Evolutions of LAGB% ($2° < \theta < 15°$), HAGB% ($\theta > 15°$), Twin B% ($\theta \approx 60^{\circ}$), for γ and α' under tensile loading are tabulated in Table 4-4. HAGB% of the γ decreases because γ disappears as transformation progresses. However, Table 4-4 shows that the HAGB% of the α' does not increase with loading progression, contrary to expectations. The low indexing can explain it during data acquisition.

Table 4-4 Evolution of LAGB%, HAGB% and Twin B% for γ and α′ under tensile loading

Specimen ID	LAGBs	HAGBs	Twin Bs	LAGBs	HAGBs	Twin Bs
		(%γ)			(%α')	
0-strain	14.03	18.38	0.29	21.92	16.97	0.97
1st load	21.36	5.59	0.19	26.61	14.80	0.71
2nd load	26.78	3.71	0.11	29.55	13.12	0.52
3rd load	27.44	2.42	0.21	32.02	10.56	0.35
Failed	25.90	3.09	0.31	33.17	0.09	0.32

4.2.4 Kernel average misorientation

Dislocation density increases with the progression of tensile loading due to the new dislocation formation source. Dislocation pile-up during loading impedes α' transformation and strengthens the material by strain hardening.

Kernel average misorientation maps of α' are presented in Figure 4-5 (f). Accumulated residual stress due to formation of dislocations, shown by KAM values for the γ and α' phases, is demonstrated in Table 4-5. Colour coding of KAM maps proves that induced strain (i.e. residual stress) increases during loading. Dislocation density nucleation is saturated at the end and formed the platea format. The formation of dislocation cells and increase of dislocation densities during plastic deformation can stabilize the remaining austenite and prevent the growth of martensite lath.

Table 4-5 Average of local misorientation of γ and α' during loading

Specimen ID	KAM (γ),	KAM (α')
0-strain	0.74	1.26
1st load	1.27	1.54
2nd load	1.47	1.67
3rd load	1.53	1.76
Failed	1.54	1.77

4.2.5 Microtexture

The EBSD maps were applied to run orientation distribution function (ODF) analysis to evaluate the texture of the α' and γ during in-situ tensile loading.

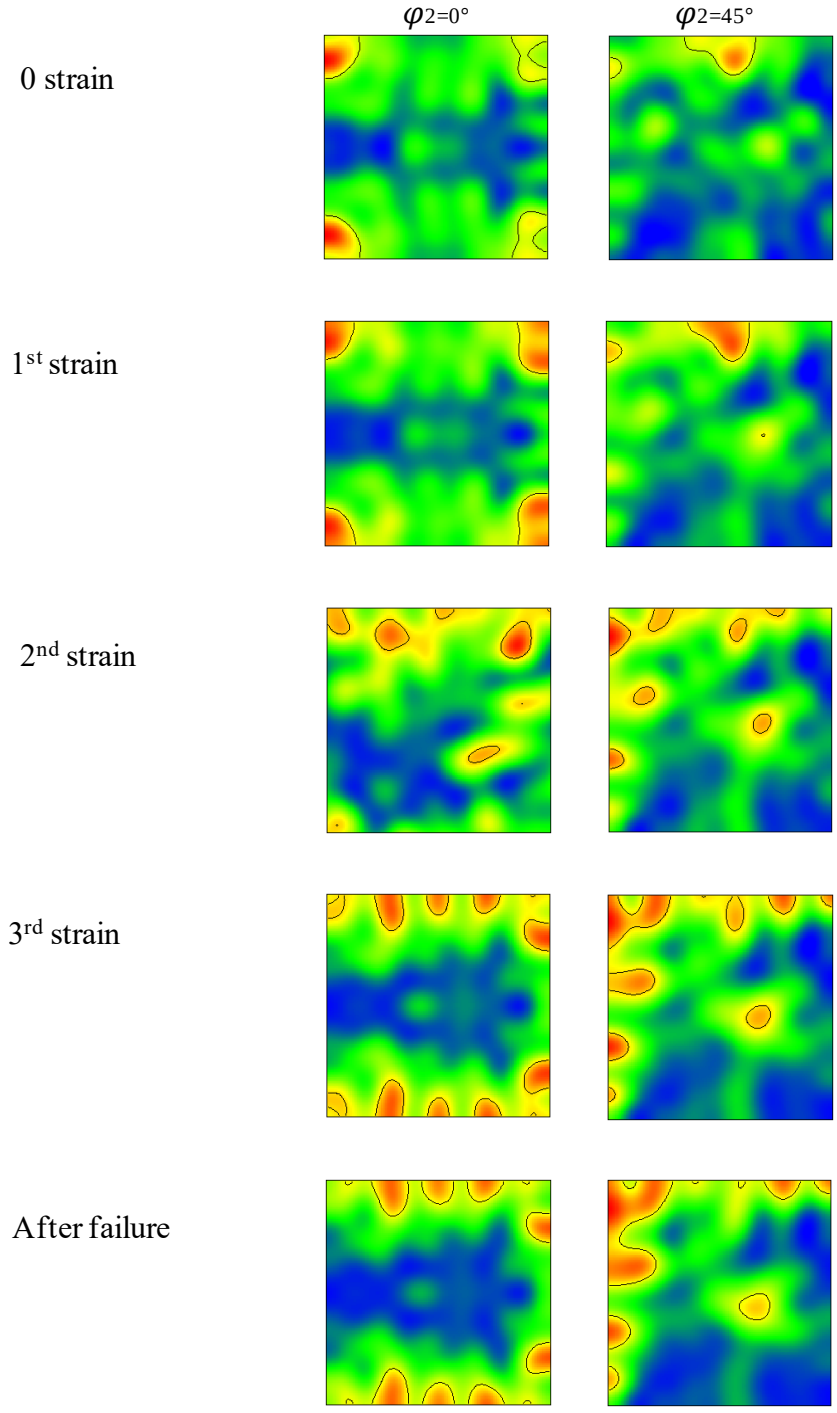

Figure 4-6 φ2=0° and 45° ODF sections for the α′phase of the as-built SLM

The BCC phase (Figure 4-6) has a random maximum intensity of 3.4 times that before straining. (001)[100] texture is eliminated by increasing the strain and leads to the formation of α-fiber and (111)[0-11] orientation on γ-fiber, which is known as a deformation component of BCC metals [133-135]. α-fiber is a cold-rolling texture in steels with BCC crystal structure [136]. Also, Figure 4-6 shows that the formation of α-fiber begins with (112)[1-10] and (001)[1-10] components. Moreover, a new {001}<210> component at Euler angles of 26°/64° 0°/90° 0° (φ_1 Φ φ_2) is formed by increasing the strain.

Before straining (Figure 4-7), the dominant texture is a rotated cube (100)[110] with weak G/B texture. Rotated cube was seen in unidirectional rolling for low reductions [137]. By increasing strain, the intensity of G/B increases, and a partial α-fiber forms from goss (G) to G/B texture at the expense of rotated cube texture.

Formation of Cu, D and G-T, after the first straining step and before G texture, indicates that twinning was one of the deformation mechanisms in the γ phase. After failure, a strong partial α-fiber and weak G-T, D and Cu texture formed, indicating large plastic deformation in retained γ. These textures have been reported in cold-rolled austenitic steels with low stacking fault energy [138, 139].

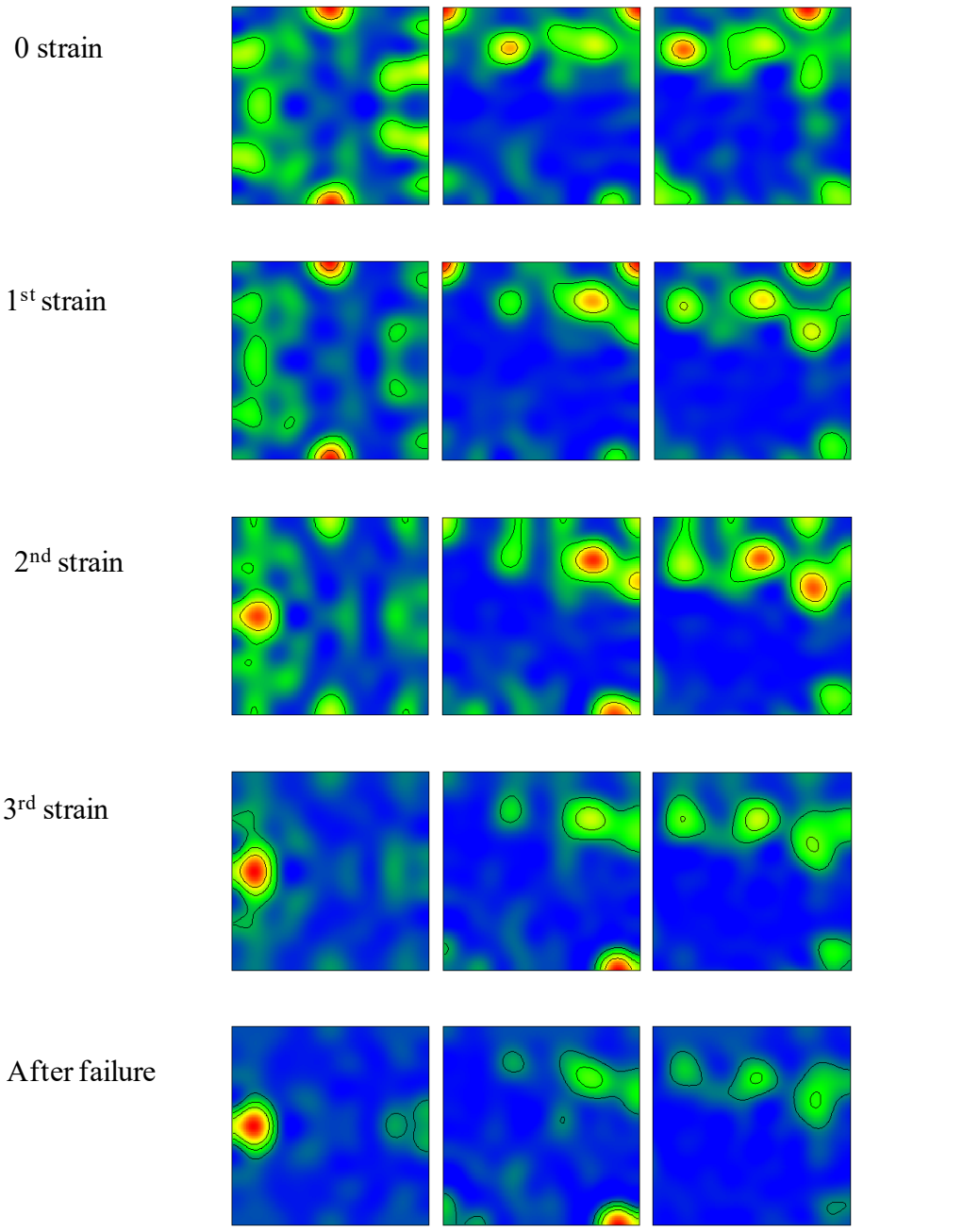

Figure 4-7 φ2=0°, 45°and 65° ODF sections for the γ phaseof the as-built SLM

4.3 **Summary**

For a better understanding of the microstructural features' evolution thru loading progression, in-situ tensile was implemented. This investigation enabled us to design a better microstructure by SLM processing parameters and post-processing for the required deformation.

EBSD analysis during the in-situ tensile test revealed transformation induced by plasticity (TRIP effect) of $\gamma \rightarrow$ ά. The area fraction of retained γ in SLMed part decreased from 26.2% in stage I (zero strain) to 0.49% in stage IV (failure). It is evident that the majority of γ phase transformed into α' after applying ≈10% strain. Lath and acicular shape retained γ transformed faster to α' than the blocky shape γ. Some grains rotated in different directions leading to grain subdivision by LABs and even grain division by HABs. The average grain size of γ phase also decreased from 1.54μm at zero strain to 0.93μm at the failure point. It was also observed that by tensile loading progression, strain field for γ and α'were developed by newly formed dislocations.

Chapter 5 Effect of subsequent thermal processing on retained/reverted γ and mechanical properties of 17–4 PHSS processed by SLM

This chapter describes the results of an investigation of the effects of standard and non-standard heat treatment procedures on SLM 17-4 PHSS's hardness and tensile properties. Corresponding microstructures are also provided for correlation purposes. This study enabled determination of whether the microstructure and properties achieved using standard heat treatment procedures for wrought material are feasible when using SLM 17-4 PHSS. This study also identified the optimum heat treatment condition(s) for the intended applications.

5.1 Experimental procedures

Powder fabrication, the SLM process, finishing procedures (refer to 3.1.1), mechanical testing set-ups (refer to 3.1.3 and 3.1.4), microscopy techniques sett-up, and sample preparation procedures for microscopy observation (refer to 3.2) are described in 3.1. This section focuses on the applied heat treatment procedures. Any alterations from the procedures described previously are reported below.

Figure 5-1 presents the manufacturing process from the design step to the fabrication of miniature tensile specimens. SLM specimens were prepared in smaller geometry to reduce the cost and make it more reasonable. Figure 5-2 illustrates the dog bone-shaped miniature tensile specimens, manufactured according to ASTM E8-16 [140]. The gauge length and gauge width of the specimens were 12 mm and 3 mm, respectively.

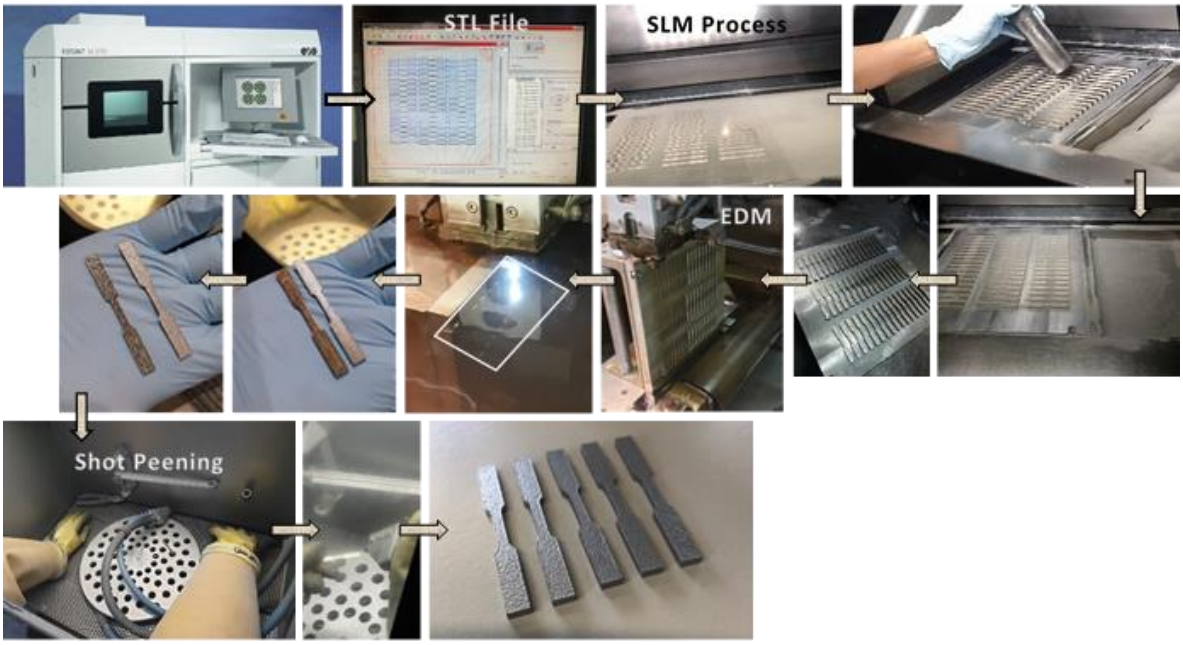

Figure 5-1 Graphical methodology for the SLM fabrication of miniature specimens

(a) (b)

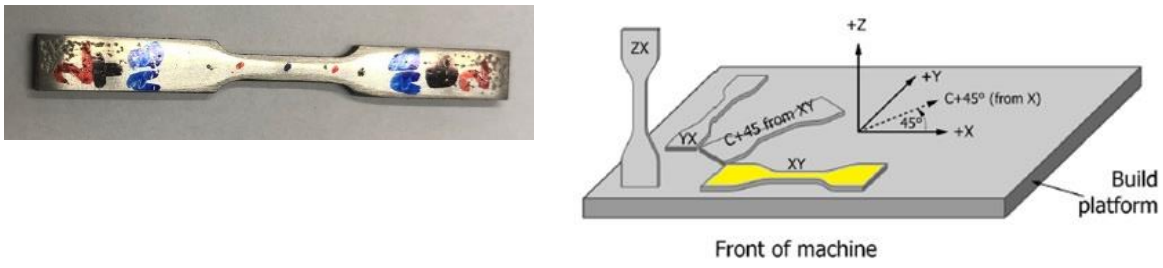

Figure 5-2 (a) Miniature tensile test coupon, and (b) built orientation of specimens on a build platform [141]

5.2 Post-processing

Heat treatment and surface treatment were applied to the SLM parts to study the effects of post-processing on their microstructural and mechanical properties.

5.2.1 Heat-treatment procedures

Figure 5-3 illustrates the applied heat treatment procedures and the microstructural transformation during the heating. Table 5-1 summarises the applied heating conditions.

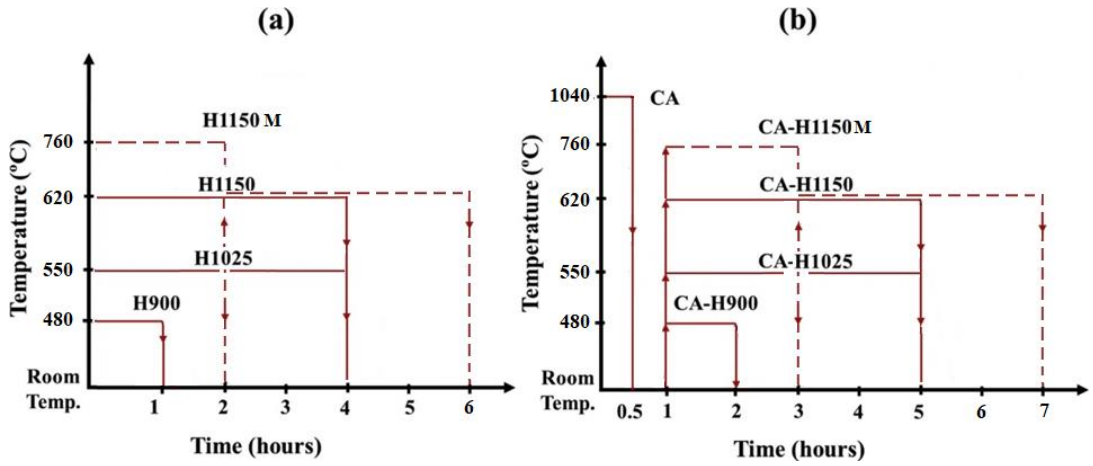

Figure 5-3 Schematic of precipitation hardening heat treatment procedures for the as-built SLM 17-4 PHSS (a) designed direct-ageing procedures, and (b) solutionised ageing procedures

Two groups of heating procedures were designed to improve the material's properties. The first group of specimens underwent solution annealing before receiving ageing procedures at a defined temperature and soaking time. The second group underwent ageing procedures only. This experimental design enabled identification of the effect of the SLM process and induced thermal histories during fabrication – specifically, whether the SLM process has the same influence as the solution annealing process.

An Across International controlled atmosphere vacuum muffle furnace was used to apply solution heat treatment to the Condition A state (1040℃ for 30 min). Solutionised specimens were water quenched to 30℃. Salt baths containing a GS 430 salt (a mixture of alkali and earth alkali chlorides) were used for ageing heat treatments. The specimens were heated with 20°C/s rate to standard ageing temperatures (480°C, 550°C, 620°C and 760°C), (refer Table 5-1), water quenched to room temperature eventually. All specimens' surfaces, including tensile test coupons and microscopy specimens, were polished after heat treatment to eliminate roughness, and any oxide layers that might form during heat treatment.

Table 5-1 Applied heat treatment procedures for the as-built SLM 17-4 PHSS

Procedure	Temperature (℃)	Duration (hrs)	Procedure	Temperature (℃)	Duration (hrs)
			Condition A (CA)	1040	0.5
H900	480	1	**CA+H900**	1040	0.5
				480	1
H1025	550	4	**CA+H1025**	1040	0.5
				550	4
H1150	620	4	**CA+H1150**	1040	0.5
				620	4
H1150M	760	2	**CA+H1150M**	1040	0.5
	620	4		760	2
				620	4

5.2.2 Tensile test

Miniature specimens were used for studying the effects of heat treatment on the mechanical properties of the SLM 17-4 PHSS. After applying the heat treatment procedures outlined above, specimens were mechanically ground and polished using # 320, 400, 600, and 1200-grit SiC sandpapers to eliminate roughness and contamination due to SLM and heating. Polished, mirror-finish specimens are shown in Figure 5-2 (a). The gauge section thickness of the polished parts was 1.8±0.2 mm. All miniature tensile specimens were fabricated in the horizontal direction, as shown in Figure 5-2 (b). Before conducting tensile tests, the specimens' width and thickness at multiple points of the gauge area were measured and marked. The tensile testing was implemented using an Instron 5567 testing machine with a 10 kN load cell at room temperature. The tensile testing were conducted with a crosshead speed of 0.6 mm/min, correlating to correlating to an engineering strain rate of 8.3e-4 sec^{-1} of the specimen. A contact extensometer with a gauge length of 10 mm was applied to record the accurate strain of the specimens during conducting tests.

5.2.3 Microscopy

To enable comparison of heat treatment effects on microstructural features, samples were prepared from the heat treated specimens from the centre of the specimen in the tensile coupons' cross-section.

5.3 Results and discussion

Due to the nature of AM fabrication, mostly polycrystalline AM products have an undesirable texture owing to anisotropic behaviour. Generating an equiaxed microstructure by applying appropriate processing and post-processing procedures can prevent anisotropic behaviour. A refined equiaxed microstructure can enhance mechanical properties such as strength, ductility and fracture toughness. A solidification map is commonly used to create refined equiaxed grains to improve strength and ductility (refer to 2.7.1).

The cooling rate of the SLM process is high enough to promote full α' transformation; however, some effective γ stability alters the material and causes retained γ formation (discussed in Chapter 3). The phase transformation and microstructure revision in SLM 17-4 PHSS due to the applied heat treatment procedures are outlined below. Mechanical properties were characterised by hardness and tensile tests, and are presented and discussed after the microscopy investigations.

5.3.1 Microstructural features

Figure 5-4 depicts Ternary phase diagrams generated for SLM 17-4 PHSS using Thermo-Calc software, sourced from [35].

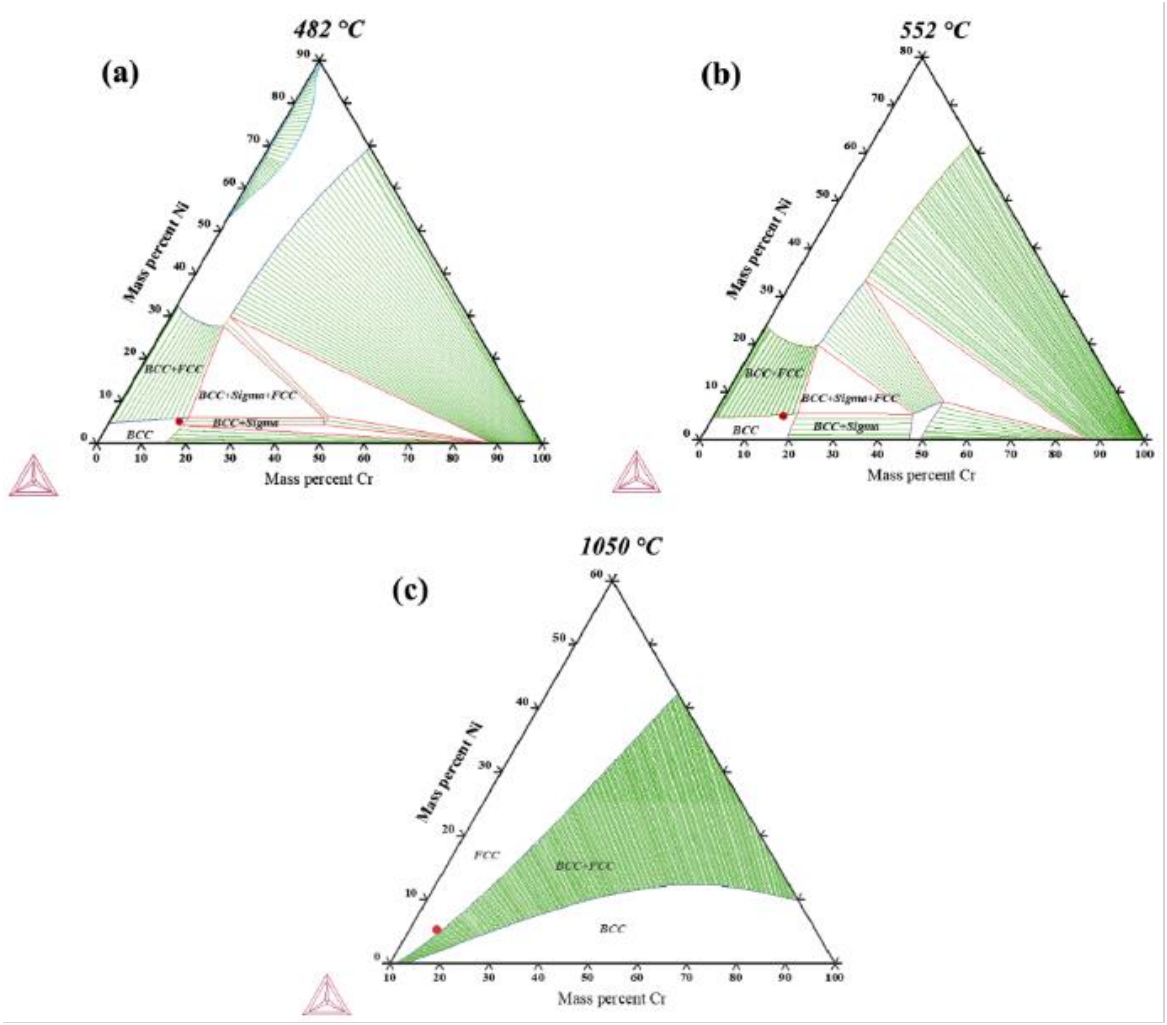

Figure 5-4 Ternary phase diagrams generated using Thermo-Calc software cross-sectioned at temperatures of (a) 482℃ (H900) (b) 552℃ (H1025) and (c) 1050℃ (CA) [35]

Figure 5-4 shows that solutionised SLM 17-4 PHSS at 1050℃ belongs to the γ region. After ageing treatment at 482℃, nearly fully α' is predicted for the resultant microstructure. Increasing ageing temperature to 552℃ is expected to generate a small amount of γ in the microstructure.

An evolution similar to that presented in Figure 5-5 was expected in the SLM 17-4 PHSS in this study. The evolution of α' laths and precipitation after quenching and tempering is shown in Figure 5-5. Transformation of the dislocations, α' microstructure and precipitation are identified as the origins of the strength evolution

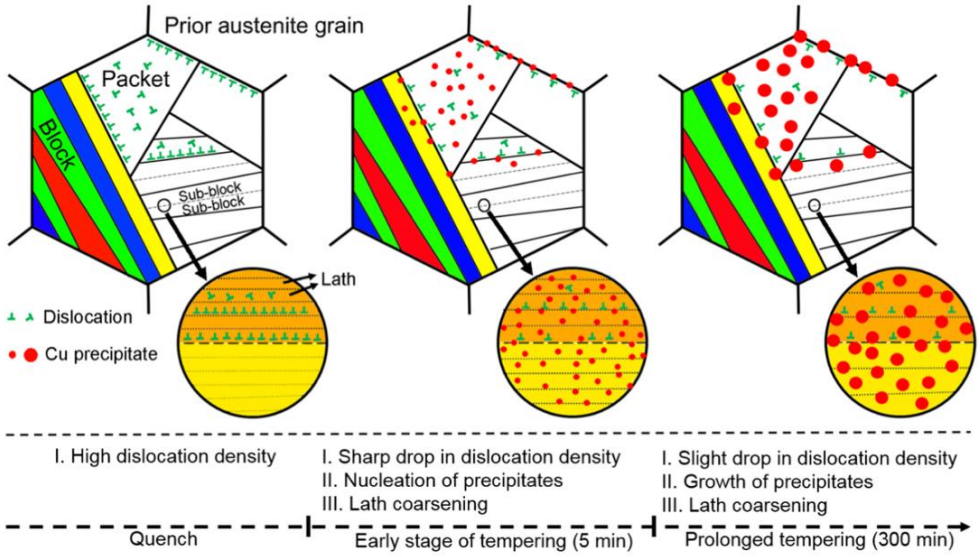

Figure 5-5 Schematic of illustration of microstructural evolution of lath martensite after quenching and tempering [142]

Microstructural features of the as-built SLM PHSS in heat-treated conditions are provided in Figure 5-6 to Figure 5-11. The recrystallisation, homogenisation, and level of visibility of the materials' interfacial regions in different heat-treated conditions are discussed below. Microscopy assessments of the as-built SLM and heat-treated materials include phase fraction, grain size, phase boundary orientation relationship, and strain distribution in phases. EDS maps of the material in the CA-H1150M condition are provided in Figure 5-12.

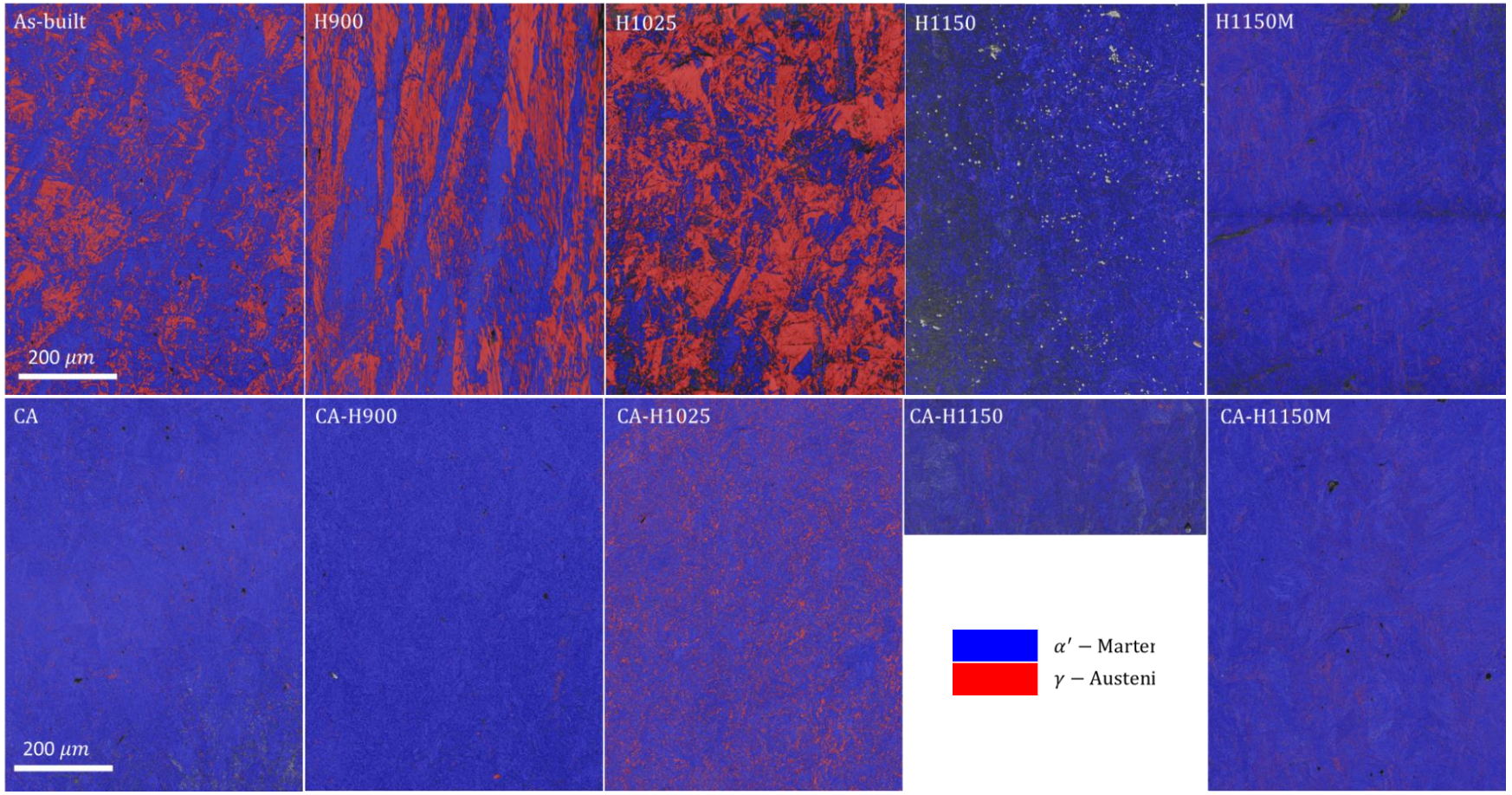

Figure 5-6 BC+Phase maps (α′ in blue, and γ in red) for the as-built SLM and heat-treated specimens

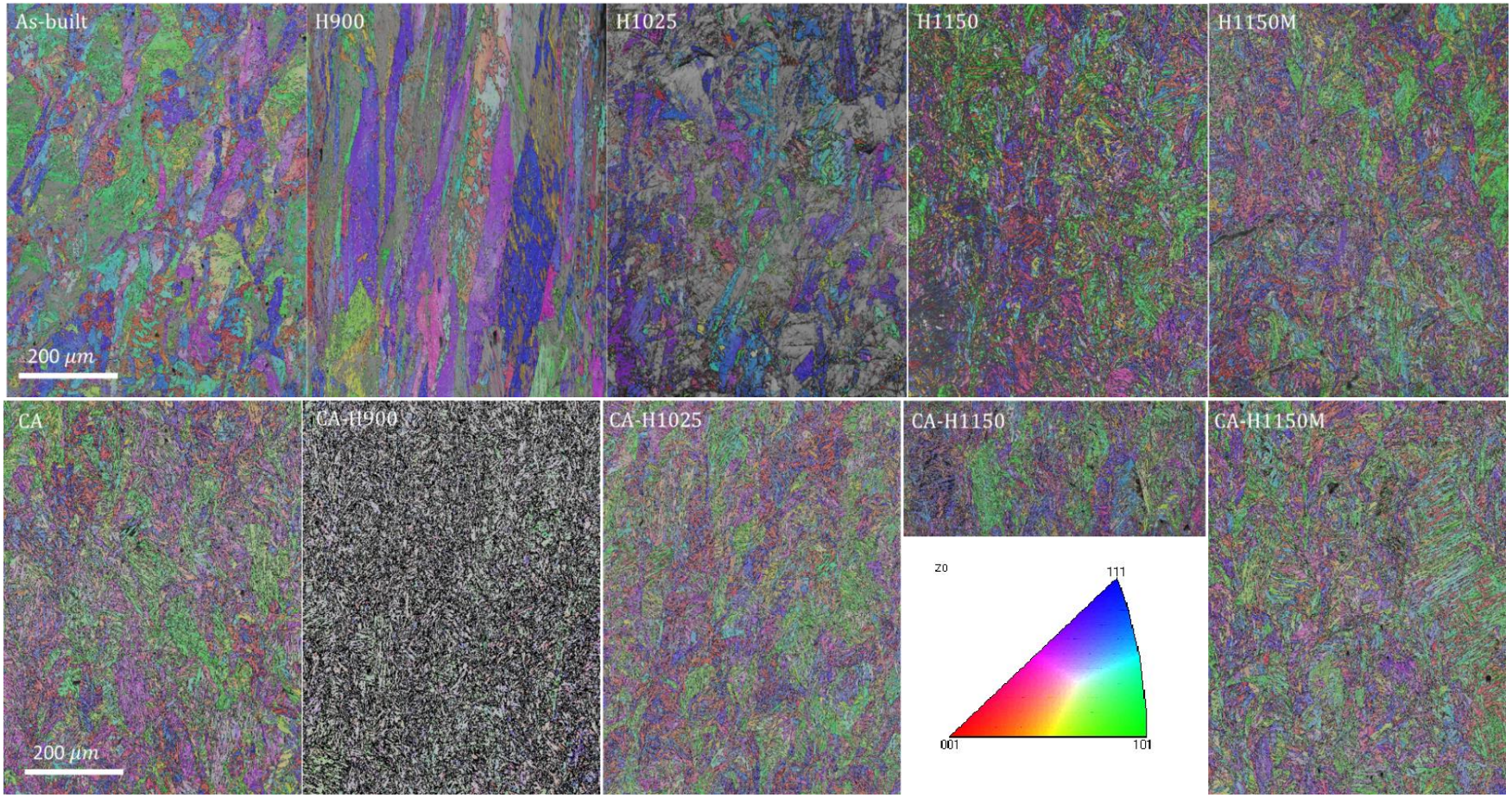

Figure 5-7 BC+IPF-Z with LAGBs and HAGBs for α′ for the as-built SLM and heat-treated specimens

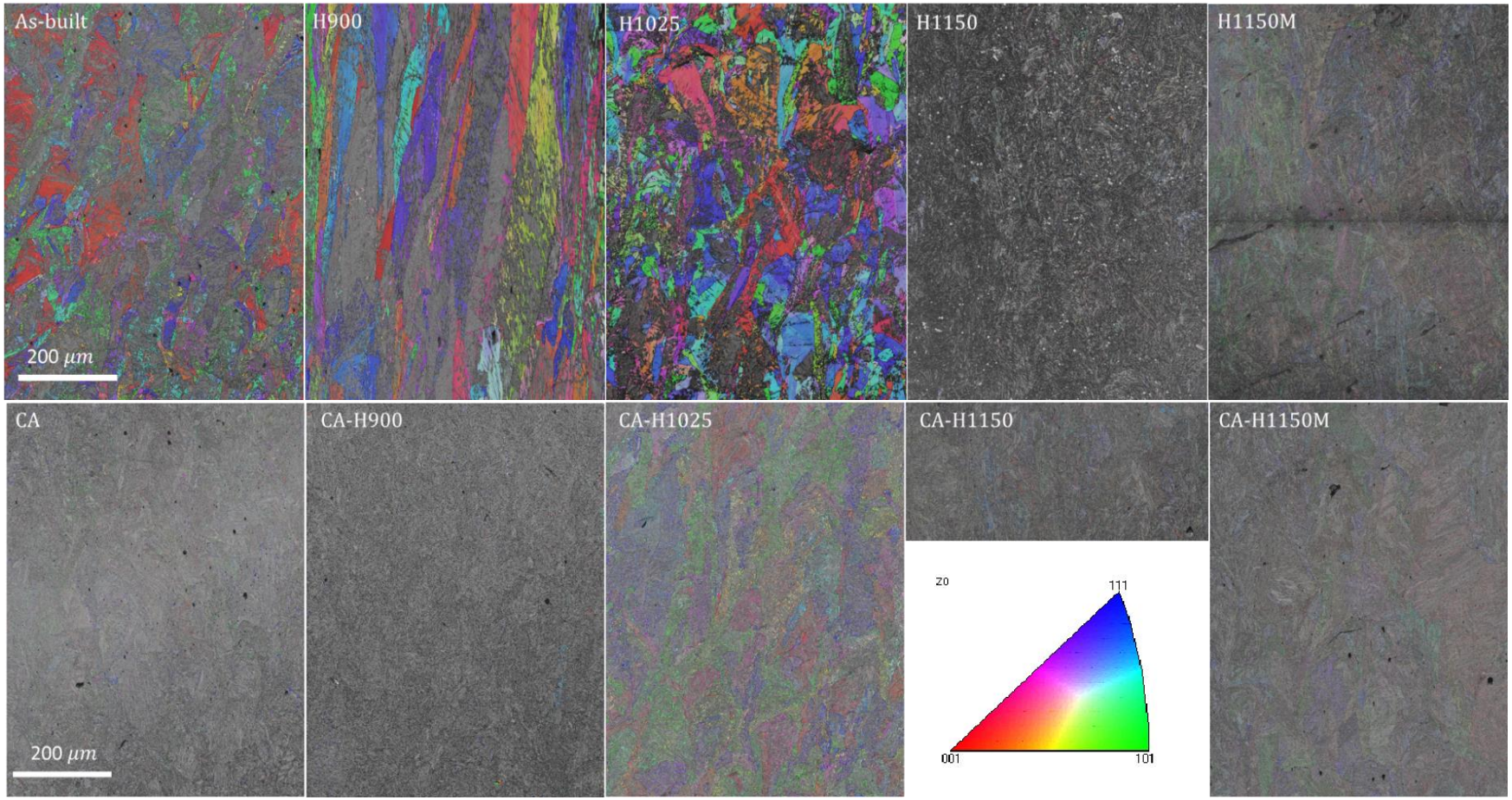

Figure 5-8 BC+IPF-Z with LAGBs and HAGBs for γ for the as-built SLM and heat-treated specimens

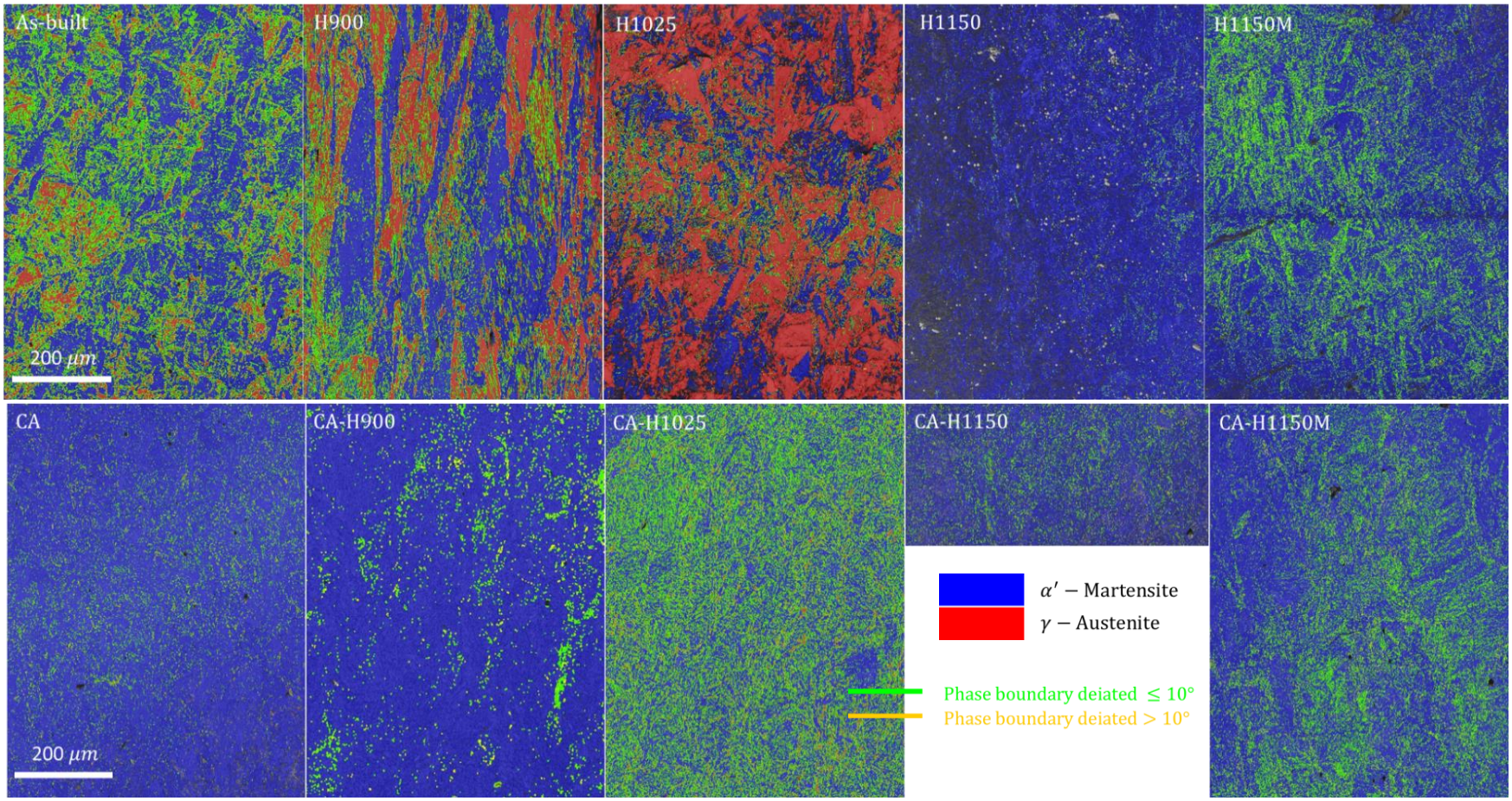

Figure 5-9 Phase boundary orientation relationship: BC+Phase map+Phase boundaries between α′ and γ for the as-built and heat-treated specimens (green and yellow lines indicate phase boundaries with deviation angles less and more 10 ° from KS OR respectively

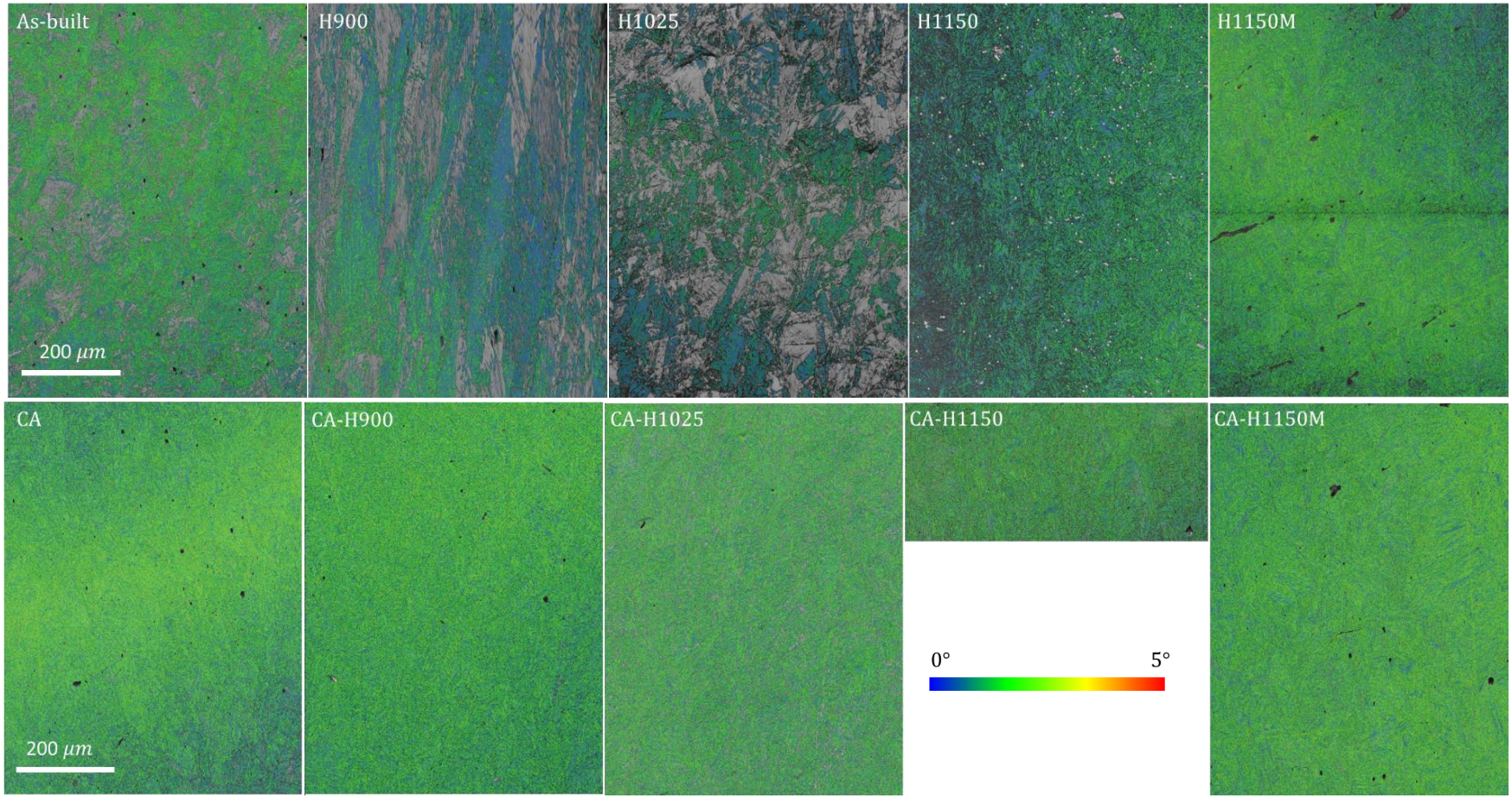

Figure 5-10 KAM of α′ for the as-built SLM and heat-treated specimens

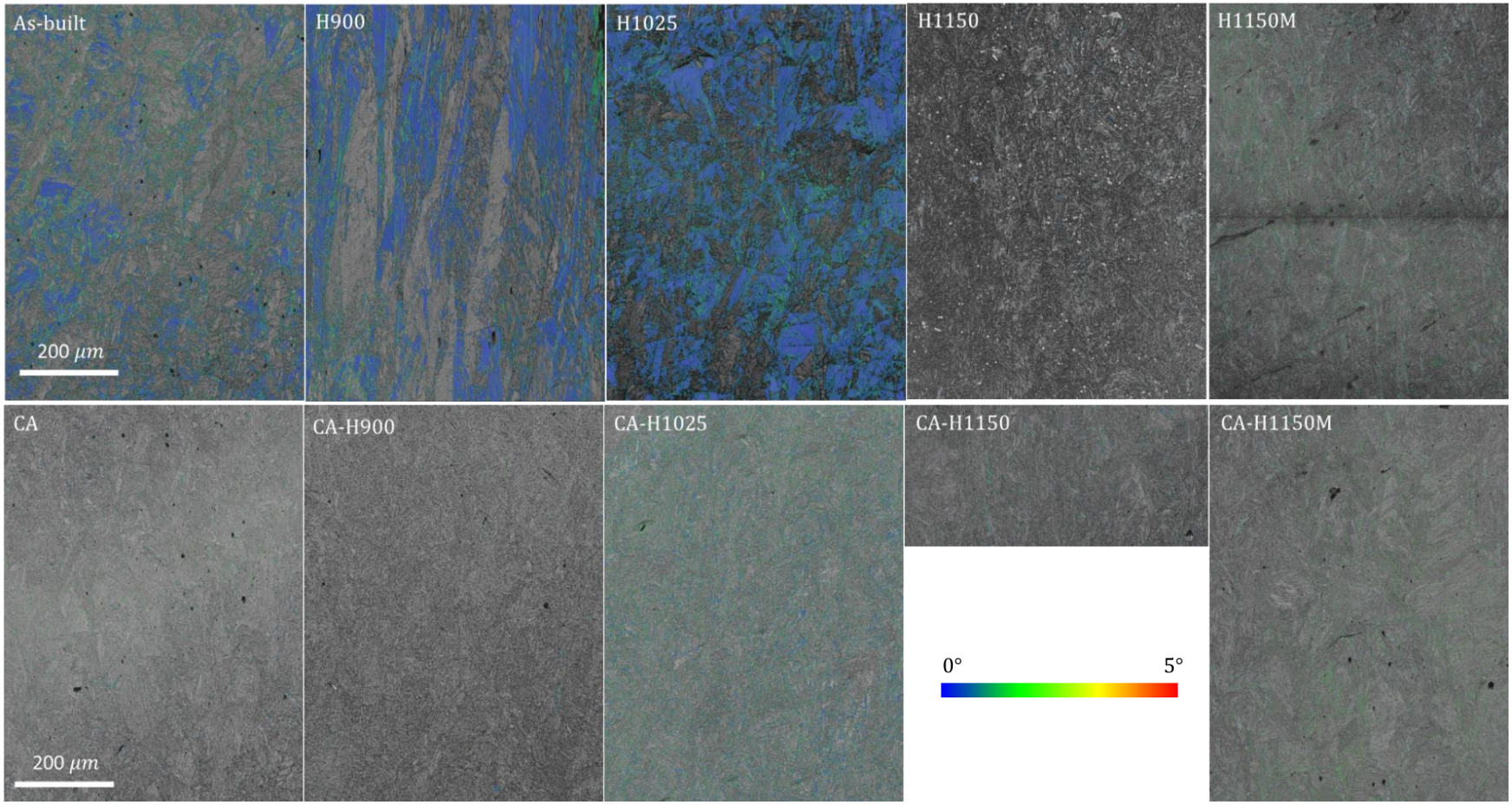

Figure 5-11 KAM of γ for the as-built SLM and heat-treated specimens

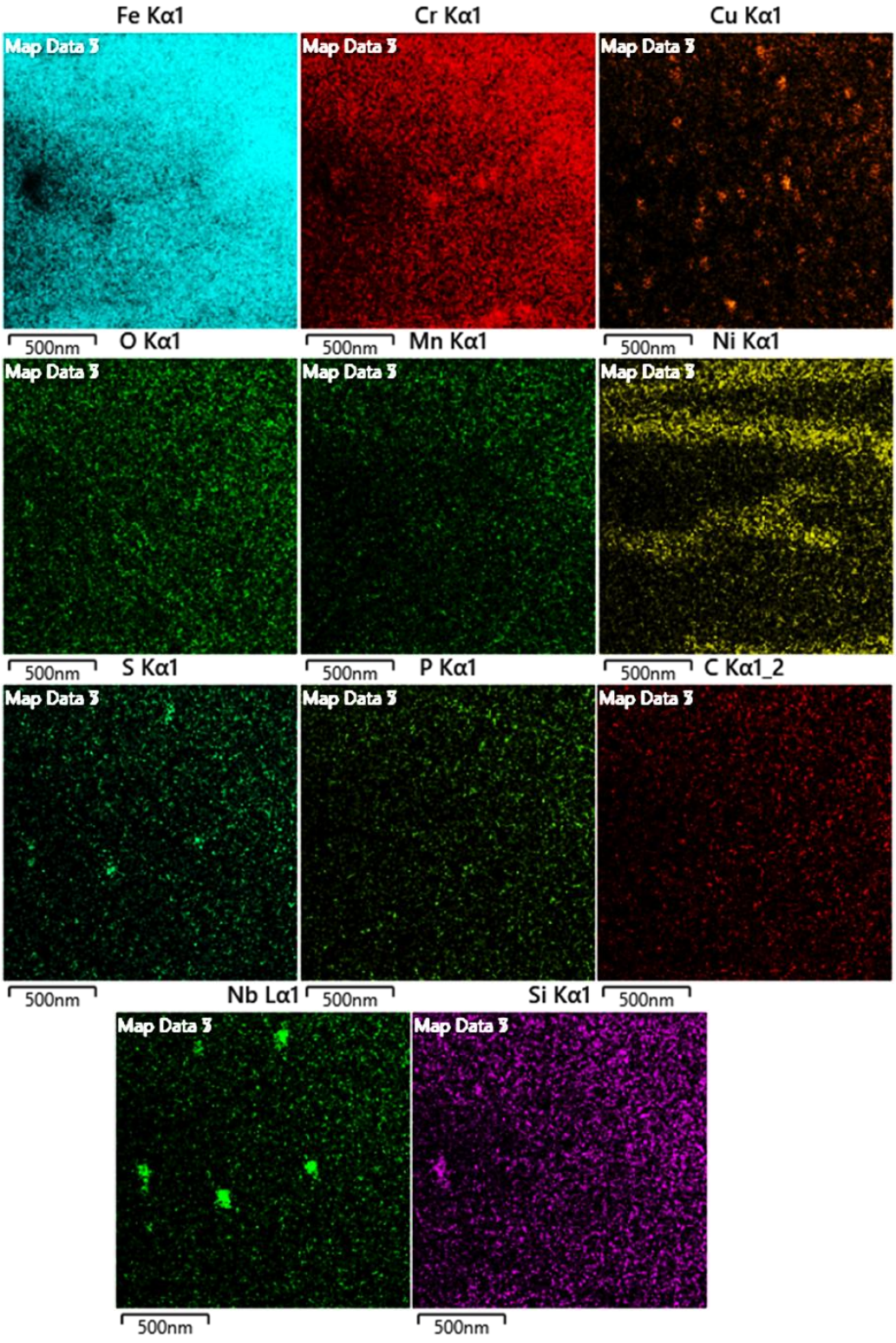

Figure 5-12 Energy dispersive X-Ray (EDS) maps of CA-H1150M specimen

- *Phase fraction*

The identification and distribution of γ and α' in different conditions in the as-built SLM, direct-aged, and CA-aged materials are presented in IQ-phase maps in Figure 5-6. γ and α' fractions are tabulated in Table 5-2.

Table 5-2 Phase fractions of γ and α' as a function of solution annealing, temperature and length of ageing

Specimen ID	Zero solution %	γ %	α'%	Specimen ID	Zero solution %	γ%	α' %
As-built	1.2	38.73	60.03[2]	**CA**	8.3	2.53	94.2
H900	4.8	38	57.1	**CA-H900**	1.6	0.48	97.8
H1025	16	55.1	29	**CA-H1025**	2.4	19.3	78.3
H1150	30	0.97	69.3	**CA-H1150**	3.18	3.14	93.7
H1150M	19	4.64	76.3	**CA-H1150M**	1.4	5.22	93.4

Phase fraction evolutions in the different conditions were as follows. Prior γ grains in the as-built SLM have columnar morphology. In this material, due to the lower C%, α' morphology is lath shaped. Due to the small size of the laths, they are invisible and are grouped and allocated in the packets visible in the prepared maps (refer to Figure 3-14). The IQ-phase map of the as-built specimen (Figure 3-14) shows that the retained γ grains distributed at packet boundaries, and prior γ grains boundaries mainly have columnar morphology. It has been suggested that the retaining γ within SLM-fabricated martensitic steels is a result of mechanical stabilisation by hydrostatic pressures generated during initial formation [143].

Solution treatment at 1040°C transforms BCT α' back into FCC parent γ which is associated with the elimination of residual stresses introduced during manufacturing and recrystallization of the grains.

Subsequent aging process forms coherent BCC cu-rich precipitates which can pin dislocations during plastic deformation leading to higher hardness and mechanical strength. Extended aging temperature or holding time would transform coherent BCC cu-rich precipitates into non-coherent FCC cu-rich precipitates resulting in lower strength and higher ductility [123, 144].

[2] Average of 3 locations of transverse cross-sectional plane of as-built SLM specimen

Reduction in mechanical stabilisation in a solution heat treatment at 1040°C for 30 min promotes α' transformation by cooling below the expected M_f. The strain developed at the HAGBs during quenching suppressed the α' transformation in the localised regions, leading to small amounts of γ being retained in the CA material (2.53% retained γ in CA condition). γ was retained in the material along the prior γ grain boundaries (high magnification map not shown). Retained γ grains were also formed between the fine α' laths due to the higher presence of γ stabiliser such as C and Mn along the fine α' boundaries. After CA, retained γ are mainly located in the α' lath boundaries and have higher γ stability than retained γ allocated in the prior γ grain boundaries and triple junctions. Applying solution annealing to the SLM 17-4 PHSS fully recrystallised its microstructure and homogenised them. The continuous layer's interface area and the molten pools' boundaries disappeared completely (Figure 5-6).

The volume fraction of γ in H900 condition (without a solution treatment) did not change when compared to as-built condition. A dramatic increase in γ% occurred in the H1025 condition ($\gamma\% \geq \%55$) in coarse blocky morphology. This is due to the reverse transformation of α' to γ which can associated with the precipitation of Cu-rich particles and segregation of Ni. The segregation of Ni atoms during aging tends to shift the M_s temperature at local regions to below room temperature stabilizing γ phase [122, 123, 145]. In addition, the formation of Cu-rich clusters at the sites of their precipitation can lower the M_f temperature even further whereby leading to the stabilization of γ at room temperature [30]. A significant reduction in γ% was observed in prolonged ageing, both after heating to 620℃ and in two-step ageing. Substantial refinement in γ is also visible for both prolonged ageing conditions. A temperature of 620℃ in the H1150 condition is probably sufficient for residual stress elimination, thereby explaining the reduction. In the two-step ageing, reduction in residual stress may also act to lower γ stability. However, in H1150M sample, the volume fraction of γ suddenly dropped to 4.6%. Aging at temperature above 727°C allows the relaxation and decrease of residual thermal stress leading to considerable decrease of dislocation densities. In addition, the microsegregation of alloying elements (such as Ni) decreases upon aging at higher temperatures leading to a decrease of chemical and mechanical stability of γ permitting $\gamma \rightarrow \alpha'$ upon cooling to room temperature. This perhaps explains the decrease of γ fraction in H1150M condition.

While in direct-aged materials, Cu's solubility in high γ% hinders the ageing hardening mechanism by preventing precipitation formation [30]. This could be studied by transmission

electron microscopy (TEM) observation of the elements' aggregation, and was out of the study's scope (the author plans to employ this technique in future research).

Chemical composition, α' parent grain size after solutionising, ageing temperature and soaking time, and heating rate are influential parameters in reverted γ formation. While Bhambroo et al. claimed that the γ reversion mechanism has still not been fully conceptualised for conventional 17-4 PHSS [65].

The as-built SLM PHSS and the direct-aged specimens have higher metastable γ than the CA-aged specimens. The CA process eliminates the metastable γ phase fraction by α' transformation due to quenching. Ageing following CA imposes reverted γ, which has higher stability than retained γ. The reversion or local stabilisation of γ by the diffusion of Cu and Ni during ageing maintains the observed γ concentrations above zero. Through ageing, fresh/untempered α' produced in the CA condition is tempered, and can be distinguished by the presence of carbides from the fresh/untempered α'. Ageing tempers the α' matrix, which appears as a needle-like structure. Increasing temperature and soaking time of ageing approach to fineness needle-like α' matrix. Fineness is due to increasing rejection of C from the α' matrix with increasing temperature and time. Finer α' laths lead to a higher chance of γ formation in their boundaries.

Reverted γ is mostly allocated in random locations in blocky morphology [65], but could not be detected at the magnification available in this study.

Minimum $\gamma\%$ was observed for the CA-H900 condition ($\gamma\% \geq \%0.5$). Considerable growth of γ occurred in the CA-H1025 condition ($\gamma\% \geq 19.3\%$). Coarser equiaxed/blocky morphology of γ was detected for this condition. Similar to H1025 condition (aging without solutionising), reverse transformation of α' to γ occurred in CA-H1025 condition (aging after solution treatment) upon aging at 550°C. However, the fraction of reversed γ in CA-H1025 (≈19.3%) was found to be much lower than the H1025 (≈55.1%). This perhaps can be attributed to the decrease of dislocation densities (easy diffusion path for interstitial and substitutional elements) and elimination of microsegregation in local regions during solution treatment which decreases the chemical and mechanical stability of γ after quenching.

NbC-type carbides were also observed in the microstructure. Strong carbide formers such as Nb, and Ti are usually added to the stainless steels due to their high affinity to react with carbon to minimize the precipitation of Cr-rich carbides at the grain boundaries leading to sensitization

and localised corrosion attack in stainless steels. Some inclusions such as MnS and SiO_2 were also observed in the matrix which might have been introduced during powder processing and inherited by the SLM process [103, 109].

93.7% α' and 3.14% γ were measured for CA-H1150. This specimen contains a lower fraction of γ than the wrought specimen produced under the same heat-treated condition (see 3.3.3).

- *Grain orientations*

The IPF-Z maps, along with the IPF colour key, denote the grain orientations evolutions for α' and γ for the as-built SLM PHSS and the heat-treated materials in Figure 5-7 and Figure 5-8, respectively. IPF-Z maps of α' and γ reveal entirely dissimilar orientation for the direct-aged and CA-aged categories. No pattern is detectable in the microstructure in the CA-aged category. Table 5-3 summarises the average grain sizes of γ and α' of the as-built SLM and heat-treated materials.

Referring to Table 3-4 and Table 5-3, the as-built grain sizes for both phases were larger than those for the wrought specimen, consistent with yield strength.

Table 5-3 shows that the CA material's microstructure is more refined and uniform than that of the as-built specimen. In the CA condition, γ grain size decreased significantly (42%), and α′ grain size also reduced (18%) compared to the as-built specimen due to the recrystallization and formation of equiaxed grains.

Table 5-3 Average grain size measurements of γ and α' as functions of solution annealing, temperature and length of ageing procedures

Specimen ID	Average grain size of γ (µm)	Average grain size of α' (µm)	Specimen ID	Average grain size of γ (µm)	Average grain size of α' (µm)
As-built	1.62	2.80	**CA**	0.68	2.31
H900	4.24	4.97	**CA-H900**	0.69	2.43
H1025	4.78	3.11	**CA-H1025**	0.99	1.85
H1150	0.68	2.15	**CA-H1150**	0.73	2.11
H1150M	0.60	1.96	**CA-H1150M**	0.51	1.93

For CA-aged parts, firstly growth in γ grain size was reported from 480℃ to 550℃, then refinement was observed at 620℃ in single-step ageing. A reduction in grain size of α′ occurred between 480℃ and 550℃, then growth was detected between 550℃ and 620℃. In this group, specimens with the CA-H900 condition had the largest grain size (2.43 um and 0.7 um for α′ and γ respectively) and the finest grain size occurred under the CA-H1150M condition (1.93 um and 0.51 um for α′ and γ respectively).

Direct-aged materials initially showed an increase in γ grain size (from 480℃ to 550℃). Substantial grain growth was observed at 550℃. Massive reduction and refinement occurred at 620℃ due to recrystallizsation.

The variation of grains size at each condition is attributed to the reverse transformation of α' to γ during aging at lower temperature and/or transformation of γ back to α' when γ is no longer stable during cooling.

- *KS-OR relationship*

Figure 5-9 shows the phase boundary orientation relationship for the as-built and heat-treated specimens. γ and α' phases boundaries deviated $< 10°$ from the KS OR during loading for heat-treated conditions are tabulated in Table 5-4. This relationship is discussed comprehensively in 3.3.3.

Table 5-4 γ and α′ phases boundaries deviated $< 10°$ from the KS OR during loading as a function of solution annealing, temperature and length of ageing procedures

Specimen ID	x<10° KS OR (%)	x>10° KS OR (%)	Specimen ID	x<10° KS OR (%)	x>10° KS OR (%)
As-built	92.77	7.24	**CA**	88.90	11.10
H900	92.60	7.40	**CA-H900**	87.15	12.85
H1025	90.06	9.94	**CA-H1025**	94.22	5.78
H1150	95.66	4.34	**CA-H1150**	92.50	7.50
H1150M	95.02	4.98	**CA-H1150M**	93.87	6.13

Solutionising reduced this coherency from the as-built condition. Under solutionised ageing in the CA-H900 condition, the lowest value for this relationship was observed. The maximum value belongs to CA-H1025. In prolonged ageing, an initial reduction in CA-H1150 and later an increase in CA-H1150M was observed.

From H900 to H1025, a large reduction in coherency was measured. A huge increase is detected in H1150 condition. In two-step ageing, a small reduction was observed. By assuming H1025 as peak-aged condition in direct-aged category, surprisingly defined coherency between phases are decreasing.

- *Kernel average misorientation*

Figure 5-10 and Figure 5-11 show qualitative KAM maps for the as-built SLM PHSS and heat-treated conditions in γ and α' respectively. Corresponding KAM values are shown in Table 5-5.

Table 5-5 Average of local misorientation of γ and α' phases during loading

Specimen ID	KAM (α'),	KAM (γ)	Specimen ID	KAM (α'),	KAM (γ)
As-built	1.02	0.65	**CA**	1.05	0.88
H900	0.80	0.52	**CA-H900**	1.07	0.84
H1025	0.84	0.55	**CA-H1025**	1.05	0.83
H1150	0.87	0.73	**CA-H1150**	1.06	0.88
H1150M	0.99	0.90	**CA-H1150M**	1.07	0.96

Residual stress in the as-built specimens is higher than in the direct-aged group, which reflects the elimination of residual stress during the direct ageing processes.

It is observed that the KAM value of α' decreased from 1.02° in as-built to 0.8° in H900 condition. This is due to the recovery and decrease of dislocation densities during aging. However, the reverse transformation of $\alpha' \rightarrow \gamma$ (microsegregation of Ni and formation of Cu-rich clusters) and transformation of $\gamma \rightarrow \alpha'$ because of aging at temperature ≥620°C (due to the decrease in stability of γ) imposing strains and introducing dislocations, led to the increase of KAM values from 0.8% in H900 to 0.99% in H1150M condition.

The KAM values of α' after solution treatment and aging seem to have remained almost unchanged. This is attributed to the recrystallization and decrease of dislocation densities. However, it can be seen that the KAM value in CA condition is slightly higher than the as-built samples which can be due to the considerable grain refinement and formation of more grain boundaries after recrystallization. γ as a soft phase is affected more by the "solution annealing + aging" process and is strained more by the surrounding matrix which can introduce more

dislocations into γ (because of $\gamma \rightarrow \alpha'$ upon cooling) resulting in the increase of KAM value of α from 0.84% in CA-H900 to 0.96% in CA-H1150M.

5.3.2 Clusters, ageing precipitates (enriched in Cu), carbides ($Cr_{23}C_6$)

Due to restrictions on access to microscopy facilities during the COVID-19 pandemic, TEM observation of the precipitation hardening formation was not conducted. In-depth research to investigate clustering, ageing precipitation, and carbide formation is needed to identify the microstructural features and mechanical behaviour of as-built SLM and heat treated materials. Nevertheless, as a preliminary to a full investigation of precipitation and chemical aggregation of SLM 17-4 PHSS and heat treated materials, EDS maps of the material in the CA-H1150M condition are provided in Figure 5-12. They show a higher intensity of Cu precipitates in the CA-H1150M condition, and Ni partitioning also might occured in it. Further facts about precipitation formation, which can be used in a discussion of mechanical properties, are presented below.

It has been shown that peak strength is achieved at any given temperature after a specific ageing duration. Beyond the duration of ageing corresponding to peak strength, the material's strength always reduces [146, 147]. There is no literature on the kinetics of ageing in SLM 17-4 PHSS. Therefore, it is highly recommended that new heat treatment procedures are designed to achieve the corresponding peak-aged conditions.

The predominant factor in precipitation formation is the strain field formed around the precipitates. In 17-4 PHSS, a near-full α' microstructure is a prerequisite for precipitation formation. EOS (the SLM machine manufacturer) recommends solution annealing before peak ageing. Researchers reported that when as-built SLM parts were subjected to direct ageing at 482℃, age hardening did not occur [128]. Cu-rich precipitates can be formed within the α' matrix during the ageing process, but this does not occur spontaneously in the as-built specimen [105].

Precipitate-strengthening particles are located in grains in CA-aged conditions; however, in direct-aged conditions, they are formed along the grain boundaries. The volume fraction and size of Cu precipitates play an essential role in changing the microstructure. It is quite common for a coherent precipitate to form and then drop coherency when the particle reaches a critical

size. Coherent precipitates produce a high strain field in the matrix, while the imposed strain is decreased due to the loss of coherence.

NbC-type carbides were also observed in the microstructure. Strong carbide formers such as Nb, and Ti are usually added to the stainless steels due to their high affinity to react with carbon to minimize the precipitation of Cr-rich carbides at the grain boundaries leading to sensitization and localised corrosion attack in stainless steels. Some inclusions such as MnS and SiO_2 were also observed in the matrix which might have been introduced during powder processing and inherited by the SLM process [103, 109].

5.3.3 Mechanical properties

- *Hardness*

The hardness evolutions of the standard and non-standard heat-treated SLM 17-4 PHSS parts, as a function of location in the transverse plane from bottom to top (refer to Figure 5-13 (a)), are shown in Figure 5-13 (b,c) and Figure 5-14 (a,b). Figure 5-13 (b) shows specimens subjected to ageing conditions including H900, H1025, H1150 and H1150M without the intermediate, post-SLM solution heat treatment. It also depicts a hardness variation of the as-built SLM PHSS without any additional thermal processing. Figure 5-14 (a) shows a similar comparison, but with solution annealing following ageing under CA-H900, CA-H1025, CA-H1150 and CA-H1150M conditions. It also offers a reference variation for a specimen following only a solution heat treatment and the as-built specimen. Hardness values of the as-built specimen under all heat-treated conditions are tabulated in Table 5-6.

Micro-hardness data are mostly unaffected by internal defects. Hardness measurements show the microstructural features' actual effect, such as phases, average grain sizes, precipitate particles, and alloy compositions.

It is apparent that the hardness increased with increasing temperature and soaking time for the direct-aged category, consisting of single-step and two-step ageing monotonically. Solutionised aged parts show the same rising trend with increasing temperature and time. The average STD of hardness for the direct aged specimens was ≈ 14 HV, while the H1025 condition produced a higher value, which can be explained by experimental error (Table 5-6).

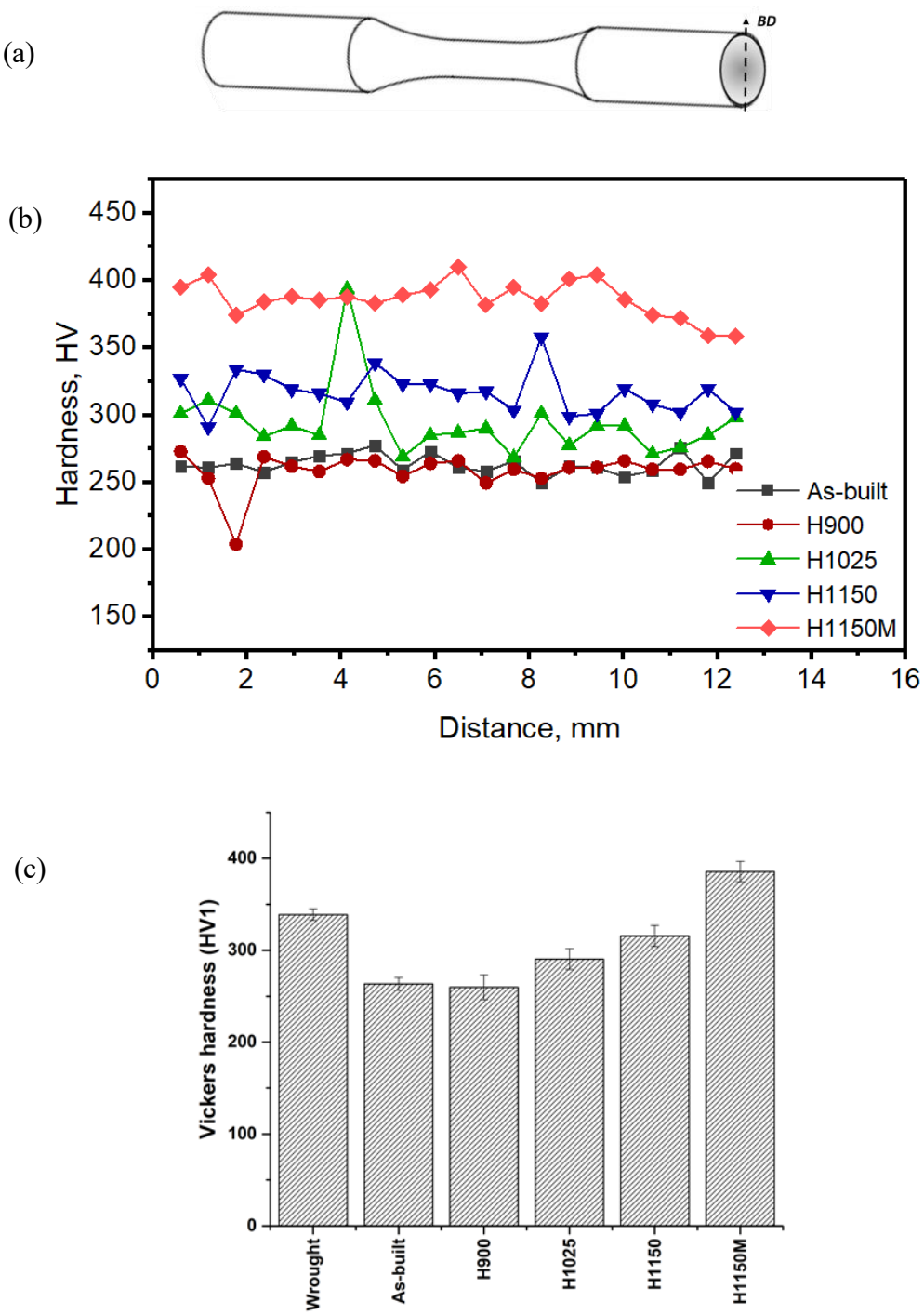

Figure 5-13 (a) Schematic of the indented locations in the specimens from the bottom to the top of the cross-section, (b) hardness of the as-built SLM and direct-aged specimens, and (c) bar chart with error bar representation of hardness of the wrought, as-built and direct-aged ones

(a)

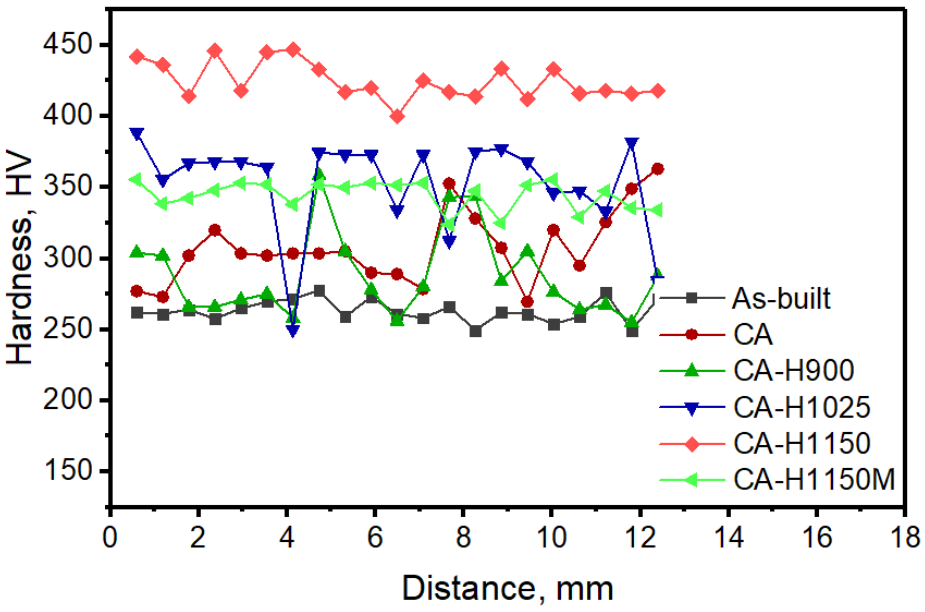

(b)

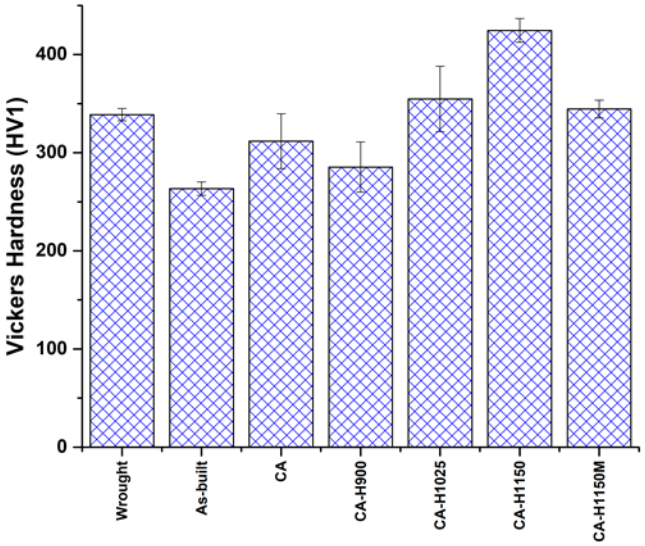

Figure 5-14 (a) Hardness of the as-built SLM, solution-annealed and solutionised aged specimens, (b) bar chart with error bar representation of hardness of the wrought, as-built and direct-aged ones

Average grain size is one of the most influential parameters in hardness (refer to Table 5-3); H900 and H1025 have coarse γ and α' grains due to γ stability. In the H900 condition, α' has quite coarse grains, and γ is coarse too. However, in the H1025 condition, α' grain is finer and γ grain is coarser than in the H900 condition. In this research, the H1150 condition produced α' grain size reduction, as well as a significant reduction in γ, which cannot be reliable due to the low indexing in data acquisition. The H1150 M condition associated with two-step ageing

gave the finest grain sizes in both phases. A reduction in grain size led to higher HV. The fraction of dislocation density in the direct-aged parts (Table 5-5) increases KAM values for both phases by increasing temperature and soaking time. Due to higher residual stress, higher HVs are attained. Residual stress in the as-built specimens is higher than in the direct-aged group.

From a precipitation strengthening point of view, due to not applying solution annealing, which is labelled CA prior to aging treatment, in direct aged conditions, according to the researches [30, 128], precipitate particles may not formed due to higher solubility of Cu in high γ% in H900 and H1025 conditions. To investigate precipitation hardening on hardness, further microscopy observation is recommended as future work.

Hardness in solutionised condition is higher than the as-built SLM one (Table 5-6). CA condition is mainly (fresh) α' and delivers only a small amount of retained γ (Table 5-2). In other words, the CA process is applied to eliminate the metastable γ. Dislocation density (residual stress) shown by KAM values is higher than for the as-built specimen, and is associated with a considerable grain refinement during solutionizing (Table 5-5). Higher KAM values bring higher hardness due to the deformed structure. γ and α' grain size, reduced 2.3 and 0.82 times in the specimens with the CA condition in comparison with the as-built specimens (Table 5-3), is another reason for higher HVs.

Effective factors discuss hardness evolutions in the solutionised aged conditions below; the hardness of PHSS processed under CA-aged conditions was increased considerably by ageing progression in a single-step ageing procedure. In two-step ageing, the hardness of CA-H1150M was reduced compared to the CA-H1150 condition, while increased compared to the as-built specimen.

It is seen in Table 5-6 that STD values for solutionised aged conditions at 480℃, 550℃ and 620℃ are approximately in the same ranges (≈ 30); however, a minor difference is observed for the CA-H1150M condition, which can result from homogenisation.

CA-aged conditions generate a high fraction of tempered α'. This may be the reason for this group's high hardness compared to the direct-aged group. Dislocation density (residual stress) by heat treatment progression decreased from CA-H900 to CA-H1025 and increased from CA-H1025 to CA-H1150 in single-step ageing for both phases. For two-step ageing, KAM value

rises from CA-H1150 to CA-H1150M for both phases. The solutionised aged parts' dislocation density is higher than that of the direct-aged group (refer to Table 5-5). Higher dislocation density is associated with higher hardness values. The average grain size of γ and α' of the specimens produced under CA-aged conditions are smaller than those of the direct-aged specimens (Table 5-3), further explaining the higher average hardness achieved in CA-aged conditions. The precipitation's effect on hardness means there is a possibility that peak age occurred in the CA-H1150 condition by increasing hardness values, despite ASTM reporting peak age appearing at the CA-H900 condition for wrought PHSS [48]. So, precipitation formation and coarsening may not happen in a standard manner for standard heat treatment proceudres in this study.

When the same ageing conditions were applied to direct-aged and solutionised specimens, solutionised aged parts showed higher mean hardness. The average HVs of the solutionised aged and direct-aged specimens were 352±25 and 314±16.5, respectively (Table 5-6). However, the opposite occurred with the two-step ageing process, CA-H1150M. Minimum HV was achieved in the H900 condition, while the maximum was associated with CA-H1150.

Hardness values reported by ASTM indicate that by increasing temperature and soaking time during ageing, conventionally manufactured parts' HVs drop monotonically [48]. LeBrun et al. reported reducing hardness by increasing ageing temperature and soaking time[30]. In another study, Sun et al. illustrated lower hardness for the as-built than the wrought specimen, and the CA condition produced a slightly higher HV than that of the as-built specimen [37].

- *Tensile properties*

Engineering stress–strain curves of the heat-treated specimens are presented in Figure 5-15. Figure 5-15 (a) shows specimens treated with direct ageing conditions, including H900, H1025, H1150 and H1150M. It also offers a stress–strain curve of the as-built SLM PHSS. Figure 5-15 (b) shows a similar comparison, with solution ageing using CA-H900, CA-H1025, CA-H1150 and CA-H1150M. It also offers a curve for a solution heat-treated specimen as well as an as-built specimen.

When upper and lower yield points are reported, the upper yield point is presented as the yield strength. The average values of all tensile properties were based on at least three measurements for each condition (six repetitions were applied when incompatible behaviour was observed).

Average values of Vickers hardness (HV), Young's modulus (E), yield strength (YS)/proof stress (0.2% elastic offset), ultimate tensile strength (UTS), strength ratio defined as ($^{YS}/_{UTS}$), uniform elongation (UEl), total elongation (TEL), and UTS*TEL index for the various tested conditions are tabulated in Table 5-6. To evaluate the effect of heat treatments on deformation characteristics, the mechanical properties are discussed separately.

The tensile data demonstrate that deformation characteristics were more strongly affected by the applied solutionised-aged conditions than the as-built and direct-aged conditions. Figure 5-15 (b) shows that the CA-aged group's stress–strain behaviour was consistent with that of standard heat-treated 17-4 PHSS [48]. Different stress–strain behaviour was revealed for the direct-aged group specimens (Figure 5-15 (a)).

(a)

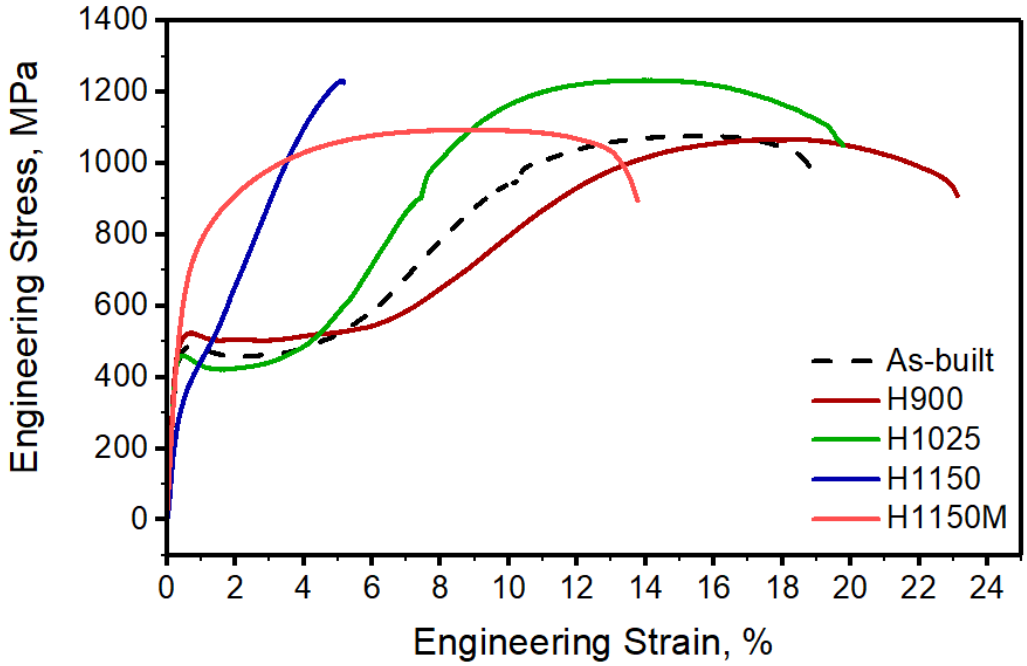

(b)

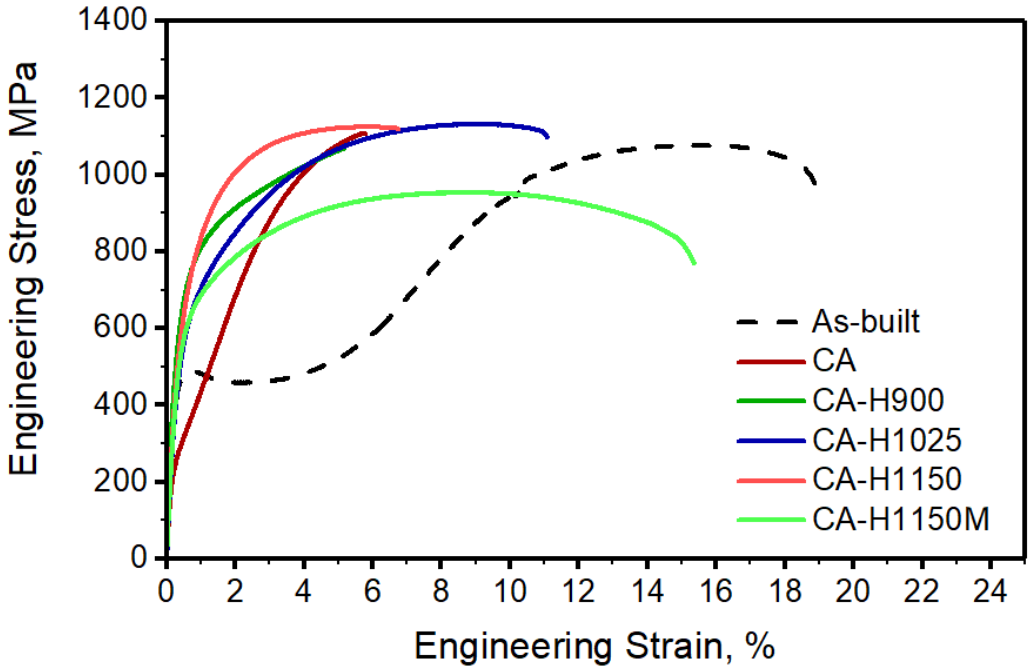

Figure 5-15 (a) Stress–strain curves of the as-built SLM and direct-aged PHSS, and (b) stress–strain curves of the as-built SLM, solution-annealed and solutionised aged specimens

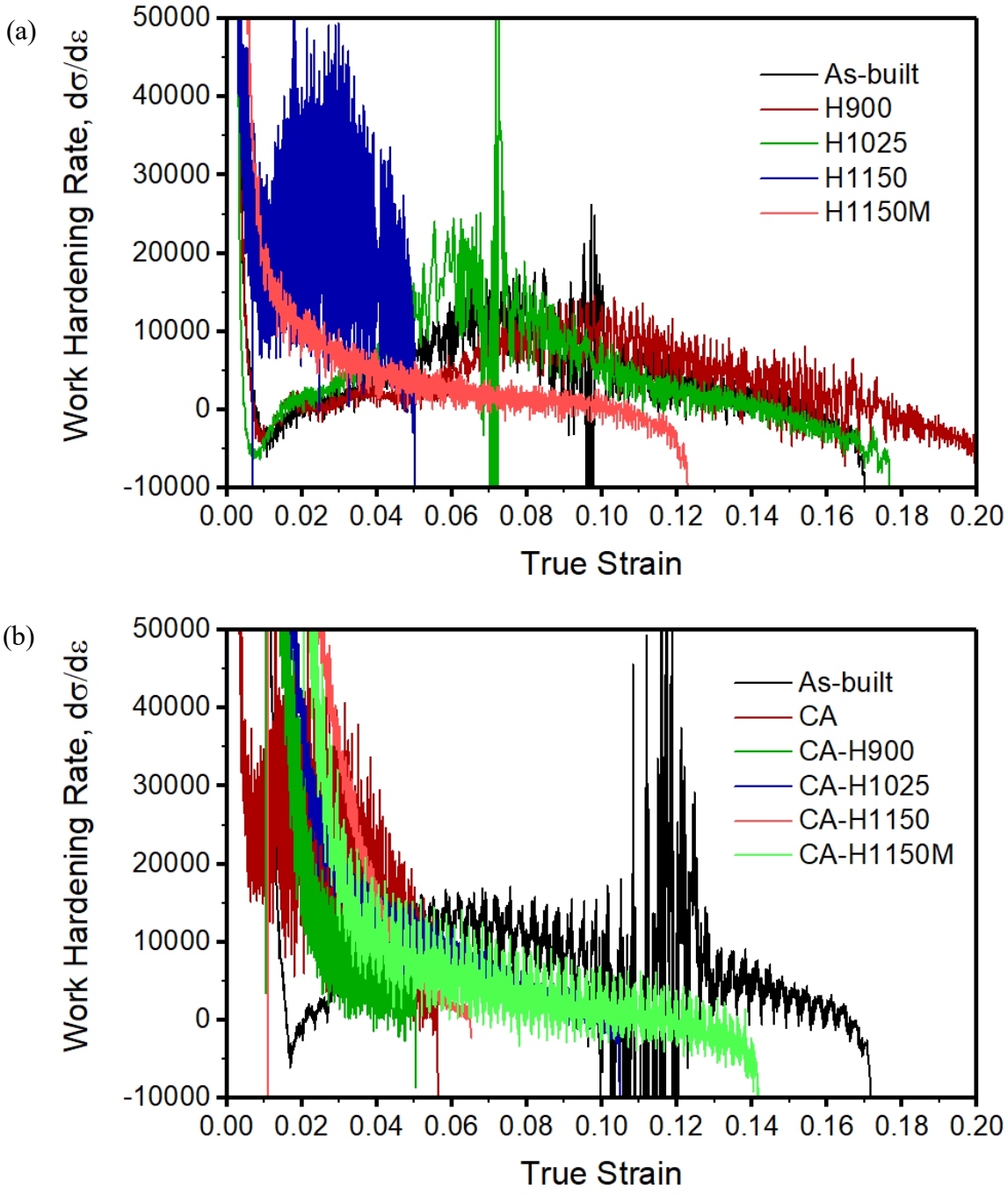

Figure 5-16 (a) Work-hardening of the as-built SLM and direct-aged PHSS, and (b) work-hardening of the as-built SLM, solution-annealed and solutionised aged specimens

Table 5-6 Hardness and tensile properties of the as-built SLM and heat-treated specimens

Specimen ID	Hardness (HV)	E (GPa)	σ_y (MPa)	σ_{UTS} (MPa)	Strength ratio (σ_y/σ_{UTS})	UEL (%)	TEL (%)	UTS*TEL
As-built	269±34	169±3	477±3	1073±5	0.445	14.72±1.24	16.88±2.82	18116
H900	260±14	175±21	522±17	1068±0	0.489	18.14±0.41	22.25±1.24	23758
H1025	294±24	176±5	465±7	1243±14	0.374	13.91±0.23	18.29±2.1	22737
H1150	316±15	172±26	360±21	1073±	0.335	5.45±	5.48±	5880
H1150M	385±13	178±9	637±18	1095±23	0.581	8.36±0.4	12.25±1.32	13420
Average	314±16.5	175±15	496±16	1119.75±	0.445	11.46±	14.57±	16449
Average single-step ageing	290±18	174±17	449±15	1128±	0.399	12.5±	15.34±	17458
As-built	269±34	169±3	477±3	1073±5	0.445	14.72±1.24	16.88±2.82	18116
CA	313±32	178±14	339±1	846±57	0.4	4.12±1.02	4.4±1.04	3722
CA-H900	287±29	186±8	602±	1028±	0.585	5.16±	5.16±	5304
CA-H1025	355±33	182±3	575±7	1128±6	0.51	8.7±0.5	10.29±1.2	11606
CA-H1150	422±27	183±9	592±18	970±14	0.587	5.82±0.19	6.47±1.1	7221
CA-H1150M	345±10	184±10	605±34	958±8	0.631	8.25±0.66	11.23±3.62	10757
Average	352±25	184±8	593±15	1021±	0.576	6.98±	8.29±	8722
Average single-step ageing	355±30	184±7	590±8	1042±	0.560	6.56±	7.31±	8044

- *Young's modulus*

Stiffness is mainly influenced by atomic bonding. Strong atomic bonding means a high Young's modulus (E), high melting point, and low thermal expansion coefficient. E is mostly associated with chemical compositions and phase fractions. Increasing γ% leads to a lower E in this study.

The H1150 condition was associated with the lowest E in direct-aged parts. The E of the specimen produced using CA-H1025 is lower than those produced under the other conditions, and is related to higher γ%.

The average E of CA-aged specimens is higher than that of direct-aged specimens (174±17 GPa and 184±7 GPa for the single-step ageing of the direct-aged and solutionised aged specimens respectively). It is related to the high fraction of α' comparably. As enhanced elastic properties are the most desirable in industrial applications, CA-aged conditions are more expected as a proper condition for the industries.

- *Yield strength* (σ_y)

The heat treatments' effect on the strength (yield and ultimate strength) of PHSS is attributable to alterations in microstructure characteristics, consisting of phase fraction, grain size, morphology, and second-phase hardened precipitates in the matrix. There is a gradual transition from elastic to plastic behaviour, and the point at which plastic deformation begins is difficult to define precisely. A 0.2% offset method was applied to calculate the YS. The grain size of γ is closely related to this property in the elastic region. The Hall-Petch relation was used to explain the effect of grain size on this parameter (refer to Equation 2-3).

For the direct-aged conditions, σ_y decreased for single-step ageings; however, YS was highest for two-step ageing. Reduction in σ_y in the H1025 condition was associated more strongly with growth in γ grain size and fraction than in the H900 condition. The H1150M condition shows the highest σ_y in the direct-aged category, due to the finest grain sizes of the γ. A stress–strain curve of the H1150M condition shows that solutionising may occur at 760℃ in the first ageing step.

The σ_y of the CA specimen is lower than that of the as-built specimen. The presence of fresh α' is the only explanation.

For CA-aged specimens, σ_y decreased from CA-900 to CA-H1025 due to the larger γ grain sizes and higher fraction of γ. Despite being selected as the peak age condition, CA-H1025 owing to the largest γ grain size, the lowest value is recorded for the σ_y. The YS for CA-H1150 and CA-H1150M were higher than CA-H1025, consistent with the γ grain sizes (Table 5-3). Flow curves were documented for all conditions for CA-aged specimens. Solutionising converts retained γ induced by the SLM process to mainly fresh α' with tiny retained γ. Due to the elimination of metastable γ% by imposing CA prior to ageing processes, the TRIP effect did not appear in this group.

In the same ageing conditions, in general, the CA-aged category gives higher σ_y than direct aging (590±8 MPa and 449±15 MPa were the average σ_y for single-step ageing for the CA-aged and direct-aged specimens, respectively). The reverse occurs with two-step ageing; CA-H1150M shows a slight reduction in yield. Note that the minimum σ_y value for CA was 339±1 MPa, while the maximum – 637±18 MPa – was associated with the H1150M condition.

ASTM reports by increasing ageing temperature and soaking time during ageing, σ_y value decreases monotonically [48]. LeBrun et al. and Nezhadfar et al., in two different research works, showed similar behaviour in aged specimens following intermediate solution heat treatment conditions consistent with the ASTM [30], [34].

- *Yield point elongation*

The yield point phenomenon is a localised heterogeneous transition from elastic to plastic deformation that produces a yield point in the stress–strain curve. The load increases steadily with elastic strain, drops suddenly, fluctuates about some approximate constant value of load, and rises with further strain. The deformation occurring throughout the yield point elongation (YPE) is heterogeneous. Lauders bands form at several points of stress concentrations at approximately 45° to the tensile axis. Each peak corresponds to the formation of a new Lauder band. After the Lauder bands have propagated to cover the entire length of the (gauge length) specimen, the flow increases with strain in a typical manner. The yield point phenomenon was found originally in low-carbon steels, but a similar progressive evolution in yielding behaviour has been observed in dual-phase steels [71]. Note that grain size, chemical composition and specimen geometry are the parameters that most strongly influence YPE.

The as-built, H900 and H1025 conditions all have discontinuous YPE. In this research, H1150 and H1150M conditions showed continuous flow curves due to the smaller γ grain size than the as-built, H900 and H1025 conditions. Low C% and specimen geometry effect are negligible, since all the materials were prepared with the same chemical compositions and specimen geometry. Continuous behaviour is more desirable for industrial applications due to lack of localised deformation during loading. All the remaining CA and CA-aged specimens showed continuous yielding.

- *Ultimate strength (σ_{UTS})*

Table 5-6 reports the average ultimate strength values for the as-built, direct-aged and solutionised aged specimens. The σ_{UTS} increased relatively fast with ageing progression for the direct-aged specimens from 480℃ to 550℃, while reduction occurred from 550℃ to 620℃. Increasing strength was detected from 620℃ in the two-step ageing condition. Complex dislocation interactions control behaviour near ultimate strength.

The σ_{UTS} increased faster with aging progression for solutionised aged specimens from 480℃ to 550℃ (1024±61 to 1128±6 MPa) dropped slightly from 550℃ to 620℃, and reduced continuously from 620℃ in the two-step ageing condition to the minimum value.

For direct-aged conditions, the H1025 condition shows the highest value of σ_{UTS}; the other conditions are in a similar range. For CA-aged specimens, similar to the direct-aged ones, maximum σ_{UTS} occurred in CA-H1025. Due to the higher fraction of the metastable retained γ in H1025, the TRIP effect progresses, and specimens are strain hardened substantially. In CA-H1025, a high fraction of reverted/retained γ leads to notable strain hardening.

In the same ageing conditions for both groups, the solutionised aged parts had lower σ_{UTS} than the direct-aged parts in general. Average σ_{UTS} values for the solutionised aged and direct-aged specimens in single-step ageing were 1042 MPa and 1128 MPa, respectively. Note that the minimum σ_{UTS} value was for CA-H1150M (958±8 MPa).

The ASTM indicates that, with ageing progression, σ_{UTS} values should decrease monotonically [48]. LeBrun et al. reported similar behaviour in aged specimens following intermediate solution heat treatment conditions, consistent with the ASTM [30]. Nezhadfar et al. found a decreasing trend in σ_{UTS} in direct-aged and solutionised aged parts by increasing temperature and time consistent with the ASTM standard. In the same ageing conditions [34].

In this study, the observed σ_{UTS} evolution is not entirely consistent with the ASTM trend. Improvement of σ_{UTS} occurred in H1025 and CA-H1025 rather than H900 and CA-H900 as peak age conditions.

- *Strength ratio (work hardening)*

The stress required to produce continued plastic deformation increases with increasing plastic strain; this enhancement shows strain hardening/work hardening capacity. Higher interaction between dislocations results in higher strain hardening rate.

True stress and true strain were calculated based on the engineering stress–strain curves to study the work hardening behaviour of the materials. The slope of the stress–strain curves in the plastic deformation area implies work hardening. The work hardening behaviour of the treated materials was computed using a differentiated method. The normalised work hardening rate was calculated using Equation 5-1:

$$Normalized\ hardening\ rate\ \Theta = (d\sigma/d\varepsilon)\ /\sigma \qquad \text{Equation 5-1}$$

Normalised work hardening was plotted against true strain curves and studied. Figure 5-16 (a) shows the work hardening rate of the as-built and direct-aged specimens. Figure 5-16 (b) depicts the work hardening rate of the as-built, solutionised and CA-aged specimens.

The strength ratio index ($^{\sigma_Y}/_{\sigma_{UTS}}$) is an indicator of strain hardening capacity. The strength ratios of the conditions are summarised in Table 5-6. Higher strength ratio value indicates lower work hardening capacity.

The work hardening rate curves of the as-built, H900 and H1025 specimens show that the rates do not decrease monotonically with increasing strain. Each curve's reversal point shows the nature of the stress–strain curve in yield point elongation (YPE) (upper and lower point). The negative part of the curve indicates that softening occurs immediately after yielding.

Little to no work hardening capacity over extended regions of strain was demonstrated for CA-aged materials. Work hardening for H1150M approaching the values observed for the CA-aged category may be associated with annealing at around 760℃.

For direct-aged conditions, by ageing progression, strength ratio index decreased for single-step aged conditions, denoting increasing strain hardening from H900 to H1150 conditions. This index decreased in two-step ageing, showing that low strain hardening capacity occurred in the H1150M condition. The highest strain hardening capacity was observed in CA-H1025. CA-H900 and CA-H1150 show similar strain hardening capacity. The average strength ratio

of the solutionised aged specimens was slightly higher than that of the direct-aged parts, reflecting lower work hardening capacity in the CA-aged group.

The minimum value of 0.335 for the H1150 condition occurred in the direct-aged group, which displayed the highest strain working capacity. In contrast, the highest strength ratio of 0.631 was recorded for CA-H1150M, denoting the lowest work hardening capacity. Two-step ageing conditions in both groups were associated with the least strain hardening.

Nezhadfar et al. reported minimum strength ratio values in heat-treated conditions associated with the H900 condition [34], conflicting with the results presented here.

- *TRIP effect*

C% and meta-stable γ% are the most influential parameters with respect to TRIP behaviour (as discussed in 2.3.5). The as-built, H900 and H1025 conditions depict powerful TRIP effects due to high fractions of retained γ.

Due to small fractions of retained/reverted γ and reduced metastability, CA-aged specimens did not show the TRIP effect. As discussed, reverted γ has higher stability, so produced a low level of α' transformation and strain hardening.

- *%UEL, %TEL*

Sufficient elongation is necessary to distribute localised stress and decrease crack initiation and propagation in AM components.

For direct-aged parts, the UEL% of single-step aged conditions reduced with ageing progression is not in good agreement with γ phase fraction (Table 5-2). TEL% shows a similar trend. It is apparent that for the direct-aged specimens, elongations decreased with aging progression from 480℃ to 550℃ and 620℃, while elongation increased in the two-step ageing condition.

The solutionised aged conditions produced lower elongation to failure ($\approx$ %7) (for single-step aging) than the direct-aged conditions ($\approx$ %15), contributing to the low fractions of retained/reverted γ in CA-aged specimens. As shown in Table 5-6, the solutionised aged parts did not exhibit significant elongation and failed rapidly. After necking, plastic deformation also decreased in the solutionised aged specimens compared to the direct-aged parts. For CA-aged

specimens, both elongations increased with ageing progression from 480℃ to 550℃ due to the γ stability as discussed before and from 620℃ with the two-step solutionised aged condition. The TEL% is consistent with the γ%.

When the same ageing temperature and soaking time was applied to both groups of specimens, the solutionised aged conditions produced lower elongation than the direct-aged ones in general. (Average UEL and TEL for the direct-aged parts in single-step ageing conditions were 12.5 and 15.34, respectively.)

Minimum elongation values were observed for CA-H900 (5.16% for both UEL and TEL), while the maximum was associated with H900 (18.14% for UEL and 22.25% for TEL). The elongation evolution described herein is not completely consistent with a reported trend based on the observed standard.

Values of UEL and TEL reported by the ASTM indicate that elongation values increase monotonically with aging progression [48]. LeBrun et al. as well as Nezhadfar et al. detected similar behaviour in aged specimens following intermediate solution heat treatment conditions consistent with the ASTM trend [30], [34].

- *Ultimate strength*TEL% as an index of toughness*

The product of UTS and TEL is considered an index of formability and absorbed energy (crash energy) of steels, and is used to tailor them in the automobile industry. Table 5-6 reports the UTS*TEL indices of the all studied heat treatments.

Heat-treating progression reduced toughness in direct-aged parts. In contrast, in two-step ageing, this index improved significantly. From H900 to H1025 toughness decreased slightly, and from H1025 to H1150 a considerable decline occurred.

Overall, this index is of minor importance for CA-aged parts compared to direct-aged parts, which can experience weak/reduced work hardening capacity. Elimination of the metastable γ in the CA-aged group may be the main reason. The index increased with increasing temperature and soaking times at 480℃, 550℃ and in the two-step solutionised aged condition, and decreased at 620℃ (CA-H1150). Note that the minimum value was observed for CA-H900 (5304), while the maximum was associated with H900 (23758).

5.3.4 Fractography

Yadollahi et al. applied spot analysis of EDS to determine the chemical composition of secondary phase particles in the research. Their EDS results indicated particles were enriched in C, O, Cr and Fe, and proved that carbides and oxides (Cr and Fe) form mostly along the grain boundaries. The formation of these particles is detrimental to the ductility and toughness of SLM parts [41]. It is suggested to conduct EDS analysis of the fractured surfaces in different heat-treated conditions in future work.

Micro-crack nucleation starts from porosities, voids and second-phase particles due to stress concentration around them. Induced SLM defects (discussed comprehensively in 2.6.3) are a significant factor in SLM parts fractography. Separation of boundaries due to their embrittlement originates from the aggregation of some chemical elements and particles. The aggregation is one of the most effective factors in studying fracture mechanisms, which should be considered in this material. Segregation causes to have a brittle strike of elements leads to having a brittle fracture in transgranular form. In failure, prevention of the brittle manner is chiefly essential.

In brittle failure, due to the lack of plastic deformation around cracks, they propagate quickly; cleavage-type ruptures in the surface are typically observed. In this research, transgranular cleavage failure was more prevalent in brittle failure. In ductile failure, the vicinity of cracks experienced large plastic deformation under loading, which reduced the crack propagation speed, and failure occurred more slowly.

Figure 5-17 shows the fractured surface of specimens treated with H900, CA-H900, H1025 and CA-H1025. The images highlight the macro-scale texturing in the ruptured surfaces.

H900 and H1025 showed high strain-hardenability during tensile testing whilst CA-H900 and CA-H1025 fractured shortly after necking. The fracture surfaces of H900 and H1025 seem to be smoother than CA-H900 and CA-H1025 and contain micro size dimples. The considerable work-hardening after yielding and stress-induced transformation of austenite to martensite resulted in typical cup and cone features in H900 and H1025. Defects such as microporosities and local shearing around these defects are quite observable on the fracture surfaces (see yellow arrow). The fracture morphology of CA-H900 and CA-H1025 is irregular and some isolated micro dimples are seen between the quasi-cleavage facets. The quasi-cleavage facets are quite

visible in the fracture surface and seem to be the main characteristics in CA-H900 and CA-H1025. The volume fraction of austenite after solution treatment is lower as compared to directly aged samples (without solution treatment) and this results in a lower strain-hardening capacity after yield point and before fracture. The dotted white rectangle in Figure 5-17 outlines the tear ridge in CA-H900 condition.

In direct-aged fractured surfaces, the micro-scale dimple structure suggests localised ductility. The direct-aged group shows quite long non-uniform stretching from the necking point to the final fracture associated with more ductile fracture features (Figure 5-17 (a, b)). The difference between UEL% and TEL% in the CA-aged specimens is lower than in the direct aged ones and can relate to brittle failure (Figure 5-17 (c,d)).

Cleavage failure was more prevalent in the CA-aged conditions due to the elimination of the metastable γ. The CA-aged parts experienced more brittle failure (mainly by approximately flat fracture surface) than the direct-aged parts. The direct-aged parts mostly showed 45° failure. Nonetheless, fracture behaviour was observed for each category despite variations in the ageing temperature and time. H1150 and H1150M illustrate facets that improve brittle behaviour with a low number of dimples with small size and flat appearance on the tensile fractured surfaces. (has not provided here)

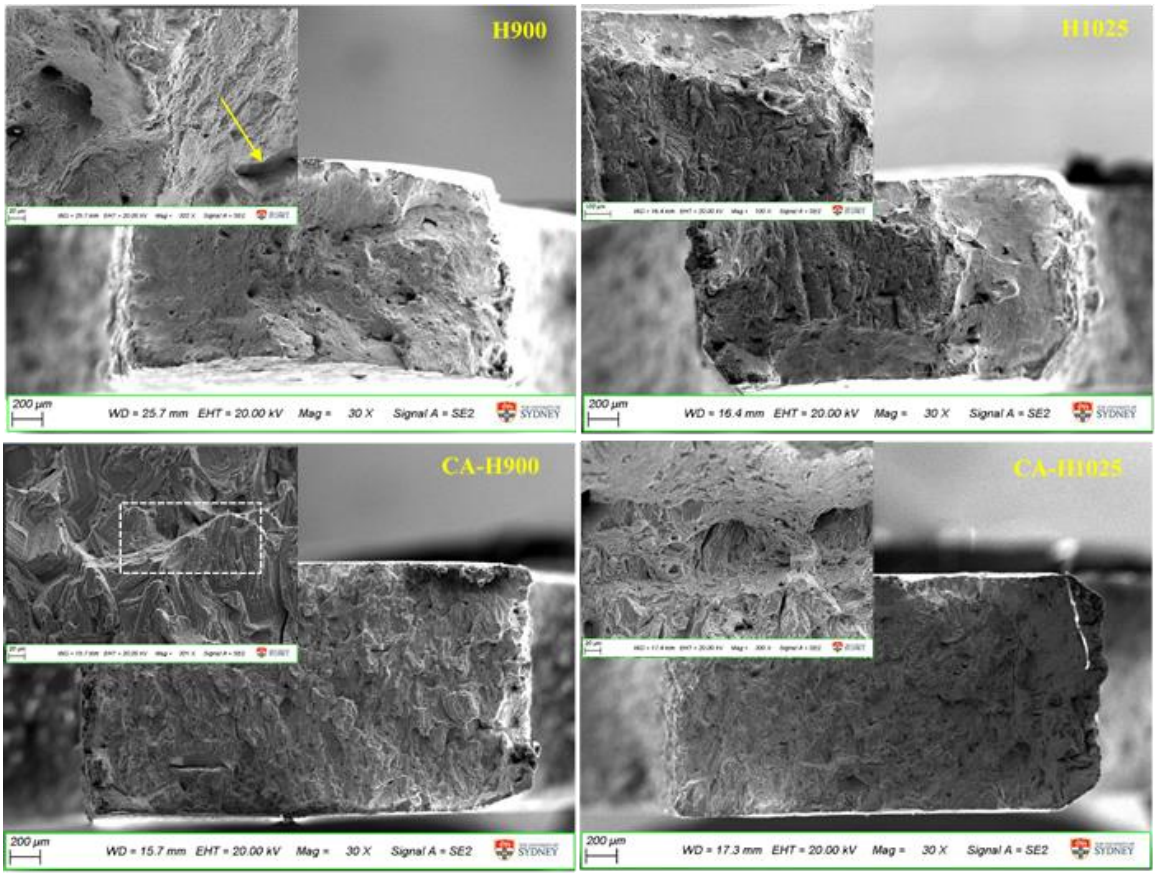

Figure 5-17 SEM images of the fractured heat-treated specimens as labelled heat treatment condition

5.3.5 Discussion of mechanical properties

It is important to compare the relative hardening and strengthening of the heat-treated materials in this study. Mirzadeh and Najafizadeh [64] used Equation 5-2 to define the relative percentage of hardening:

$$H_t = \left(\frac{H - H_0}{H_0}\right) * 100 \qquad \text{Equation 5-2}$$

Where H_t describes the alteration in hardness due to the non-heat-treated specimen as the starting condition (including as-built one and solutionized condition), H_0, and the heat-treated aged hardness, H.

Great to apply tensile testing properties as they reveal more information about yielding and plastic deformation of heat treated specimens that hardness cannot reveal about them directly. Equation 5-3 [30] express the relative increase in strength in different heat treatment conditions

$$S_t = \frac{S - S_0}{S_0} * 100 \qquad \text{Equation 5-3}$$

The alteration of strength due to the aging relative to the non-heat-treated specimen as the initial condition (including as-built condition and solutionized one), S_0, and the heat-treated aged strength, S.

It is very valuable to provide hardness/ strength in a vast range of tempering temperature and time while many charts just provide a few conditions. Larson–Miller or Hollomon–Jaffe tempering parameter (P), Equation 5-4, indicates the relation between temperature and time of tempering as independent parameters:

$$P = T(C + \log(t)) * 10^{-3} \qquad \text{Equation 5-4}$$

T is the absolute temperature in Kelvin and t is the tempering time in hours, while C is the materials constant in the range of 10 to 20, which in many applications is considered 20.

In this study, relative hardening and strengthening were calculated and are provided in Figure 5-18 and Figure 5-19.

Figure 5-18 demonstrates that H1025 and CA-H1025 are peak aged conditions. It shows that relative strengthening for the direct-aged category is lower than for the CA-aged specimens; however, the opposite behaviour is associated with the H1025 condition.

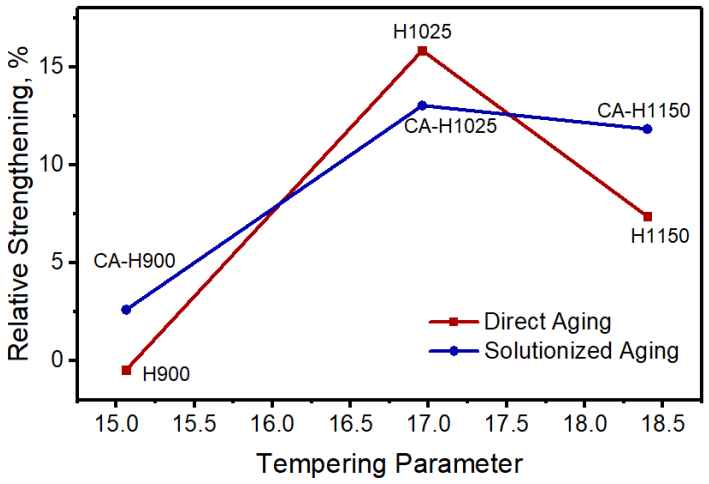

Figure 5-18 Relative strengthening of the heat-treated 17-4 PH SS

Figure 5-19 shows relative hardening improves with increasing temperature and time of ageing. It shows that relative hardening for the direct-aged category is mainly less than for CA-aged specimens; the opposite behaviour was detected for the H900 condition relative to CA-H900. Figure 5-19 denotes that peak ageing may happen in H1150 in the direct-aged category and in CA-H1150 or higher ageing temperature and duration for CA-aged specimens.

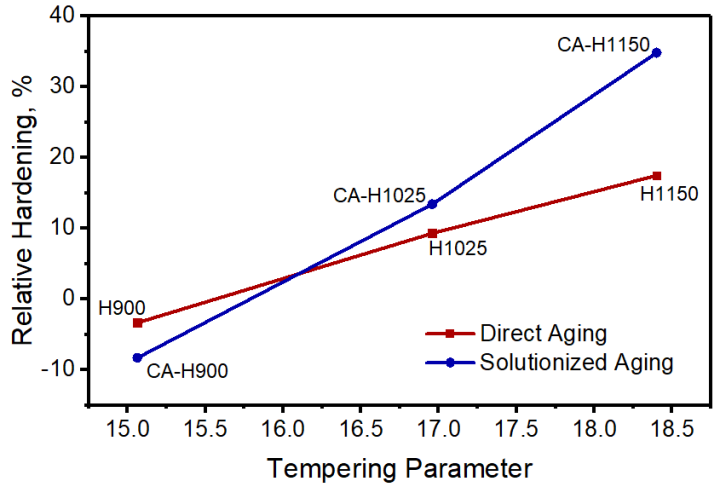

Figure 5-19 Relative hardening of the heat-treated 17-4 PHSS

Measurement of relative strengthening can help to determine the optimum condisition(s) for applications.

5.3.6 Summary

This study revealed that similar tensile behaviour of conventionally 17-4 PHSS is achievable in SLMed 17-4 PHSS by applying proper post heat treatment procedures. As an initial questioning in heat treatment effect investigation, the effect of the standard precipitation hardening treatment procedures on the SLMed 17-4 PHSS was explored. Remarkable differences in microstructural features and tensile properties were observed in standard age treated SLM parts than the conventional ones in equivalent heat treated conditions. In the conventional 17-4 PH SS, peak aged took place at 480℃. By increasing temperature and extending soaking time, $\alpha' \rightarrow \gamma$ progressed and precipitates lost the coherency led to lower strength and higher elongation to failure. However, in this study overaging at 550℃ and over it were not witnessed completely in prolonging aging treatments and substantial difference were documented. In solutionised aged category, strength lessening occurred in CA-H1150M by γ reversion and possibly precipitates coarsening.

In the following, to reduce the heat treatment procedures' time and cost, standard heat treatment procedures for precipitation hardening were reformed, and solutionising step was eliminated to see if the SLMed as-built can act as an annealing microstructure for age hardening. Entirely different microstructural features and properties were observed for the direct-aged and solutionised aged materials.

Below, the microstructural evolution of heat-treated materials was briefly summarised.

In non-heat treated SLM 17-4 PHSS, a small amount of metastable γ was retained at room temperature. The diffusion of γ stabilizers among the α' laths and mechanical stabilization of γ by hydrostatic pressure of the melt pool during the fabrication process explained it.

Employing solutionizing before age-hardening treatments refined and homogenized the microstructure. Induced dislocations in the sub-grain boundaries during SLM fabrication migrated and disappeared after solution treatment. Residual stress elimination led to progress α' transformation by rapid cooling.

By applying direct-aged and solutionised aged treatments, phase fraction evolution showed that in both categories, reverse transformation of $\alpha' \rightarrow \gamma$ were observed in the lower temperatures (480℃ and 550℃). Cu-clustering and partitioning of Ni affect the γ stability and lowered the M_s temperature locally. In the following, at higher temperatures (620℃ and 760℃), $\gamma \rightarrow \alpha'$

transformation progressed due to the elimination of residual stresses and reduced extent of segregation of the alloying elements during aging. The variation of grain size at each condition was also attributed to the reverse transformation of $\alpha' \rightarrow \gamma$ during aging at lower temperatures and/or transformation of $\gamma \rightarrow \alpha'$ at higher temperatures when γ was no longer stable during cooling.

Direct aging treatments eliminated residual stresses and showed lower KAM values than the as-built state. At lower temperatures, due to microsegregation of alloying elements such as Ni and Cu-rich precipitation formation, $\alpha' \rightarrow \gamma$ progressed, and at higher temperatures, reduction in segregation extent led to $\gamma \rightarrow \alpha'$ progression and consequently higher KAM values. Whereas, in solution aged materials, similar KAM values were reported. This could be explained by the fact that reduction of dislocation densities during solutionising had happened. It is to be noted that KAM values of solutionised part were higher than the as-built one attributed to the considerable grain refinement during recrystallization.

Due to not applying solutionising process in direct-aged conditions, precipitation hardening mechanism may not be fully activated attributed to the high solubility of Cu in the high γ%.

Subsequently, hardness and tensile properties evolution of heat-treated materials were concisely summarised.

Due to grain refinement and small γ% in solutionised condition, higher hardness was reported for the CA condition than the as-built one. The average hardness in CA-aged conditions was higher than the direct-aged ones make them suitable for the applications required higher hardness.

The average young modulus, the main elastic property in applications, of solutionised aged conditions was higher than the direct ones, 183.75±7.5 GPa and 175.25±14 GPa respectively, make CA-aged materials suitable choices for industries. Solutionised aged conditions showed remarkable grain refinement. Higher average yield strength of CA-aged ones (584.25±14.75 MPa) than direct-aged conditions (496±15.75 MPa) showed consistency with homogenized and refined grains thru solutionising. Solutionised aged showed enhanced properties in the elastic region and yield strength than the direct-aged conditions.

The direct-aged conditions showed higher strain hardening capacity than the solutionised aged ones. The as-built, H900, and H1025 indicated the TRIP effect with considerable strain

hardening after yielding before reaching UTS owed to higher metastable γ% and lower C%. Elimination of metastable γ by applying solution process produced lower strain hardening capacity in CA-ged conditions. In CA-aged, the rapid transition from nearly vertical to nearly flat was observed indicative of decreased workability and strain hardening effect.

The deformation mechanism in solutionised aged conditions under tensile loading was continuous while yield point elongation was observed for the as-built, H900, and H1025conditions in the direct-aged category. H1150 and H1150M procedures in the direct-aged category produced flow stress-strain curves such as solutionised aged parts.

The average uniform elongation was reported as 11.46% and 8.03% for direct-aged and CA-aged conditions respectively. %TEL of the CA-aged exposed lower than direct-aged ones attributed to the elimination of the metastable γ%. TEL%*UTS defined as an index to describe energy absorption capacity, reported a higher index for direct-aged parts. The best combination in UTS*TEL was related to the H900 and H1025 by having $\approx$ 25-30% enhancement in this index than the as-built one. The elimination of the metastable γ% was the main reason for the lowered index in CA-aged conditions.

Fractured surfaces of CA-aged parts demonstrated mainly brittle features than the direct-aged, which showed mostly cup and cone or 45° fracture features. Thus, a semi-ductile fracture in the direct aged category is more applicable in industries rather than having brittle fast rupture.

The enhancement of the direct-aged conditions comes from a higher work hardening capacity while CA-aged showed enhanced properties in the elastic region and yielding. Elastic properties mostly key properties in material selection for in-service products.

Based on the current study, it is promising to apply the proper heat treatment procedures for the targeted mechanical properties of the intended applications.

Chapter 6 Tribological behaviour of 17–4 PHSS fabricated by traditional manufacturing and SLM with subsequent heat treatments

The study describe in this chapter was designed to screen materials performance in different designed wear tests in order to develop proper post-process treatments for wear-resistant materials.

This chapter covers the tribological behaviour of the as-built SLM, heat-treated SLM, and wrought 17-4 PHSS parts under different designed conditions. The study consisted of three sub-studies – of (1) the effect of velocity on wear performance of the as-built SLM parts and wrought ones, (2) the effect of different applied loadings on wear behaviour of the SLM and wrought parts, and (3) the effect of heat treatment on wear performance of the as-built SLM 17-4 PHSS parts.

Rice et al. [148] wrote about wear mechanisms in metallic materials, and noted three zones defined from the contact point of the pin/ball and surface to the subsurface region. The first zone is the material's initial/base microstructure, the second region is affected by plastic deformation of the contact surface and exhibits elastic–plastic behaviour, and the third is the worn area and so-called tribolayer. Strain incompatibility due to recrystallisation of grains occurs in the plastic deformation region (second region) during the wear test. Cracks and voids are mainly observed in the second and third regions' joint surface and wear debris is produced. Note that wear condition, the nature of the material and its environment, and the material's chemical composition determine the production of debris [149].

6.1 Wear test

Figure 6-1 shows the schematic set up for the pin (ball) on disk tribometer test equipment [150]. This testing structure contains a pin (ball) pressed onto the surface of a rotating disk.

Specimen's weight before and after conducting wear test is recorded in order to calculate the specific wear rate. Specific wear rate is defined as the wear rate over the normal force:

$$w_s = \frac{\Delta m}{\rho F_N L} \qquad \text{Equation 6-1}$$

Which $\Delta m\ (kgr)$ is the mass loss of the worn specimens, $\rho\ (\frac{Kg}{m^3})$ is density, $F_N\ (N)$ is normal load, and $L\ (m)$ is sliding distance. Equation 6-1 can be rewritten as Equation 6-2:

$$w_s = \frac{\Delta m}{\rho F_N\ (2\pi r n t)} \qquad \text{Equation 6-2}$$

where $L(m)$ can be substituted by $r(m)$ as radial distance of the pin (ball) from the disk, n as the rotational speed of the tribometer, and t as the time of the wear test.

In this research, the coefficient of friction (CoF) and wear rate were characterised by a pin (ball)-on-disk method using a Nanovea tribometer, as shown in Figure 6-2. For tribology assessment, using both pin-on-disk and ball-on-disk tests, specimens were provided from grip sections of round tensile specimens. No run-in procedure was applied, so the running-in phenomenon was not considered.

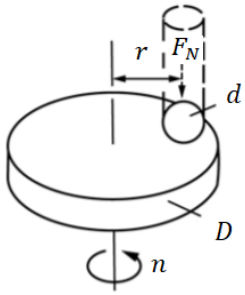

Figure 6-1 Schematic of Pin (ball) on disk [150]

The as-built SLM density and wrought specimens were measured using a pycnometer (Micromeritics AccuPyc 1340 Gas Pycnometer). Each sample was measured three times. The surface roughness of the specimens was measured by interferometry.

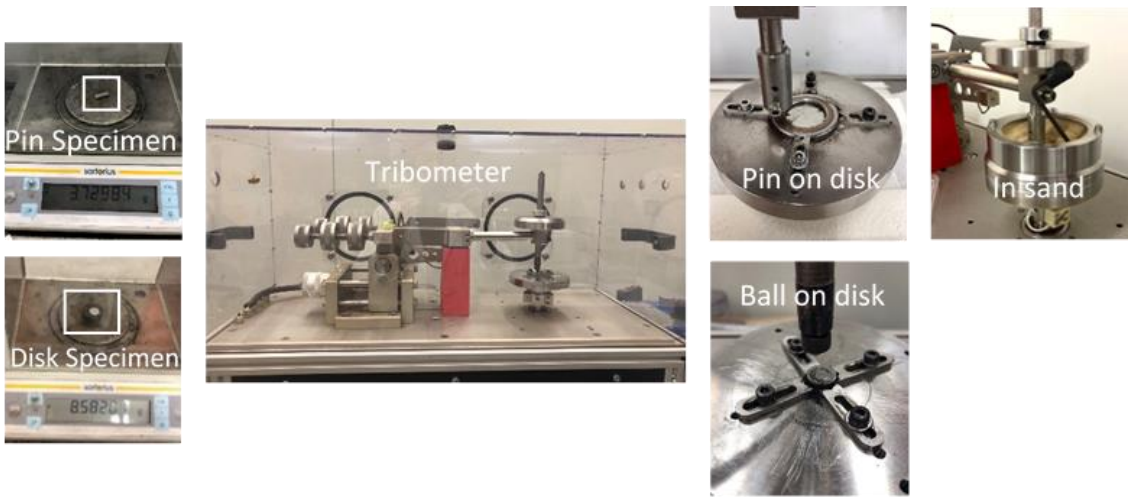

Figure 6-2 Graphical methodology of tribology testing

6.1.1 Pin-on-disk tests

For pin-on-disk tests, two sets of pins were provided, one solid and the other drilled to allow insertion of a thermocouple to track temperature changes during wear tests. All pins were cut and machined to cylinders of diameter 6.0±0.05 mm and length 5.0±0.025 mm. Holes of 2 mm diameter were drilled in half the pins. The thermocouple was glued into the holes and temperature changes were recorded during wear tests using TIM software. A thermal camera was also used to prove the thermocouple's accuracy (Figure 6-3). The pins were wear-tested to investigate the effects of three velocities at a constant load of 1 Kgf (see Table 6-1).

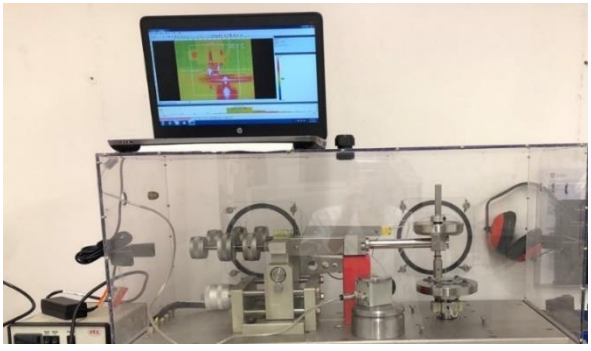

Figure 6-3 The thermal camera used to record temperature changes during wear tests

Table 6-1 Testing set-up for the effect of velocity on wear behaviour of the as-built SLM and wrought 17-4 PHSS

Force: 10 Kgf	Sliding velocity (m/s)	Revolution per minute (RPM)	Track radius (mm)	Time (min)
98.1	0.1, 0.2, 0.3	63.7, 127.3, 191	4.64 mm	120

6.1.2 Ball-on-disk

Grip sections of the round tensile specimens were cut to 5 mm long cylinders with 12.44 mm diameter. For the ball-on-disk test set-up, all cut specimens were mounted in Clarofast epoxy, ground and polished with # 320, 400, 600 and 1200-grit SiC sandpapers. After specimen preparation, the epoxy was removed, the specimen was cleaned using a sequence of acetone and then 60 s ultrasonic cleaning with methanol, and dried using a hot air blower. Balls and disks were then weighed with a resolution of 0.00001 gr to determine initial mass. After each test, the ball and disk were cleaned with acetone followed by methanol before weighing for mass. Balls made of tungsten carbide, grade 25 (WC), 4.763 mm in diameter with 70 HRC hardness, were used to apply load to the disk specimens.

The effect of load on wear behaviour was studied using three applied loads (Table 6-2).

Table 6-2 Testing set-up for load effect on wear behaviour of the as-built SLM and wrought 17-4 PHSS

Force: 10, 15, 20 Kgf	Distance (m)	Round per minute (RPM)	Track radius (mm)	Time (min)
98.1, 147.1, 196.133	349.6704	200	4.64 mm	60

Heat treatment's effect on the wear behaviour of the as-built and wrought SLM 17-4 PHSS was studied using the set-up outlined in Table 6-3.

Table 6-3 Testing set-up for heat treatment effect on wear behaviour of the as-built SLM 17-4 PHSS

Force (N): 10 Kgf	**Distance (m)**	**Round per minute (RPM)**	**Track radius (mm)**	**Time (min)**
98.1	349.6704	200	4.64 mm	60

6.2 Velocity effect

The sliding wear behaviour of the as-built SLM and wrought 17-4 PHSS at multiple sliding velocities were investigated. Three velocities (0.1, 0.2 and 0.3 $^{m}/_{s}$ at constant load – 10 Kgf – were applied for the investigation.

6.2.1 Results and discussion

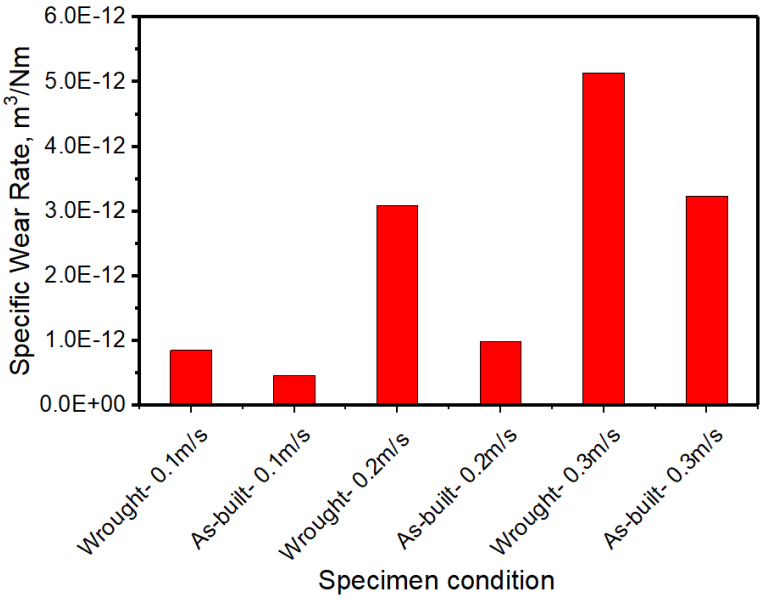

Figure 6-4 Specific wear rate of the wrought and as-built SLM in different velocities

Figure 6-4 shows that the specific wear rate (SWR) of the as-built and wrought part increased as velocity increased. Higher frequencies introduce more energy into the sliding interfaces. This energy can transfer to thermal energy, causing the material to soften and offer lower wear resistance.

For the as-built SLM PHSS, increasing linear velocity from 0.1 m/s to 0.2 m/s increased SWR from 4.62×10^{-13} $^{m^3}/_{Nm}$ to 9.89×10^{-13} $^{m^3}/_{Nm}$. Increasing velocity to 0.3 m/s resulted in an SWR of 3.23×10^{-12} $^{m^3}/_{Nm}$. Increasing velocity from 0.2 m/s to 0.3 m/s produced a larger change in SWR than increasing from 0.1 m/s to 0.2 m/s, which can be explained by greater temperature alteration and microstructural evolution. For wrought PHSS, increasing

linear velocity from 0.1 m/s to 0.2 m/s increased SWR from 8.48×10^{-13} m^3/Nm to 3.09×10^{-12} m^3/Nm. Increasing velocity to 0.3 m/s led to an SWR of 5.14×10^{-12} m^3/Nm. Similar increasing rate is reported for 0.1 m/s to 0.2 m/s as well as 0.2 m/s to 0.3 m/s. Overall, a higher SWR was measured for the wrought parts than the as-built SLM ones. During wear tests, the debris is pressed and buried into the SLM-induced defects, welded with the base material due to high contact pressure, and higher wear resistance results. Also, in similar wear test conditions, a higher fraction of γ in the as-built SLM specimen leads to a higher TRIP effect and α' transformation (and consequently, grain refinement) and thus the as-built PHSS achieved better wear resistance than wrought PHSS.

Figure 6-5 shows that the average CoF of the SLM PHSS decreased from 1.62 to 1.32 as velocity increased from 0.1 m/s to 0.2 m/s. Average CoF at 0.3 m/s was 1.2, showing that CoF decreased for the as-built PHSS. For the wrought PHSS, average CoF decreased from 0.99 to 0.95 as velocity increased from 0.1 m/s to 0.2 m/s, then increased to 1.36 at 0.3 m/s. The reduction in average CoF with increasing velocity (0.1–0.2 m/s) may be due to the smoothing of surface roughness during the test. Also, lowering averaged CoF in 0.3 m/s for the wrought, may be associated with experimental error. Overall, the average CoF of the as-built PHSS was higher than for wrought PHSS, probably due to higher surface roughness related to the layer-wise natureing of SLM products.

It is worth mentioning that the CoF trend appears constant and smooth for both the as-built SLM and wrought PHSS in dry conditions, which recommends a low wear regime.

Sliding velocity, which was applied as a variable parameter in this sub-study, also influenced the temperature of the specimens. Figure 6-6 shows average temperatures of 30.7℃ and 32.8℃ for the as-built and wrought PHSS, respectively. In general, high temperature reduces stiffness and strength, leading to softening and mass loss. Higher wear rate and mass loss were correlated to the higher temperature induced in the wrought part.

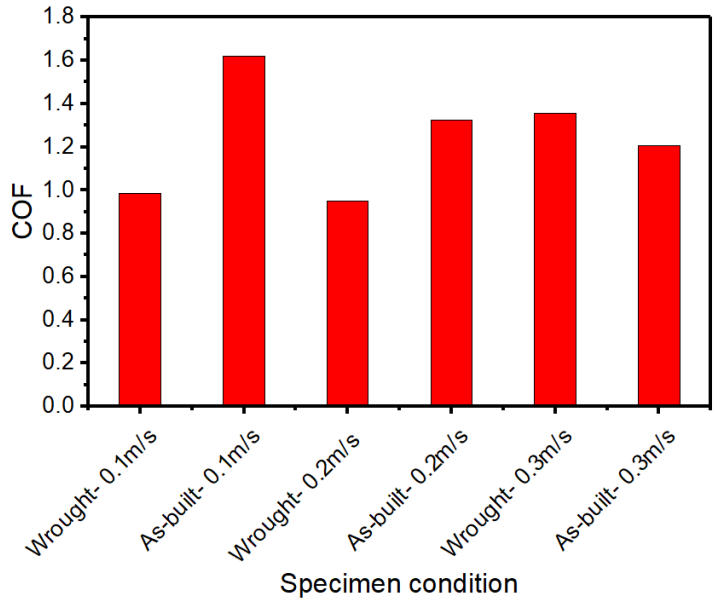

Figure 6-5 Coefficient of friction of the wrought and the as-built SLM PHSS at multiple velocities

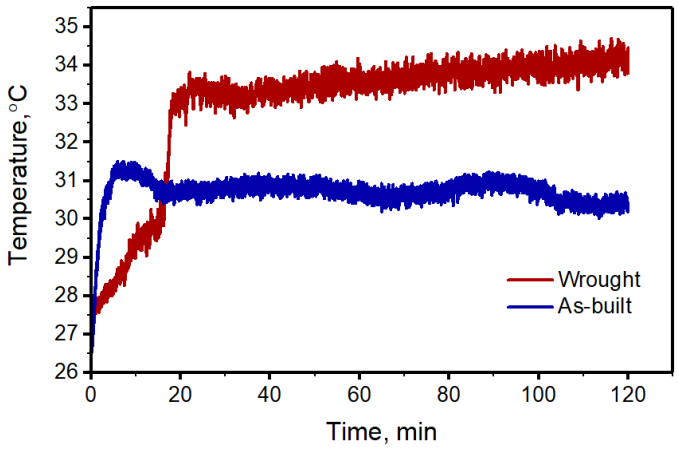

Figure 6-6 Temperature of the wrought and the as-built SLM as a function of time

Figure 6-7 depicts the worn surface of the as-built SLM PHSS at two magnifications. The worn surface is littered with debris consisting of fine flakes and coarse sheet-like particles. Deep grooves, which are an indicator of abrasive wear, can also be observed.

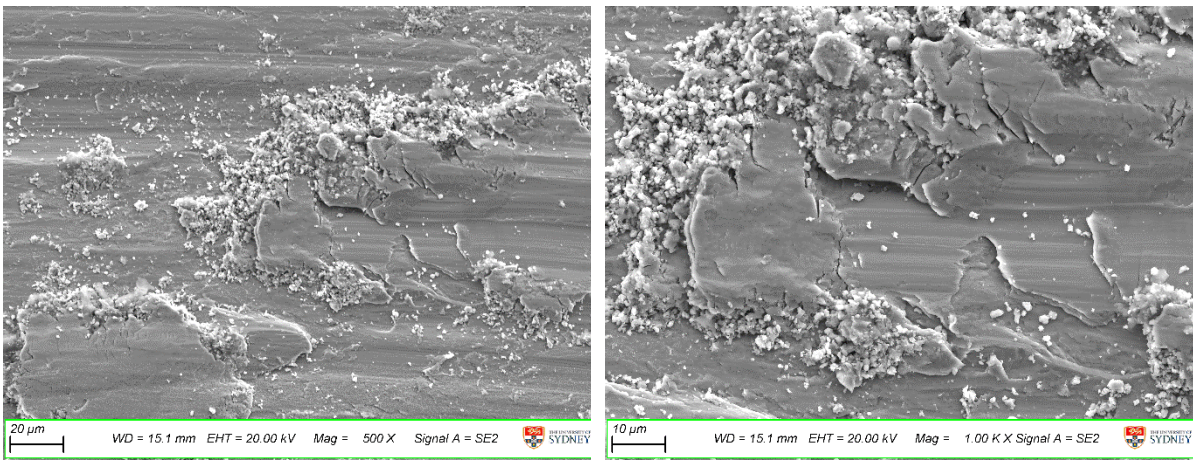

Figure 6-7 The as-built worn surface in different magnification for further investigation

Observation of the as-built and wrought pins' worn surfaces shows very different wear mechanisms operated on each (Figure 6-8). The as-built SLM PHSS experienced an abrasive–adhesive wear mechanism accompanying relatively high plastic deformation, causing in-depth plowing features and large flake-shaped delaminated chips. However, small plastic deformation with tiny scratches can be observed on the wrought PHSS. The wearing loss of the wrought PHSS was higher than for the SLM PHSS.

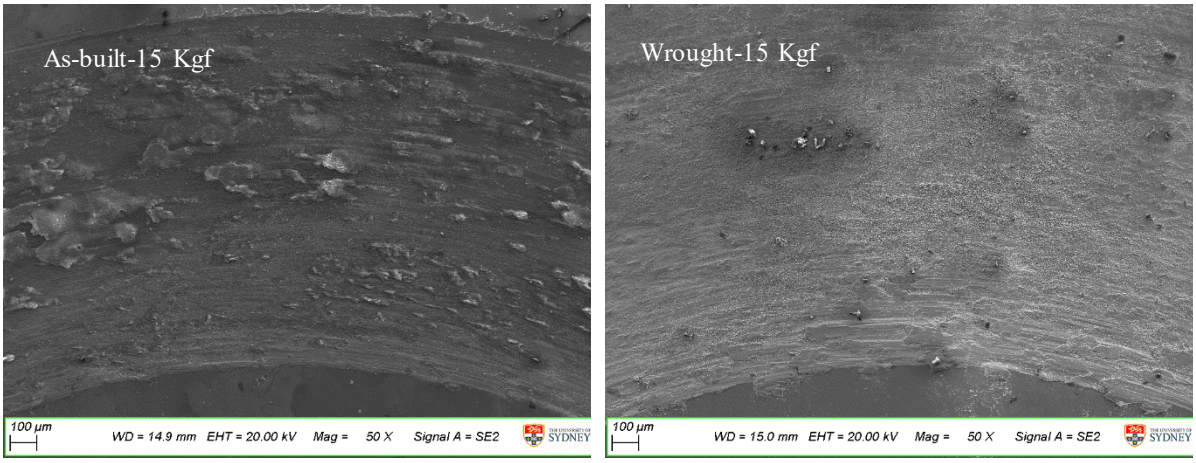

Figure 6-8 Comparison of the worn surfaces in the as-built SLM and wrought PHSS

Summary:

The effect of sliding velocity on wear performance of the as-built SLM and wrought PHSS were summarised below. Despite the lower hardness of the SLM PHSS, the wear loss of the wrought PHSS was higher. A higher fraction of metastable γ in as-built SLM progressed $\gamma \rightarrow \alpha'$. Consequently, refinement led to higher wear resistance. Also, during wear tests, debris was pressed and suppressed into the SLM-induced defects and welded with the base material due to high contact pressure, leading to higher wear resistance. On the other hand, precipitation particles in wrought PHSS reduced wear resistance by transforming a two-body abrasive mechanism to a three-body one. Worth noting wear resistance for both groups of PHSS lessened as the applied linear velocity was increased.

The average CoF of the as-built SLM PHSS was higher than that of the wrought PHSS. This might be due to higher surface roughness in the SLM PHSS attributable to the parts' layered nature. Overall, the average CoF of both groups of PHSS decreased using increasing applied linear velocity. This observation could be explained by smoothening of the surface roughness during tests. An abrasive–adhesive wear mechanism was observed for both groups of PHSS but was more severe for the as-built SLM PHSS in worn surfaces.

6.3 Environmental effects

The sliding wear behaviour of the as-built SLM and wrought 17-4 PHSS material in dry conditions and a sandy environment was investigated. The results are reported in the following.

6.3.1 Results and discussion

A sandy environment increased the SWR of the as-built and wrought PHSS. The SWR of the as-built SLM PHSS was $4.62 \times 10^{-13}\ {}^{m^3}/_{Nm}$ and $2.04 \times 10^{-11}\ {}^{m^3}/_{Nm}$ in dry and sandy conditions, respectively. For the wrought PHSS, the SWR was $8.48 \times 10^{-13}\ {}^{m^3}/_{Nm}$ and $1.29 \times 10^{-10}\ {}^{m^3}/_{Nm}$ for dry and sandy conditions, respectively (Figure 6-9).

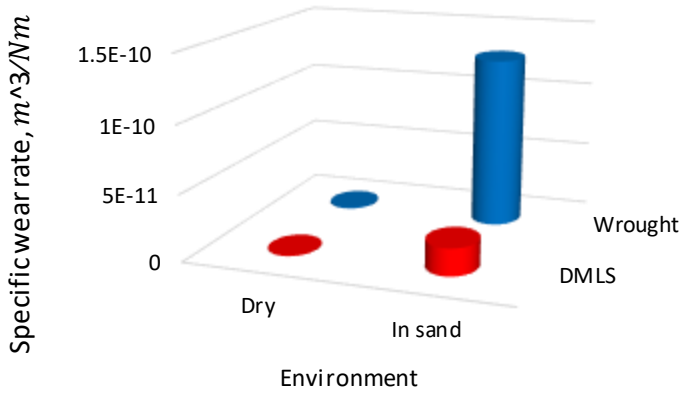

Figure 6-9 Specific wear rate of the wrought and as-built SLM PHSS in dry and sandy environments

Lower wear resistance in sandy conditions for the both as-built and wrought PHSS can be explained by a wear mechanism related to the three-body abrasive mechanism. It is genuinely severed than two-body abrasive one in a dry condition. Results show that the SWRs of the wrought PHSS in both dry and sandy environments were higher than for the as-built PHSS.

Figure 6-10 indicates that the average CoF for as-built PHSS was larger in dry than sandy conditions (1.62 vs 1.07). In contrast, the average CoF for wrought PHSS in dry conditions was 0.99, and 1.44 in sandy conditions.

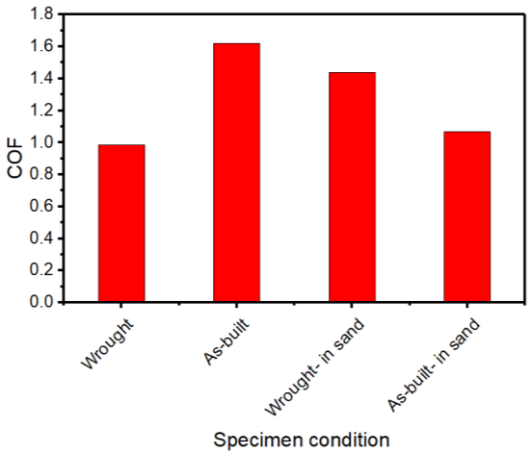

Figure 6-10 COF of the wrought and as-built SLM in dry and in sand environment

The CoF versus sliding time curves (Figure 6-11) show different patterns for the as-built and wrought PHSS specimens. The amplitude for the as-built PHSS is approximately constant over time. However, in the wrought PHSS, the amplitude increases with the wear progression in dry conditions. In the sandy environment, the CoF of the as-built PHSS shows higher amplitude at the beginning, lower amplitude in the middle of the test, and higher amplitude towards the end. The transition in wear mode can explain this pattern. In terms of the wrought in the sandy environment, the actual complex trend is reported compared. Erratic CoF patterns in the sandy condition suggest a severe wear regime.

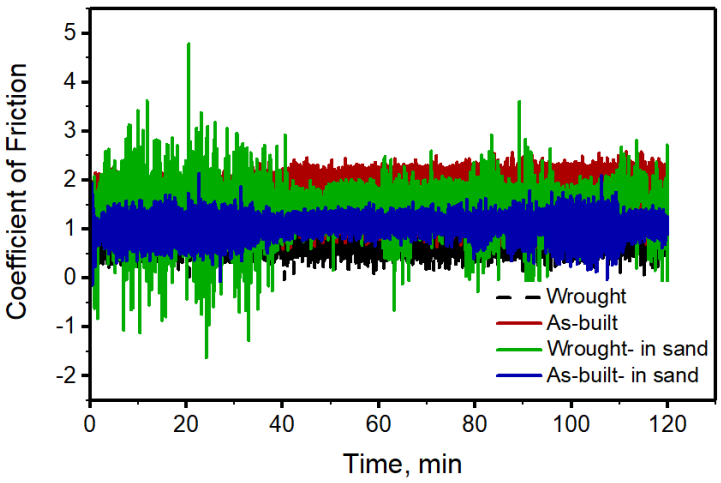

Figure 6-11 COF of the wrought and as-built PHSS as a function of time in dry and sandy environments

Summary:

The effect of different environment on wear behaviour of the as-built SLM and wrought PHSS was summaries below. The wear rate of both groups of PHSS increased in the sandy environment. The three-body abrasive mechanism was likely to be the main reason for the mass loss. The average CoF of the as-built SLM was lower than the average CoF of the wrought PHSS in sandy conditions. CoF versus sliding time curves suggested more erratic and complex wear mechanisms for the as-built and wrought PHSS in the sandy environment than in the dry environment.

6.4 Load effects

The sliding wear behaviour of the as-built SLM and wrought 17-4 PHSS materials under three loadings (10 Kgf, 15 Kgf and 20 Kgf) were investigated. The results are reported in this section.

6.4.1 Results and discussion

Figure 6-12 shows that the SWR of the as-built SLM PHSS parts under increasing loading has no defined trend. It was higher for both the 10 and 20 Kgf loads than the 15 Kgf load. In contrast, a decreasing trend was observed in the wrought PHSS. Wear resistance is increased considerably by increasing loading. It can be attributed to the progression of α' phase transformation under loading, which increases the strain hardening.

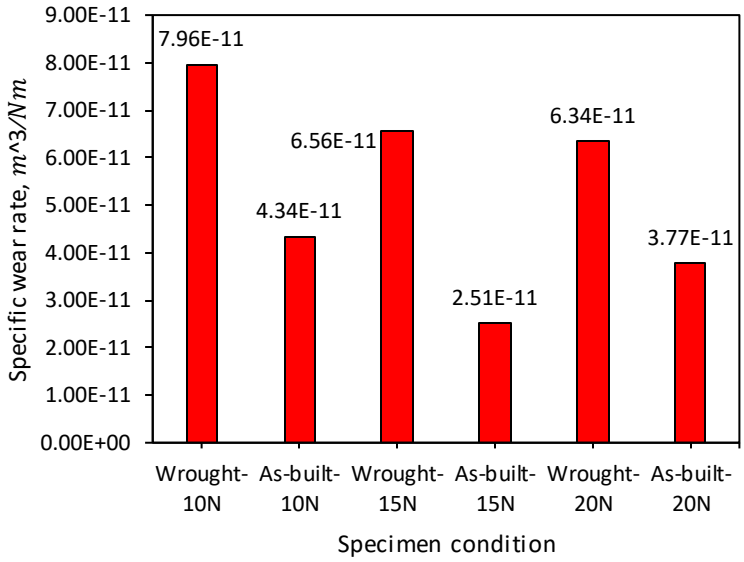

Figure 6-12 Specific wear rates of the wrought and as-built SLM PHSS under different applied loads

Overall, the SWRs of the as-built SLM PHSS parts are lower than those of the wrought parts. Despite lower hardness in the as-built SLM PHSS, higher strain hardening due to the TRIP effect improves the wear resistance. The presence of precipitates in the wrought material may be the other reason which changes the wear mechanism mode from two-body to three-body abrasive and causes higher wear resistance.

Figure 6-13 shows the average CoF of the wrought and as-built SLM materials under different applied loads. Increases in the average CoF were recorded for both groups as loads increased. Generally, the average CoF for both the as-built SLM and wrought PHSS are in the same order. And can states the normal load can influence the sliding surface roughness.

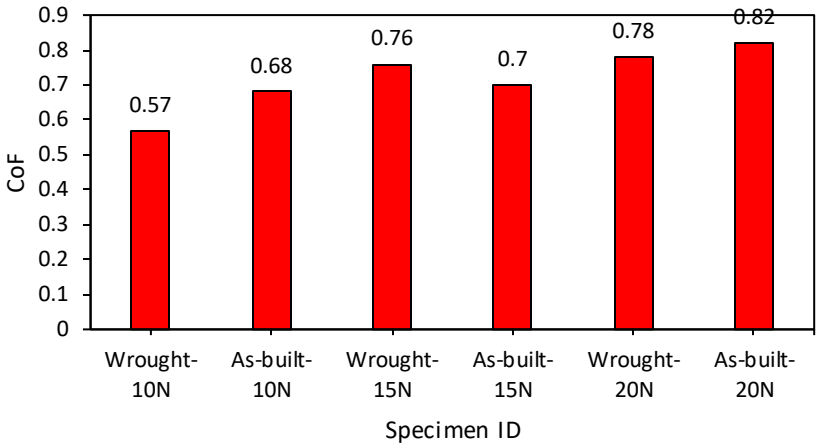

Figure 6-13 COF of the wrought and as-built SLM under different applied loads

Figure 6-14 shows the CoF of the as-built SLM and wrought PHSS under different loads as a function of time. By increasing the applied load, amplitude of the CoF decreased.

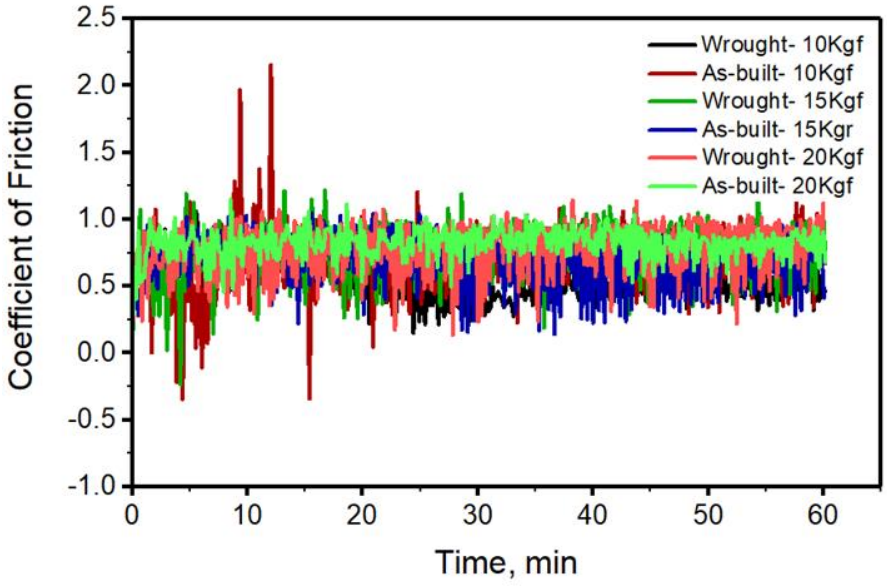

Figure 6-14 CoF of the wrought and as-built SLM PHSS as a function of time under different loads

Summary:

The effect of different applied loadings on wear behaviour of the SLM and wrought PHSS revealed that the SWRs of the as-built SLM PHSS were lower than those of the wrought ones. Despite lower hardness in the as-built SLM PHSS, higher strain hardening due to the TRIP effect improved the wear resistance. The presence of precipitates in the wrought material might be the other reason which changed the wear mechanism mode from two-body to three-body abrasive and caused lower wear resistance in wrought one. Average CoF of the as-built and the wrought PHSS increased with higher loads, suggesting increasing roughness.

6.5 Heat treatment effect

Suitable heat treatment procedures are the key to controlling or altering SLM parts' microstructure to achieve the intended performance. In the following, the wear behaviour of the standard and non-standard heat-treated SLM 17-4 PHSS is characterised.

In this study, a constant load was applied (10 Kgf) to specimens created using all targeted heat-treated conditions. This study enabled determination of the wear behaviour based on the corresponding microstructure described comprehensively in Chapter 5.

6.5.1 Results and discussion

Figure 6-15 presents the SWRs of the as-built and heat-treated SLM PHSS parts. Corresponding HVs are shown in Figure 6-16, and phase maps in Figure 6-17.

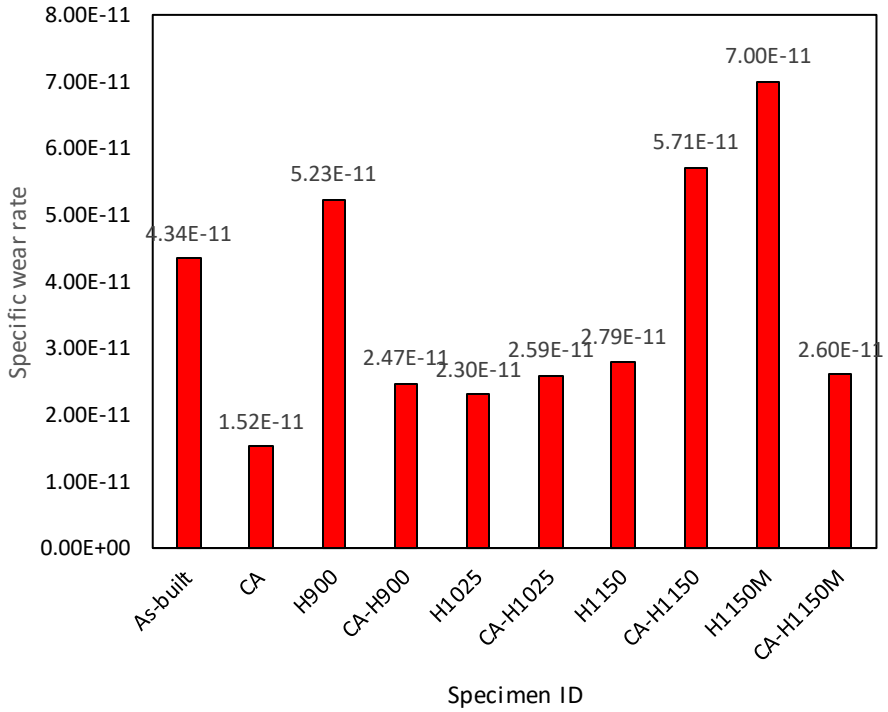

Figure 6-15 Specific wear rates of the as-built SLM and heat-treated specimens

The wear resistance of the wrought PHSS was lower than that of the as-built PHSS (refer to 6.4). This might be associated with the lower γ% and lower strain hardening capacity of the wrought than the as-built PHSS, despite the higher hardness of the wrought material.

Comparing the solutionised (CA condition) specimen and as-built SLM reveals lower SWR in the CA material (1.52×10^{-11} $m^3/_{Nm}$ and 4.34×10^{-11} $m^3/_{Nm}$ for CA and as-built respectively.) The CA's hardness (313 HV) is higher than that of the as-built (269 HV) and may result in lower wear loss. As already discussed comprehensively in 5.3.3, higher $\%\alpha'$ might be the main reason for higher hardness in the CA specimen. The results show that the CA specimen has higher wear resistance than the other conditions, attributed to the high fresh $\alpha'\%$ in the microstructure. Better wear resistance also may come from the lower extent of the inclusions.

For the solutionised aged specimens, no consistent relationship exists between the ageing processes' temperature and time. Increasing temperature from 480℃ to 550℃ reduced the SWR from 5.23×10^{-11} $m^3/_{Nm}$ to 2.3×10^{-11} $m^3/_{Nm}$. In the H900 condition corresponding to 480℃, $\gamma\%$ is high and the material experiences the α' transformation due to the TRIP effect. Due to the TRIP progression, grain refinement occurs, and the difference in grain sizes in different wear zones causes delamination. So, PHSS treated with the H900 condition was expected to have a middle level of wear resistance. High $\%\gamma$ in the H1025 (550℃) condition brings high strain hardening, leading to higher strengthening by α' transformation.

Increasing SWR was documented for the remaining conditions. A slight rise in SWR from 550℃ to 620℃ was observed (2.3×10^{-11} $m^3/_{Nm}$ to 2.79×10^{-11} $m^3/_{Nm}$). This can be attributed to the presence of high $\alpha'\%$ in the H1150 condition (direct aged at 620℃). A higher fraction of α' leads to high hardness, the most influential parameter in wear performance. Nonetheless, strain hardening was negligible in the H1150 condition.

As shown in Figure 6-15, H1150M produced the lowest wear resistance of the direct-aged conditions (SWR = 7×10^{-11} $m^3/_{Nm}$). The recrystallised microstructure might be the reason for this low wear resistance.

Among direct-aged conditions, the minimum and maximum SWR were found for H1025 and H1150M conditions. In other words, H1025 delivered the best wear resistance and H1150M was the worst condition for mass loss in this sub-study.

For the solutionised aged specimens, SWRs were similar for 480℃, 550℃ and two-step aged CA-H1150M at $2.47 \times 10^{-11}\ {}^{m^3}/_{Nm}$ and $2.59 \times 10^{-11}\ {}^{m^3}/_{Nm}$ and $2.6 \times 10^{-11}\ {}^{m^3}/_{Nm}$ respectively. However, at 620℃ a relatively large mass loss was detected (SWR = $5.71 \times 10^{-11}\ {}^{m^3}/_{Nm}$). This change in the SWR can be attributed to error in the test caused by an unstable disk. These results show that CA-H1150M delivered the lowest wear resistance among the solutionised aged materials.

CA-aged specimens had SWRs in the same order, which can be related to the presence of tempered α' in their microstructures; also, the existence of reverted γ does not help to progress the α' transformation. Precipitation-hardening particles affect wear performance. In general, CA-aged materials had lower SWR than the as-built and direct-aged materials.

In two-step ageing conditions, significantly higher wear loss was detected for direct-aged than solutionised specimens ($7 \times 10^{-11}\ {}^{m^3}/_{Nm}$ for H1150M and $2.6 \times 10^{-11}\ {}^{m^3}/_{Nm}$ for CA-H1150M).

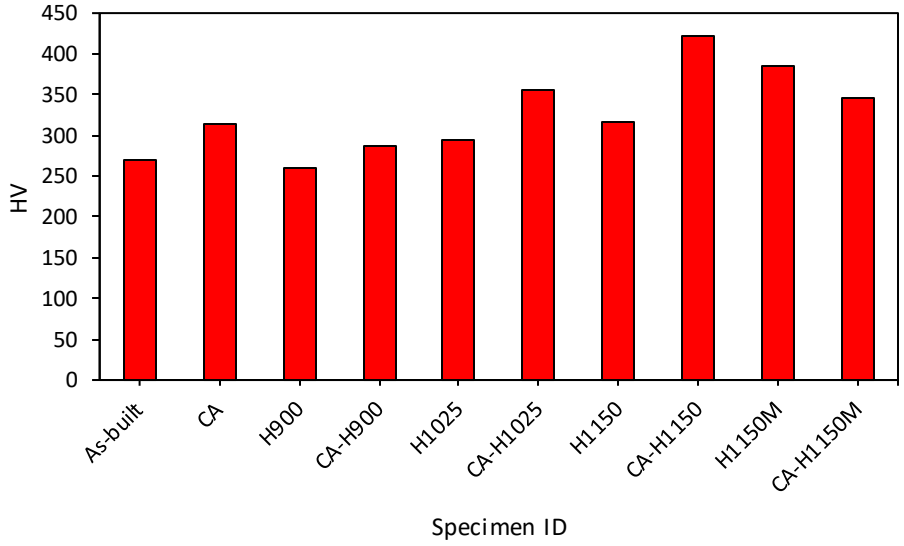

Figure 6-16 Hardness of the heat-treated 17-4 PHSS specimens

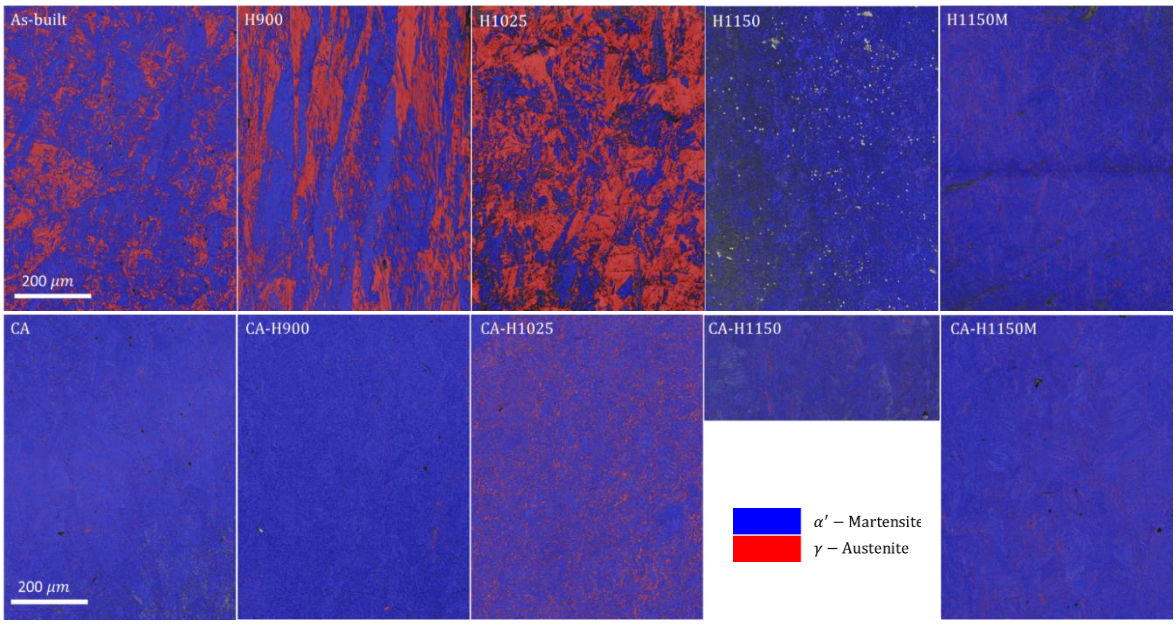

Figure 6-17 BC+Phase maps (α′ in blue, and γ in red) for the as-built SLM and heat-treated specimens

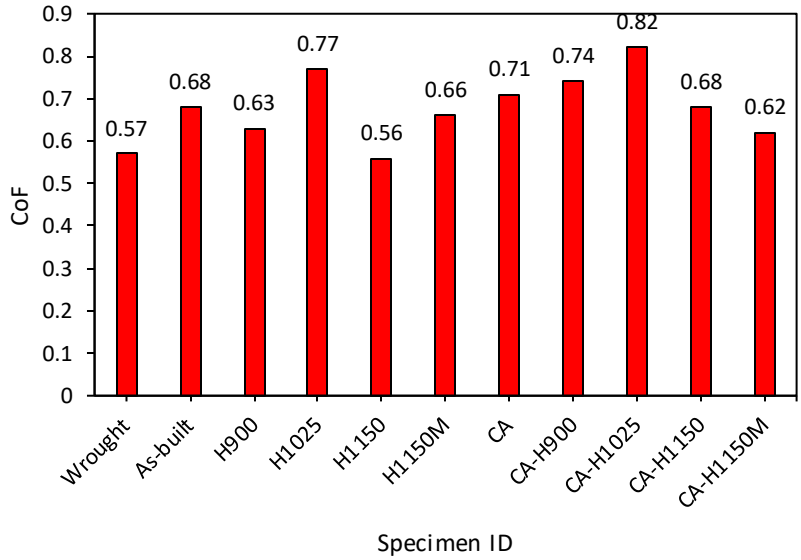

Figure 6-18 COF of the wrought, as-built SLM and heat-treated specimens

Figure 6-18 shows the effect of heat treatment on specimens' CoF. The average CoF of CA specimens is higher than that of as-built specimens (0.71 and 0.68 respectively.)

Average CoF does not follow a linear trend with increasing temperature and duration in the direct-aged parts (Figure 6-18). From 480℃ to 550℃ average CoF increased (0.63 to 0.77),

from 550℃ to 620℃ it decreased (0.77 to 0.56) and from 620℃ to the two-step aged condition increased again (0.56 to 0.66).

Solutionised aged parts mostly exhibited a decline in CoF with increasing temperature. Between 480℃ and 550℃ CoF rose from 0.74 to 0.82, but declines were observed otherwise (0.82, 0.68, and 0.62 for 550℃, 620℃ and two step aging).

Overall, average CoF was higher for the solutionised aged parts than the direct-aged parts.

Figure 6-19 displays CoF as a function of sliding time for the as-built and heat-treated materials. Note that the CoF vs sliding time curve shows the as-built material experiencing running in (wear-in). As mentioned already, conducting wear testing was problematic for CA-H1150 specimens due to the reported SWR and uneven recorded CoF as a function of time.

Worn surfaces of the as-built SLM PHSS and heat-treated materials at several magnifications are presented in Figure 6-20. Based on the mechanical properties of the heat-treated SLM parts reported in Chapter 5, the direct-aged group parts' strain hardening capacity was higher than the CA-aged group specimens. Higher average strain hardening suggests that this group of specimens was better able to resist abrasion wear. The worn surfaces of this group showed less pronounced grooves and ploughing features. However, in CA-aged materials, lower strain hardening capacity led to more brittle wearing due to their higher fractions of tempered α'. Precipitates and carbides stimulate the formation of hard wear debris particles and three-body abrasive wear, engendering more brittle behaviour. Deep grooving and more pronounced brittle wear were expected to be observed on the CA-aged materials' worn surfaces.

The worn surfaces (Figure 6-20) show that the as-built SLM PHSS specimens experienced an abrasive–adhesive wear mechanism accompanying shallow grooves and medium-sized delaminated particles. In contrast, the CA parts exhibit a substantial delaminated sheet-like and surface and subsurface cracks, which are supported by the high hardness in CA condition due to the presence of a high percentage of fresh α'.

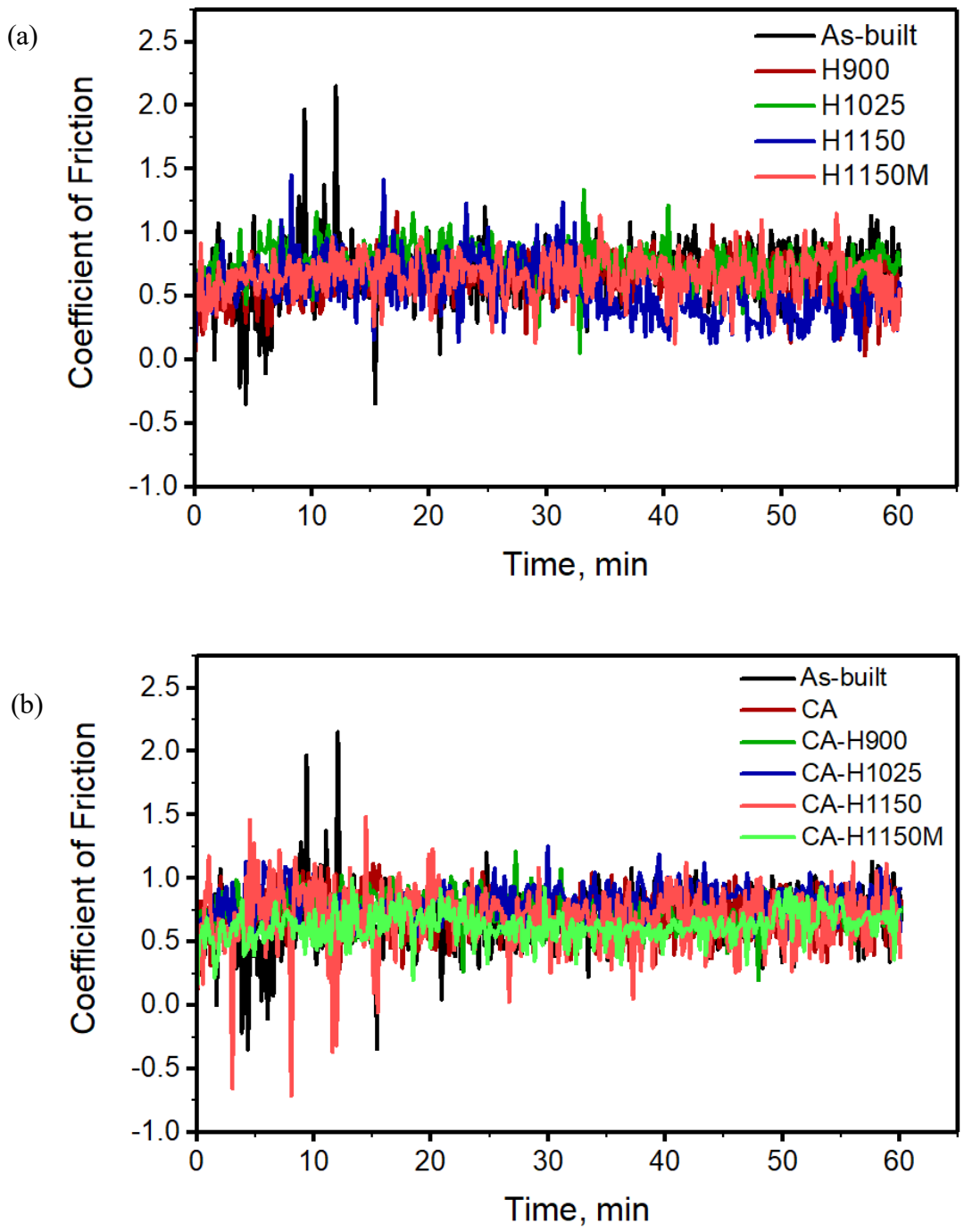

Figure 6-19 COF of (a) the as-built SLM, direct aged, and (b) solution annealed and solutionised aged specimens as a function of time

Due to higher strain hardening capacity in the H900 condition, ductile wear was observed due to the presence of tiny debris. One may observe (Figure 6-20) that the wear track is smooth and shallower for the surface of the H1025 specimen than for all other samples. This lower level of surface degradation is in good agreement with the SWR.

The specimens produced under the H1150 condition (Figure 6-20) exhibit very deep grooves on the worn surfaces due to the material's hard phase content. Two-step age condition, H1150M condition, produce a mixture of delamination and debris due to high hardness and medium strain hardening.

In the CA-aged group of materials, more brittle behaviour occurs due to lower strain hardening capacity. Similar SWRs support similar worn features in this category. A high level of tempered α' in CA-H900 led to micro-plowing and surface deformation with small debris. CA-H1025 specimens developed deep scratches and grooves as a result of their high α' and formed precipitation particles during the ageing procedure. However, the CA-H1150 worn surface is not a reliable indicator of expected wear for this category, due to a probable error in the wear test (a broadened and faded wear track supports this claim). The two-step age condition (CA-H1150M) shows a mix of coarse flakes and very tiny debris features.

Summary:

The effect of heat treatment on wear performance of the as-built SLM 17-4 PHSS parts was summarised below.

Results showed that the solutionised specimen (313 HV) showed lower wear loss than the as-built (269 HV). It also revealed the best wear resistance than the other conditions attributed to the presence of the high fresh α'% in the microstructure. Better wear resistance might also come from the lower extent of the inclusions in solutionised condition.

In direct-aged conditions, H1025 was the best wear resistance and H1150M was the worst condition in a mass loss in this sub-study. Regardless of the hardness, higher strain hardening capacity in H1025 and lower one in H1150M could be the reason for the extent of wear resistance.

Solutionised aged specimens showed similar SWR values which could be related to the presence of tempered α' dominantly with a refined homogenized microstructure. Precipitation hardening particles also had their impact on the wear performance. In general CA-aged materials indicated better SWR than the as-built and direct-aged group materials. So, it is suggested to apply the solution aged materials in industrial applications due to lower SWR as well as reproducibility.

(a)

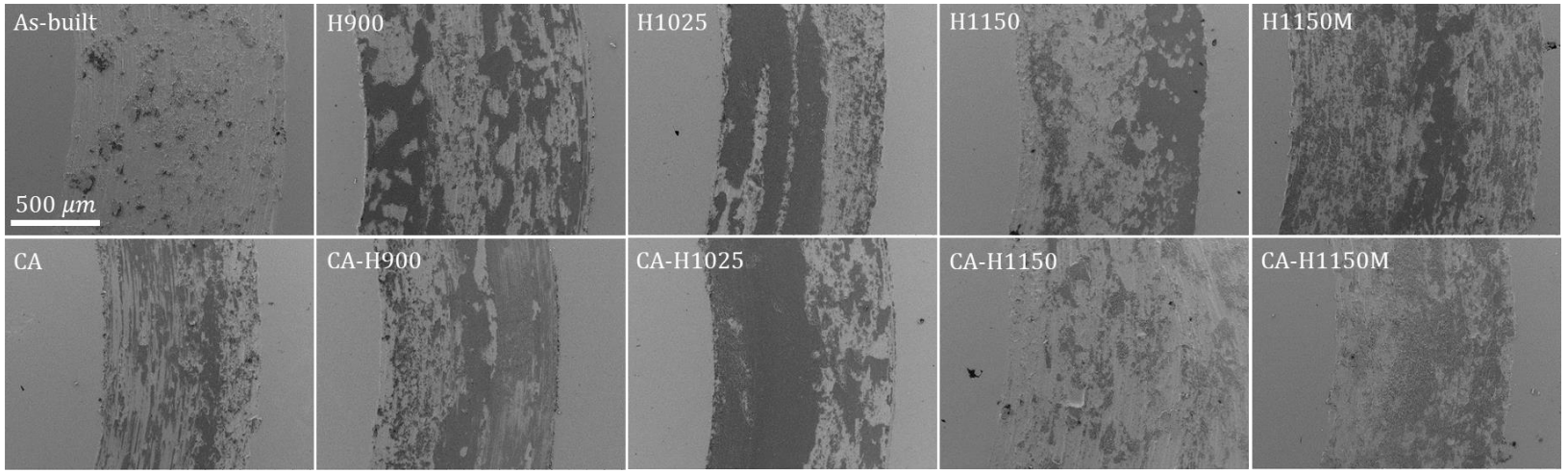
As-built
H900
H1025
H1150
H1150M
500 μm
CA
CA-H900
CA-H1025
CA-H1150
CA-H1150M

(b)

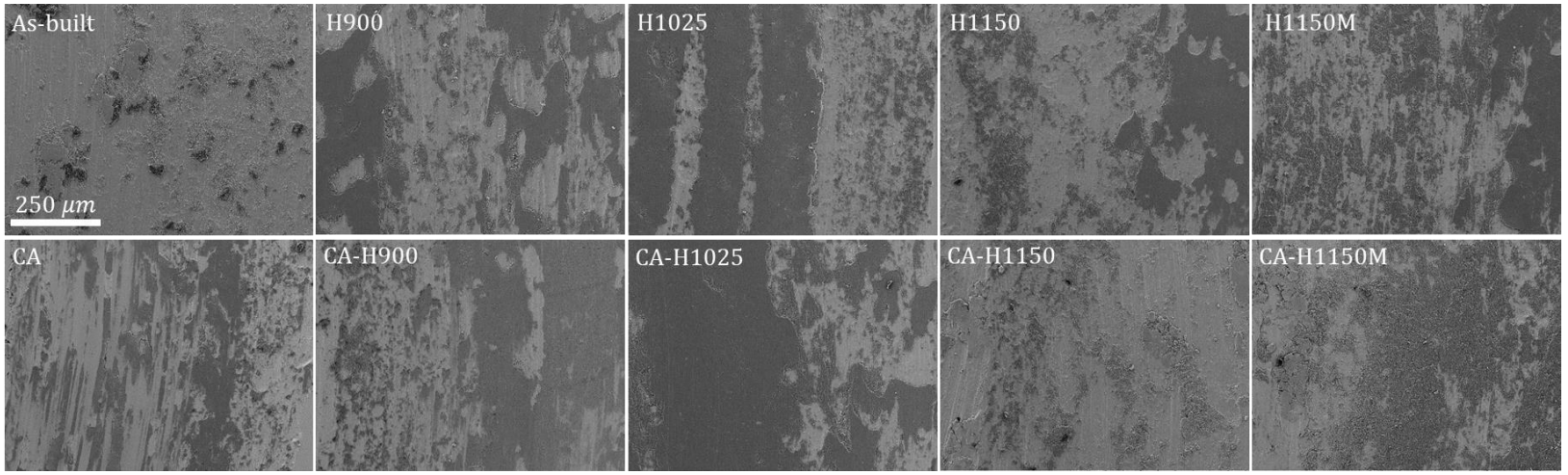
As-built
H900
H1025
H1150
H1150M
250 μm
CA
CA-H900
CA-H1025
CA-H1150
CA-H1150M

(c)

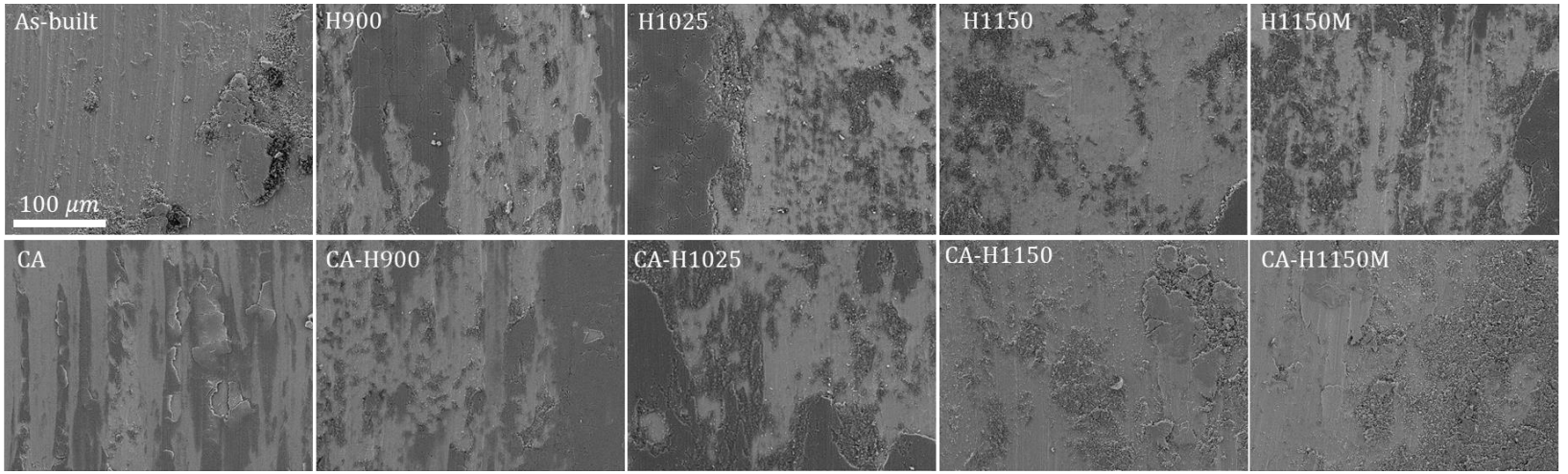

(d)

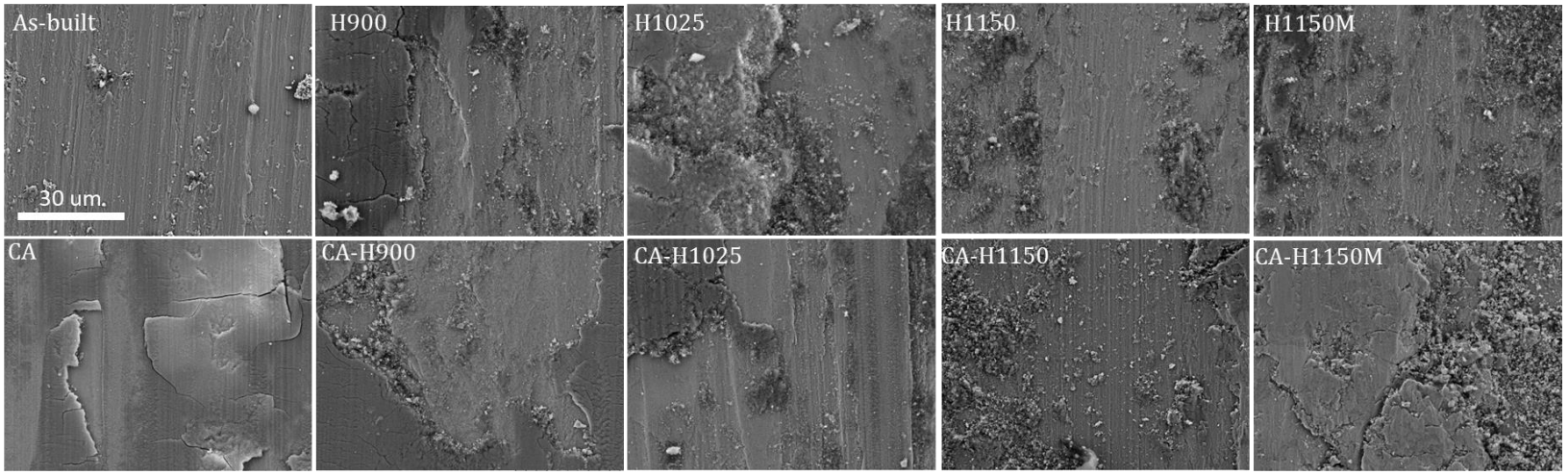

Figure 6-20 Worn surfaces of the as-built SLM, and heat-treated specimens in different magnifications for further investigation ((a)100X, (b)200X, (c)500X, (d)2KX)

Chapter 7 Microstructure and mechanical properties of SLM Ti6Al4Va alloy

The study described in this chapter involved a comparison of the SLM manufacturing method's effects on the microstructural features and mechanical properties of Ti6Al4Va and conventionally manufactured wrought Ti6Al4Va. The impact of building orientation (i.e. vertical and horizontal building) on the mechanical properties and microstructural features of Ti6Al4Va fabricated via SLM were also studied.

7.1 Experimental procedures

7.1.1 SLM-manufactured Ti6Al4Va

The feedstock material was Ti6Al4Va powder, gas-atomised in an Ar gas environment. The typical morphology of the powder, obtained using SEM, is presented in Figure 7-1. The Ti6Al4Va powder has a roughly spherical morphology. Particle size analysis indicates $D_v(50) \leq 38.7$ µm. The particle size range is (23–66 µm), with an average diameter of (39 µm). Table 7-1 shows the chemical composition of Ti6Al4Va powder, which corresponds to Grade 5 titanium alloy (UNS R56400) [151].

An EOSINTM280 Direct Metal Laser Sintering (SLM) system equipped with a maximum 400 W solid-state Yb-fibre laser was employed to fabricate specimens. The powder layer thickness was 30 µm for each melting cycle, and the scan speed was 700 (mm/s). The substrate was pre-heated to 35°C and maintained at that temperature to remove any residual moisture in the powder. Specimens were created in an Ar protective inert atmosphere to lessen oxidation during the printing process. The scanning strategy was an EOS system standard, often referred to as stripes, in which the direction of scanning is rotated by 67° between build layers (refer to

Figure 3-2 (b)). To eliminate residual stress and distortion during detaching, a support structure was applied to the parts. The following procedure was the same as 17-4 PHSS production (refer to 3.1.1). Shot peening was applied to all SLM Ti6Al4Va parts by Al_2O_3.

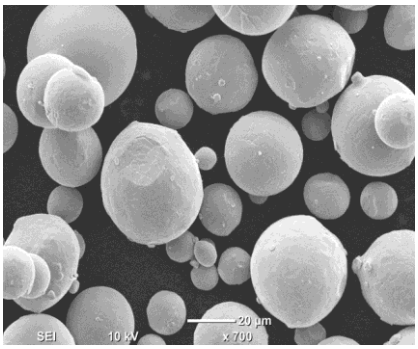

Figure 7-1 Typical morphology of Ti6Al4Va powder

Table 7-1 Chemical composition of the starting Ti6Al4Va powder, and chemical requirements for Grade 5 titanium alloy (UNS R56400) designation [79]

Alloying elements wt-%	**Ti**	**Al**	**V**	**O**	**N**	**C**	**H**	**Fe**
Provided powder	Bal	5.5-7.75	3.5-4.5	0.20	0.05	0.08	0.015	0.40
ASTM B348 Limits	Bal	5.5-6.75	3.5-4.5	max. 0.20	Max. 0.05	Max. 0.08	Max. 0.015	Max. 0.40

7.1.2 Conventionally manufactured Ti6Al4Va

Hot-rolled, forged and cold drawn bar was provided by Specialty Metals Pty Ltd.

7.1.3 Hardness test

The effect of the SLM process on the hardness of Ti6Al4Va specimens was studied. To assess hardness variation with respect to built orientation, specimens were prepared in both horizontal and vertical orientations. Cross-sectional specimens were taken from horizontally built Ti6Al4Va and longitudinal specimens from vertically built Ti6Al4Va and progressively

polished to reach a mirror-like surface finish before micro-hardness testing. Techniques similar to those employed for 17-4 PHSS (refer to 3.1.3) were applied to measure and report HVs.

7.1.4 Tensile test

Round specimens were designed and fabricated according to ASTM E466-15, as displayed in Figure 7-2 (a). Specimens were fabricated vertically and horizontally. Due to the high residual stresses during the SLM fabrication of Ti6Al4Va (discussed in 2.6.1), horizontal specimens shown in Figure 7-2 (b) were distorted during the first two fabrication runs. By applying a denser support structure, the high induced residual stress issue was fixed, and fabrication was completed in a third run.

Figure 7-2 (a) Vertical and horizontal SLM and wrought Ti6Al4Va and (b) distorted SLM horizontal specimens

Note that the third batch of horizontal SLM Ti6Al4Va specimens was warped. To straighten them, the specimens were machined, as shown in Figure 7-3.

Figure 7-3 Machined buckled horizontal SLM Ti6Al4Va tensile specimens

7.1.5 Wear test

To investigate the effect of built orientation on the wear behaviour of SLM Ti6Al4Va parts, two loads were applied to horizontal and vertical SLM Ti6Al4Va and wrought Ti6Al4Va. Details of the testing set-up are provided in Table 7-2.

Table 7-2 Testing set-up for load effect on wear behaviour of the horizontal and vertical SLM and wrought Ti6Al4Va

Force: 10, 15 Kgf	Distance (m)	Revelotions per minute (rpm)	Track radius (mm)	Time (min)
98.1, 147.1	349.7	200	4.64	60

7.1.6 Microscopy

Microstructure variations related to the horizontal or vertical built orientation of the as-built SLM Ti6Al4Va were investigated by sample preparation in multiple planes and orientations (refer to Chapter 7).

Selective laser melted tensile coupons were cut from several locations from horizontally and vertically built specimens. they were mounted, ground and polished mechanically using # 320, 1200 and 4000-grit SiC sandpapers followed by colloidal silica suspension. Depending on the acquired indexing level, electropolishing was also applied to some specimens using 10% perchloric acid ($HClO_4$) in methanol (CH_3OH) at 50 V for 90 s.

An X-ray diffractometer (XRD Shimadzu S6000) was used (rather than the EBSD analysis applied in some studies) to determine the phases present. XRD spectral analysis was performed on powder particles and as-built SLM and wrought specimens in cross-sections. Specimens were cut from the grip section of round tensile specimens and the setting reported as X-ray tube with Cu target in 40 V voltage, and 30 mA current.

7.2 Results and discussion

The results of the microstructural investigation conducted on the as-built SLM Ti6Al4Va in both built orientations and wrought Ti6Al4Va are presented below. Their mechanical properties were characterised by hardness, tensile and wear tests.

7.2.1 Microstructure features

Scan speed, powder particle size, and layer thickness are parameters that dictate surface roughness. The finishes of 1 mm*1 mm areas of the samples' surfaces were measured using a Bruker Contour Elite-K 3D microscope. Figure 7-4 shows that surface conditions vary markedly across the specimens. The average roughness of the vertically built SLM Ti6Al4Va is 18.473 μm, while the average surface roughness of the horizontally built specimens is 14.731 μm). The vertically built Ti6Al4Va has a highly textured surface with small beads, but its surface roughness is larger than that of the horizontally built specimens – a result that was unexpected given their appearances. The horizontally built specimens show large beads stuck to the surface, and have approximately 20% lower roughness than the vertical specimens.

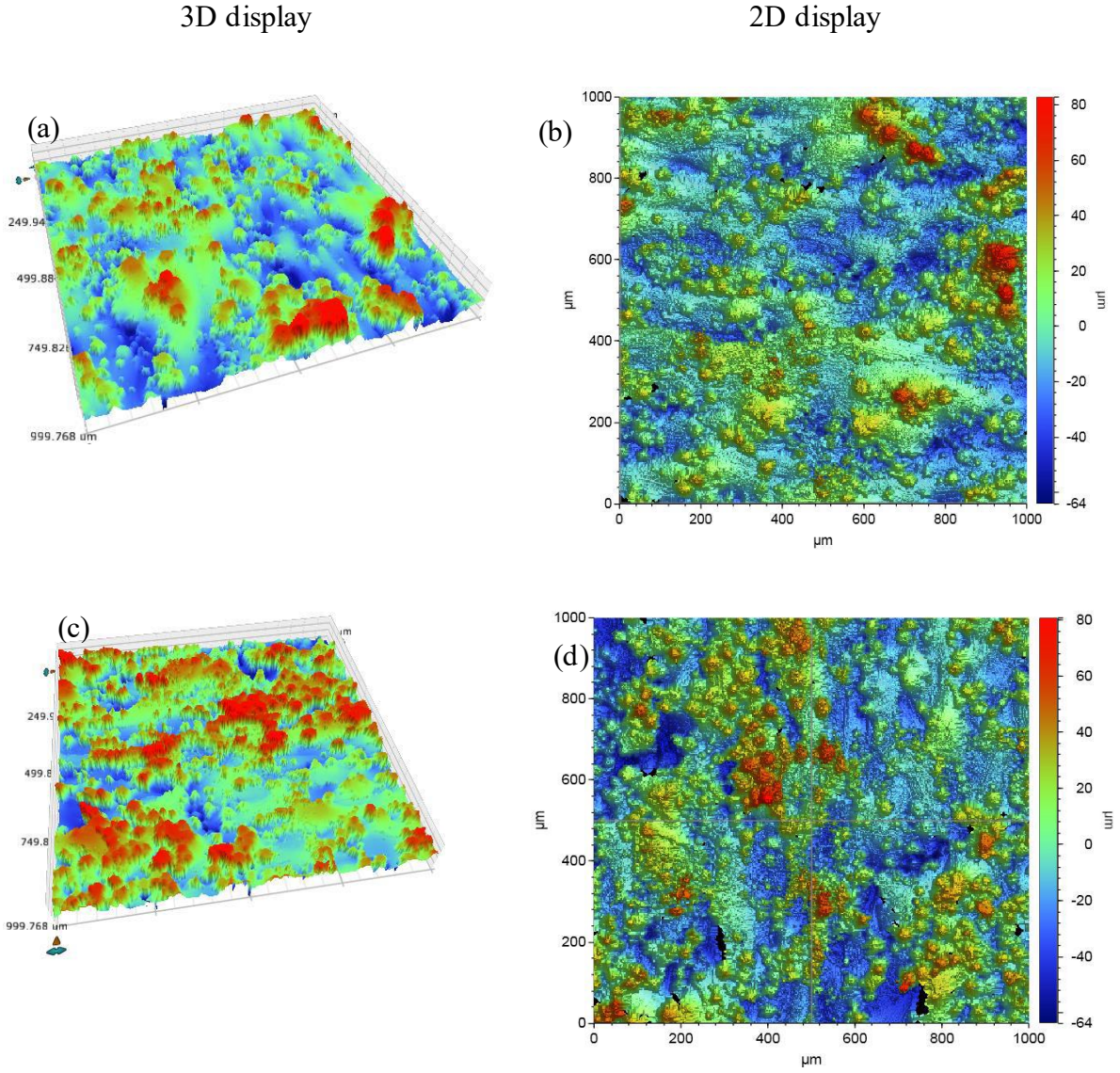

Figure 7-4 Surface finishes of (a,b) horizontally built SLM Ti6Al4Va, and (c,d) vertically built specimens

X-ray diffraction studies of the feedstock powder, the horizontal and vertical SLM specimens, and wrought specimens were performed on the cross-sections (Figure 7-5). The volume fraction of the phases is a function of the material type, applied processing parameters, and treatment parameters.

In XRD analysis, the feedstock powder produced peaks of α and β phases with a strong (110) β reflection. XRD confirmed the presence of both α and α' in both the vertical and horizontal specimens. However, the peak intensities of α' in vertical specimens explains their higher α' than in the horizontal specimens. Conversely, the higher α peak intensity of the horizontally

built specimens confirms the existence of a higher α amount rather than α'. The wrought specimen has α and β phases.

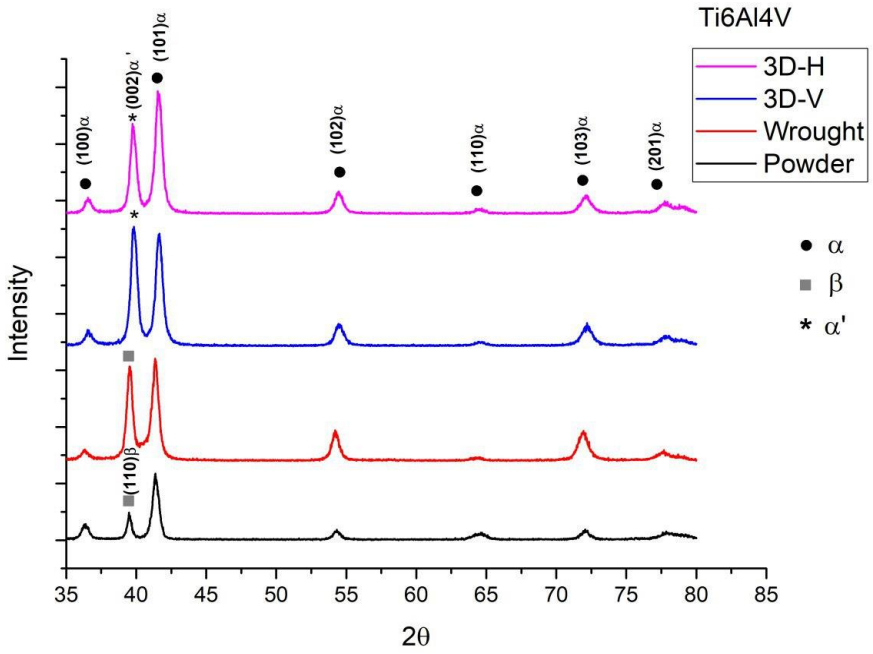

Figure 7-5 XRD patterns of Ti6Al4Va as pre-alloyed powder, wrought, horizontal and vertical SLM specimens

Optical microscopy was used to study the SLM-induced defects in the specimens. Note that the wrought specimens used for comparison were free from flaws due to their high-quality production.

The relationship between the aspect ratio of the part and the building orientation affects its SLM-induced thermal history during fabrication. In the case of the vertical round tensile coupons, vertically built specimens have a higher building aspect ratio than the horizontally built specimens. Ultimately, the aspect ratio affects the microstructure via induced defects, final grain sizes, and phase fractions.

The aspect ratio and consequently, the height of the sample, can generate different types of defects. The laser penetration depth, and therefore the size of the heat-affected zone, dictate the degree of remelting of the previous layer. Vertically built SLM Ti6Al4Va with a few tiny pores shows full penetration in subsequent layers. Those fine spherical pores are likely to originate

from gas entrapment during fabrication (refer to 2.6.3). Vertical SLM specimens have a higher density than horizontal SLM and wrought specimens, as Figure 7-6 confirms.

Distortion and loss of geometric tolerance occurred in horizontally built SLM parts during fabrication. The horizontally built SLM parts contain significant defects, including pores, unmelted and partially melted particles, and lack of fusion in regions with different morphologies including spherical, irregular and slit-shaped defects. Variation in defects is due to different thermal histories in different parts' locations. At the bottom of the cross-section of the horizontally built specimen there was conduction between the part and substrate, and there was convection and radiation at the top. As shown in Figure 7-6, the bottom and top of the cross-sectional plane of the horizontally built specimen contain many more flaws than the middle region due to higher thermal transfer.

Wrought

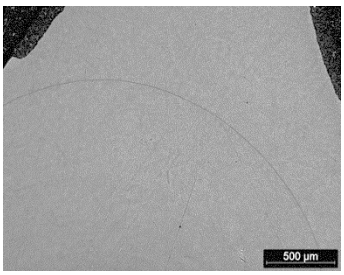

Horizontal SLM – in BD direction

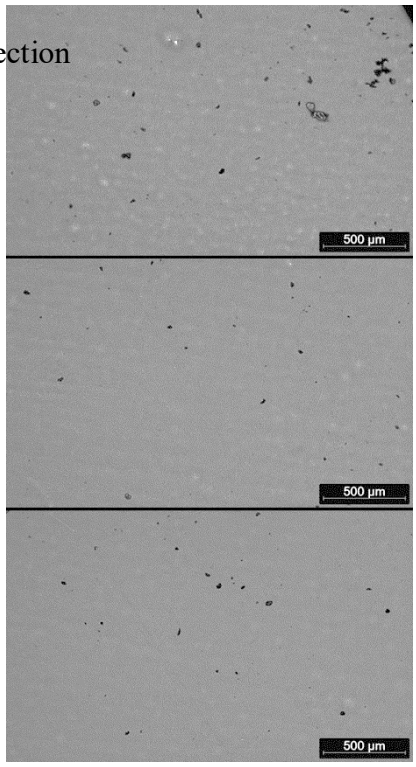

Vertical SLM – in perpendicular BD

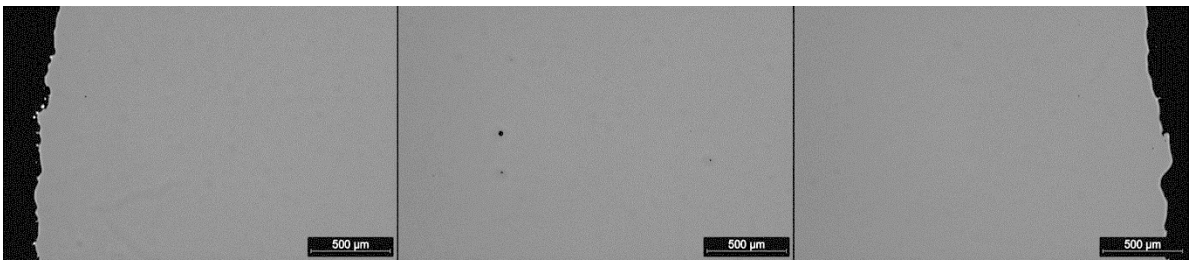

Figure 7-6 Optical images of the wrought and horizontally and vertically built SLM Ti6Al4Va specimens

A basket weave microstructure was revealed in the wrought specimen using microstructural examination (Figure 7-7 (a)). The microstructure of the vertical SLM parts is presented in Figure 7-7 (b). Typically, for Ti6Al4Va, β phase transforms to α from 875°C to room temperature, while β transforms to a diffusionless acicular α' microstructure due to a higher cooling rate (in a non-equilibrium condition) during the SLM process. Columnar grains with α' laths originate from blocky prior β grain boundaries formed upon solidification. The direction of columnar grains is along the build direction, which parallels the direction of heat flow. It is worth mentioning that the SLM process does not produce equiaxed grains during the fabrication of Ti6Al4Va [90].

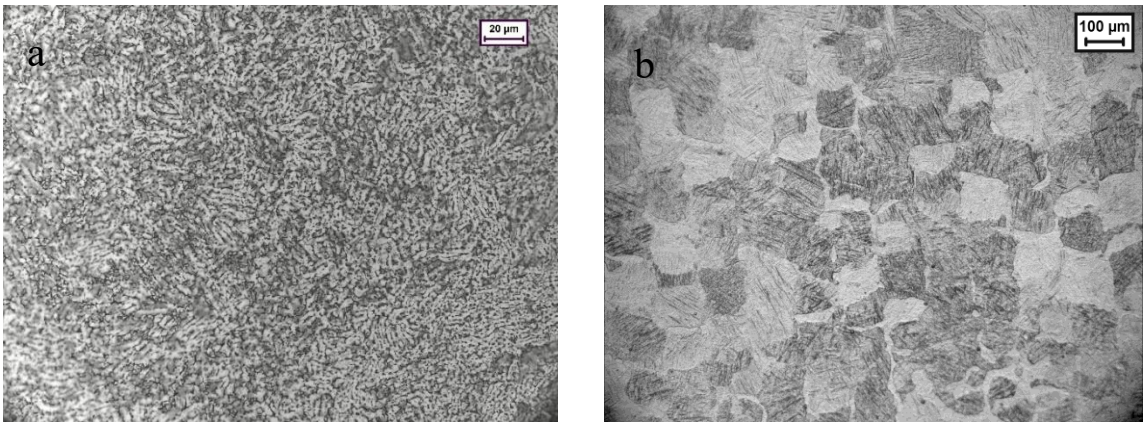

Figure 7-7 Optical microscopy images of (a) wrought Ti6Al4Va, and (b) vertical SLM Ti6Al4Va in perpendicular to built orientation

A single layer's temperature is mapped in Figure 7-8, showing that this layer experienced two liquid-solid transformations and two $\alpha - \beta$ ones. These profiles are dependent upon the SLM manufacturing parameters discussed earlier (see 2.1) [21].

The cooling rate of the tiny melt pools in SLM Ti6Al4Va was measured as 10^3 to $10^5\,{}^{\circ\mathrm{C}}/_{s}$ while α' transformation occurs at $410^{\circ\mathrm{C}}/_{s}$ in Ti6Al4Va [152]. So, SLM processing of Ti6Al4Va results in a complete α' microstructure. Acicular α' resulting from rapid cooling is primarily responsible for the high strength but inadequate tensile ductility achieved in the as-built state. Those properties compare favourably with those of wrought Ti6Al4Va consisting of globular α' and β. Note that even the smallest changes in cooling rates can have large effects on the microstructures of Ti6Al4Va.

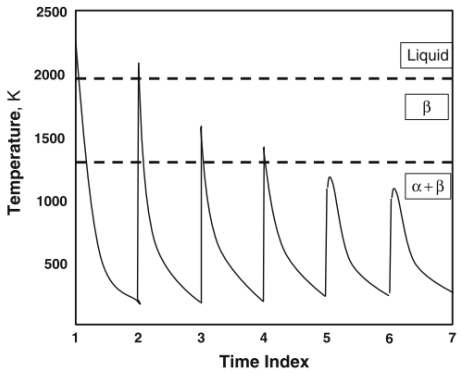

Figure 7-8 Notional thermal profile of a single layer of Ti6Al4Va during the AM process [21]

Electron backscatter diffraction maps were used to identify and quantify the phases, microstructure (e.g. grain size distribution, average grain size, morphology and orientation), grain boundaries type and distribution, and strain distribution in phases. In this section, the microstructural features of the wrought and SLM Ti6Al4Va are described via EBSD maps. Figure 7-9 indicates the targeted locations of the specimens. They are used as the references for the EBSD maps provided below.

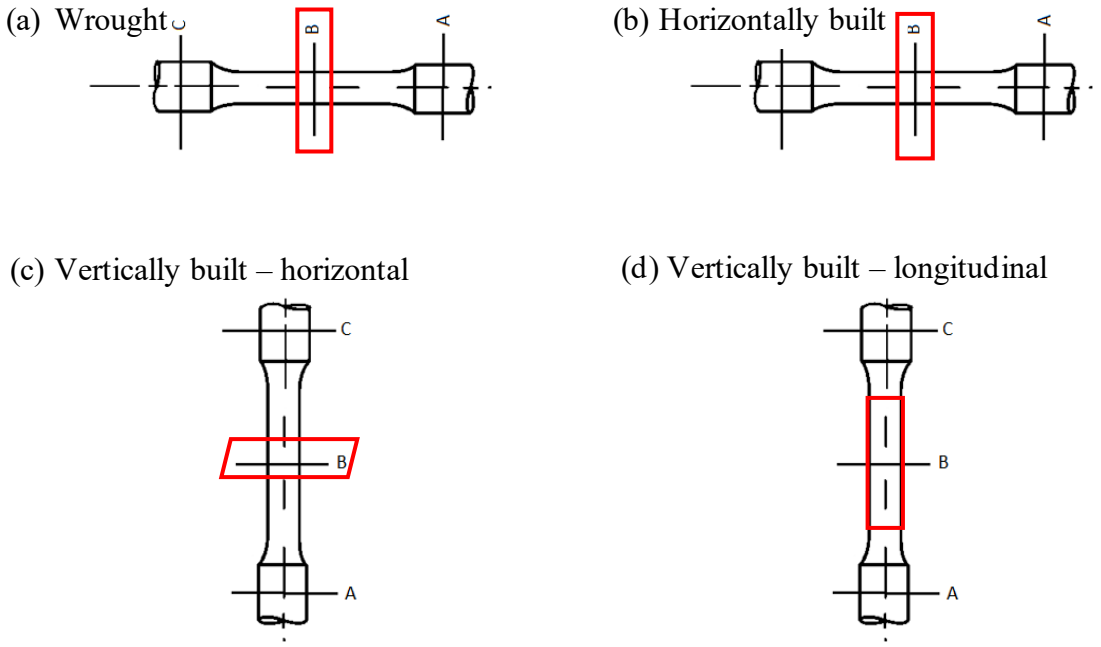

Figure 7-9 Designed regions of (a) the wrought, (b)as-built horizontal SLM, (c) as-built vertical SLM perpendicular to built direction, and (d) as-built vertical SLM parallel to the built direction

Phase maps of the specimens are presented in Figure 7-10. A dual-phase mixture of $\alpha'$and β was revealed by microstructural examination of all specimens. Phase fractions in the wrought, SLM horizontal and vertical specimens based on Figure 7-9 designations are shown in Table 7-3.

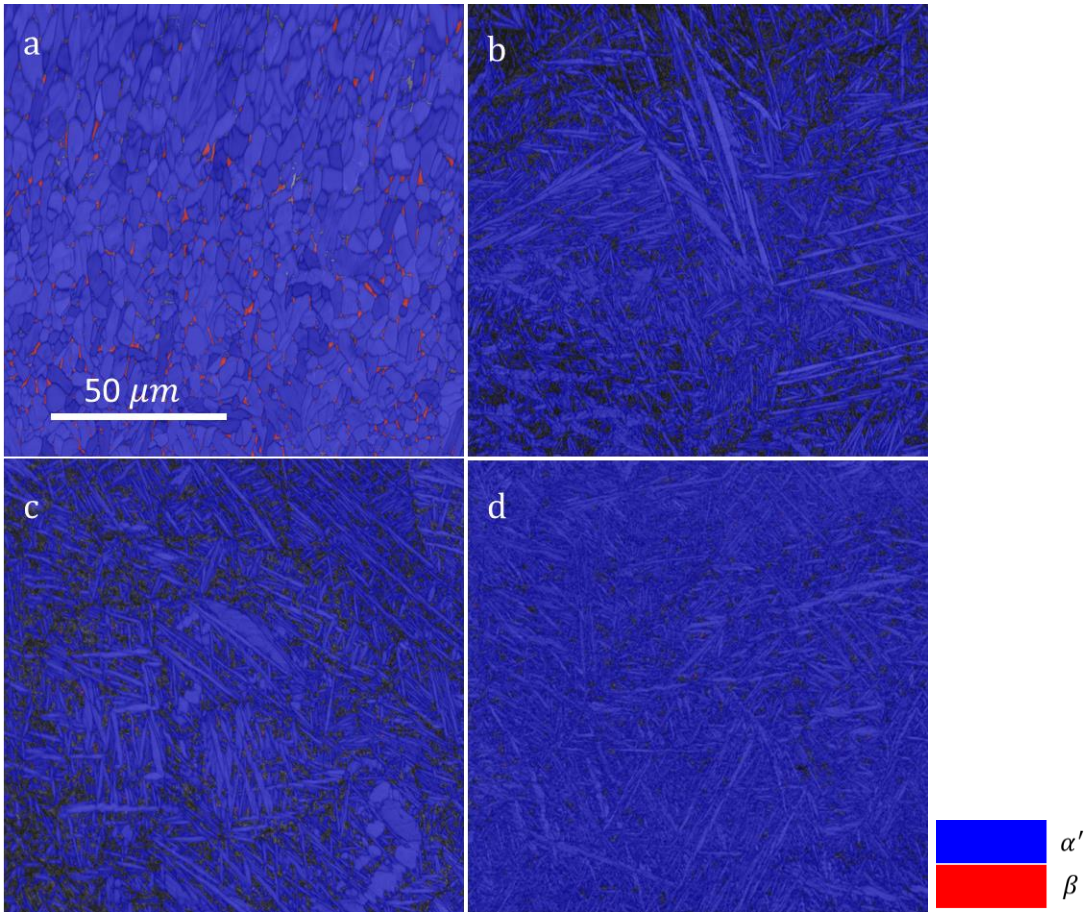

Figure 7-10 BC+Phase maps of (a) the wrought, (b)as-built horizontal SLM, (c) as-built vertical SLM perpendicular to built direction, and (d) as-built vertical SLM parallel to the built direction

Overall, wrought specimens have a higher fraction of β than the SLM parts. The phase map superimposed on the IQ image (Figure 7-10) is evidence of this claim. For the wrought specimen, the β phase is shown in red; it is formed alongside prior β grain boundaries in relatively equiaxed/blocky shapes. Horizontally and vertically built specimens both have needle-shaped acicular, α' colonised in blocky prior β boundaries. The phase maps expose the distribution of α' and β phases, consisting of a dominant α' and slight β in SLM specimens. Horizontally built parts have higher α' phase than vertically built ones.

Table 7-3 Phase fraction of α′ and β in the wrought, horizontal and vertical SLM Ti6Al4Va

Specimen ID	Zero solution, %	β (%)	α' (%)
Wrought	1.8	1.76	96.4
Horizontal as-built	23	0.02	77
Vertical as-built-Cross sectional	21	0.1	78.9
Vertical as-built-Longitudinal	3.9	0.02	96.1

IPF-Z maps superimposed on the IQ images of the specimens are provided in Figure 7-11. Average grain sizes of α' and β in the wrought, SLM horizontal and vertical specimens based on Figure 7-9 designations are shown in Table 7-4.

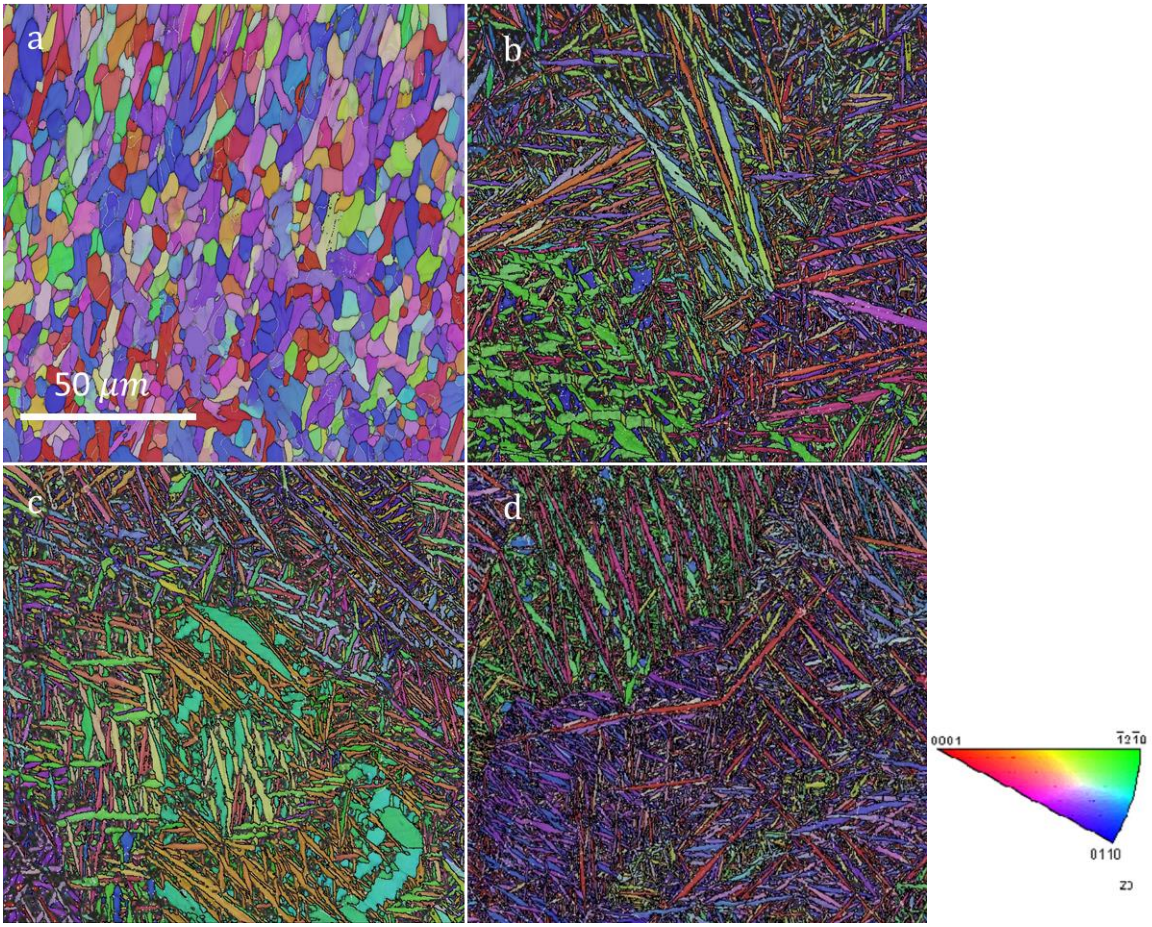

Figure 7-11 BC+IPF-Z with LAGBs and HAGBs, for α'

As shown in IPF-Z maps, grain morphology in the build direction of the horizontal and vertical SLM parts is columnar, while an equiaxed microstructure exists in the wrought part. Finer acicular α' microstructure was detected for the vertically built specimen.

In Table 7-4, the larger grain size of both phases (~3.49 µm and 0.68 µm for α' and β respectively) is shown for the wrought specimen. Based on measured grain size, the β phase is of the same size ($\sim 0.465\ \mu m$) for the horizontal and vertical built specimens in building direction; however, β phase percentages are negligible. The vertical specimen has slightly finer α' grains, at 1.14 µm and 0.97 µm for the horizontally and vertically built specimens.

Table 7-4 Grain size of β and α′ of the wrought, horizontal and vertical SLM Ti6Al4Va

Specimen ID	Average grain size of β (μm)	Average grain size of α′ (μm)
Wrought	0.68	3.49
Horizontal as-built	0.47	1.14
Vertical as-built-Cross-sectional	0.49	1.17
Vertical as-built-Longitudinal	0.46	0.97

Grain boundary maps are shown in Figure 7-12. The number fractions of grain boundaries in the wrought and horizontal and vertical SLM specimens, based on designations in Figure 7-9, are tabulated in Table 7-5.

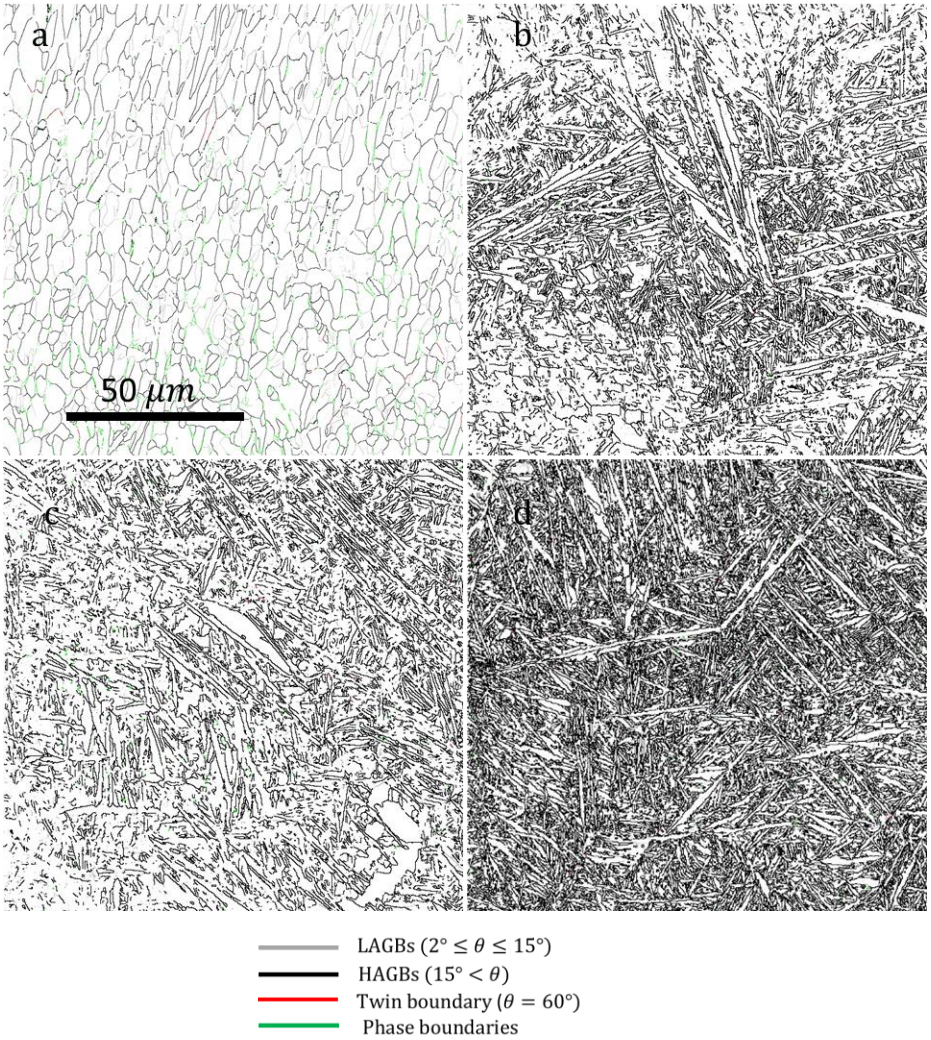

Figure 7-12 Grain boundaries, including LAGBs (silver), HAGBs (black), Interface Bs (green), Twin Bs (red)

They reveal a similar morphology in the SLM parts regardless of the orientation. The grain boundary characterisation charts show a higher density of LAGBs in the wrought specimens than the SLM specimens. The density of the LAGBs for the SLM specimens are entirely in a similar range. A low density of HAGBs was found in the wrought specimens compared to the SLM specimens. The HAGB% in the built direction of the vertical SLM parts is higher than that in the horizontal SLM parts.

Table 7-5 LAGB%, HAGB% of β and α′

Specimen ID	β		α'	
	LAGB%	HAGB%	LAGB%	HAGB%
Wrought	14.41	5.75	17.43	49.91
Horizontal as-built	7.69	0	6.59	57.51
Vertical as-built-Cross-sectional	24.51	1.96	6.47	58.01
Vertical as-built-Longitudinal	25.32	0	6.22	69.87

Kernel average misorientation maps of the specimens are shown in Figure 7-13, along with a colour key. They show that vertical SLM specimens have the maximum values of KAM value than other parts.

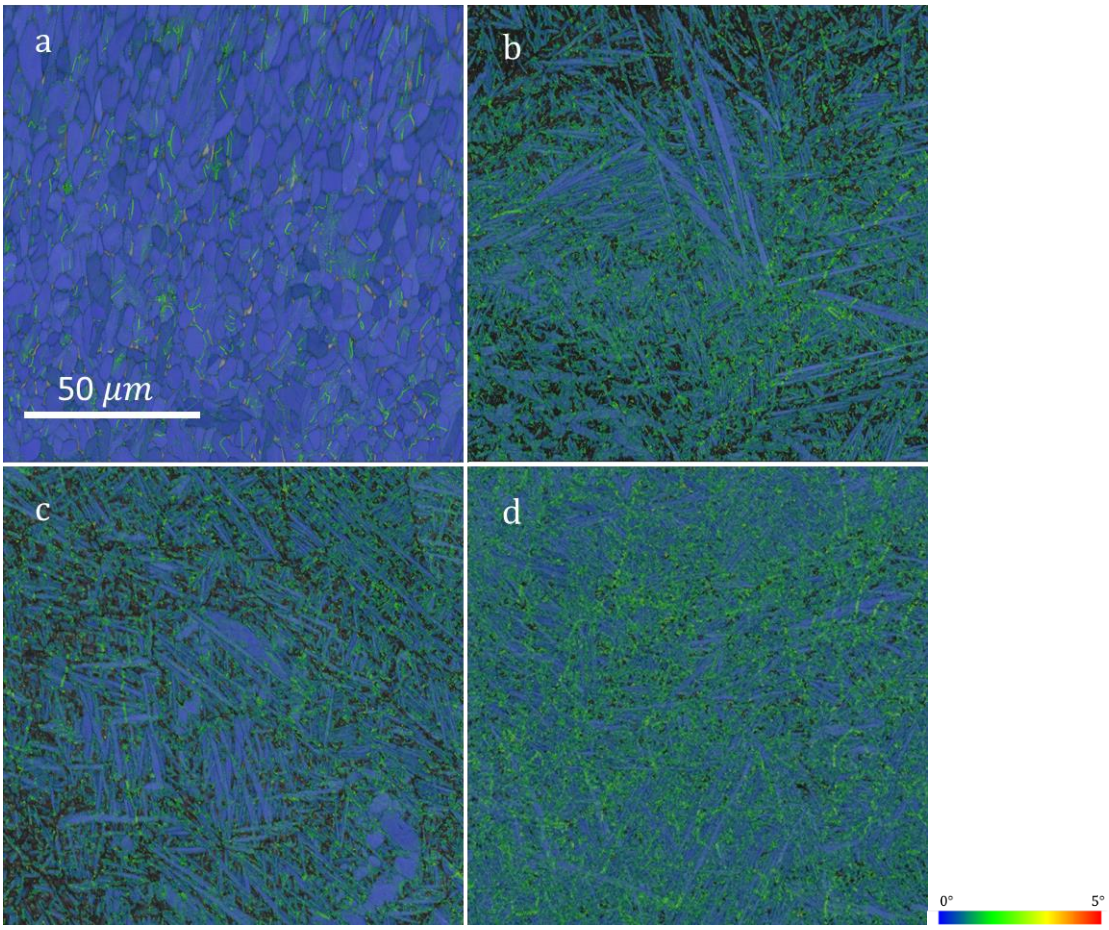

Figure 7-13 KAM maps of α′

The recrystallised/deformed maps in Figure 7-14 and corresponded data in Table 7-7 show that deformed α' has a higher stored strain in the vertical SLM specimen in building direction (longitudinal direction) than the other parts. It is also apparent that the specimen with the second-highest stored strain is the horizontal SLM. High deformed regions in the SLM parts have higher residual stresses trapped during AM fabrication than wrought parts. Wrought specimens are mainly free from residual strain.

Table 7-7 Recrystallised, substructure, deformed structure density of β and α′

Specimen ID	*Recrystalized*	*Substructured*	*Deformed*	*Recrystalized*	*Substructured*	*Deformed*
		β%			α′%	
Wrought	53.39	30.56	16.04	46.01	53.43	0.55
Horizontal as-built	56.04	2.20	41.76	10.85	62.04	27.11
Vertical as-built-Cross-sectional	53.59	2.10	44.31	12.03	65.26	22.70
Vertical as-built-Longitudinal	53.05	3.71	43.24	12.57	53.37	34.06

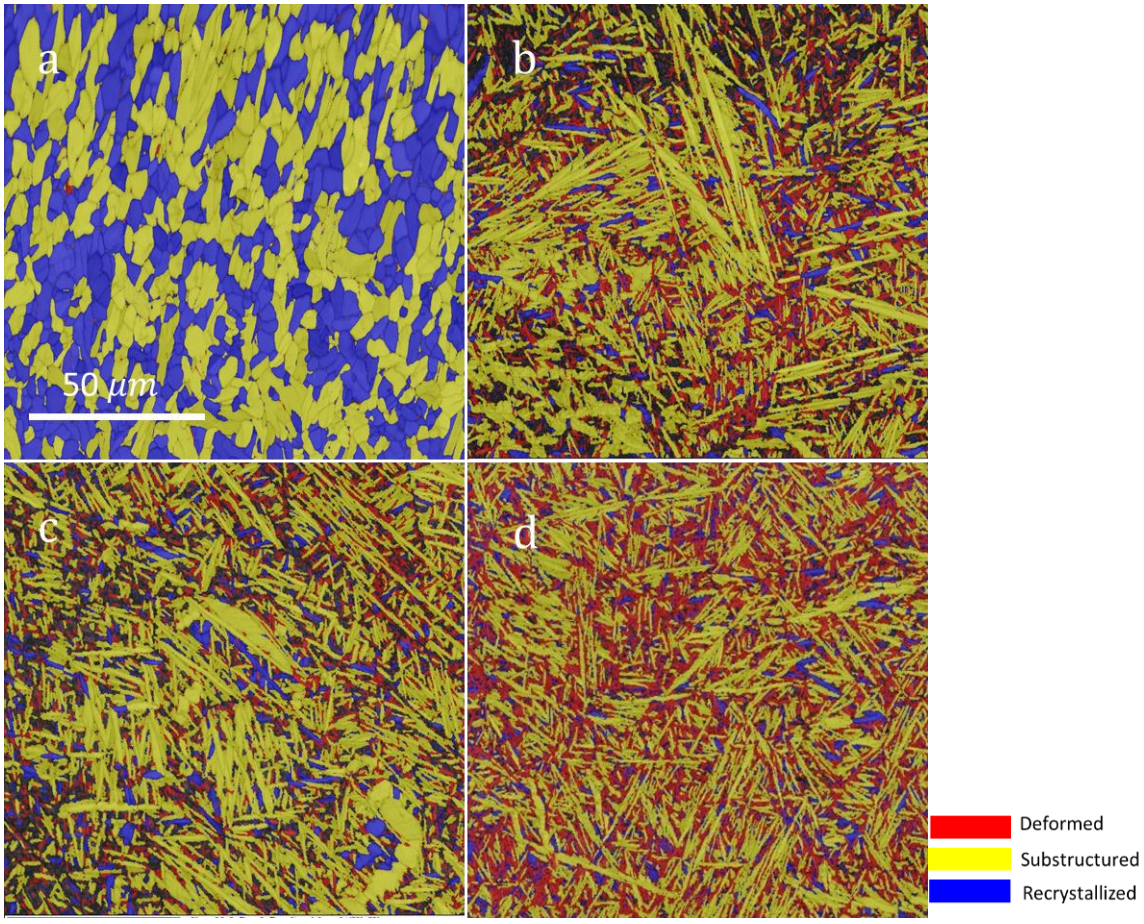

Figure 7-14 Recrystalized-substructure, and deformed maps to report percentages of each in both phases

7.2.2 Hardness

Figure 7-15 (a) shows micro-hardness and manufacturing processes as a function of the selected region's location. The micro-hardness values of the as-built SLM parts were 385±15 and 374±12 HV for the horizontally built and vertically built specimens respectively – much higher than that of the wrought specimen (~ 338±12 HV). This difference is attributed to the high density of dislocation aggregation in some regions, leading to higher residual stress. KAM maps show higher residual stresses in the SLM parts than the wrought ones (Figure 7-13). The standard deviation of the hardness shows relatively homogeneous behaviour.

Figure 7-15 (b) illustrates the hardness evolution in the vertically built specimen along building direction in three regions: the bottom, gauge length in the middle, and the top. The average HV of the middle region (374±12) is smaller than that in the bottom and top regions (399±12 and 396±18, respectively). Lower cooling rates explain the lower HV in the vertical specimen's middle region. Location dependency introduces lower residual stresses in this region (refer to Figure 7-13).

The wrought specimens have higher retained β than the SLM specimens, which gives higher ductility. Horizontally built specimens have lower retained β than vertical ones (Table 7-3). The other factor that can explain hardness behaviour is grain size. Table 7-4 and Figure 7-10 show that the α' average grain size of the wrought specimens is substantially higher than that of the SLM parts.

(a) Wrought and horizontal specimen

Vertical

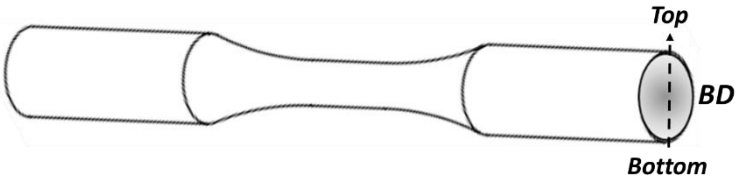

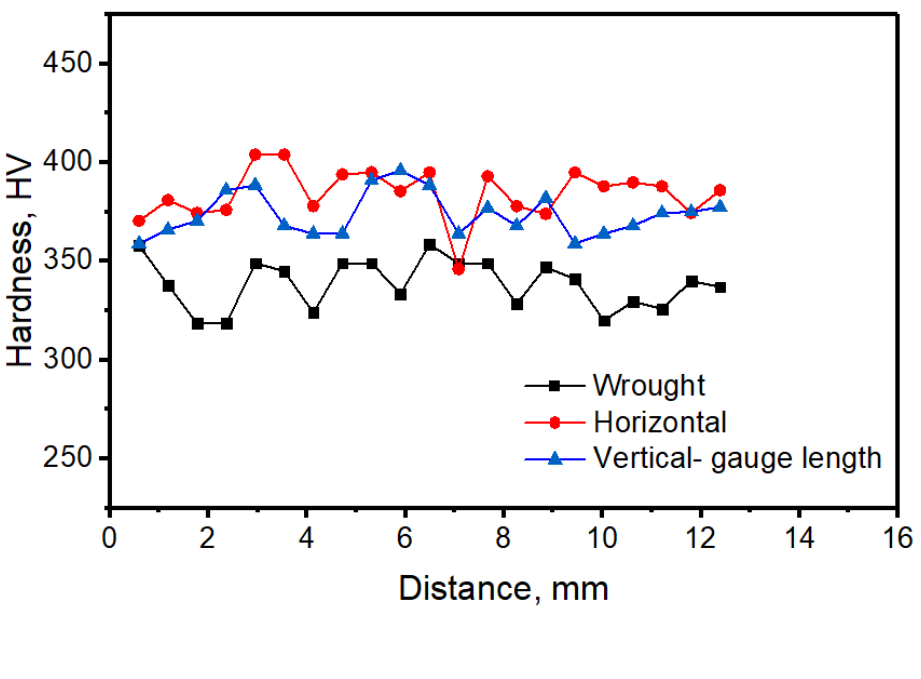

(b)

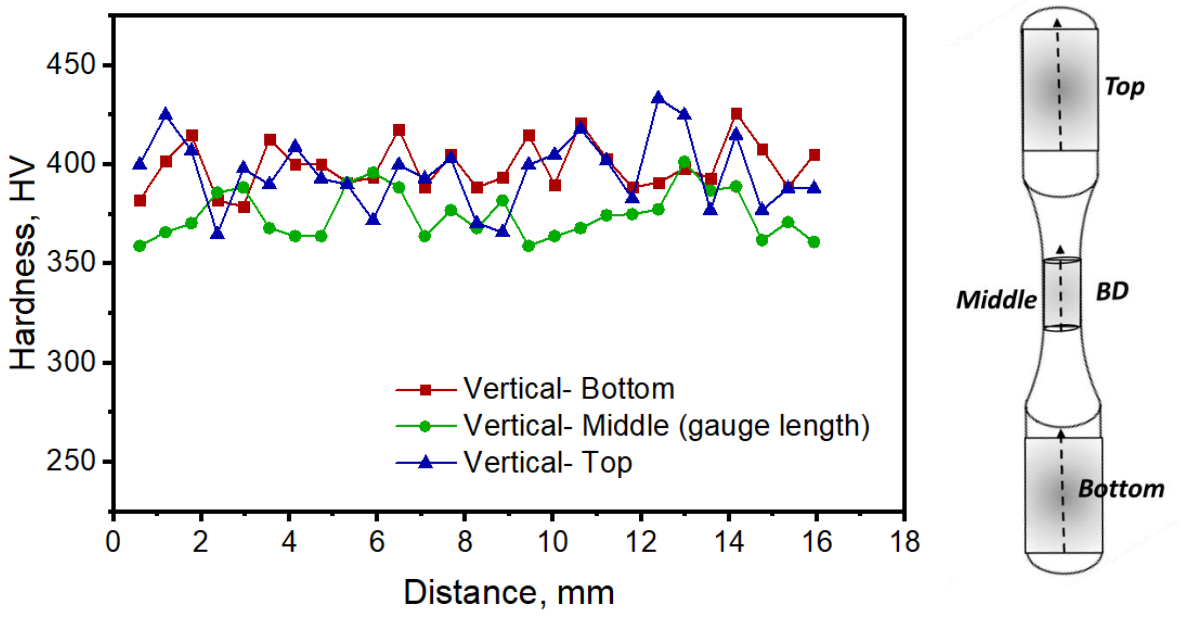

Figure 7-15 (a) Hardness of the wrought, horizontal SLM, and vertical SLM Ti6Al4Va, (b) hardness of the vertical SLM Ti6Al4Va in built direction as shown

7.2.3 Tensile characteristics

A monotonic tensile test was applied to compare the as-built SLM Ti6Al4Va parts' mechanical properties with those of the wrought ones. SLM coupons were fabricated horizontally and vertically (refer to Figure 7-2); the tensile loading axis was parallel and perpendicular to the scan lines. Tensile properties of as-built SLM Ti6Al4Va parts are usually higher than those of wrought ones [82] (refer to Figure 7-16).

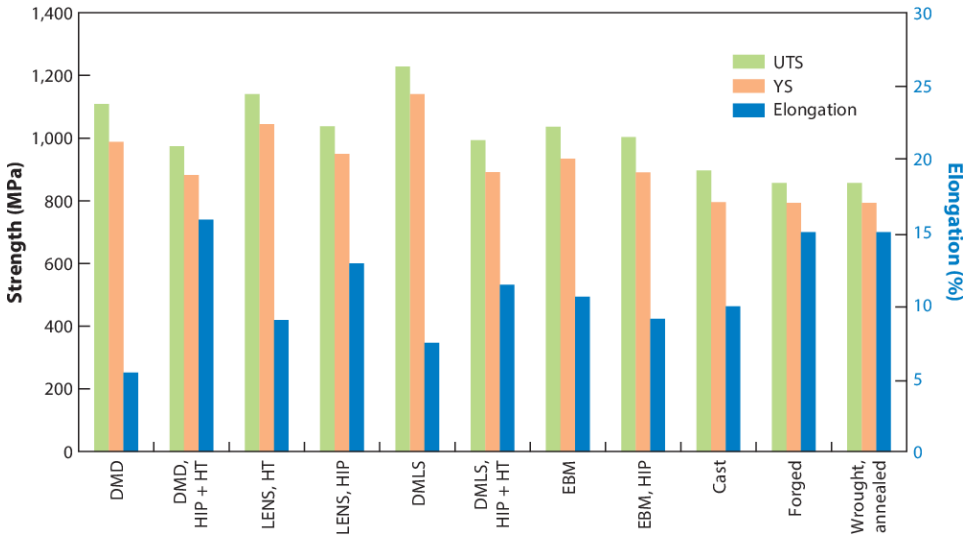

Figure 7-16 Summary of Ti6Al4Va AM tensile properties. Abbreviations: DMD, direct metal deposition; DMLS, direct metal laser sintering; EBM, electron beam melting; HT, heat-treated; LENS, laser-engineered net shaping; UTS, ultimate tensile strength; YS, yield stress [80]

Stress–strain curves of the horizontally and vertically built and wrought parts are presented in Figure 7-17.

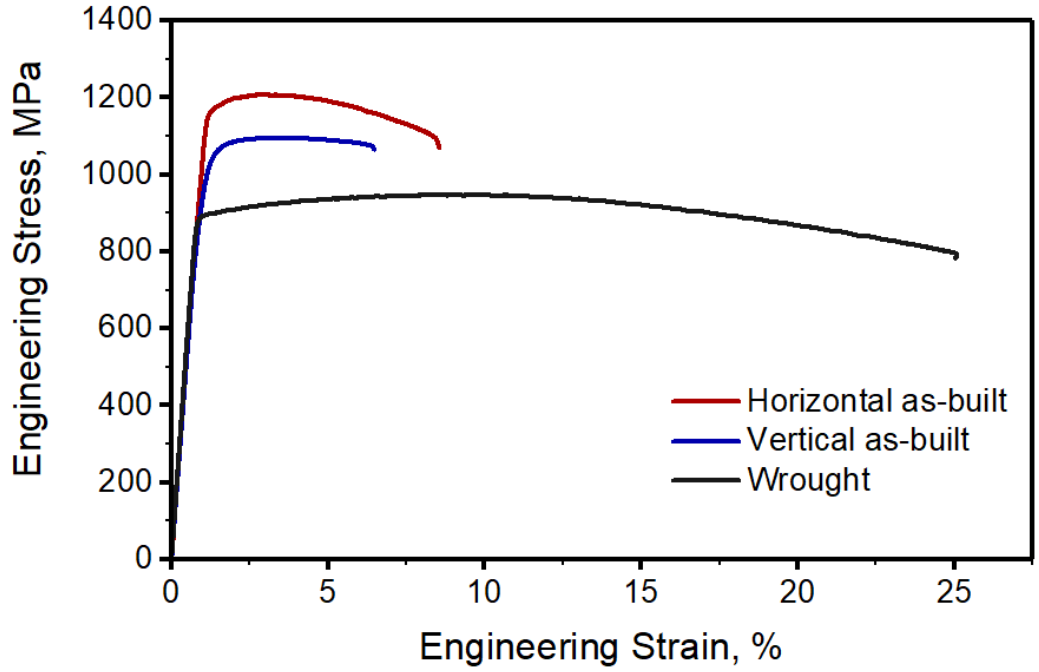

Figure 7-17 Stress-strain curves of the wrought, horizontal SLM, and vertical SLM Ti6Al4Va

Corresponding values of the stress–strain curves are shown in Table 7-9.

Table 7-9 Hardness and tensile properties of the horizontal and vertical SLM and wrought Ti6Al4Va parts

Specimen ID	Hardness (HV)	E (GPa)	σ_y (MPa)	σ_UTS (MPa)	Strength ratio (σ_y/σ_{UTS})	UEL (%)	TEL (%)	UTS*TEL
Horizontal As-built	385± 15	113±5	1111±55	1220±3	0.911±0.047	3±0.07	7.03±2.05	8579±2495
Vertical As-built	374± 12	104±2	1001±52	1097±2	0.913±0.047	3±0.3	7.29±1.91	7989±2097
Wrought	338± 12	115±1	907±11	955±6	0.949±0.006	8.2±0.7	33.5	32234

The horizontally built parts' E is quite similar to that of the wrought one. The vertical SLM part has a lower E. Different imposed phase fractions associated with the manufacturing processes and chemical composition are the determining factors.

Yield strength (σ_y) was lower for the vertical than the horizontal SLM parts. The wrought parts have the lowest average value. The factors that explain these differences are outlined below.

Grain sizes significantly influence yield strength. Refinement of the SLM parts in both directions gives higher yield strength (refer to Table 7-4). Moreover, retained β is destructive for strength. Because a higher fraction of retained β was detected in the wrought parts (Table 7-3), lower strength is logical. σ_y, the early plastic deformation property, is also influenced by dislocations. So (refer to Table 7-7), dislocation densities of the as-built parts are higher than those of the wrought parts due to the SLM process. The yield strength data also conform to the results of the bulk hardness tests.

The (σ_{UTS}) of the wrought specimens is approximately 20% lower than that of the horizontal as-built ones. Strength ratio, defined as σ_y/σ_{UTS} indicates all specimens regardless of manufacturing methods, have a low work hardening rate beyond the yield point. Note that lower interaction between dislocations results in a lower strain hardening rate.

Uniform elongation of the horizontally and vertically built specimens is approximately 37% lower than for the wrought ones. As retained β is beneficial for stretching, a higher fraction of β in the wrought specimen explains this result. Total elongation of the as-built parts are also lower than the wrought parts. SLM parts have small non-uniform elongation. Low TEL is strongly associated with a high fraction of destructive internal defects that cause rapid departed integrity and quick fracture after necking compared to wrought one.

The TEL*UTS index shows the required energy for failure. The index is higher for wrought Ti6Al4Va, making this material more appropriate for industrial applications. The horizontal as-built Ti6Al4Va specimens have a higher value than the vertical ones.

Tensile ductility emerges as a shortcoming of the as-built SLM Ti6Al4Va specimens, despite their higher strength. Heat treatment can expand ductility at the expense of strength. Heat treatment is recommended in future work to enhance ductility properties.

Testing the materials under monotonic loading showed the SLM process had opposite effects on the tensile properties of 17-4 PH SS and Ti6Al4Va. SLM hardened the Ti6Al4Va, but enhanced the ductility of 17-4 PH SS.

7.2.4 Fractography

The tensile fracture surface morphology of the horizontally and vertically built SLM specimens and wrought ones are shown in Figure 7-18. Substantial variances were detected in the coupons in line with their tensile properties.

The tensile fractured surface of the horizontal as-built SLM parts (Figure 7-18 (a,b)) displays a quasi-cleavage mode (a mixed mode of brittle and ductile fracture). The surface reveals micro-void coalescence and cleavage modes. It is characterised by dimples indicating intense plastic deformation around micro-voids. Intergranular fracture was mostly detected, showing dominant brittle behaviour. Unmelted particles, porosities and unmelted regions were detected at the tensile fractured surface. Pores and unmelted regions can act as crack nucleation sites under applied loading. Particle matrix interfaces (including unmelted particles and secondary phase particles) also act as crack nucleation sites under loading.

Prevention of brittle failure is essential for industrial purposes. The vertical as-built SLM specimens show relatively flat surfaces denoting low fibrous features (Figure 7-18 (c,d)). Unmelted particles, porosities and unmelted regions were detected in the fractured surfaces.

Wrought specimens' fractured surfaces show a cup and cone profile (Figure 7-18 (e,f)) This type of failure occurs more often in commercial structures due to the formation of porosities and micro-voids. In cup and cone fracture, existing plastic flow causes very tiny voids to form within the part. As the flow continues, these voids grow and coalesce, and shear fracture causes rupture.

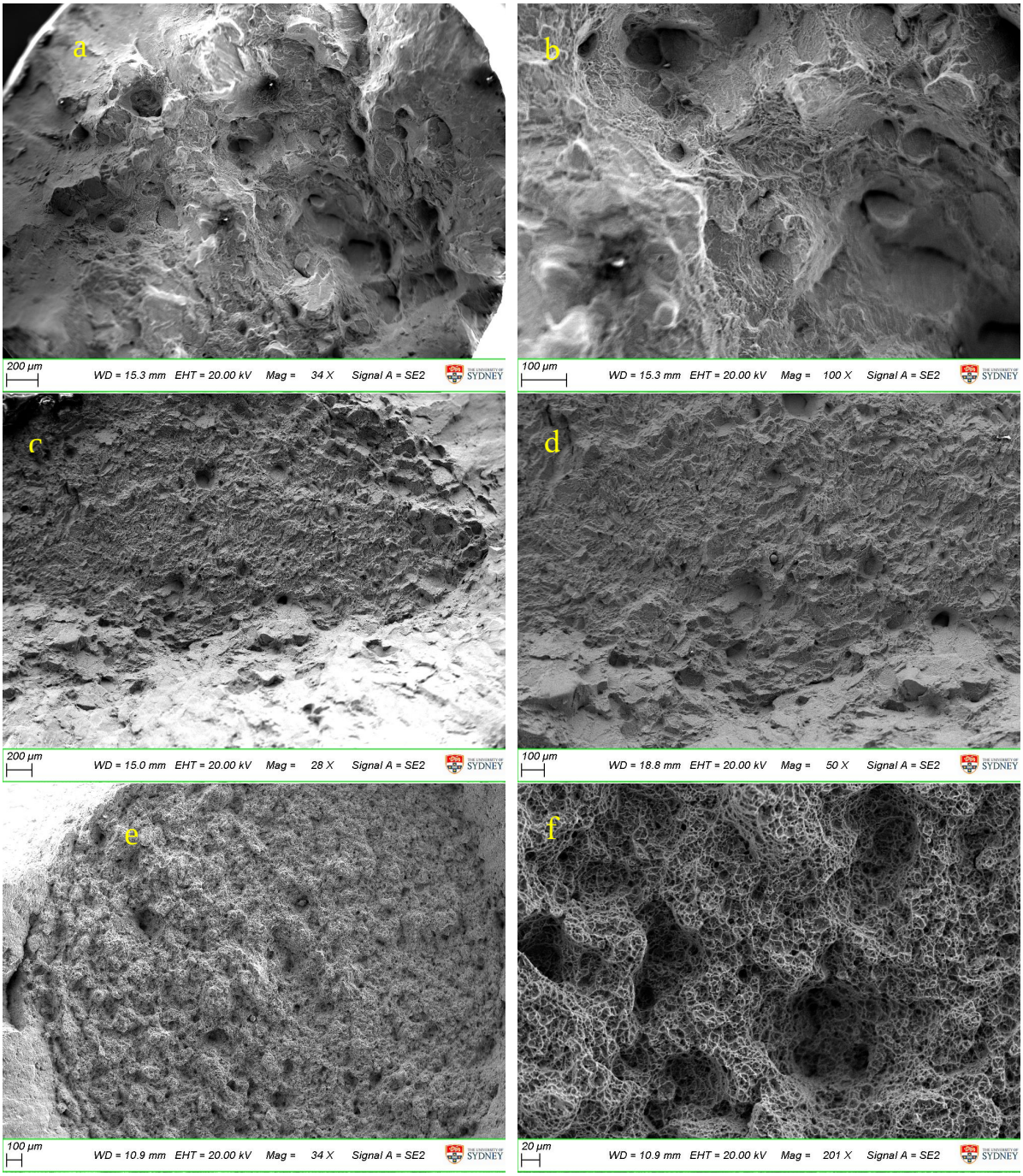

Figure 7-18 Tensile fractured surface of (a) a horizontal SLM part; (b) higher magnification; (c) a vertical SLM part; (d) higher magnification; (e) the wrought Ti6Al4Va and (f) higher magnification

7.2.5 Wear properties

The tribological behaviour of the as-built SLM and wrought Ti6Al4Va was studied to consider the effects of manufacturing methods. As [153] reported, tribocorrosion performance of Ti6Al4Va is affected by manufacturing methods. The SLM built orientation effect on wear behaviour under different loads was investigated as follows.

Firstly, the effect of manufacturing methods (i.e. additive and conventional manufacturing) of Ti6Al4Va on wear characteristics were studied at a constant applied load of 10 Kgf. In the subsequent investigation, wear performance under a higher applied load (15 Kgf) was considered.

The SWR of the horizontal built SLM Ti6Al4Va alloy, vertically built alloy, and wrought alloy in dry conditions are shown in Figure 7-19. The SWR of the wrought specimens (6.68×10^{-11} $m^3/_{Nm}$) is slightly lower than those of the horizontal and vertical SLM specimens (6.72×10^{-11} $m^3/_{Nm}$ and 6.92×10^{-11} $m^3/_{Nm}$ respectively). It is apparent that the wear loss of the vertical SLM is higher than the horizontal one, which can be attributed to its lower hardness. So, it can be concluded that manufacturing methods affect Ti6Al4Va wear properties.

The pattern reported here is inconsistent with the HVs documented. Conversely, note that the wrought and as-built SLM wear rates are independent of the hardness. This may be due to carbides (of irregular shapes and size) that protrude from the matrix, thereby isolating the matrix from the aspertities of the counter-ball and resulting in less material being removed.

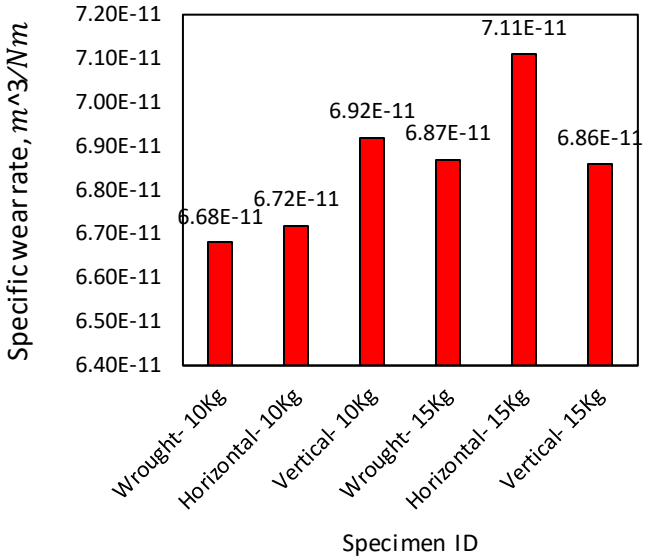

Figure 7-19 Specific wear rate of the wrought, horizontal and vertical SLM under different applied loads

Increasing the applied load from 10 Kgf to 15 Kgf increased both the wrought and horizontal SLM wear rate. The SWRs of the wrought specimens at 10 Kgf and 15 Kgf were 6.68×10^{-11} $m^3/_{Nm}$ and 6.87×10^{-11} $m^3/_{Nm}$ respectively. A similar trend was detected for the horizontal specimens: 6.72×10^{-11} $m^3/_{Nm}$ and 7.11×10^{-11} $m^3/_{Nm}$ for 10 Kgf and 15 Kgf loads. In contrast, decreasing SWR with increasing load was measured for vertical SLM parts – 6.92×10^{-11} $m^3/_{Nm}$ and 6.86×10^{-11} $m^3/_{Nm}$ for 10 Kgf and 15 Kgf, respectively. This decrease is reasonable due to the lower strain hardening capacity in Ti6Al4Va alloy regardless of the manufacturing methods and the built orientation effect in SLM fabrication.

Coefficients of friction of worn specimens are provided in Figure 7-20. Regardless of the applied load, the average CoF of the horizontal SLM parts was lower than for the vertical SLM parts, and this difference increased by increasing the applied loads. The average CoF for wrought ones decreased by increasing the applied load (0.55 and 0.37 for 10 Kgf and 15 Kgf respectively). The roughness of the contacted surfaces generally decreases with increasing load, but here the SLM parts' roughness was increased by continuous rubbing.

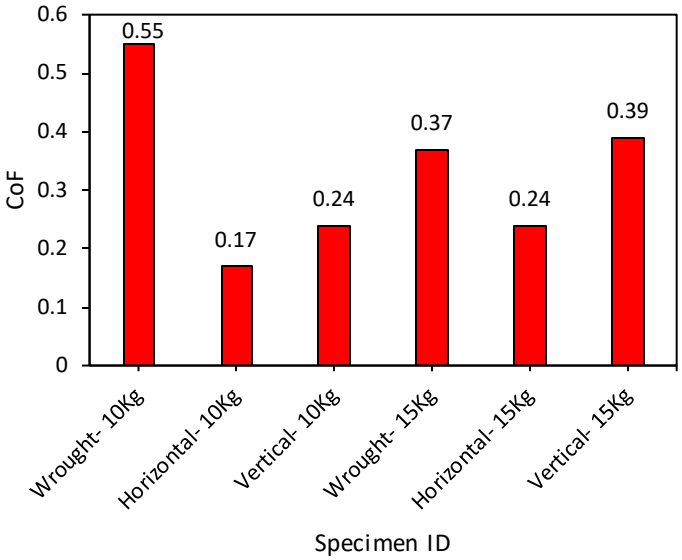

Figure 7-20 COF of the wrought, horizontal and vertical SLM parts under different applied loads

The evolution of CoF with sliding distance, for all specimens, is presented in Figure 7-21. The general progress shows that smoothening did not occure during wearing for almost conditions.

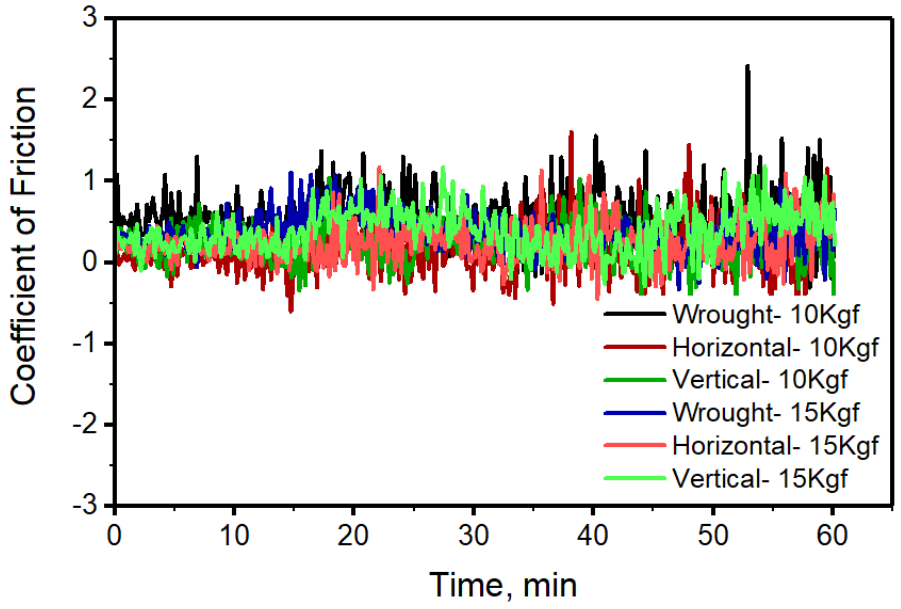

Figure 7-21 COF of the wrought, horizontal and vertical SLM as a function of time in different applied loads

Figure 7-22 shows the worn surfaces under 10 Kgf load. Different wear mechanisms were detected for the parts. For the horizontally built SLM parts (Figure 7-22 (a, b, c)), a mix of grooves and coarse flake debris is visible. For vertically built parts, the worn surface (Figure

7-22 (d, e, f)) mainly shows thick surface deformation and broad grooves. Abrasive-like wear scratches, proving the highest SWR and showing lower strain hardening. The worn surface of a wrought part (Figure 7-22 (g,h,i)) shows less surface deformation than the SLM parts, which is in good agreement with wrought parts' lower SWR. Fine debris in the wrought part also indicates better wear resistance than the SLM parts.

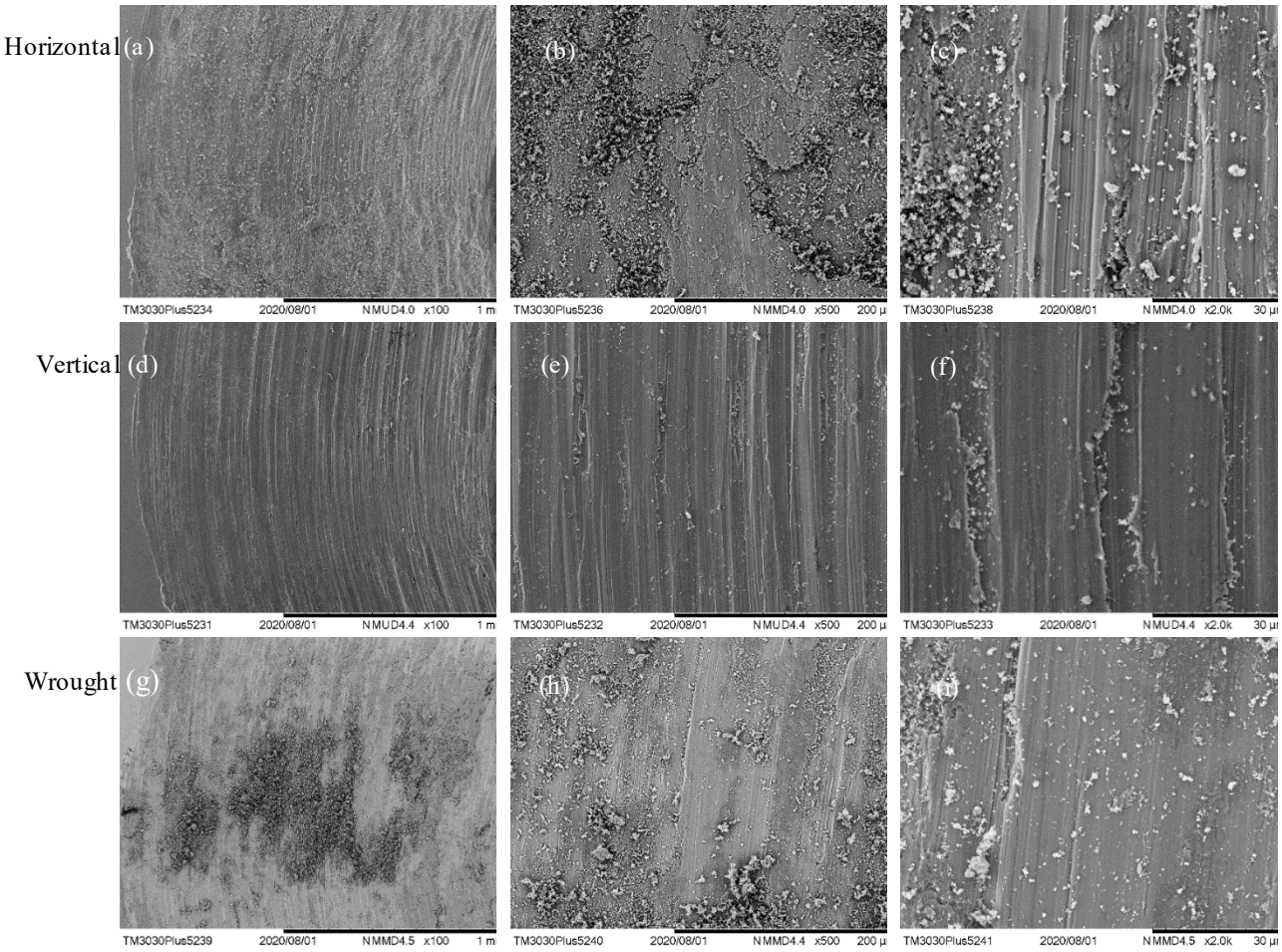

Figure 7-22 Worn surfaces of (a,b,c) the horizontal SLM, (d,e,f) vertical SLM, and (g,h,i) wrought specimens at 100X, 500X, and 2KX magnifications

7.3 **Summary**

Ti6Al4Va has many applications in aerospace, biomedical, etc. Essential properties for biomedical products may not the same for aerospace components. For instance, the higher hardness possessed by α' phase may be beneficial for certain applications and it may be

detrimental for some other ones. So, selection of the manufacturing technique is highly subjected to the intended applications and should be negotiated.

Relatively similar microstructural features were detected for horizontal and vertical built SLM parts. Acicular α' with a slight fraction of needle-shaped β were detected for both SLM Ti6Al4Va. Average grain sizes of horizontal built SLM in built direction was slightly higher than that in vertical one in built direction. Residual stress in the vertical SLM along the built direction was a little higher than the horizontal in built direction.

Built orientation effect on microstructural features and mechanical properties of SLM Ti6Al4Va was investigated. The built orientation effect in Ti6Al4Va SLM products revealed slight variations in the microstructural features. It can be stated that microstructural features has not high impact on tensile properties and mainly affected by the layered nature and SLM imposed defects during fabrication.

In vertical SLM part, due to higher imposed thermal in the middle region ended up to the higher fraction of soft β phase, hardness values variation was significant in the built direction and showed the lower value in the middle region. Due to this observation, it is suggested to consider the aspect ratio in products before manufacturing. Worth mentioning that in a vertical specimen, residual stress in the built direction was remarkably higher than that in a perpendicular direction. So, the selection of built direction, as well as the direction of loading in service, is vital for real applications.

Horizontal SLM showed petty higher σ_y and σ_{UTS} values than that in the vertical one. The as-built horizontal SLM specimen failed in quasi-cleavage mode with a highly irregular fractured surface; however, the vertical one failed in a brittle form. So, due to the higher strengths and elongation and preferable fractured surfaces, horizontal specimen (smaller aspect ratio) is more pronounced for reality.

The differences between SLMed and conventional manufactured Ti6Al4Va was highlighted in this study. Clear differences in microstructure, tensile and wear properties were observed. The main reason for the variations in microstructural features and mechanical properties were the unique imposed thermal and mechanical stresses during fabrication.

Basket weave microstructure was detected for the wrought Ti6Al4Va while acicular α' microstructure was revealed for the SLM ones regardless of the built orientation. Higher

retained soft β was reported for the wrought one than the SLMs regardless of the built orientation. Reported phases fraction was in good agreement with the lower elongation to failure of SLMs than the wrought specimens. Higher $\beta\%$ showed positive characteristics resulting in a substantial elongation before fracture for wrought one. The homogenous coarse microstructure of the wrought led to having lower yield strength compared to the enhanced tensile strength of the as-built SLM ones. The as-built SLM specimens, regardless of the built direction, showed superior tensile properties compared to the conventional ones. The tensile behaviour in the as-built SLM ones, as well as the conventional ones, was characterized by very small work-hardening which is not desirable and it is a good idea to chase for the solution to increase work hardening capacity.

%UEL of the SLMs was relatively smaller than that of the wrought one which is a detrimental factor for most applications. %TEL of the wrought one was 5 times higher than the SLMs which is irresistible for the applications. The fractured surface of the wrought one was industrial and failed in a cup and cone manner. Horizontal SLM fractured in semi-ductile (semi cleavage) and the vertical one failed in brittle profile with tiny fibrous.

Detected residual stresses were relatively high in SLMs parts compared to the wrought ones. It showed the SLM process generates more residual stress in the microstructure of SLM Ti6Al4Va. So, stress relief is highly suggested for the SLM Ti6Al4Va products.

The wear loss of the SLMs regardless of the built orientation was higher than the wrought ones despite the higher hardness. Thus, applying wrought Ti6Al4Va can be a good choice for wear applications.

To tailor the microstructure for optimum properties, transforming the non-equilibrium submicron acicular α' without coarsening into submicron near-equilibrium lamellar (α+β) is suggested. This theory has recently been supported through in situ decomposition during SLM fabrication [152].

Chapter 8 Conclusion

8.1 Research objectives

The following conclusions can be drawn based on the experimental results and analysis:

Chapter 3

While several microstructural features were observed in the built direction of as-built SLM 17-4 PHSS, hardness evolution did not vary noticeably. This can be explained by the fact that the substructural features of the SLM 17-4 PH SS – including microsegregation, precipitation-hardening particle formation and dispersion, and dislocation density –effectively eliminate hardness variation. Surface hardening and phase transformation by mechanical forces and induced heat during sample preparation are also factors. The microstructural features that could not be considered in this study should be the subjects of future research.

Comparison of the microstructural features and mechanical properties of 17-4 PHSS components manufactured using SLM and conventionally exposed the inferior tensile properties (yielding point, and to a lesser extent, ultimate tensile strength and ductility) of the as-built SLM parts. Note that the inferior tensile properties of the as-built SLM can be attributed entirely to the powder characteristics and SLM design and processing set-up parameters during fabrication. Induced thermal histories and cooling rates generated by the imposed energy and positioning of the specimens during fabrication are the most influential factors. The results agreed with other studies showing that the strength was mostly affected by the γ% of the as-built SLM, while elongation to failure was mainly affected by the SLM induced defects. It is worth emphasising that the reproducibility of data generated in previous research should be considered carefully, due to the variety of empirical AM set-ups reported. It was shown that post heat treatments improved the strength of SLM parts, making them comparable or superior to typical conventionally made ones (refer to Chapter 5). Reduction in the size and morphology of the induced SLM defects via SLM processing parameters was out of scope for this study and is proposed as future work.

Chapter 4

In-situ tensile testing facilitated the monitoring and tracking of the evolution of microstructural features throughout deformation. Due to a lower C fraction (0.05 %wt.) and a higher fraction of metastable γ (26.2 %) in SLM 17-4 PHSS, the TRIP effect was observed through high strain hardening capacity, which did not occur in the conventional 17-4 PH SS samples. During in-situ tensile loading, the fraction of LAGBs and their misorientation angles increased. Some of these evolved into HAGBs, leading to grain subdivision. It was also observed that by tensile loading progression, the strain field for γ and α'were developed thorough newly formed dislocations. It is worth mentioning that that whether this is a benefit depends on the intended application, the resultant deformation mechanism (explained in Chapter 4) can be tailored by alloying and post treating to achieve desired properties.

Chapter 5

Through the application of heat-treatment processes, different properties were achieved resulting from microstructural evolution. This study novelty determined results not fully consistent with those of other researches [30, 34]. Which should encourage further study into the kinetics of aging in SLM 17-4 PHSS.

Remarkable differences in microstructural features and tensile properties were observed in standard age treated SLM parts as compared to conventional ones using equivalent heat treatments. However, in the conventional 17-4 PHSS, peak age took place at 480℃ for 1 hr, in this study overaging at 550℃ and over, was not completely witnessed in the prolong aging treatments and substantial differences were documented. Subsequently, direct aging procedures were applied to monitor if the initial as-built SLM microstructure could act as if solutionised, to reduce the cost and time of post heat treatment. According to the initial microstructure of each category (i.e. direct-aged and solutionised aged), substantial differences in microstructural features were achieved after heat treating. The differences originating from the refined and homogenized solutionised microstructure, with higher induced residual stresses in CA-aged group, as compared to the initial SLM microstructure. In both categories, similar phase fraction evolution occurred. Reverse transformation of $\alpha' \rightarrow \gamma$ were observed at lower temperatures (480℃ and 550℃). Whilst at higher temperatures (620℃ and 760℃), $\gamma \rightarrow \alpha'$ transformation progressed. In the direct aging category, the precipitation hardening mechanism might not be fully activated, attributed to the higher solubility of Cu in the high metastable γ%.

Higher average yield strength of CA-aged samples (584.25±14.75 MPa) compared to direct-aged conditions (496±15.75 MPa) showed consistency with homogenized and refined grains through solutionising. The as-built, H900, and H1025 from the direct-aged group, exhibited the TRIP effect with considerable strain hardening after yielding while in CA-aged category, insignificant workability was observed. The deformation mechanism in solutionised aged conditions under tensile loading was continuous, while yield point elongation was detected for the as-built, H900, and H1025 conditions in the direct-aged group. The best combination in UTS*TEL index was related to the H900 and H1025 conditions resulting in ≈ 25-30% enhancement compared to the as-built samples.

In summary, the enhancement of the direct-aged conditions was credited with a higher work hardening capacity, while CA-aged conditions showed enhanced properties in hardness, the elastic region properties and yielding. Discontinuity in direct-aged conditions is not desirable due to softening but can be eliminated by modified alloying with keeping higher workability in the direct-aged group. As an offer for implication in industrial applications, H1150M from the direct-aged group, CA-H1150M and CA-H1025 from the CA-aged group could be the most widespread conditions for the industrials applications by having great combinations of strength and elongation thru flow deformation. Ought to be noted that depends on the prerequisite properties for intended applications, appropriate heat treatment(s) can be nominated from the documented properties in Chapter 5.

Chapter 6

Despite the lower hardness of SLM 17-4 PHSS, the wear loss of the SLM part was lower than the wrought one. The TRIP effect and existence of pores in the structure of SLM products explained the higher wear resistance of SLM products. The presence of precipitates in the wrought material was responsible for the higher mass loss, by shifting the wear mechanism from a two-body to three-body abrasive in wrought PHSS. It is worth noting that wear loss for both SLM and wrought PHSS increased when increasing the linear velocity, however this lowering in wear resistance was not observed with enhanced applied loading.

The wear rate of both groups of PHSS increased in the sandy environment when compared to dry conditions. The three-body abrasive mechanism was likely to be the main reason for the mass loss in sandy conditions. CoF versus sliding time curves suggested more erratic and complex wear mechanisms were involved for the as-built and wrought PHSS in the sandy

environment as compared to the dry one. In conclusion, SLM PHSS is highly recommended for applications over wrought where wear is a consideration.

The effect of heat treatment in SLM is in general still poorly understood, and as shown in this study is very important in producing parts for real applications. This study showed that the solutionised specimen had lower wear loss than as-built one. These also showed the best wear resistance as compared to other heat-treatment conditions. In this research it was shown that for direct-aged conditions, H1025 had the best wear resistance and H1150M was the worst condition in mass loss. Regardless of the hardness, higher strain hardening capacity in H1025 and lower one in H1150M, could be the reason for the difference in wear resistance. CA-aged specimens showed similar SWR, which could be related to the presence of tempered α' with a refined homogenized microstructure. In general CA-aged materials indicated better SWR than the as-built and direct-aged group materials. Thus the application of CA-aged materials is recommended in industrial applications due to lower SWR.

Chapter 7

Despite only slight differences in their microstructural features, differences in hardness, tensile and wear properties were measured in horizontally and vertically built SLM Ti6Al4Va parts. These features were unable to be studied comprehensively in this study; future researchers should investigate the substructural features of horizontally and vertically built specimens, such as inclusions and precipitation formation during fabrication. Nonetheless, it is clear that the SLM process affects the properties of Ti6Al4Va considerably; therefore, for industrial applications, it is strongly recommended that aspect ratio and loading directions be considered when selecting the best possible built direction for fabrication and service.

Comparison of the SLM technique and conventional manufacturing effects on the microstructural features and mechanical properties of Ti6Al4Va showed superior tensile strength of the as-built SLMs, regardless of building direction compared to the conventional one. On the other hand, substantial inferior ductility was observed for SLM products, which made them less applicable to industrial use. To overcome this strength–ductility trade-off for SLM Ti6Al4Va components, proper in-situ treatment during manufacturing or post heat treatment are essential to achieve industrially desirable characteristics. Induced residual stress during SLM fabrication was also relatively high compared to conventionally manufactured parts. Accordingly, stress relief is strongly recommended after Ti6Al4Va SLM fabrication.

While the hardness of the SLM Ti6Al4Va parts was higher than that of conventionally manufactured ones, the wear loss of the former was greater. That could be explained by the fact that the presence of debris changes a two-body wear mechanism to a three-body mechanism. Although porosities and TRIP improved the wear resistance of the 17-4 PHSS, note that the porosity of SLM Ti6Al4Va parts was negligible on one side, and no TRIP effect was observed in the SLM Ti6Al4Va specimens. Therefore, two different wear behaviour were observed in SLM 17-4 PHSS and SLM Ti6Al4VA.

8.2 Recommendations

Potential future work in this research field is described below.

- Due to AM and specifically SLM technology's uniqueness and recent emergence, some aspects of the mechanical properties of AM 17-4 PHSS and Ti6Al4Va materials have not yet been studied. Extensive work has been done on the tensile behaviour and fatigue performance of SLM products. In contrast, areas such as low cycle fatigue, fatigue crack growth, fracture toughness, impact, creep, creep-fatigue, fatigue under multi-axial loads have been neglected.
- A critical aspect of research into SLM steel deformation and heat treatment is to transform experimental results into empirical parametric equations, that can be used to predict behaviour. Although these kinds of equations were developed and successfully applied for traditionally manufactured steels, these need to be extended to cover SLM steels, or even other AM materials. Therefore, future researchers could characterise SLM steel parameters and develop equations enabling prediction of behaviour and performance [82].
- Due to the importance of the fabrication environment on SLM 17-4 PH SS for obtaining the desired microstructure, the effect of purging with argon gas on the microstructure during fabrication is another avenue of research.
- It is also suggested to investigate tailoring the microstructure by using chemical means (i.e., grain refiner agents) and/or mechanical means (i.e., ultrasonic or magnetic treatment) to induce the nucleation of equiaxed grains during manufacturing, resulting in isotropic microstructure [154].
- To improve understanding of the deformation mechanism of heat treated SLM 17-4 PHSS, in situ observation under tensile loading is suggested.
- Wider investigations into the influence of various heat treatments on the evolution of microstructure are crucial, also considering high-efficiency and low-cost methods. These include post-processing methods to transform retained γ to α' including sub-zero treatment or cryogenic treatment and tempering.
- In the present study, the role of precipitation strengthening was not considered. TEM investigation of the precipitation particles, carbide and inclusion formation during fabrication was beyond the scope. Investigations to characterise precipitation hardening

and carbide formation during SLM fabrication and heat treated 17-4 PHSS would be beneficial.

- Investigation of the partitioning and segregation of the alloying elements during SLM processing, and through post-heat treatment processing, by atom probe microscopy is strongly suggested.
- Crack initiation and propagation originated from precipitation are also suggested for study. With one possible focus being on reducing detrimental AM induced defects such as micro-notches and pores.
- As a novel work in the research field of 17-4 PHSS, precipitation strengthening by cyclic plasticity is proposed.
- Further work is required to understand the tribocorrosion mechanisms of SLM 17-4 PHSS to develop guidance for the development of new materials with high performance. Surface treatments and coatings are suggested to improve bulk materials' wear resistance for SLM 17-4 PHSS production.
- Microstructure evolution and transition in the wear behaviour of SLM 17-4 PHSS during wear tests under different heat-treated conditions should be investigated using EBSD.
- Tailoring the microstructure of Ti6Al4Va SLM during fabrication to overcome strength-ductility dilemma
- Adding alloys to tailor and improve the strength-to-density ratio of SLM 17-4 PHSS to match Ti6Al4Va's properties to make the productions cost effective [61].
- Due to huge variation in the effective pre-, para- and post-processing parameters during SLM, achieving reliable and reproducible mechanical properties in AM products is not as easy as in traditionally manufactured materials. Processing set-ups for most AM processes are designed individually, therefore research to date has not produced reproducible data for comparison. As a consequence, learning how the pre-, para- and post- processing factors of AM affect the reproducibility of data is a valuable objective [155].

8.3 Contributions to knowledge

1. *Heat Treatment Effect on Microstructural and Mechanical Properties of Additively Manufactured 17-4PH Stainless Steel,* Journal target is Materials Science and Engineering A

   Materials Science and Engineering A has published many important studies of the properties, microstructure and processing of materials similar to those investigated in this research. The contents of chapters 3, 4, and 5 contribute to this manuscript.

2. *Tribological Properties of 17-4PH Stainless steel,* Journal target is Wear

   Wear is dedicated to the promotion of basic and practical knowledge in the field of material wear. This manuscript was based on chapter 6.

3. *Microstructural Characterisation and Mechanical Properties of Additively Manufactured Ti6Al4V,* Journal target is Materials Science and Engineering A

   As noted above, this journal includes many relevant articles. The manuscript was based on the content of chapter 7.

References

1. ASTM, *Standard terminology for additive manufacturing technologies*, in *ASTM Standard F2792-12a*. 2012.
2. Gu, D.D., et al., *Laser additive manufacturing of metallic components: Materials, processes and mechanisms.* International Materials Reviews, 2012. **57**(3): p. 133-164.
3. Kruth, J.P., M.C. Leu, and T. Nakagawa, *Progress in Additive Manufacturing and Rapid Prototyping.* CIRP Annals - Manufacturing Technology, 1998. **47**(2): p. 525-540.
4. Guo, N. and M.C. Leu, *Additive manufacturing: technology, applications and research needs.* Frontiers of Mechanical Engineering, 2013. **8**(3): p. 215-243.
5. MacDonald, E. and R. Wicker, *Multiprocess 3D printing for increasing component functionality.* Science, 2016. **353**(6307).
6. Barnatt, C., *3D Printing*. Third Edition ed. 2016.
7. Gibson, I., D.W. Rosen, and B. Stucker, *Additive manufacturing technologies: Rapid prototyping to direct digital manufacturing*. Additive Manufacturing Technologies: Rapid Prototyping to Direct Digital Manufacturing. 2010. 1-459.
8. Bose, S., S. Vahabzadeh, and A. Bandyopadhyay, *Bone tissue engineering using 3D printing.* Materials Today, 2013. **16**(12): p. 496-504.
9. Murphy, S.V. and A. Atala, *3D bioprinting of tissues and organs.* Nat Biotech, 2014. **32**(8): p. 773-785.
10. Parthasarathy, J., B. Starly, and S. Raman, *A design for the additive manufacture of functionally graded porous structures with tailored mechanical properties for biomedical applications.* Journal of Manufacturing Processes, 2011. **13**(2): p. 160-170.
11. Mota, C., et al., *Additive manufacturing techniques for the production of tissue engineering constructs.* Journal of Tissue Engineering and Regenerative Medicine, 2015. **9**(3): p. 174-190.
12. Sidambe, A.T., *Biocompatibility of advanced manufactured titanium implants-A review.* Materials, 2014. **7**(12): p. 8168-8188.
13. Larosa, M.A., et al. *Custom-built implants manufacture in titanium alloy by Direct Metal Laser Sintering (DMLS)*. in *High Value Manufacturing: Advanced Research in Virtual and Rapid Prototyping - Proceedings of the 6th International Conference on Advanced Research and Rapid Prototyping, VR@P 2013*. 2014.
14. Maidin, S., et al., *Bone scaffold geometrical design and material selection by using analytical hierarchy process for additive manufacturing process.* Jurnal Teknologi, 2015. **77**(32): p. 141-149.
15. Salmi, M., et al., *Patient-specific reconstruction with 3D modeling and DMLS additive manufacturing.* Rapid Prototyping Journal, 2012. **18**(3): p. 209-214.
16. Gebhardt, A., et al. *Additive Manufacturing by Selective Laser Melting: The realizer desktop machine and its application for the dental industry*. in *Physics Procedia*. 2010.

17. Cohen, A., et al., *Microscale metal additive manufacturing of multi-component medical devices.* Rapid Prototyping Journal, 2010. **16**(3): p. 209-215.

18. Uhlmann, E., et al., *Additive Manufacturing of Titanium Alloy for Aircraft Components.* Procedia CIRP, 2015. **35**: p. 55-60.

19. Manfredi, D., et al., *Direct Metal Laser Sintering: An additive manufacturing technology ready to produce lightweight structural parts for robotic applications*. Metallurgia Italiana, 2013. **105**(10): p. 15-24.

20. Frazier, W.E. *Direct digital manufacturing of metallic components: Vision and roadmap*. in *21st Annual International Solid Freeform Fabrication Symposium - An Additive Manufacturing Conference, SFF 2010*. 2010.

21. Frazier, W.E., *Metal Additive Manufacturing: A Review.* Journal of Materials Engineering and Performance, 2014. **23**(6): p. 1917-1928.

22. Munsch, M., *15 - Laser additive manufacturing of customized prosthetics and implants for biomedical applications A2 - Brandt, Milan*, in *Laser Additive Manufacturing*. 2017, Woodhead Publishing. p. 399-420.

23. Wang, X., et al., *Topological design and additive manufacturing of porous metals for bone scaffolds and orthopaedic implants: A review.* Biomaterials, 2016. **83**: p. 127-141.

24. Uriondo, A., M. Esperon-Miguez, and S. Perinpanayagam, *The present and future of additive manufacturing in the aerospace sector: A review of important aspects.* Proceedings of the Institution of Mechanical Engineers, Part G: Journal of Aerospace Engineering, 2015. **229**(11): p. 2132-2147.

25. Li, N., et al., *Progress in additive manufacturing on new materials: A review.* Journal of Materials Science & Technology, 2019. **35**(2): p. 242-269.

26. Fayazfar, H., et al., *A critical review of powder-based additive manufacturing of ferrous alloys: Process parameters, microstructure and mechanical properties.* Materials & Design, 2018. **144**: p. 98-128.

27. Sames, W.J., et al., *The metallurgy and processing science of metal additive manufacturing.* International Materials Reviews, 2016. **61**(5): p. 315-360.

28. Mower, T.M. and M.J. Long, *Mechanical behavior of additive manufactured, powder-bed laser-fused materials.* Materials Science and Engineering: A, 2016. **651**: p. 198-213.

29. 2016; Available from: http://www.custompartnet.com/wu/selective-laser-sintering, .

30. LeBrun, T., et al., *Effect of retained austenite on subsequent thermal processing and resultant mechanical properties of selective laser melted 17–4 PH stainless steel.* Materials & Design, 2015. **81**: p. 44-53.

31. AlMangour, B. and J.M. Yang, *Improving the surface quality and mechanical properties by shot-peening of 17-4 stainless steel fabricated by additive manufacturing.* Materials and Design, 2016. **110**: p. 914-924.

32. AlMangour, B. and J.-M. Yang, *Integration of Heat Treatment with Shot Peening of 17-4 Stainless Steel Fabricated by Direct Metal Laser Sintering.* JOM, 2017. **69**(11): p. 2309-2313.

33. Cheruvathur, S., E.A. Lass, and C.E. Campbell, *Additive Manufacturing of 17-4 PH Stainless Steel: Post-processing Heat Treatment to Achieve Uniform Reproducible Microstructure.* JOM, 2016. **68**(3): p. 930-942.

34. Nezhadfar, P.D., et al., *Fatigue behavior of additively manufactured 17-4 PH stainless steel: Synergistic effects of surface roughness and heat treatment.* International Journal of Fatigue, 2019. **124**: p. 188-204.

35. Nezhadfar, P.D., et al., *Fatigue crack growth behavior of additively manufactured 17-4 PH stainless steel: Effects of build orientation and microstructure.* International Journal of Fatigue, 2019. **123**: p. 168-179.

36. Rafi, H.K., et al., *Microstructure and Mechanical Behavior of 17-4 Precipitation Hardenable Steel Processed by Selective Laser Melting.* Journal of Materials Engineering and Performance, 2014. **23**(12): p. 4421-4428.

37. Sun, Y., R.J. Hebert, and M. Aindow, *Effect of heat treatments on microstructural evolution of additively manufactured and wrought 17-4PH stainless steel.* Materials & Design, 2018. **156**: p. 429-440.

38. Muhammad, M., et al., *Effect of heat treatments on microstructure/small-scale properties of additive manufactured Ti-6Al-4V.* The International Journal of Advanced Manufacturing Technology, 2019.

39. Greitemeier, D., et al., *Effect of surface roughness on fatigue performance of additive manufactured Ti–6Al–4V.* Materials Science and Technology, 2016. **32**(7): p. 629-634.

40. Mahmoudi, M., et al., *Mechanical properties and microstructural characterization of selective laser melted 17-4 PH stainless steel.* Rapid Prototyping Journal, 2017. **23**(2): p. 280-294.

41. Yadollahi, A., et al., *Effects of building orientation and heat treatment on fatigue behavior of selective laser melted 17-4 PH stainless steel.* International Journal of Fatigue, 2016.

42. Shrestha, R., et al., *An investigation into specimen property to part performance relationships for laser beam powder bed fusion additive manufacturing.* Additive Manufacturing, 2019. **29**: p. 100807.

43. Mengucci, P., et al., *Effects of build orientation and element partitioning on microstructure and mechanical properties of biomedical Ti-6Al-4V alloy produced by laser sintering.* Journal of the Mechanical Behavior of Biomedical Materials, 2017. **71**: p. 1-9.

44. Rafi, H.K., T.L. Starr, and B.E. Stucker, *A comparison of the tensile, fatigue, and fracture behavior of Ti–6Al–4V and 15-5 PH stainless steel parts made by selective laser melting.* The International Journal of Advanced Manufacturing Technology, 2013. **69**(5): p. 1299-1309.

45. Alexander S. Mete, M.M.S., Sergey V. Fedoro, and Anna A. Okunkov, *Power Density Distribution for LaserAdditive Manufacturing (SLM): Potential,Fundamentals and Advanced Applications.* Technologies 2019. **7**(1): p. 5.

46. Slotwinski, J.A., et al., *Characterization of Metal Powders Used for Additive Manufacturing.* Journal of research of the National Institute of Standards and Technology, 2014. **119**: p. 460-493.

47. Roberts, I.A., et al., *A three-dimensional finite element analysis of the temperature field during laser melting of metal powders in additive layer manufacturing,*. International Journal of Machine Tools and Manufacture, 2009. **Volume 49**(Issues 12–13): p. 916-923.

48. ASTM, *ASTM A564/A564M* in *Standard Specification for Hot-Rolled and Cold-Finished Age-Hardening Stainless Steel Bars and Shapes*. 2002.

49. ASM, *Properties and Selection: Irons, Steels, and High-Performance Alloys*, in *ASM Handbook Volume1*. 1990.

50. Bahrami Balajaddeh, M. and H. Naffakh-Moosavy, *Pulsed Nd:YAG laser welding of 17-4 PH stainless steel: Microstructure, mechanical properties, and weldability investigation.* Optics & Laser Technology, 2019. **119**: p. 105651.

51. Caballero, A., et al., *Wire + Arc Additive Manufacture of 17-4 PH stainless steel: Effect of different processing conditions on microstructure, hardness, and tensile strength.* Journal of Materials Processing Technology, 2019. **268**: p. 54-62.

52. Arisoy, C.F., G. Başman, and M.K. Şeşen, *Failure of a 17-4 PH stainless steel sailboat propeller shaft.* Engineering Failure Analysis, 2003. **10**(6): p. 711-717.

53. Atxaga, G., A. Pelayo, and A.M. Irisarri, *Failure analysis of a set of stainless steel disc springs.* Engineering Failure Analysis, 2006. **13**(2): p. 226-234.

54. Tavares, S.S.M., J.S. Corte, and J.M. Pardal, *Chapter 17 - Failure of 17-4PH stainless steel components in offshore platforms*, in *Handbook of Materials Failure Analysis with Case Studies from the Oil and Gas Industry*, A.S.H. Makhlouf and M. Aliofkhazraei, Editors. 2016, Butterworth-Heinemann. p. 353-370.

55. Tian, J., et al., *Cracking due to Cu and Ni segregation in a 17-4 PH stainless steel piston rod.* Engineering Failure Analysis, 2016. **65**: p. 57-64.

56. Al Dawood, M., et al., *Thermal aging of 16Cr – 5Ni – 1Mo stainless steel Part 1 – Microstructural analysis.* Materials Science and Technology, 2004. **20**(3): p. 363-369.

57. Al Dawood, M., et al., *Thermal aging of 16Cr – 5Ni – 1Mo stainless steel Part 2 – Mechanical property characterisation.* Materials Science and Technology, 2004. **20**(3): p. 370-374.

58. Murthy, A.S., *Role of alloy additions on strengthening in 17-4 PH stainless steel*, in *Materials Science and Engineering*. 2012, Missouri University of Science and Technology.

59. Abrahams, R.A., *The Development of High Strength Corrosion Resistant Precipitation Hardening Cast Steels*, in *Industrial Engineering*. 2010, Penn State University: Penn State University.

60. Vunnam, S., et al., *Effect of powder chemical composition on the as-built microstructure of 17-4 PH stainless steel processed by selective laser melting.* Additive Manufacturing, 2019. **30**: p. 1-12.

61. Hamlin, R.J., *Microstructural Evolution and Mechanical Properties of Simulated Heat Affected Zones in Cast Precipitation Hardened Stainless Steels 17-4 and 13-8+Mo* in *Materials Science and Engineering* 2015, Lehigh University.

62. Verhoeven, J.D., *Steel Metallurgy for the Non-Metallurgist*. 2007: ASM International.

63. Murayama, M., K. Hono, and Y. Katayama, *Microstructural evolution in a 17-4 PH stainless steel after aging at 400 °C*. Metallurgical and Materials Transactions A, 1999. **30**(2): p. 345-353.

64. Mirzadeh, H. and A. Najafizadeh, *Aging kinetics of 17-4 PH stainless steel.* Materials Chemistry and Physics, 2009. **116**(1): p. 119-124.

65. Bhambroo, R., et al., *Effect of reverted austenite on mechanical properties of precipitation hardenable 17-4 stainlesssteel.* Materials Science and Engineering A, 2013. **568**: p. 127-133.

66. Eizadjou, M., *Design of Advanced High Strength Steels*, in *Faculty of Engineering & IT/ Australian Centre for Microscopy and Microanalysis*. 2017, The University of Sydney.

67. Kaibyshev, R., *Microstructural evolution in 9%Cr heat resistant steels under creep conditions* Materials Science Forum, 2012. **715-716**: p. 813-818.

68. Koistinen, D.P. and R.E. Marburger, *A general equation prescribing the extent of the austenite-martensite transformation in pure iron-carbon alloys and plain carbon steels*. Acta Metallurgica, 1959. **7**(1): p. 59-60.

69. Barbier, D., *Extension of the Martensite Transformation Temperature Relation to Larger Alloying Elements and Contents.* Advanced Engineering Materials, 2014. **16**(1): p. 122-127.

70. Soleimani, M., A. Kalhor, and H. Mirzadeh, *Transformation-induced plasticity (TRIP) in advanced steels: A review.* Materials Science and Engineering: A, 2020. **795**: p. 140023.

71. Dieter, G.E. and D.J. Bacon, *Mechanical metallurgy*. 1988, London: McGraw-Hill.

72. Honeycombe, R.W.K. and H.K.D.H. Bhadeshia, *Steels : microstructure and properties*. 1995, London: Edward Arnold.

73. ASM, *ASM Handbook Volume 8, Mechanical Testing and Evaluation*. 2000, ASM International.

74. Dalmau, A., C. Richard, and A. Igual – Muñoz, *Degradation mechanisms in martensitic stainless steels: Wear, corrosion and tribocorrosion appraisal.* Tribology International, 2018. **121**: p. 167-179.

75. Gülsoy, H.Ö., *Dry sliding wear in injection molded 17-4 PH stainless steel powder with nickel boride additions.* Wear, 2007. **262**(3): p. 491-497.

76. Colaço, R. and R. Vilar, *On the influence of retained austenite in the abrasive wear behaviour of a laser surface melted tool steel.* Wear, 2005. **258**(1): p. 225-231.

77. Esfandiari, M. and H. Dong, *The corrosion and corrosion–wear behaviour of plasma nitrided 17-4PH precipitation hardening stainless steel.* Surface and Coatings Technology, 2007. **202**(3): p. 466-478.

78. Manova, D., et al., *Wear behaviour of martensitic stainless steel after PIII surface treatment.* Surface and Coatings Technology, 2005. **200**(1): p. 137-140.

79. ASM, *ASM Handbook Volume 1, Properties and Selection: Nonferrous Alloys and Special-Purpose Materials*. 1990.

80. Lewandowski, J.J. and M. Seifi, *Metal Additive Manufacturing: A Review of Mechanical Properties*, in *Annual Review of Materials Research*. 2016. p. 151-186.

81. Lütjering, G. and J.C. Williams, *Titanium*. Second edition ed. EngineeringMaterialsandProcesses. 2007: Springer.

82. Yadollahi, A. and N. Shamsaei, *Additive manufacturing of fatigue resistant materials: Challenges and opportunities.* International Journal of Fatigue, 2017. **98**: p. 14-31.

83. Collins, P.C., et al., *Microstructural Control of Additively Manufactured Metallic Materials.* Annual Review of Materials Research, 2016. **46**(1): p. 63-91.

84. Dilip, J.J.S., et al., *Influence of processing parameters on the evolution of melt pool, porosity, and microstructures in Ti-6Al-4V alloy parts fabricated by selective laser melting.* Progress in Additive Manufacturing, 2017. **2**(3): p. 157-167.

85. Pal, S., D. Igor, and T. Brajlih, *Physical Behaviors of Materials in Selective Laser Melting Process*, in *DAAAM International Scientific Book* 2018. p. 239-256.

86. Withers, P.J. and H.K.D.H. Bhadeshia, *Residual stress Part 2 – Nature and origins.* Materials Science and Technology, 2001. **17**(4): p. 366-375.

87. Mercelis, P. and J.P. Kruth, *Residual stresses in selective laser sintering and selective laser melting.* Rapid Prototyping Journal, 2006. **12**(5): p. 254-265.

88. Li, P., et al., *Critical assessment of the fatigue performance of additively manufactured Ti–6Al–4V and perspective for future research.* International Journal of Fatigue, 2016. **85**: p. 130-143.

89. Li, C., et al., *Residual Stress in Metal Additive Manufacturing.* Procedia CIRP, 2018. **71**: p. 348-353.

90. DebRoy, T., et al., *Additive manufacturing of metallic components – Process, structure and properties.* Progress in Materials Science, 2018. **92**: p. 112-224.

91. Elmer, J.W., et al., *The Effect of Ar and N-2 Shielding Gas on Laser Weld Porosity in Steel, Stainless Steels, and Nickel.* Weld J, 2015. **94(10)**.

92. Kudzal, A., et al., *Effect of scan pattern on the microstructure and mechanical properties of Powder Bed Fusion additive manufactured 17-4 stainless steel.* Materials & Design, 2017. **133**: p. 205-215.

93. Makoana, N.W., et al., *EVALUATION OF SINGLE TRACKS OF 17-4PH STEEL MANUFACTURED AT DIFFERENT POWER DENSITIES AND SCANNING SPEEDS BY SELECTIVE LASER MELTING.* 2016, 2016. **27**(3): p. 9.

94. *Weld Metal Solidification I: Grain Structure*, in *Welding Metallurgy*. p. 170-198.

95. Kobryn, P.A. and S.L. Semiatin, *Microstructure and texture evolution during solidification processing of Ti–6Al–4V,.* Journal of Materials Processing Technology,, 2003. **Volume 135, Issues 2–3,**: p. 330-339,.

96. Kobryn, P.A. and S.L. Semiatin, *Microstructure and texture evolution during solidification processing of Ti–6Al–4V.* Journal of Materials Processing Technology, 2003. **135**(2): p. 330-339.

97. Bajaj, P., et al., *Steels in additive manufacturing: A review of their microstructure and properties.* Materials Science and Engineering: A, 2020. **772**: p. 138633.

98. Alnajjar, M., et al., *Evidence of austenite by-passing in a stainless steel obtained from laser melting additive manufacturing.* Additive Manufacturing, 2019. **25**: p. 187-195.

99. Murr, L.E., et al., *Metal Fabrication by Additive Manufacturing Using Laser and Electron Beam Melting Technologies.* Journal of Materials Science and Technology, 2012. **28**(1): p. 1-14.

100. Vunnam, S., et al., *Effect of powder chemical composition on the as-built microstructure of 17-4 PH stainless steel processed by selective laser melting.* Additive Manufacturing, 2019. **30**: p. 100876.

101. Hu, Z., et al., *Experimental investigation on selective laser melting of 17-4PH stainless steel.* Optics and Laser Technology, 2017. **87**: p. 17-25.

102. Rashid, R., et al., *Effect of scan strategy on density and metallurgical properties of 17-4PH parts printed by Selective Laser Melting (SLM).* Journal of Materials Processing Technology, 2017. **249**: p. 502-511.

103. Lashgari, H.R., et al., *Microstructure, Tribological Properties and Corrosion Behaviour of Additively Manufactured 17-4PH Stainless Steel: Effects of Scanning Pattern, Build Orientation, and Single vs. Double scan.* Materials Today Communications, 2020. **25**: p. 101535.

104. Murr, L.E., et al., *Microstructures and Properties of 17-4 PH Stainless Steel Fabricated by Selective Laser Melting.* Journal of Materials Research and Technology, 2012. **1**(3): p. 167-177.

105. Zai, L., et al., *Laser Powder Bed Fusion of Precipitation-Hardened Martensitic Stainless Steels: A Review* Metals, 2020. **10**(2): p. 255.

106. Ramesh, C.S., C.K. Srinivas, and K. Srinivas, *Friction and wear behaviour of rapid prototype parts by direct metal laser sintering.* Tribology - Materials, Surfaces & Interfaces, 2007. **1**(2): p. 73-79.

107. Zhu, Y., et al., *Material characterization and lubricating behaviors of porous stainless steel fabricated by selective laser melting.* Journal of Materials Processing Technology, 2018. **262**: p. 41-52.

108. Kc, S., et al., *Tribological behavior of 17–4 PH stainless steel fabricated by traditional manufacturing and laser-based additive manufacturing methods.* Wear, 2019. **440-441**: p. 203100.

109. Lashgari, H.R., et al., *Microstructure, post thermal treatment response, and tribological properties of 3D printed 17-4 PH stainless steel.* Wear, 2020. **456-457**: p. 203367.

110. Bressan, J.D., et al., *Influence of hardness on the wear resistance of 17-4 PH stainless steel evaluated by the pin-on-disc testing.* Journal of Materials Processing Technology, 2008. **205**(1): p. 353-359.

111. Rafi, H.K., et al., *Microstructures and Mechanical Properties of Ti6Al4V Parts Fabricated by Selective Laser Melting and Electron Beam Melting.* Journal of Materials Engineering and Performance, 2013. **22**(12): p. 3872-3883.

112. Thijs, L., et al., *A study of the microstructural evolution during selective laser melting of Ti–6Al–4V.* Acta Materialia, 2010. **58**(9): p. 3303-3312.

113. Yadroitsev, I. and I. Smurov. *Surface morphology in selective laser melting of metal powders*. in *Physics Procedia*. 2011.

114. Lu, J., et al., *In-situ investigation of the anisotropic mechanical properties of laser direct metal deposition Ti6Al4V alloy.* Materials Science and Engineering: A, 2018. **712**: p. 199-205.

115. Leuders, S., et al., *On the mechanical behaviour of titanium alloy TiAl6V4 manufactured by selective laser melting: Fatigue resistance and crack growth performance.* International Journal of Fatigue, 2013. **48**: p. 300-307.

116. Gorsse, S., et al., *Additive manufacturing of metals: a brief review of the characteristic microstructures and properties of steels, Ti-6Al-4V and high-entropy alloys.* Science and Technology of Advanced Materials, 2017. **18**(1): p. 584-610.

117. Criales, L.E., et al., *Laser powder bed fusion of nickel alloy 625: Experimental investigations of effects of process parameters on melt pool size and shape with spatter analysis.* International Journal of Machine Tools and Manufacture, 2017. **121**: p. 22-36.

118. ASTM, *ASTM E384, Standard Test Method for Microindentation Hardness of Materials*. 2017.

119. ASTM, *ASTM E466, Standard Practice for Conducting Force Controlled Constant Amplitude Axial Fatigue Tests of Metallic Materials*. 2015.

120. Gourgues-Lorenzon, A.F., *Application of electron backscatter diffraction to the study of phase transformations.* International Materials Reviews, 2007. **52**(2): p. 65-128.

121. Facchini, L., et al., *Metastable Austenite in 17–4 Precipitation-Hardening Stainless Steel Produced by Selective Laser Melting.* Advanced Engineering Materials, 2010. **12**(3): p. 184-188.

122. Song, Y.Y., et al., *Reversed austenite in 0Cr13Ni4Mo martensitic stainless steels*. Materials Chemistry and Physics, 2014. **143**(2): p. 728-734.

123. Lashgari, H.R., et al., *Microstructure, post thermal treatment response, and tribological properties of 3D printed 17-4 PH stainless steel.* Wear, 2020. **456-457**.

124. Meredith, S.D., et al., *Impact of composition on the heat treatment response of additively manufactured 17–4 PH grade stainless steel.* Materials Science and Engineering: A, 2018. **738**: p. 44-56.

125. Bhaduri, A.K., et al., *Optimised post-weld heat treatment procedures and heat input for welding 17–4PH stainless steel.* Science and Technology of Welding and Joining, 1999. **4**(5): p. 295-101.

126. Yadollahi, A., et al., *Effects of building orientation and heat treatment on fatigue behavior of selective laser melted 17-4 PH stainless steel.* International Journal of Fatigue, 2017. **94**: p. 218-235.

127. Gao, S., et al., *Recrystallization-based grain boundary engineering of 316L stainless steel produced via selective laser melting.* Acta Materialia, 2020. **200**: p. 366-377.

128. Shellabear, M. and O. Nyrhila, *Materials for Direct Metal Laser-Sintering*, in *Whitepaper*. EOS GmbH.

129. Pasebani, S., et al., *Effects of atomizing media and post processing on mechanical properties of 17-4 PH stainless steel manufactured via selective laser melting.* Additive Manufacturing, 2018. **22**: p. 127-137.

130. Yadollahi, A., et al., *Mechanical and Microstructural Properties of Selective Laser Melted 17-4 PH Stainless Steel.* 2015(57359): p. V02AT02A014.

131. *Tensile Testing up to 10kN*. Available from: https://www.kammrath-weiss.com/en/products/materials/tensile-compression.html.

132. Koh-ichi Sugimoto, M.M., Mitsuyuki Kobayashi, Hidenori Shirasawa, *Effects of Second Phase Morphology on Retained Austenite Morphology and Tensile Properties in a TRIP-aided Dual-phase Steel Sheet.* ISIJ International, 1993. **33**: p. 775-782.

133. Huh, M.Y. and O. Engler, *Effect of intermediate annealing on texture, formability and ridging of 17%Cr ferritic stainless steel sheet.* Materials Science and Engineering: A, 2001. **308**(1): p. 74-87.

134. Huh, M.-Y., et al., *Effect of Through-Thickness Macro and Micro-Texture Gradients on Ridging of 17%Cr Ferritic Stainless Steel Sheet.* steel research international, 2005. **76**(11): p. 797-806.

135. Raabe, D. and K. Lücke, *Selective particle drag during primary recrystallization of Fe-Cr alloys.* Scripta Metallurgica et Materialia, 1992. **26**(1): p. 19-24.

136. Hölscher, M., D. Raabe, and K. Lücke, *Rolling and recrystallization textures of bcc steels.* Steel Research, 1991. **62**(12): p. 567-575.

137. Hashmi, S., et al., *Comprehensive Materials Processing*. 2014.

138. Tewary, N.K., et al., *Influence of cold rolling on microstructure, texture and mechanical properties of low carbon high Mn TWIP steel.* Materials Science and Engineering: A, 2014. **615**: p. 405-415.

139. Oh, K.H., et al., *The evolution of the rolling and recrystallization textures in cold-rolled Al containing high Mn austenitic steels.* Materials Chemistry and Physics, 2015. **161**: p. 9-18.

140. ASTM, *ASTM E8/E8M, Standard Test Methods for Tension Testing of Metallic Materials*. 2016.

141. ASTM, *ASTM F2971, Standard Practice for Reporting Data for Test Specimens Prepared by Additive Manufacturing*. 2013.

142. Zhou, T., et al., *Exploring the relationship between the microstructure and strength of fresh and tempered martensite in a maraging stainless steel Fe–15Cr–5Ni.* Materials Science and Engineering: A, 2019. **745**: p. 420-428.

143. Colaço, R. and R. Vilar, *Stabilisation of retained austenite in laser surface melted tool steels.* Materials Science and Engineering: A, 2004. **385**(1): p. 123-127.

144. Lashgari, H.R., et al., *Microstructure, Tribological Properties and Corrosion Behaviour of Additively Manufactured 17-4PH Stainless Steel: Effects of Scanning Pattern, Build Orientation, and Single vs. Double scan.* Materials Today Communications, 2020. **25**.

145. Bhambroo, R., et al., *Effect of reverted austenite on mechanical properties of precipitation hardenable 17-4 stainlesssteel.* Materials Science and Engineering: A, 2013. **568**: p. 127-133.

146. Hsiao, C.N., C.S. Chiou, and J.R. Yang, *Aging reactions in a 17-4 PH stainless steel.* Materials Chemistry and Physics, 2002. **74**(2): p. 134-142.

147. Viswanathan, U.K., S. Banerjee, and R. Krishnan, *Effects of aging on the microstructure of 17-4 PH stainless steel.* Materials Science and Engineering: A, 1988. **104**: p. 181-189.

148. Rice, S.L., H. Nowotny, and S.F. Wayne, *Characteristics of metallic subsurface zones in sliding and impact wear.* Wear, 1981. **74**(1): p. 131-142.

149. Eizadjou, M., et al., *Sliding Wear behavior of Severely Deformed 6061 Aluminum Alloy by Accumulative Roll Bonding (ARB) Process* Materials Science Forum, 2010. **667-669**: p. 1107-1112.

150. ASTM, *ASTM G99, Standard Test Method for Wear Testing with a Pin-on-Disk Apparatus*. 2017.

151. ASTM, *ASTM B348/B348M, Standard Specification for Titanium and Titanium Alloy Bars and Billets*. 2019.

152. Xu, W., et al., *Ti-6Al-4V Additively Manufactured by Selective Laser Melting with Superior Mechanical Properties.* JOM, 2015. **67**(3): p. 668-673.

153. Buciumeanu, M., et al., *Tribocorrosion behavior of additive manufactured Ti-6Al-4V biomedical alloy.* Tribology International, 2018. **Volume 119**: p. 381-388.

154. Zhang, D., et al., *Grain Refinement of Alloys in Fusion-Based Additive Manufacturing Processes.* Metallurgical and Materials Transactions A, 2020. **51**(9): p. 4341-4359.

155. Dowling, L., et al., *A review of critical repeatability and reproducibility issues in powder bed fusion.* Materials & Design, 2020. **186**: p. 108346.